Electrochemical and chemical reactivities of titanium oxide-based materials with chloroaluminate ionic liquid electrolyte for aluminium batteries

Maxime Sorriaux

Sorbonne Université

ED 388 – Chimie Physique et Chimie Analytique de Paris Centre

Laboratoire Physicochimie des Electrolytes et Nanosystèmes Interfaciaux

Réactivité électrochimique et chimique des matériaux à base d'oxyde de titane avec un liquide ionique chloroaluminé pour batteries à l'aluminium

Par Maxime SORRIAUX

Thèse de doctorat de Chimie

Dirigée par Damien DAMBOURNET

Présentée et soutenue publiquement le 27/03/2024

Devant un jury composé de :

Dr. Valérie PRALONG	Directeur de Recherche, CRISMAT, Caen	Rapporteur
Dr. Romain BERTHELOT	Chargé de Recherche, ICGM, Montpellier	Rapporteur
Dr. Sathiya MARIYAPPAN	Chargé de Recherche, Collège de France, Paris	Examinateur
Pr. Christophe LEGEIN	Professeur, Le Mans Université, Le Mans	Examinateur
Pr. Christel LABERTY-ROBERT	Professeur, Sorbonne Université, Paris	Examinateur
Dr. Damien DAMBOURNET	Maître de conférences, Sorbonne Université, Paris	Directeur

Sorbonne Université

ED 388 – Chimie Physique et Chimie Analytique de Paris Centre

Laboratoire Physicochimie des Electrolytes et Nanosystèmes Interfaciaux

Electrochemical and chemical reactivities of titanium oxide-based materials with chloroaluminate ionic liquid electrolyte for aluminium batteries

By Maxime SORRIAUX

Ph.D. Thesis in Chemistry

Supervised by Damien DAMBOURNET

Presented and defended in public on 27/03/2024

In front of the jury:

Dr. Valérie PRALONG	Senior Researcher, CRISMAT, Caen	Referee
Dr. Romain BERTHELOT	Researcher, ICGM, Montpellier	Referee
Dr. Sathiya MARIYAPPAN	Researcher, Collège de France, Paris	Examiner
Pr. Christophe LEGEIN	Professor, Le Mans Université, Le Mans	Examiner
Pr. Christel LABERTY-ROBERT	Professor, Sorbonne Université, Paris	Examiner
Dr. Damien DAMBOURNET	Associate Professor, Sorbonne Université, Paris	Supervisor

Abstract

Societal changes drive the need for new energy storage systems. Forecasts consider that lithium-ion batteries will cease to meet the demand for energy storage within the next decade. In this regard, the development of new battery technologies is mandatory. Since 2015, interest in the Al-ion battery has progressively grown. Indeed, the aluminium ion Al^{3+} displays a high theoretical specific capacity (8.05 Ah/cm^3), and is widely abundant. These properties made the aluminium ion a promising charge carrier for battery systems. This work proposes to study both the electrolyte and the positive electrode material, for the electrochemical intercalation of Al^{3+} ions. The selected electrolyte is the acidic EMImCl:$AlCl_3$ ionic liquid. Investigations have evidenced the dynamic equilibria, leading to the formation of high oligomeric anionic species and long-range structuration. Three positive electrode materials, based on defective titanium oxide derivatives, have been proposed. The Al^{3+} ion intercalation has been witnessed to occur in both the crystal interstitial sites, and the defective titanium vacancy sites of the electrode materials. Nonetheless, cyclability was not achieved, as the monitored discharge-charge specific capacity was observed to decay quickly. Further analyses concluded on the irreversible intercalation of the aluminium ion, and on the dissolution of the electrode material by the acidic electrolyte.

Contents

General introduction

Energy is a key sector of human society development. Each energy vector is characterised by its transfer efficiency and storage properties. For instance, the great storage properties of oil made possible the development of most of the modern transportation means. Nonetheless, the higher energetical efficiency provided by electricity made it favoured in late history. Overall, technological progress has always improved the energetical efficiency of the energy vectors. Paradoxically, along with this energetical efficiency improvement, global energy consumption is observed to increase. For example, **Figure 1.** shows the share in worldwide energy consumption from 1965 to 2022, by source. There, global consumption is seen to dramatically increase by around 290%, over the nearly 60 years span. This phenomenon has been theorised and is known as the Khazzoom-Brookes postulate [1]. In short, technological progress makes the use of energy both more efficient and more available. Consequently, over time, a cheaper amount of energy is required to produce the same work. Therefore, as a rebound effect, an increase in the consumption of energy occurs.

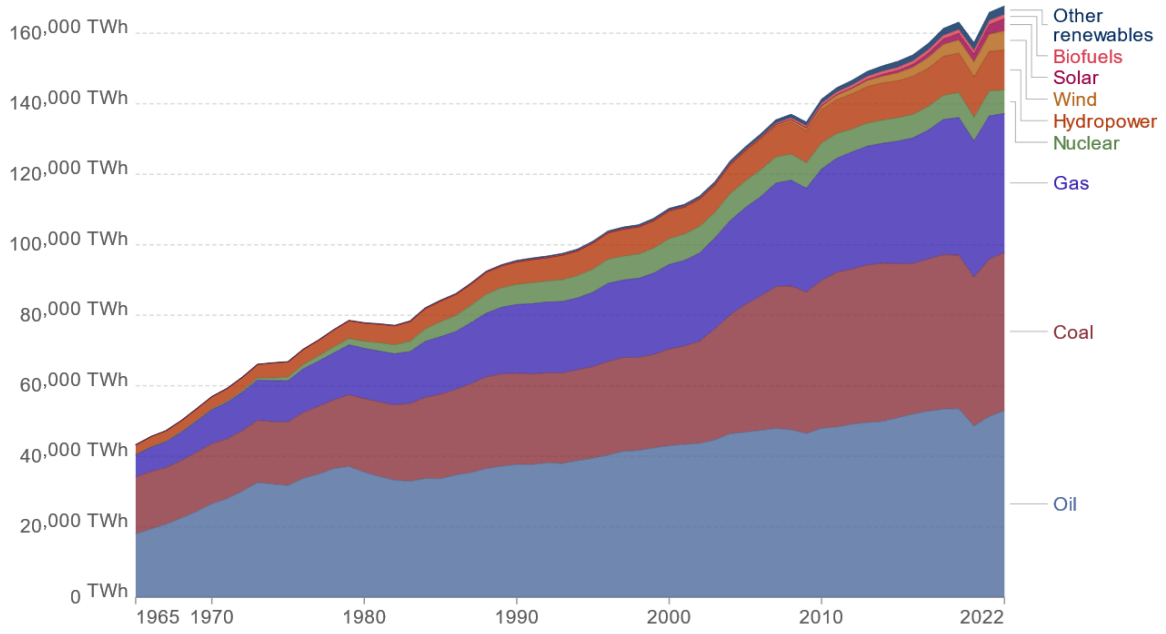

Figure 1. Share in the worldwide energy consumption by source, from 1965 to 2022. Adapted from [2].

Nowadays, this energy consumption is mainly based on fossil fuels. Their use releases alarming levels of greenhouse gas into the atmosphere (CO_2, CH_4, ...) [3], causing global warming. An energetical transition, and sustainable development are therefore needed. Among the various resolutions undertaken by nations worldwide, such as the Paris Agreement [4], the deployment of renewable energy production facilities appears inevitable. These power plants produce electricity as energetical vector. However, unlike fossil fuels, electricity is notoriously badly stored. Electrical storage systems (such as rechargeable batteries, hydrogen, flywheels, Carnot batteries, ...) are all limited by their efficiency, energy and power density, volume, life span, or cost.

Among these, the rechargeable battery is the most promising system for wide use in renewable energy storage. The dominant technology is the lithium-ion battery. Its high energy density allowed for the widespread of battery-based devices in modern society. The evolution of the demand for Li-ion batteries is forecasted to skyrocket in the near future, due to the mass conversion to electric vehicles [5]. Nonetheless, several issues are raised by the extensive use of Li-ion batteries. Indeed, several critical metals are needed in Li-ion batteries (such as Li, Co, Ni, ...). Their mining raises numerous environmental, geopolitical, and ethical issues [6–9]. In addition, this ever-growing demand for lithium is foreseen to cross the supply between 2030 and 2040 [5]: there is not enough lithium on earth to meet the world demand.

There is therefore an absolute need for other battery technologies, to be developed. In this view, several approaches are proposed, based on earth-abundant elements. The most regarded technology for short-term use is the sodium-ion battery. However, in the long term, multivalent ion batteries (Mg^{2+}, Al^{3+}, ...) gain more focus. This is due to their higher theoretical capacity (2.06 Ah/cm^3 for Li, 3.83 Ah/cm^3 for Mg, and 8.04 Ah/cm^3 for Al) , promising high energy densities. Notably, aluminium is the element exhibiting the highest theoretical properties, and is the most abundant metal on earth.

However, the development of such systems involves unexplored chemistries. Indeed, most of the systems developed for the Li-ion technology are not viable for multivalent ion batteries. Two major battery components challenge the development of these batteries: the positive electrode, and the electrolyte.

In aluminium-ion battery research, the proposed electrolytes are mainly ionic liquids, based on the aluminium chloride $AlCl_3$ chemistry [10]. Their reactivity ensures the aluminium ion delivery necessary to operate the battery. Nonetheless, their high acidity and their expensive cost are still drawbacks to overcome. On the other hand, the positive electrode must fulfil one task: reversibly intercalate the chosen ion. This is particularly challenging in the case of aluminium ion batteries. Indeed, the aluminium ion exhibits a strong polarising power, making this diffusion slow and its intercalation irreversible. One proposed way to overcome these difficulties is the use of amorphous materials [11]. This particularly aims at enhancing the solid-state diffusion of the Al^{3+} ion. In addition, the defect chemistry has been reported to be suited for ion intercalations [12–14]. Indeed, defects (such as cationic vacancies) can be favourable insertion sites for ions, opening the door to reversibility.

The objective of this thesis is therefore to assess the compatibility between the electrolyte and the positive electrode materials, for aluminium-ion batteries. To do so, battery systems will be proposed, using three titanate materials at the positive electrode, and an acidic chloroaluminate ionic liquid as the electrolyte. This manuscript is structured in six chapters:

The first chapter provides an overview of the current research for rechargeable battery technologies. There, the fundamentals of battery science are summarised, taking as an example the Li-ion battery. The discussion then focuses on the need for new battery systems, and the choice of aluminium as the charge carrier for the battery system. The theoretical advantages and inconveniences of the aluminium-ion battery are therefore discussed. Finally, a review of the current research on Al-ion batteries is proposed.

The second chapter describes both the analytical techniques and the experimental methods used throughout this work. The basics and principles behind the main analytical techniques are therefore explained. In addition, the protocols used for the various syntheses performed are provided. Lastly, the setups used for the electrochemical measurements are detailed.

The third chapter focuses on the aluminium ion battery electrolyte. There, a brief review of the literature is first proposed. Then, the EMImCl:$AlCl_3$ ionic liquid is selected as the reference electrolyte for this work. The chemical and structural features of this chloroaluminate ionic liquid are investigated.

The fourth chapter presents the studied positive electrode materials. These are three titanate materials: a defective amorphous lepidocrocite-type titanate, a defective anatase, and a pure anatase. Characterisations will provide both chemical and structural features of these three materials.

The fifth chapter investigates a battery system using the defective amorphous lepidocrocite-type titanate material as the positive electrode, and the acidic 1:1.5 EMImCl:$AlCl_3$ ionic liquid as the electrolyte. The electrochemical properties of the hereby proposed battery system are examined, in regard to the Al^{3+} ion intercalation. This chapter also addresses issues from chemical compatibility between the electrode material and the electrolyte.

The sixth chapter investigates electrode materials closely related to the lepidocrocite-type titanate material, in the same electrochemical system as in the fifth chapter. These electrode materials are the defective crystallised anatase material, and the crystallised anatase material. The chemical and electrochemical properties of these three analogous electrode materials are then discussed.

Chapter 1. Aluminium-ion batteries state of the art

Batteries are energy storage devices, that are able to perform electrochemical reactions (redox) to convert stored chemical energy into electrical energy. In addition, batteries can reverse the electrochemical reactions to deliver the electrical energy back to an external electrical circuit. In this view, batteries can be both used as electrolytic cells and galvanic cells respectively. Hereafter, the terms 'electrochemical cell' and 'battery' will be used indifferently.

Batteries are therefore used in cycles, alternating between an electrolytic and a galvanic use. When used as an electrolytic cell, the electrochemical cell stores electrons and undergoes what is called a charge. When used as a galvanic cell, the electrochemical cell provides electrons and undergoes what is called a discharge. For clarity, these cycles are referred to as 'discharge-charge cycles'.

In this chapter, the necessary basics to understand the state of the art of battery research will be provided. The composition, parameters, and mechanism occurring inside a battery will be explained. This will then allow to present the various kinds of batteries existing, and to showcase the current works on the aluminium-ion battery.

1. Battery fundamentals

As lithium-ion batteries are the current leading battery technology, this part will extensively rely on examples and illustrations from Li-ion batteries to provide a general description of the battery science fundamentals [15–17].

1.1 The electrochemical cell components

As illustrated in **Figure 2.**, an electrochemical cell consists of three main components: the positive electrode, the negative electrode, and the electrolyte.

The electrolyte is the intermediate medium, between the two electrodes. It can be aqueous or organic solutions, water- or solvent-in-salts, ionic liquids or solids. In either case, it is an ionic conductive material. The role of the electrolyte is to allow the battery charge carriers to transfer from one electrode to the other. These charge carriers are the required species, for the electrodes to undergo redox reactions. Ideally, a high conductivity of the charge carrier ions is looked for in the electrolyte. Moreover, additional factors are considered for the choice of the electrolyte such as: the physical and chemical compatibility towards the other battery components, the thermal and voltage stability, the viscosity, or the toxicity and safety hazards.

The positive electrode undergoes reduction during the discharge of the battery, and oxidation during the charge. The material of the positive electrode is chosen for its ability to perform the desired electrochemical reaction. Eventually, the chosen positive electrode material is limited by various properties (stability issues, poor ionic or electrical conductivity). In this case, the use of additives is common. Thus, the positive electrode material becomes a composite material, and the electrochemically active material is referred to as the 'active material'.

Symmetrically, the negative electrode is the one where oxidation occurs during the discharge, and reduction during the charge. The negative electrode is chosen according to the charge carrier nature. A metallic plate is used to exploit the high energy density stored in the metallic phase. Alternatively, graphitic materials can be used to avoid the various safety issues coming from the use of reactive metallic phases. Graphite is for example used, at the negative electrode, in most of the common Li-ion batteries.

Other components are also usually found inside batteries. For instance, the current collector ensures conductivity between the electrodes and the external electrical circuit, while the separator prevents short circuits. Notably, in order to be used, the battery must be connected to an external electrical circuit. This is virtually an external component of the battery system. All in all, these other components do not participate in the electrochemical reactions of the system, but allow to harness the energy stored in the battery.

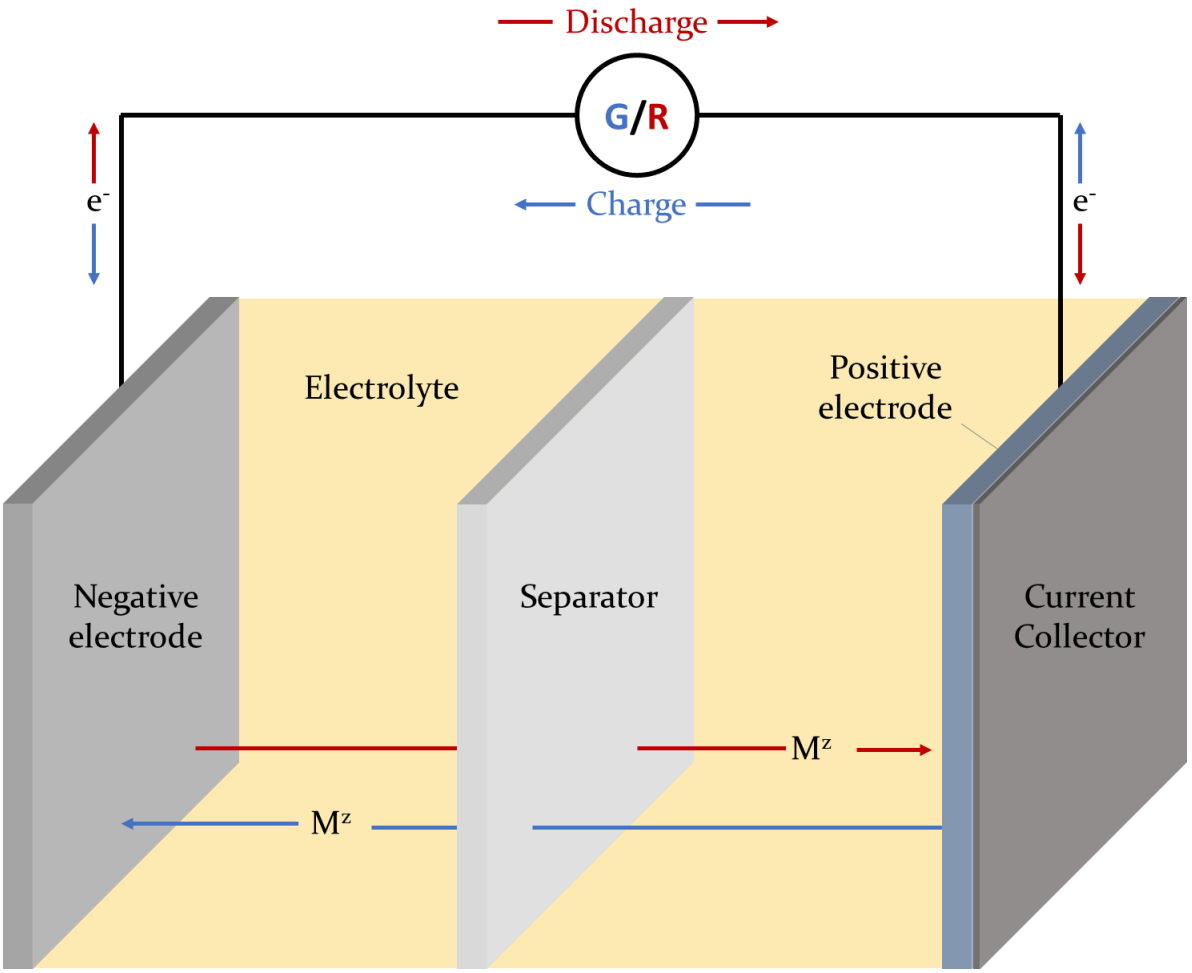

Figure 2. Scheme of a typical electrochemical cell. M indicates the charge carrier ion, and z its charge. Redrawn from [15].

1.2 Battery characteristics

Voltage

In an electrochemical cell, two redox reactions occur at the electrodes. The difference in the reduction potential of the negative electrode, and the oxidation potential of the positive electrode provides the theoretical cell voltage (V_{cell}). When the battery is used (discharge or charge), the redox reactions vary the measured potential (E) at the electrodes. The cell voltage then corresponds to the difference of potential between the positive and negative electrodes. Notably, the battery components are chosen to be electrochemically inactive within this voltage window.

Specific capacity

During the discharge and the charge of an electrochemical cell, electrons are exchanged through redox reactions at the electrodes. The quantity of charges stored at an electrode can therefore be measured. This quantity is called the specific capacity of the battery (Q in mAh/g), and is usually provided normalised by the mass of the active material in the electrode considered. In the case of an ideal total reaction, the theoretical specific capacity (Q_{th}) of a battery is given by:

$$Q_{th} = \frac{n_c n_e F}{M}$$

Where M is the molecular weight of the active material in the limiting electrode, F is the Faraday constant (26801.48 mAh/mol), n_c is the number of redox-active centres in the limiting electrode, and n_e is the number of electrons exchanged by the redox reaction. Practically, the specific capacity retrieved during the discharge phase (Q_{dis}) and the charge phase (Q_{cha}) of the cycle are differentiated. Those are measured by integrating the monitored current intensity (I), over the time of the discharge/charge (t), normalised by the mass of the active material in the electrode (m), following:

$$Q = \frac{It}{m}$$

Reversibility

During the charge, the reactions occurring at an electrode are the opposite of those occurring during the discharge. The reduced materials are oxidised back, and vice-versa. However, the electrochemical cells are not ideal systems. Various side reactions can occur between the discharge and the charge, such as phase transition, passivation of the electrode, or charge carrier neutralisation.

For this reason, a hysteresis can be observed between the discharge phase and the charge phase in a battery. As an illustration, **Figure 3.** shows the profile difference between the two phases of a cycle. The hysteresis between the two phases of the same cycle is called reversibility, and is estimated by the coulombic efficiency (CE) [18]. Usually, a battery lifespan is estimated satisfying if the CE remains over 98% over 100 cycles. The lifespan of a battery can also be described by the part of the capacity maintained after an n^{th} cycle. This is called the capacity retention (CR). Both the CE and CR are calculated by:

$$CE(\%) = 100\ \frac{Q_{cha}}{Q_{dis}} \quad ; \quad CR(\%) = 100\ \frac{Q_{n^{th}}}{Q_{1st}}$$

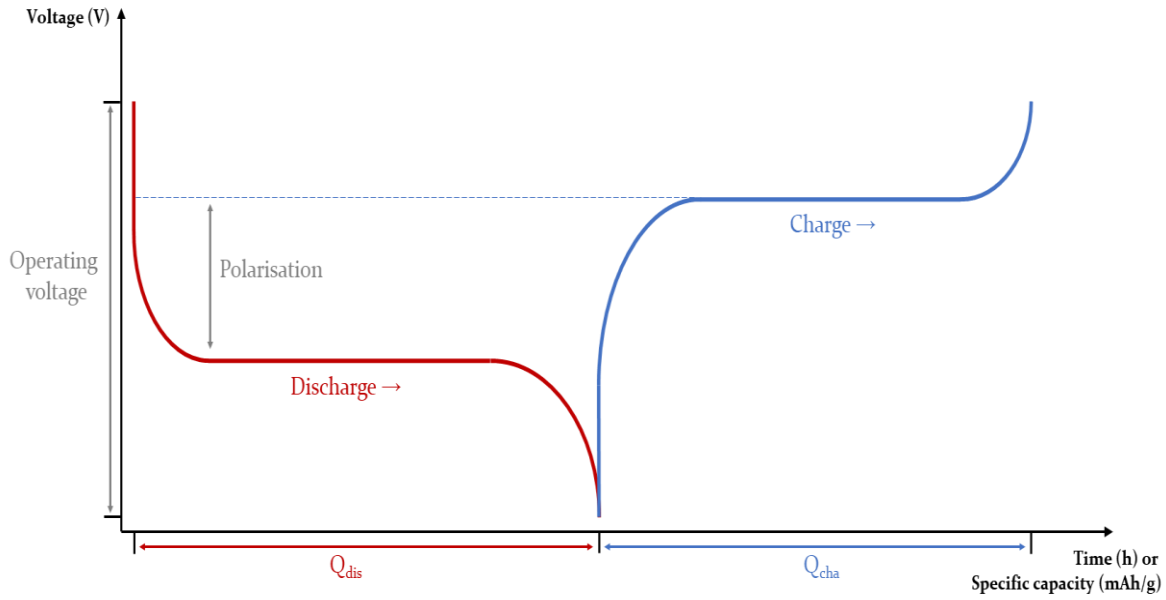

Figure 3. Typical discharge-charge profile of an electrode in an electrochemical cell. Redrawn from [17].

1.3 Electrochemical mechanisms

The first batteries developed were based on electro-plating/electro-stripping of the electrode materials. However, since the development of the Li-ion battery, the main reactional mechanisms have been moved to be a 'rocking-chair' mechanism. In this case, a charge carrier (*i.e.* the lithium-ion) transits back and forth between the two electrodes, through the electrolyte, during the charge and the discharge of the battery. This mechanism usually provides a higher specific capacity, longer cyclability, and improved safety compared to the previous ones.

In Li-ion batteries, the most common reaction is intercalation (or insertion) of the charge carrier. Indeed, Li^+ is a small ion that can be inserted in various materials, without major phase transition. This last point ensures the reversibility of the intercalation reaction. For example, in a battery using $LiCoO_2$ as the positive electrode and graphite as the negative electrode, the two electrode redox reactions are modulated by insertion/ de-insertion of the lithium-ion following:

$$\text{at the negative electrode :} \quad 6C + xLi^+ + xe^- \underset{\text{Discharge}}{\overset{\text{Charge}}{\rightleftharpoons}} Li_xC_6$$

$$\text{at the positive electrode :} \quad LiCoO_2 \underset{\text{Discharge}}{\overset{\text{Charge}}{\rightleftharpoons}} Li_{1-x}CoO_2 + xLi^+ + xe^-$$

Various materials have been shown to reversibly intercalate lithium-ions. Indeed, lithium is known to mostly form ionic bonds with other materials. In addition, to provide a high energy density, the diffusion of the lithium ion must also be high through the material. In this view, various structures have been identified to display both of these characteristics, as shown in **Figure 4.**. These channels can be 1D (olivine), 2D (lamellar metal oxides, metal sulphides, graphite), or 3D (spinel). These architectures allow the lithium-ion to intercalate inside bulk vacant sites, bulk interstitial sites, or inside the diffusion channels.

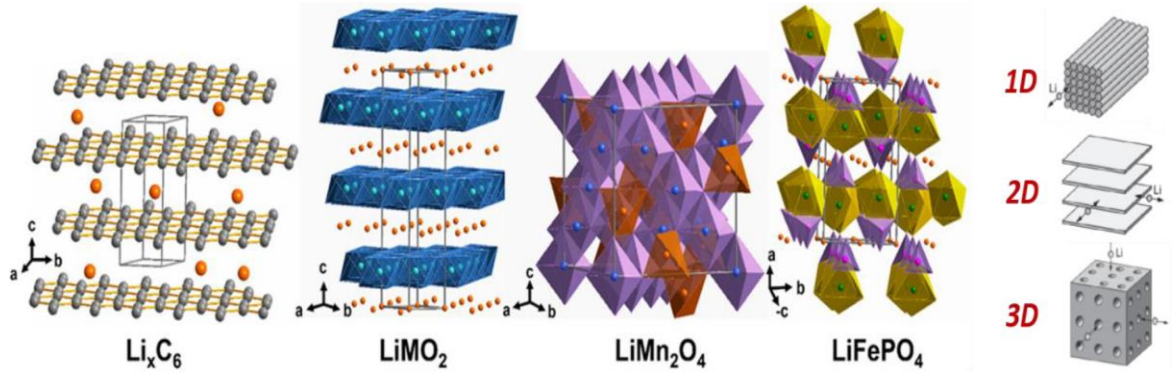

Figure 4. Various lithium-ion intercalation positive electrode materials. Consistently, the lithium-ion is displayed in orange. The diffusion of Li^+ can be whether 3D (such as in the spinel $LiMn_2O_4$), 2D (such as in the lamellar $LiMO_2$ or graphite), or 1D (such as in the olivine $LiFePO_4$). Adapted from [17].

Electrochemical cells can also operate through conversion mechanisms. In these systems, the electrode material is consumed and restored, by a reaction with the charge carrier. Conversion reactions are usually restricted to the positive electrode, and are defined as:

$$M_aX_n + (b.n)Li^+ + (b.n)e^- \underset{\text{Charge}}{\overset{\text{Discharge}}{\rightleftharpoons}} aM^0 + nLi_bX$$

Where M is a transition metal, and X is an anion. Notably, the transition metal is not necessary for conversion batteries, such as in Li-air [19] or Li-S [20] systems. Conversion batteries have been hypothesised to deliver higher specific capacities than intercalation ones, due to the exploitable multiple-redox of the metallic centre. However, no such system has yet shown satisfactory characteristics. Indeed, various additional constraints (such as poor conductivity and the formation of electrochemically inactive species) have severely hindered the obtained capacities.

Other batteries, exploiting the alloying/de-alloying of a metal electrode, have also been proposed [21–23]. These systems focus on alloying p-block elements (Si, Ge, and Sn), with the charge carrier of the battery. These systems stand out by transposing the redox centre to the charge carrier – rather than on the electrode material. Unfortunately, these batteries suffer from high electrode volume variations, preventing further applications.

Nevertheless, whether the studied battery is an electro-plating/electro-deposition, an insertion, a conversion, or an alloying battery, the redox reactions are controlled by the interface between the electrode and the electrolyte. This interface is indeed a mandatory gateway for the charge carrier, before diffusing in the electrode bulk. Therefore, every battery system has seen an increased interest in the development of nano-sized systems. However, the inherent drawbacks of the surface reactions remain. For instance, as the battery is charged (or discharged), redox reactions occur at the electrodes. These reactions change the composition – thus the surface charge – of the electrode. As an effect the double layer is altered, changing the species concentration gradient. This new gradient can cause the electrolyte ionic conductivity to be lowered, slowing the battery reaction kinetics. In addition, these surface localised constraints often result in the formation of passivation films, on top of the electrodes. These films are called Solid Electrolyte Interfaces (SEI) when localised upon the negative electrode material, or Cathode Electrolyte Interfaces (CEI) when upon the positive electrode. Their formation has been documented to severely impact the overall battery properties [24–26].

2. The aluminium-ion battery

Since their first commercialisation in 1991, Li-ion batteries have become the dominant battery technology. This is primarily due to the properties of the lithium-ion for intercalation. Indeed, the lithium-ion displays a high theoretical specific capacity of 3.86 Ah/g. In addition, Li^+ is a small ion (0.76 Å), allowing to diffuse through interstitial sites of the host material. Moreover, upon intercalation the bonds formed with the lithium ions are mostly ionic, making the intercalation process easily reversible. Lastly, the standard redox potential of Li^+/Li is at -3.04 V vs SHE. This is one of the lowest reported redox potentials, ensuring high energy storage at the device scale.

However, Li-ion batteries are not expected to meet the requirements of future energy storage technologies. Indeed, the demand for lithium is forecasted to cross the supply between 2030 and 2040 [5]. Furthermore, the positive electrode materials used in various Li-ion batteries bring additional constraints. For instance, LCO (Lithium Cobalt Oxides), NCA (Nickel Cobalt Aluminium), and NMC (Nickel Manganese Cobalt) batteries use Cobalt or Nickel in their electrode materials. Both of these metals are expensive, and their mining raises environmental and ethical issues [6–9]. For all these reasons, new energy storage technologies are needed.

2.1 Beyond lithium technologies

To meet the demand for such "beyond Lithium" technologies, various charge carriers are investigated. The alkali ions (Na^+, K^+) [27,28] are abundant, and exhibit electrochemical features similar to those of Li. Nonetheless, the energy densities of the Na-ion and K-ion batteries remain below those of the Li-ion batteries. One way to overcome this density limit is to use a charge carrier of higher valence. In this view, the multivalent (MV) technologies focus on the divalent alkaline earth ions (Mg^{2+}, Ca^{2+}) [29,30], but also on the Zn^{2+} [31] or Al^{3+} [32–35] ions. These MV batteries aim to exploit double- or triple-electron exchange reactions. As a guideline, Yang et al. [36] constructed the comparative graph showed in **Figure 5.**.

From all these ions, aluminium stands out as it presents by far the highest theoretical volumetric capacity (8.05 Ah/cm^3), and the closest theoretical gravimetric capacity (2.98 Ah/g) to the one of Li. These capacity values are inherited from the three charges carried by the Al^{3+} ion, paired with an even smaller ionic radius (0.53 Å) than the Li^+ ion. In addition, aluminium is cheap and is the most abundant metal on earth. All these characteristics have made the Al-ion battery a promising 'beyond Lithium' battery technology [37].

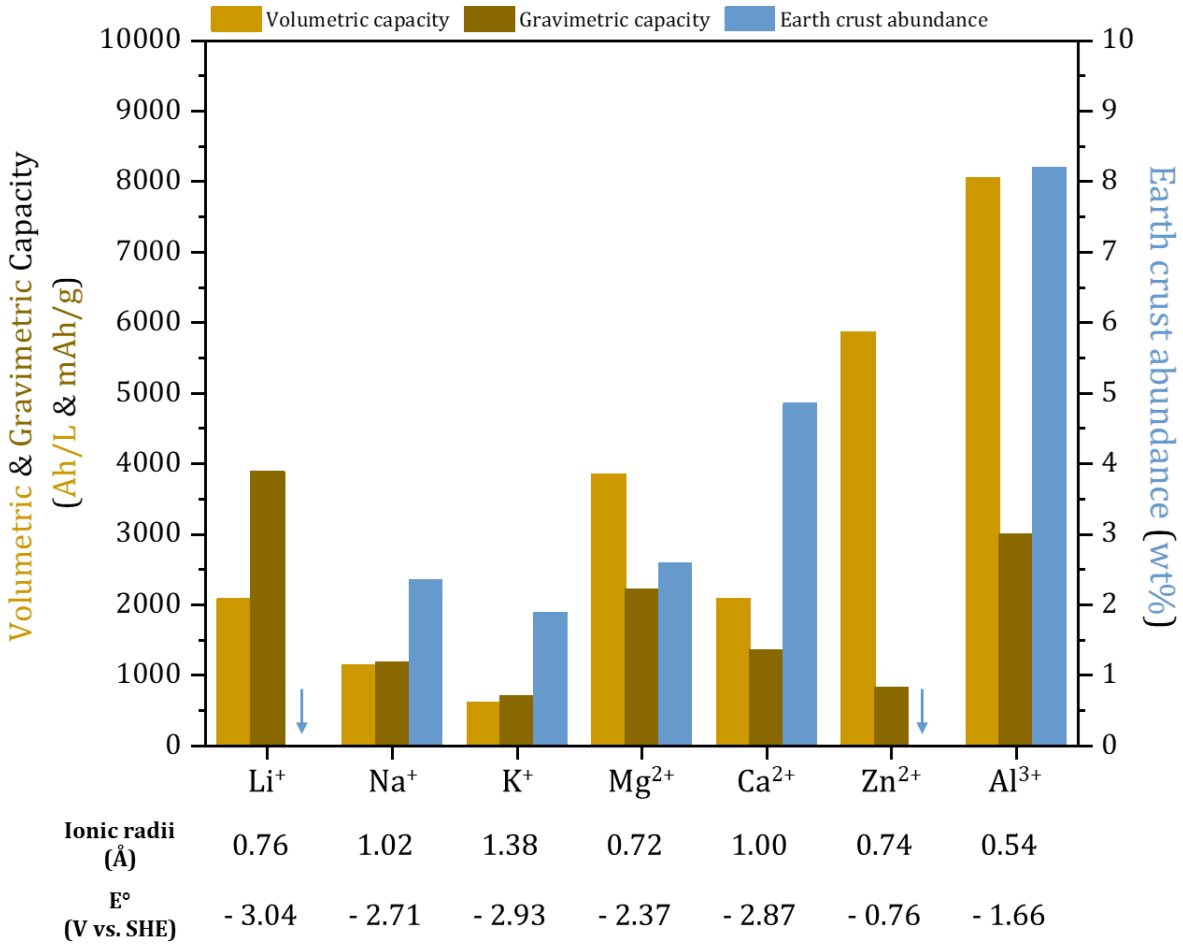

Figure 5. Comparison diagram of the elemental abundance, the gravimetric and volumetric capacities of different metal negative electrodes. The corresponding ionic radii and standard electrode potential are also joined. Adapted from [36].

However, the Al-ion is also exhibiting important drawbacks that are still needed to be overcome. The main one comes from the same reason as its former appeal: the charge over size ratio (Z/r). From this ratio derivates the polarising power (Z/r^2), which describes the ability of a cation to distort the electronic cloud of its first anionic neighbours. The polarising power of the aluminium ion is high (10.68 $e/Å^2$) in regards to the one of the lithium-ion (1.73 $e/Å^2$). Hence, the electrostatic interactions between the anionic sublattice of the host material and the intercalated aluminium ion are strong. The bonds formed therefore tend to be mostly covalent. Consequently, the aluminium intercalation is made rather irreversible. The high charge density of the aluminium ion also hinders its diffusion in the host material. Indeed, the strong electrostatic interactions generate a high energy diffusion barrier, which causes its solid-state diffusion to be sluggish in the host structure.

In addition, the standard redox potential of the Aluminium is -1.66 V vs SHE. This redox potential is high, in regards to the lithium ion one. The Al-ion batteries might then suffer from a poor final energy density. Finally, the intercalation chemistry of the Al^{3+} is yet ununderstood. The chemical reactions in the bulk of the electrode material are poorly documented, as well as those occurring at the electrode-electrolyte interface.

Nevertheless, the aluminium-ion battery technology remains attractive and some prospection on different Al-ion systems is already reported.

2.2 Aluminium-ion battery prospects

In the literature, the first traces of aluminium electrodeposition date back to the early 1970s [38,39]. The considered system used heated molten salts of Aluminium-Alkali-Chlorides to perform electrochemistry. These electrolytes were mainly used to study the electrochemical properties of the chloroaluminate ions, rather than the intercalation of aluminium ions. Further developments of these electrolytes were needed in order to be used in this way. A quick review of the various electrolytes for Al-ion batteries is later proposed in **Chapter 3**.

The global interest, in research for aluminium-ion batteries, only started in 2015, with the publication of an electrochemical cell operating at room temperature [40] . The proposed system achieved a 65 mAh/g capacity, over 7500 charge-discharge cycles, over a 2.0 V range. To do so, the research team used graphite as the positive electrode, metallic aluminium as the negative electrode, and the room temperature EMImCl:$AlCl_3$ ionic liquid as the electrolyte. The aluminium metal is used as the negative electrode to benefit from the aforementioned high theoretical specific capacity of the aluminium. The use of ionic liquid as the electrolyte is motivated by compatibility reasons. Indeed, in aqueous media, the aluminium negative electrode is covered by an oxide film, acting as a passivation layer. In acidic chloroaluminate ionic liquids – such as the EMImCl:$AlCl_3$ ionic liquid – no such passivation layer is reported, allowing to exploit the metallic aluminium negative electrode. In addition, the stability window of the ionic liquids (2.0 – 2.5 V) is higher than the one of aqueous electrolytes (1.23 V), enhancing the electrochemical cell voltage. Finally, graphite has been chosen as the positive electrode material for its ability to intercalate the aluminium chloride ion $AlCl_4^-$. The proposed battery system was therefore asymmetrical, using Al^{3+}/Al redox at the negative electrode and C[$AlCl_4^-$]/$AlCl_4^-$ at the positive electrode.

Then numerous other systems, using carbonaceous materials at the positive electrode have been developed [41–48]. This allowed to document the chemistry and mechanisms of the chloroaluminate ion $AlCl_4^-$ insertion into graphitic materials [49–51]. However, these battery systems suffer from the same inconvenience: the single-electron exchange mechanism. Indeed, the intercalation of the chloroaluminate anion only provides only a single charge. Therefore, the obtained capacity is highly limited. Further investigations on organic-based positive electrode materials archived intercalation of other chloroaluminate ions ($AlCl_2^+$ and $AlCl^{2+}$) [52–56]. But to this date, no intercalation of the trivalent Al^{3+} ion was reported in such electrode materials.

Notably, research was performed on non-organic non-metal electrode materials for Al-ion batteries. B, N, and P based species were therefore investigated as the positive electrode for conversion batteries [37]. However, their cyclability was shown to quickly decay, as their development remains in a too early stage.

From there, the quest for a positive electrode material, that is able to reversibly intercalate the trivalent Al^{3+} ion, is mainly pursued by inorganic transition metal-based material. Metal halide positive electrodes were discarded early due to the solubility of such materials in the chloroaluminate ionic liquids [57,58]. For this reason, research focuses on metal chalcogens positive electrode materials. In this view, various positive electrode materials were then proposed for Al-ion battery applications [32,34–36,59].

The first chalcogen-based positive electrode materials developed were transition metal sulphides. The choice of sulphur over oxygen is motivated by the lower electronegativity, and thus the weaker bonds formed with it. Soon, the Chevrel phase was identified to be able to electrochemically intercalate the aluminium ion [60–62]. Indeed, this material is composed of Mo_6S_8 octahedral clusters, linked to one another by two S bonds. As illustrated in **Figure 6.**, in between each of these Mo_6S_8 building blocks, two kinds of interstitial sites exist in the structure. This phase was first investigated to intercalate the Mg^{2+} ion, but has also shown to be able to intercalate the Al^{3+} ion too, although through other intercalation mechanisms.

Other sulphide materials were also reported as positive electrode materials. These exploit different architectures to enhance the Al^{3+} ion diffusion. For instance, 3D materials (Ni_3S_2 [63], Co_9S_8 [64]), as well as 2D lamellar materials (WS_2 [65], MoS_2 [66,67], TiS_2 [68,69], VS_2 [70]), have all been reported to reversibly intercalate the aluminium ion. Notably, amorphous transition metal sulphide materials have also been reported to display enhanced capacities when used as host materials for Al^{3+} intercalation [11]. However, these systems suffer from a reduced voltage, imposed by the sulphide materials.

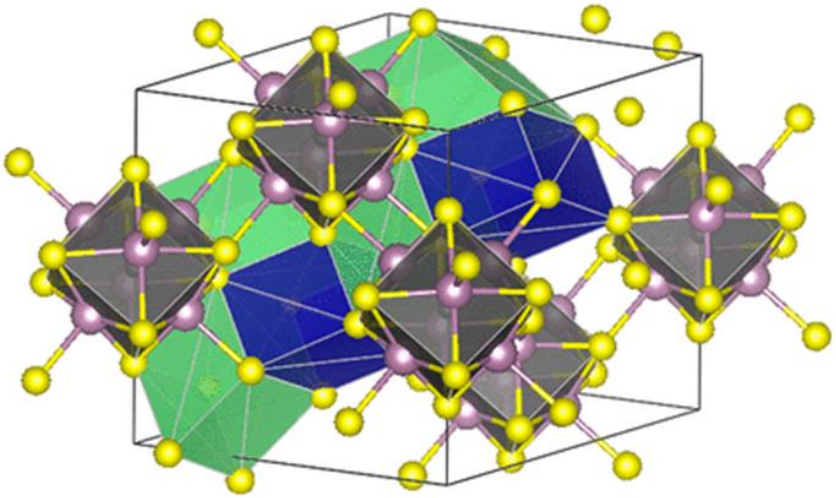

Figure 6. Structure of the Chevrel phase. Molybdenum are displayed in pink, and sulphur in yellow. The Mo_6S_8 building block is shown in the grey area, and the insertion sites in blue and green. Adapted from [71].

Heavier chalcogens, such as selenium and tellurium, displayed similar promising positive electrode material properties. However, these metal-selenides or -tellurides systems likewise suffer from the higher molecular weight of Se and Te atoms [72–74]. Nonetheless, the pure chalcogens are considered for conversion-type aluminium batteries positive electrodes. Indeed, several works investigate the so-called Al-S [75–77], Al-Se [78], and Al-Te [79] batteries.

Finally, the metal oxide materials were for long considered electrochemically inactive toward the Al^{3+} intercalation. Indeed, most of the commonly used positive electrode material for Li-ion systems does not accept aluminium ion intercalation. However, some notable materials were observed to display satisfying electrochemical behaviours: MnO_2 [80,81], VO_2 [82], V_2O_5 [83–85], and TiO_2 [86–89].

Vanadium oxides were the first to be regarded as positive electrode materials for aluminium-ion batteries. The vanadium pentoxide V_2O_5 has been the most researched among these metal oxide materials. However, Wen et al. proved the chemical incapability between this positive electrode material and the chloroaluminate ionic liquid [90]. They observed a dissolution of the oxide positive electrode material, and the appearance of mixed subspecies, such as: $VOCl_3$, VO_2Cl, and $AlCl_3VO_3^-$.

After the vanadate, the titanates are the most regarded positive electrode materials. Interstitial sites of the anatase phase TiO_2 have been shown to intercalate the Al^{3+} ion. However, the retrieved specific capacity is low at only 25 mAh/g [86]. This poor capacity has been overcome by Wang et al. by design on the material morphology [87]. Concomitantly, Koketsu et al. [14] developed a fluorinated anatase, able to present a 120 mAh/g specific capacity. This enhanced behaviour originates from the structural defects of the material. Indeed, the introduction of fluorine in the anatase structure caused the generation of titanium vacancies, as illustrated in **Figure 7.**. These cationic vacancies are favourable and accessible insertion sites for the aluminium ions.

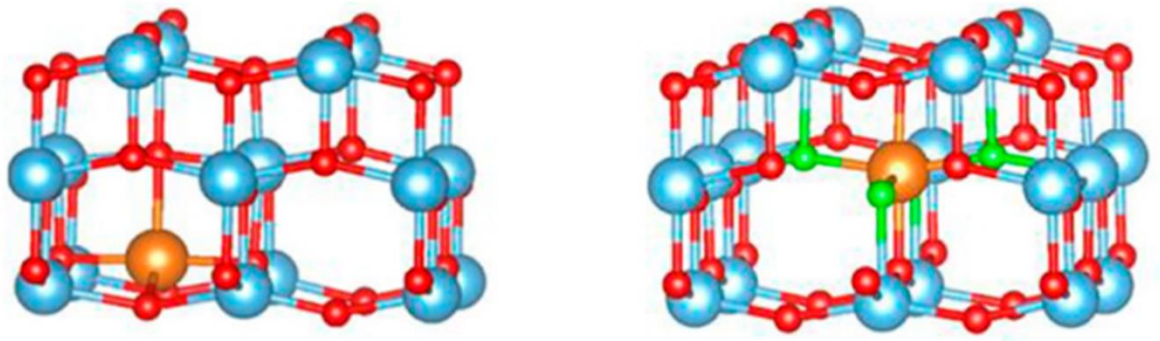

Figure 7. Structure of the anatase (left) and the defective fluorinated anatase (right). A metal ion is shown inserted in the interstitial site of the anatase, and in the titanium vacancy of the fluorinated one. Titanium is displayed in blue, oxygen in red, fluorine in green, and the inserted metal ion in orange. Adapted from [14].

Chapter 2. Analytical & experimental methods

1. Analytical characterisations

In this section, all the analytical techniques used throughout this work will be presented. Fundamentals about each method will be provided. These presentations do not intend to provide exhaustive descriptions, but rather to provide the necessary information to understand the following works.

1.1 Scattering techniques

Scattering techniques are widely used across fields of material science and chemistry. This is due to the broad range of data provided (from the local environments to the long-range orderings) about the sample.

Scattering techniques are usually defined as experimental methods, that observe the effects, on an incident radiation, of an interaction with matter. The incident radiation is usually electromagnetic radiation (photons). Nonetheless, this radiation is commonly extended to electron beam, or neutron beam as well. In this work, only electromagnetic radiation is used.

The scattering phenomenon exhibits two main properties: the coherence and the elasticity [91]. The coherence of the scattering refers to the homogeneity of the scattered radiation, across the sample. A scattering is called coherent if the scattered radiation emanates from a homogeneous behaviour of a group of particles, and is incoherent otherwise. The elasticity of the scattering refers to the change in energy of the scattered radiation. A scattering is called elastic if the energy of the scattered radiation is unchanged, and inelastic if dissipated. Each of these properties is caused by specific matter behaviours, from the sample. These therefore yield different insights on the probed material.

Elastic Bragg scattering

Bragg diffraction is a coherent elastic scattering technique, allowing for characterising the long-range orderings of a sample. The probed sample can be in various states (monocrystalline, powder, …) The diffraction phenomenon happens, at an angle θ, for the wavelength λ of the incident radiation which is about the same order as the lattice spacing d_{hkl} of the probed sample, following:

$$\lambda = 2d_{hkl}\sin(\theta)$$

In this case, the spacing between each lattice plane hkl acts as a new radiation source. This is typically observed when using X-rays ($\lambda \sim 1$ Å) as the incident radiation. For this reason, this technique is usually referred as to X-ray diffraction (XRD). The resulting figure is a diffraction diagram, expressed as a function of d_{hkl} or 2θ.

Typical diffraction diagrams exhibit well-defined peaks (called Bragg peaks). These peaks are parameterised by the crystalline lattices, and thus the long-range orderings of the probed sample. From the Bragg peak position, the crystalline system and unit cell are retrievable. From the peak intensities, the atomic nature of the crystal is obtainable. From the peak shapes, the disorder is estimable. Indeed, any periodicity breaks (defects, internal strains, distortions, …) contribute to the signal broadening. Eventually, for an amorphous sample, only a diffuse signal is observable.

One way to quantitively estimate the disorder in a sample, from an ideal crystalline reference, is provided by diffraction data refinements. Various models exist, such as Lebail or Rietveld, depending on which parameters are refined. For instance, Lebail refinement only considers the geometrical properties of the sample, whereas Rietveld refinement considers every property of the sample.

The powder-XRD analyses were performed in collaboration with Mohamed Selmane, from the LCMCP laboratory. The apparatuses used are part of the Federation de Chimie des Materiaux de Paris Centre (FCMat) platform. The diagrams were acquired on a Bruker D8 Discover diffractometer, with a one-dimensional LynxEye XE-T detector. The analysis was performed using the Kα1 and Kα2 doublet from a Cu anode. Acquisitions were performed either over the 10°-80° or the 20°-120° 2θ range.

Total scattering spectroscopy

Total scattering spectroscopy is a diffraction experiment that collects all the elastic scatterings from a sample [92–94]. This allows for obtaining insights about both the long-range periodical structures (carried by the Bragg scattering), and the short-range local disorder (carried by the diffuse scattering) of the probed material. The result is usually provided in the reciprocal space, by the structure factor function S(Q):

$$S(Q) = \frac{I(Q) - \langle f(Q)^2 \rangle + \langle f(Q) \rangle^2}{\langle f(Q) \rangle^2}$$

Where I(Q) is the scattered intensity collected, and f(Q) is an atomic form factor depending on the nature of the probed material. Both are functions of the reciprocal space scattering vector Q. This last is defined with λ the incident X-ray wavelength, θ the diffraction angle, and d_{hkl} the real space equivalent lattice spacing, such as:

$$Q = \frac{4\pi \sin(\theta)}{\lambda} = \frac{2\pi}{d_{hkl}}$$

The reciprocal space structure factor S(Q) can be converted into the real space G(r) function. This G(r) function is the pair distribution function (PDF). This provides the distribution of all the distances r, between each couple of atoms in the sample. The PDF is particularly used to characterise defective materials, highly disordered materials, or even liquids-state materials. The G(r) function is obtained by Fourier transform of S(Q) over Q, following:

$$G(r) = \frac{2}{\pi} \int_{Q_{min}}^{Q_{max}} Q\,(S(Q) - 1) \sin(Qr)\, dQ$$

Where Q_{min} and Q_{max} refer to Q-values depending on the measurement apparatus limitations. Q_{min} is limited by the incident X-ray beam direct contribution, while Q_{max} is limited by the incident X-ray beam wavelength λ.

In this work, the total scattering experiment was used to characterise both liquid-state ionic liquid electrolytes (see **Chapter 3**), and solid-state powders from the electrode materials (see **Chapter 4**). In either case, the analysed samples were packed in Kapton capillaries, inside of an Ar-filled glove box. Packed samples were then sent to the Argonne National Laboratory for analysis. The high-energy X-ray (λ = 0.2128 Å) synchrotron diffraction data were collected at the 11-ID-B beamline of the Advanced Photon Source (Argonne National Laboratory), by Olaf Borkiewicz. One-dimensional diffraction data were obtained by integration of two-dimensional (2D) total scattering data with Fit2D [13]. Pair distribution functions (PDFs) were extracted using PDFgetX3. The PDF refinements were performed using the software PDFgui.

1.2 Spectroscopy techniques

Spectroscopy is a broad field of physics and chemistry, from which entire disciplines belong. Its applications can provide a wide variety of data on the probed sample, ranging from crystal and molecular characterisations to the elemental nature of the sample.

Spectroscopy techniques are defined as experimental methods that analyse the variation of energy of a system, after a radiative stimulation. This stimulation can be caused by any kind of radiative energy (particle beams, electromagnetic, acoustic, etc ...). Various phenomena, spreading the radiation energy, can be measured to obtain the corresponding spectra. Among these, feature absorption, emission, and inelastic scattering.

Inelastic scattering spectroscopy

Raman spectroscopy is a coherent inelastic light scattering technique. The incident light beam used is usually a visible or IR laser. When such light is scattered by a sample, electrons get excited and then relax. If the relaxed electronic state matches the former electronic state, the scattering is elastic and is called Rayleigh. In opposition, when the relaxed electronic state differs from the former one, the scattering is inelastic and is called Raman-shifted. From this energy shift originate the collected spectra.

The energy shift is due to the interactions between the incident light beam and the electric field from the sample, specifically the vibrational energy levels. Raman spectroscopy is therefore used to characterise vibration modes in a sample. The vibration modes can be lattice modes, or molecular modes (symmetrical or asymmetrical, stretching or bending). In this work, Raman spectroscopy is used to characterise ionic liquids samples, therefore only the molecular vibrations are investigated.

The Raman spectra collection was done in collaboration with Ludovic Bellot-Gurlet, Gwenael Gouadec, Assia Hessani, and Aline Percot from the MONARIS laboratory. The equipment used was part of the PLASVO analytical platform, in MONARIS. The spectra were acquired using a Bruker RFS100/S Raman spectrometer (Bruker optics), coupled by optical fibre on a Bruker RamanScopeIII FT-Raman microscope, with a Leitz x40 LWD/IR lens. The analyses were performed by interferometry, with a 77K-cooled Ge detector, and Rayleigh Notch filter. The excitation was carried by a near-infrared 1064nm Nd:YAG laser (Coherent Compass 1064-500N, 500mW maximum power), and set so that the samples receive an effective laser power of 110mW. The samples were prepared in an argon-filled glovebox, and sealed in septum-capped Pyrex tubes. The spectra were obtained by combining 30000 scans, over the 50 cm^{-1} to 3500 cm^{-1} range. Notably, in this range, the studied samples display a fluorescence pattern. This fluorescence was first minimized by the near-infrared laser excitation, and then removed by baseline. An example of untreated acquired data is provided in **Figure S17.**.

Emission spectroscopy

Energy-dispersive X-ray spectroscopy (EDX), is an emission spectroscopy technique that is often coupled to scanning electron microscopy (SEM). In this case, the SEM electron beam is used as an incident excitation source. Indeed, when exposed to this beam, the electrons of the analysed sample are excited. As the electrons relax, X-rays are eventually emitted. Both the energy and the intensity of these X-rays provide data on the chemical composition of a sample. In the end, elemental analyses can be performed on selected areas of the sample, or elemental mapping can be realised.

The EDX spectroscopy analyses have been realised in collaboration with Françoise Pillier and Stephanie Delbrel, from the LISE laboratory. The EDX spectra were acquired using a Brucker Quantax spectrometer with SDD, coupled on a ZEISS ULTRA 55 SEM-FEG.

Nuclear Magnetic Resonance spectroscopy

Nuclear magnetic resonance (NMR) spectroscopy is a technique used to gain insights on a molecule structure, or on the local environment of a probed atom. The measurement, of a sample, consists of analysing the re-alignment of atomic nuclei spins. The probed nuclei must nonetheless present non-zero nuclear spins ($I \neq 0$).

A NMR spectrum is obtained as follows: A sample is first polarized in a constant magnetic field (all the spins become aligned). Then, an oscillating near-field is applied. As an effect, the spin orientations of the probed nuclei are perturbed. Eventually, if the near-field frequency matches the probed nuclei intrinsic frequency, resonance is observed. This resonance phenomenon is indicative of the absorption of electromagnetic radiation. When the near-field is removed, the probed nuclei relax, emit back the electromagnetic radiation, and re-align back with the former polarizing magnetic field.

The NMR spectrum therefore displays the measured resonance frequencies (or chemical shifts) of the probed nuclei, in a sample. The resonance frequency of an atomic nucleus is determined by the intensity of the polarizing magnetic field, the intrinsic magnetic properties, as well as the chemical environment of the probed nucleus. The chemical shift is relative to the absorbed/emitted energy, and is defined as a relative deviation of the measured resonance frequency compared to a reference.

NMR spectroscopy can be performed on both liquid-state and solid-state samples. However, the solid-state sees the appearance of additional spin interactions. This leads to an overall signal broadening, and an increased signal-over-noise ratio. This is usually overcome by using very high magnetic fields, or magic angle spinning (MAS).

The solid-state MAS NMR spectroscopy was performed by Vincent Sarou-Kanian from the CEMHTI laboratory. The apparatus used was part of the Infranalytics research infrastructure. The measurements were realised using a Bruker Avance Neo 850WB spectrometer, with a HXY triple resonance probe. The analysed samples were prepared inside an argon-filled glovebox, and sealed in Bruker 1.3 mm MAS rotors. The acquisitions were performed under a high magnetic field (20 T), and at a 60 kHz sample spinning frequency. The ^{27}Al spectra were obtained via single pulses, after 8192 accumulations, with a 1s recycle delay. The ^{1}H spectra were obtained via 2-period spin echo analysis, after 32 accumulations, with a 2.5s recycle delay. In addition, ^{1}H MAS NMR spectroscopy was also performed by Monique Body and Christophe Legein from the IMMM laboratory, using a 300 MHz field.

The liquid-state NMR spectroscopy was done in collaboration with Baptiste Rigaud, from the LCMCP laboratory. The spectra were acquired using an 11.7 T magnetic field and a Bruker Avance NEO spectrometer. The samples were prepared in an argon-filled glovebox, and sealed in septum-capped Pyrex tubes. D2O capillaries have also been introduced in the sample tubes, to assert the stability of the magnetic field during the experiment. The ^{1}H, the ^{13}C, and the ^{27}Al nuclei were probed at 500.07 MHz, 125.75 MHz, and 130.30 MHz respectively. In addition, the ^{37}Cl nucleus was also intended to be probed at 49.00 MHz, without success. Indeed, the poor sensitivity of the ^{37}Cl nuclei prevented meaningful data from being recorded.

1.3 Computational methods

Density functional theory calculations

Density functional theory calculations have been realised by Kyle Reeves, in an internal collaboration within the PHENIX laboratory, that aimed to study the insertion of multivalent ions inside the lepidocrocite-type titanate material [12,13,95].

The layered lepidocrocite structure was computed using a simulation cell of two titanate layers (4x4x1 supercell) and two layers of interlayer water with an overall composition of $Ti_{63}\square_1O_{124}(OH)_4 \cdot 32H_2O$, where the $\square$ represents a single Ti^{4+} vacancy whose charge is compensated by the four hydroxides. The spacing between titanate layers was fixed at 11.5 Å. The simulation cell was computed using periodic boundary conditions. The choice to simplify the system was made to control the role of the vacancy and to eliminate significant contributions from disorder in the structure.

From this approach, the behaviour of intercalated Al^{3+} ions and the structure and thermodynamics of stable structures in the vacancy and interlayer positions were investigated. Density functional theory (DFT) calculations were performed using the CP2K code via the Quickstep algorithm [96,97]. Electrons were described using the PBE exchange-correlation function with a plane wave cut-off of 400 Rydberg. DZVP-MOLOPT-SR-GTH basis sets were used along with Goedecker-Teter-Hutter pseudopotentials [98,99]. Systems are computed with a total neutral charge to simulate the state of the electrode following a discharge process.

Based on the Wyckoff positions, the energy of formation was computed for two different sites within the lepidocrocite structure: the aluminium ion in the water interlayer and the aluminium ion in the Ti^{4+} vacancy. To determine the energy of formation of the ion within the lepidocrocite structure, the structure was relaxed for the ion in each of the two positions. This allows for both the ion and the electrode atoms to move freely. When this relaxed structure is determined, the total energy of the system is then recomputed for this arrangement of atoms but without the intercalated ion. The energy of formation is then computed via the formula:

$$E_f = E[Al^{3+}+TiO_2] - (E[Al^{3+}] + E[TiO_2])$$

where the first term represents the combined system and the terms in parentheses represent the sum of energies of the Al^{3+} ion, and titanate systems computed independently.

Each vacancy represents an octahedral void where the Ti^{4+} had previously been 6-fold coordinated. Previous work has suggested that the charge balance is achieved by four additional hydroxide ions, that are located in the vacancy. The relative positions of these four hydroxide ions can vary amongst the six possible positions of the oxygens that were previously coordinated to the now missing Ti^{4+}. In total, this represents a total of fifteen possible arrangements. Although this number could be reduced based on the symmetry of the titanate, all fifteen structures were explicitly computed in the case that distortion was introduced into the structure that would break this symmetry.

Molecular dynamic calculations

Simulations for five different molar ratios were performed by Camille Bacon and Alessandra Serva, using MetalWalls software [100]. The $EMIm^+$ cation is described as non-polarizable. This choice is based on the fact that polarization effects are dominated by the chloride anions, and that reducing the number of polarizable species allows to reduce the computational cost of the simulation. For all the intramolecular /intermolecular interactions involving the $EMIm^+$ cation only, the parameters were taken from the CLP force field [101]. The parameters for all other interactions were previously developed in our group [102].

A first NPT run was performed at ambient pressure and temperature of 473 K for 800 ps. Each system was then annealed by increasing the temperature to 600 K in the NVT ensemble for 3 ns and then slowly decreasing it using a ramp of 50 K every 500 ps, until the final temperature of 473 K was reached. Then, the simulation was carried out in the NVT ensemble for 20 ns, using a timestep of 1 fs, and saving the trajectory every 1 ps. The equations of motion were integrated using the velocity-verlet algorithm, and a chain Nosé-Hoover thermostat was used to keep the temperature constant. Analysis of the simulation was performed using TRAVIS software as well as in-house written codes [103].

1.4 Electrochemical techniques

Electrochemical analyses aim to understand and characterise the electrochemical reactions (redox) occurring inside a studied system. Any redox reaction can be described, with 0x the oxidised species and Red the reduced species, as:

$$0x + ne^{-} \rightleftharpoons Red$$

Redox reactions involve the exchange of charges (electrons) – by a n amount. Thus, if connected to an electrical circuit, an electrical current (I) is generated. In an electrochemical cell, this current is measured between the Working electrode (W or WE) and the Counter electrode (C or CE). The studied Redox reactions only occur at the WE. The CE provides electrons back to the system, and is chosen to be chemically inert in the operating window.

The variation in concentration at the WE, of the charged redox active species (Ox and Red) causes a difference of potential (E). While the redox reactions are occurring, Ox and Red species are progressively converted into their counterparts. As a result, their concentration varies in time, hence the electrode potential. The dependency between the electrode potential and the redox species concentrations is then given by the simplified Nernst equation:

$$E = E^{0} + \frac{RT}{nF} \ln\left(\frac{[Ox]}{[Red]}\right)$$

Where E is the measured potential at the electrode, E^{0} is the standard potential, R is the ideal gas constant, T is the temperature, n is the number of exchanged electrons by the redox reaction, F is the Faraday constant, [Ox] and [Red] are respectively the concentrations of the oxidised and reduced species at the WE.

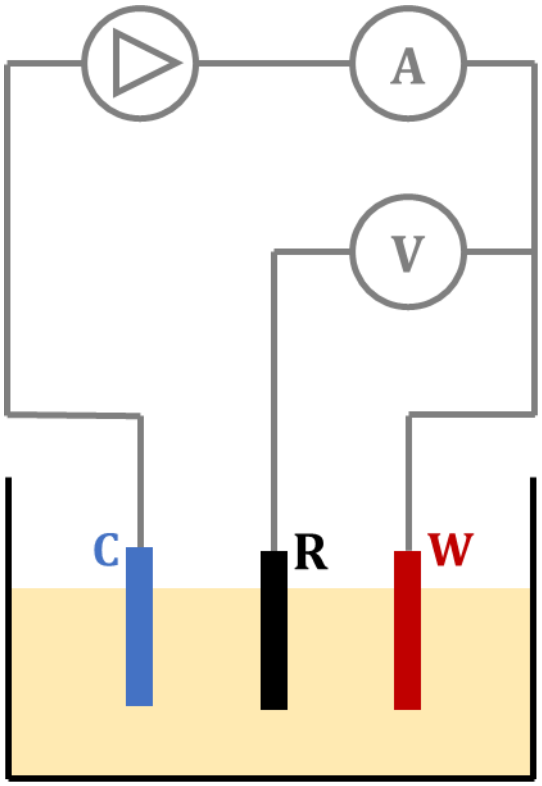

Figure 8. Scheme of a 3-electrode electrochemical cell setup. The Working electrode is displayed in red, the Counter electrode in blue, the Reference electrode in black, the electrolyte in yellow, and the external electrical circuit in grey. The ▷ symbolises the potentiostat.

Notably, as the CE also provides electrons to the system, another species concentration gradient is observed at the CE interface. This additional gradient is similarly influencing the difference in potential between WE and CE. For this reason, a third chemically inert electrode is introduced in the electrochemical cell. This electrode is called the reference electrode (R or RE). No current flows through this electrode, which allows for measuring the difference in potential (or voltage), in respect to the WE (Ewe) or the CE (Ece) independently. This setup is called a 3-electrode electrochemical cell setup, and is illustrated in **Figure 8.**.

Throughout this work, two kinds of electrochemical experiments have been performed: potential-controlled and current-controlled experiments. A key highlight of each electrochemical technique used is provided below.

Potential-controlled experiments

Potential-controlled experiments maintain a difference of potential between the working and the reference electrode. If the potential of the WE differs from the equilibrium voltage, the Nernst equation is not respected. Therefore, the redox active species concentrations evolve to the newly imposed equilibrium. Hence, the redox reaction is forced, and a current is observed.

The first potential-controlled experiment performed is a ChronoAmperometry (CA). In this technique, a constant voltage is applied, over time. The observed variations of the forced current then give insights into the electrochemical reactions occurring at this voltage. For instance, if the recorded current is cathodic (negative) a reduction is observed. The CA is mainly used for the electroplating of a species from the electrolyte.

The second potential-controlled experiment performed is a Cyclic Voltammetry (CV) [104]. **Figure 9.** proposes schematic views of the input and output signals observed during a typical CV experiment. The CV is a potentiodynamic technique: the working electrode voltage is linearly swept. This potential sweep occurs between two threshold values – determining the voltage window – and at a determined speed (*i.e.* the scan rate). Repeating the potential scan back and forth, between the two thresholds, makes the cycling. The forced current is monitored, and results are typically presented as I vs. E plots, called voltammograms. On those graphs, a redox reaction appears as a single peak. As the scans are cycled, peaks are usually observed in pairs. The shape, position, and intensity of these peaks provide data on the various electrochemical processes in the analysed system. For instance, it is commonly admitted that, if a pair of peaks is separated by more than 57 mV, the redox reaction is irreversible [104]. In addition, on a voltammogram, if a peak does not belong to a pair, this can be indicative of a chemical reaction occurring spontaneously in the system. Indeed, the redox activity of the former species (Ox or Red) might be lost after side reactions with other components of the system [105].

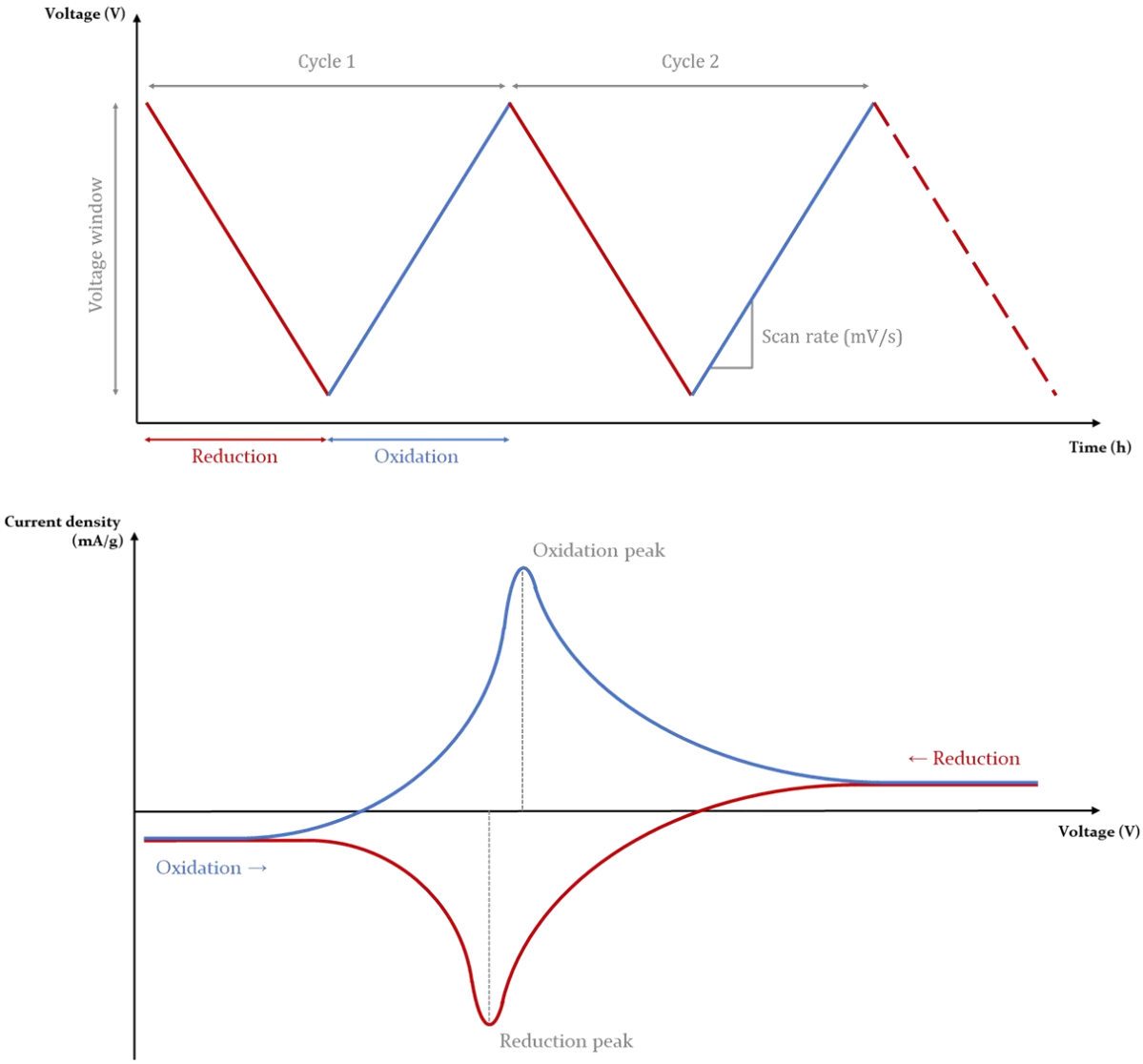

Figure 9. Scheme of the input (top) and output (bottom) signals of a typical cyclic voltammetry experiment.

The CV is therefore used as a qualitative analytical technique. Notably, the bulk reactions as well as the surface redox phenomena are probed by this method. In the realised experiments, reduction phases are displayed with negative current values, and oxidation phases are displayed with positive current values.

Current-controlled experiments

Current-controlled experiments provide the electrochemical cell electrodes with an electrical current. This supply (or withdrawal) of electrons forces the redox reaction at the electrode. Therefore, according to the Nernst equation, the difference of potential between the working and the reference electrode varies, and is monitored.

The first current-controlled experiment performed is an Open Circuit Voltage (OCV) measurement. In this technique, no current flows through the electrochemical cell (I=0). In such a case, the system is expected to be at the thermodynamic equilibrium. However, if the cell 'rest' voltage is recorded to evolve in time, this means that the system has not reached this equilibrium. The OCV measurement therefore provides insights into the equilibrium state of an electrochemical cell.

The second current-controlled experiment is the Galvanostatic Cycling with Potential Limitation (GCPL) technique. In this technique, a constant current is applied to the electrodes – hence the galvanostatic condition. Consequently, the electrode voltages are monitored to evolve freely, in between two potential thresholds. Upon reaching one of the thresholds, the current supplied is reversed, until the other threshold is met. Switching, between positive ('charge') and negative ('discharge') current phases, makes the cycling. Schematic views of the input and output signals observed during a typical GCPL experiment are proposed in **Figure 10.**. The results of a GCPL are typically shown as E vs. Q plots. The specific capacity (Q) is calculated by: $Q = \frac{I*t}{m}$, using the mass of the active material at the WE. The shape of those plots informs on the mechanism occurring at the electrode. Indeed, purely capacitive mechanisms provide linear responses. On the contrary, faradic mechanisms exhibit potential plateaus [106]. If the plateaus are flattened, the electrode undergoes phase separation, while the redox reactions happen. Whereas if the plateaus present a slope, the redox reactions occur in a solid solution in the electrode. GCPL is then able to probe the electrode material bulk. This technique is therefore mainly used to get insight on the structure of the bulk electrode.

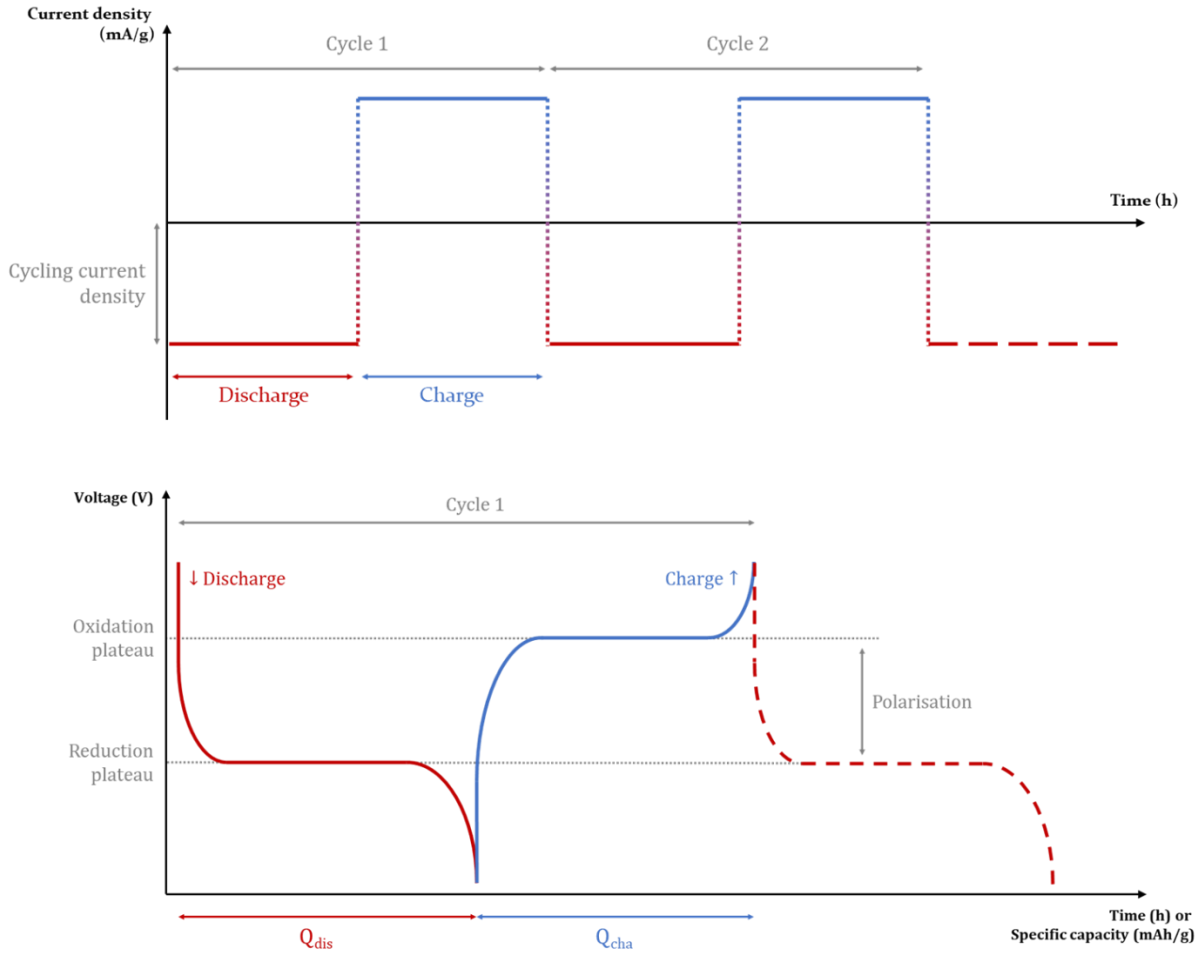

Figure 10. Scheme of the input (top) and output (bottom) signals of a typical galvanostatic cycling experiment.

Notably, the data acquired through the GCPL technique can be compared to the CV one. Indeed, as current is constant during a phase, $\frac{dQ}{dE} \propto I$. Plotting the $\frac{dQ}{dE}$ vs. E graph from the GCPL should then provide comparable data to the I vs. E one from the CV. However, discrepancies can arise from the difference in kinetics between the two techniques (*i.e.* galvanostatic vs. potentiodynamic). From these discrepancies, insights into the properties of the studied redox reactions can further be understood.

2. Experimental protocols

2.1 Syntheses

Electrode material syntheses

The positive electrode materials studied in this work are titanium oxi-hydroxides. Throughout the literature, numerous routes have been proposed to synthesize such materials. The two main are the 'solid-state chemistry' and the 'soft-chemistry' processes. The soft-chemistry process offers a higher control of the product morphology, while requiring less energy than the solid-state chemistry. For these reasons, the soft-chemistry process has been preferred here.

The performed Soft-chemistry process consists of a Sol-Gel synthesis. This synthesis involves hydrolysis and condensation reactions, from a molecular precursor in a solvent. The molecular precursor is typically a metal alkoxide $M(OR)_n$. By water hydrolysis, this precursor produces both a metal hydroxide and an alcohol. This alcohol can then conveniently be chosen as the solvent of the system.

$$\text{Hydrolysis:} \quad M\text{–}OR + H_2O \rightarrow M\text{–}OH + ROH$$

The formed metal hydroxide is subject to condensation by nucleophilic substitution. The result is the formation of bridges between the metal centres. These bridges are either oxo (M-O-M) or hydroxo (M-OH-M) bridges. This can be achieved via olation, oxolation, or alcoxolation:

$$\text{Olation:} \quad M\text{–}OH + M\text{–}OH_2 \rightarrow M\text{–}OH\text{–}M + H_2O$$

$$\text{Oxolation:} \quad M\text{–}OH + M\text{–}OH \rightarrow M\text{–}O\text{–}M + H_2O$$

$$\text{Alcoxolation:} \quad M\text{–}OH + M\text{–}OR \rightarrow M\text{–}O\text{–}M + ROH$$

These reactions lead to the formation of clusters, and then nanoparticles of metal oxides or metal hydroxides. Numerous parameters modulate the number, shape and size of these particles, such as the temperature, the pH, the hydrolysis rate, or the equilibrium between hydrolysis and condensation kinetics. As a result, a colloidal system is obtained – namely the Sol. The Sol is either precipitated to form particles, or polymerized to form an oxide framework that traps the solvent – namely the gel. The gel can eventually be dried out to finally form an aerogel.

The studied materials are titanium oxides derivatives, and are further described in **Chapter 4**. Ma et al. [95] proposed a low-temperature solvothermal synthesis route for the studied materials. This protocol was followed and adapted for the entirety of this work. The titanate materials were therefore made as follows:

> In a beaker, 15.19 mL of isopropanol and 810 µL of water are mixed together. In another beaker, 4 mL of titanium (IV) isopropoxide is mixed with 10 mL of isopropanol. Then, the two beakers are mixed together. The obtained solution is tinted with a milky white colour. This mix is left to homogenise for 10 minutes under stirring. Then the mix is poured into an autoclave for a 12-hour solvothermal treatment. After the solvothermal treatment, a white xerogel is obtained. The isopropanol and the unreacted precursors are removed by successive washing and centrifugation cycles. The washings are performed with absolute ethanol. This treatment destroys the gel structure; instead, particles are obtained. Finally, the remaining solvents are left to dry for 4 hours in an 80°C oven. After the drying, the result is ground and a fine white powder is obtained.

The influence of the thermal treatment temperature will later be studied in this work (see **Chapter 4**). In this view, three temperatures were chosen for the synthesized materials: 90°C, 110°C and 150°C. Between the three, differences appear from the end of the thermal treatment. Indeed, a more pronounced shrinkage of the obtained gel was observed with the higher treatment temperatures. The final densities of these three materials appear to be widely different too. Indeed, for the same mass of synthesized material, the volume of the 90°C material is about three times bigger than the two other materials.

Electrolyte syntheses

Choices of electrolytes for Al-ion batteries are spares. A state-of-the-art about the electrolytes for Al-ion batteries is provided in **Chapter 3**. The chosen electrolyte, for the electrochemical intercalation of aluminium ions inside electrode materials, is the acidic 1-ethyl-3-methylimidazolium chloride (EMImCl) and aluminium chloride ($AlCl_3$) mix. This EMImCl:$AlCl_3$ mix is widely studied across the literature. The proper ties of this ionic liquid are also known to be dependent on the ratio between the two salts. Indeed, aluminium chloride is a strong Lewis acid. Therefore, the mix can inherit this property. Investigations about the acidity of this ionic liquid will be addressed in **Chapter 3**. Aluminium chloride is highly sensitive towards moisture. For this reason, it must be kept and used under an inert atmosphere. The ionic liquid electrolyte was therefore synthesised and stored in an argon-filled glovebox. The synthesis protocol is given as follows:

> In a glovebox, a set amount of EMImCl is weighted and poured into a glass vial. The right amount of aluminium chloride, to add to the mix for the desired ionic liquid acidity, is calculated from the mass of EMImCl. Aluminium chloride is so-weighted and poured into another glass vial. Then $AlCl_3$ is progressively added to the EMImCl. As a result, the mix is locally melted. Caution needs to be taken here, as the reaction between $AlCl_3$ and EMImCl is highly exothermic. For this reason, $AlCl_3$ is incorporated only by a few amounts into the EMImCl. In addition, the mix is agitated between each $AlCl_3$ incorporation, to dissipate the generated heat.

If caution is not taken while mixing $AlCl_3$ with EMImCl, the generated heat might degrade the organic EMImCl. If this is the case, smoke is usually observable when the $AlCl_3$ is poured over the EMImCl. Indeed, excessive temperature has been proven to mainly damage the methyl and ethyl groups of the EMImCl [107]. Moreover, if excessive heat has been produced during the mix, the resulting acidic ionic liquid will not display the goldish-yellow colour expected. Instead, a dark-brownish colouration would be obtained.

When a few $AlCl_3$ is added to the EMImCl, the mix is a viscous goo of unreacted EMImCl and EMImCl:$AlCl_3$ melt. With an increasing amount of $AlCl_3$ in the mix, the liquid phase starts to appear while most of the EMImCl remains solid. Eventually, the EMImCl become entirely melted, with enough added $AlCl_3$. This equilibrium is reached before stoichiometry. At this point, the basic ionic liquid is a clear yellow-greenish melt. At around 1:0.9 EMImCl:$AlCl_3$, the mix suddenly turns turbid. Past this composition, the mix quickly turns back to a clear goldish-yellow liquid. Finally, the aspect of the ionic liquid does not vary any more, with the addition of $AlCl_3$.

Previously, the EMImCl was outgazed at 130°C for 72h under vacuum, prior to being mixed with the aluminium chloride [108]. This was made in order to eventually purify the EMImCl from volatile pollutant traces. However, this turned the synthesis highly unpractical, as the molten EMImCl quickly solidified back. This often resulted in the EMImCl becoming solid, while inside pipettes, during the precise mass measurement. Tests were realised to determine the need for this outgazing. Samples were made with a 72h outgazing at 130°C under vacuum, with a 72h outgazing at 90°C under vacuum, or without outgazing. Those three samples were then analysed via Raman spectroscopy and were revealed to be highly similar. For this reason, the synthesis of the ionic liquid electrolytes was thereafter made at room temperature, and without any outgazing of the EMImCl.

2.2 Experimental setups

Electrode preparation

In order to be used as electrodes for electrochemical tests, the previously synthesised titanate materials need to be processed. Electrodes are therefore prepared via drop casting, with the following protocol:

> In a mortar, the chosen synthesised titanium material is first mixed with a carbon black powder. The goal here is to obtain a homogeneous paste. This will ensure conductivity and prevent charge accumulation in the electrode during the electrochemical tests. Once a homogeneous paste is obtained, PTFE in a 5 w% dilute solution is added as a binder. The titanium oxide material, the carbon, and the PTFE are mixed in an 80:10:10 mass ratio. Water is lastly used as a solvent here. In the end, the obtained slurry is an ink, ready to be drop cast onto the desired subtract. This substrate will be the current collector for the following electrochemical testing. Once cast, the electrodes are left overnight to fully dry. Finally, the dried electrodes are put in a 60°C oven for an hour, to remove the adsorbed water, and quickly stored in an argon-filled glovebox.

Kang studied the use of binders for slurry making, in his works [108]. He compared the use of carboxymethyl cellulose, styrene-butadiene rubber, and a 5 w% dilute PTFE solution, as binders. He concludes with the better performances of the PTFE. For this reason, it has been the chosen binder in this work.

If the three components are not homogeneously mixed, the resulting electrode will present a flecked pattern: some darker area will be observable among the dark grey cast. This is a simple visual aid to assert the good quality of the realised drop cast. This heterogeneity comes from the excessive use of solvent. Indeed, if too much solvent is added, the mix agglomerates and flocculates. For this reason, care should be taken with the amount of solvent used to make the slurry.

Another aid is the smooth aspect of the slurry. If the electrode presents cracks, its use is unadvised. Those cracks come from a too-quick drying. Indeed, the electrodes were originally dried, as soon as they were made, for 4 hours in a 70°C oven under vacuum. This drying protocol usually resulted in electrodes exhibiting multiple cracks. The drying protocol has therefore been changed to the softer one previously presented.

Swagelo k cell setup

Electrochemical experiments were performed inside a PFA tubed Swagelok® cell. This choice was motivated by its airtightness, and was inspired by the previous works of Kang [108]. However, several improvements have been made to his cell configuration setup. A representation of this configuration is proposed in **Figure 11.**. Inside an argon-filled glovebox, the electrochemical cell is built as follows:

> The selected working electrode is about 1mg to 2 mg, of a synthetized titanium material slurry. This electrode was cast on a 8 mm diameter Mo foil current collector, during the fabrication process. Both counter and reference electrodes are high-purity aluminium (>99.99%). An aluminium rod is used as the reference electrode, while a 10mm aluminium foil is used as the counter electrode. Each of the three electrodes is separated from one another by glass fibre separators. A 100 µL of acidic 1:1.5 EMImCl:$AlCl_3$ ionic liquid is used as the electrolyte, and soaked onto the separators. Current is outed, from the electrodes, by SS316 stainless steel rods. Finally, to prevent the electrolyte to corrode these last, glassy carbon spacers are put between the working electrode, the counter electrodes and their respective SS316 rods. To prevent any electrolyte leakage towards the stainless steel, the glassy carbon spacers are wrapped in PTFE tape and encased into an additional PTFE case. In the end, this whole system is inserted and sealed inside a three-electrode Swagelok casing.

The surface status of the glassy carbon spacer has been shown to influence the electrochemical response of the cell [108]. For this reason, these spacers are kept mirror-polished for every cell. As glassy carbon is already used in the system, one could question the use of Mo foil as the current collector. The answer is in the ease of process. Indeed, parts from used cells are washed and reused for the following cells. The removal of a working electrode slurry, drop cast directly on top of the glassy carbon spacer, would scratch the mirror polishing. It is then easier to scrape it off from a Mo subtract. That is why, at a lab scale, the use of Mo foil is preferred as the current collector for the system.

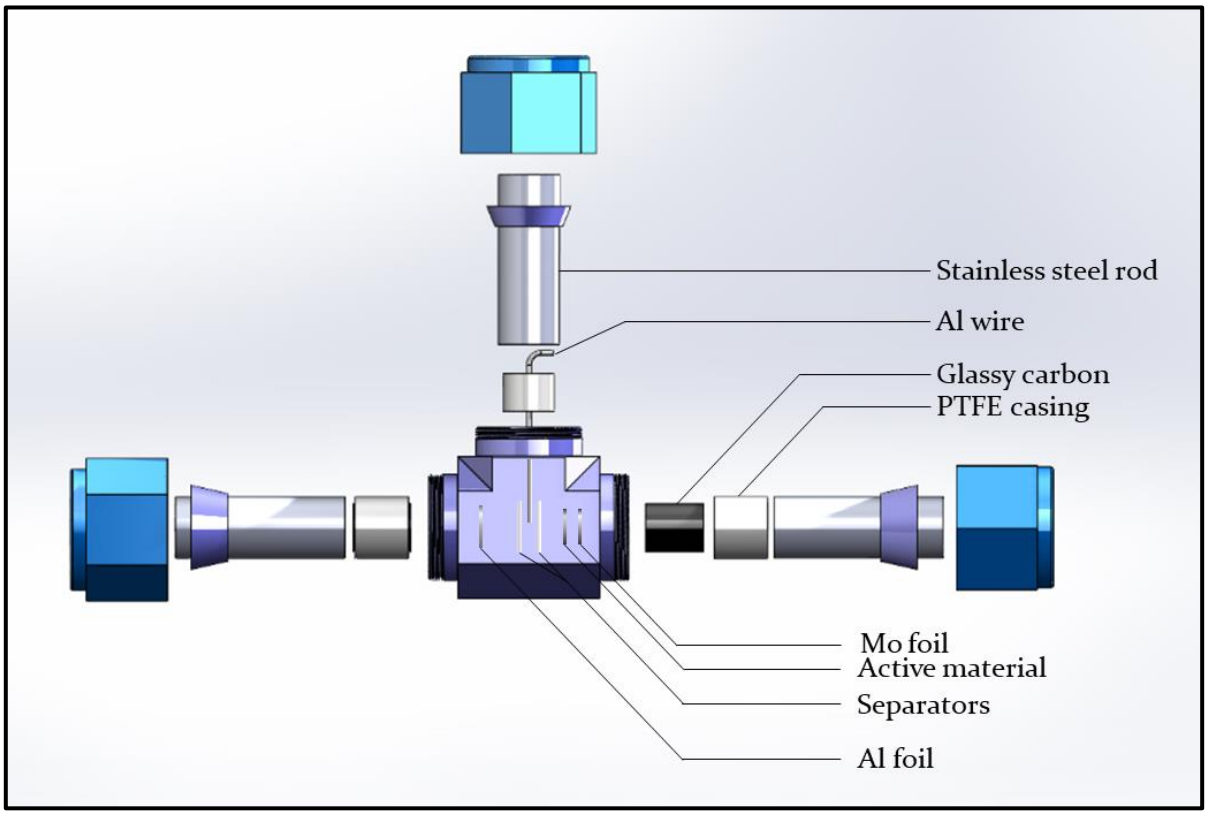

Figure 11. Scheme of the Swagelok cell configuration.

Glovebox cell setup

Other electrochemical experiments were performed in a three-electrode glass cell setup, inside an argon-filled glovebox. This allows for measurement of the electrochemical response, while directly visually observing the system evolve. A scheme of the experimental setup is proposed in **Figure 12.**. This setup consists of 2 mL of the acidic ionic liquid electrolyte, poured into a 5 mL glass cell. This glass cell is covered by a PTFE lid, which presents three holes through which the three electrodes go through. Both the counter and the reference electrode are high-purity (>99.99%) aluminium rods. The choice of the working electrode would depend on the electrochemical test intended.

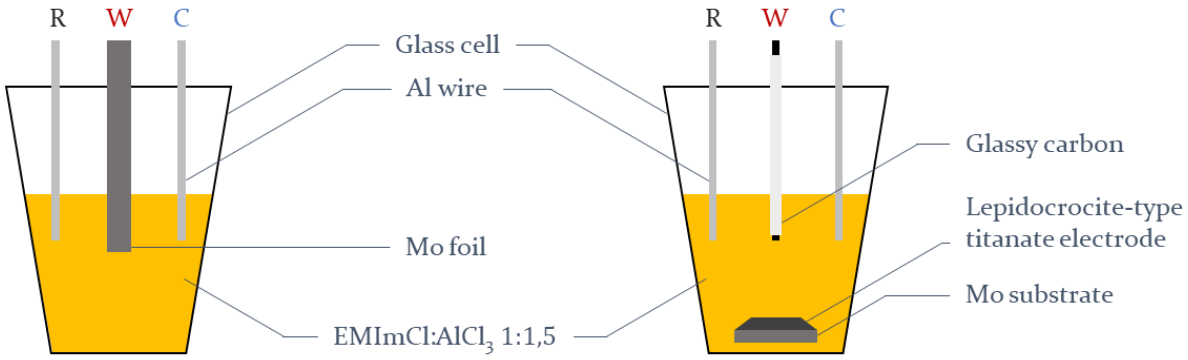

Figure 12. Schemes of the glovebox cell configuration. Two experiments use this cell configuration as illustrated. The working electrodes used are interchangeably a Pt, Mo, or glassy carbon electrode.

It is to be noted that, in this cell configuration, the working electrode is in a large excess of electrolyte. Therefore, the glovebox cell use is restricted to electrochemical characterisations of the electrolyte (redox reactions, stability window, ...). Bulk reactions (i.e. ion intercalation) are preferably observed using the Swagelok cell configuration.

Post-electrochemical treatments

After the various electrochemical tests, cells are disassembled. The glassy carbon spacers and the Mo current collectors are kept and washed to be reused in later electrochemical cells, while the other components are thrown away. The spacers are washed with soap water and ethanol. To wash the Mo discs, the working electrode material is first scratched from the current collectors. These are then poured into a 1M H_2SO_4 solution for 1 to 2 days. They are then washed in acetone overnight. They are finally laminated, using weighting paper as protection.

However, some analyses aim to gain data on the working electrode, after the electrochemical test is performed. To do so, cells are disassembled inside an argon-filled glovebox. The electrode material although remains wetted from the electrolyte. The literature diverges on which solvent to use for removing the ionic liquid from the electrode [40,41,45,88,109,110]. Indeed, if the ionic species from the EMImCl:$AlCl_3$ mix are easily solubilized by any polar solvent, the electrode material can also react with the solvent. Notably, Kravchyk et al. [45] pointed out the reductive aspects of the most commonly used solvents. For this reason, Mo foils were immersed in the ionic liquid and then washed in various solvents: diethyl ether (Et_2O), dimethyl carbonate (DMC), acetonitrile (MeCN) and methanol (MeOH). The ability of the solvent to remove the remaining electrolyte was estimated by EDX. The most suitable wash was performed by immersion for 2 days in a volume of DMC, and then a quick immersion in another volume of DMC. Regular gentle stirs were added to improve washing efficiency. This process ensures a complete removal of the ionic liquid from the electrode material.

DMC is usually considered as oxidative. Therefore, during the DMC wash, the electrodes might have undergone oxidation. In the studied systems, a distinction between the discharge (reduction) and the charge (oxidation) phase would eventually be made. A bias might then be introduced toward the post-electrochemistry measurements of the discharged electrodes. However, the wash should not alter the charged electrodes.

2.3 Electrochemical cells parameter adjustments

The aforementioned protocols and setups were developed in order to analyse the electrochemical properties of the synthesised titanate material electrodes, in the EMImCl:$AlCl_3$ electrolyte. They are believed to minimise side reactions, and to provide meaningful results. Nonetheless, various tests were needed beforehand to determine these experimental details. The investigations about the effect of the electrolyte acidity will be discussed later in **Chapter 3**.

First of all, the reference electrode is chosen to be a pure aluminium wire. This reference electrode is therefore a quasi-reference. In addition, Kravchyk and Kovalenko measured the Al^{3+}/Al redox potential in the 1:1.3 EMImCl:$AlCl_3$ ionic liquid, against a standard reference electrode (SHE) [111]. As shown in **Figure 13.**, the redox potential of the Al^{3+}/Al couple is moved, from -1.66 V vs. SHE in aqueous solution, to -0.7 V vs. SHE in the chloroaluminate ionic liquid. Thereafter, to reflect this shift in potential, the recorded electrode voltages will systematically be reported against Al^{3+}/Al in EMIm:$AlCl_3$.

Similarly, the Cl_2/Cl^- couple is shifted from 1.36 V vs. SHE in aqueous solution, to 1.84 V vs. SHE in the ionic liquid. As an effect, the potential window (between the two degradation reactions of the electrolyte) is diminished to only be 2.54 V in the 1:1.3 ionic liquid.

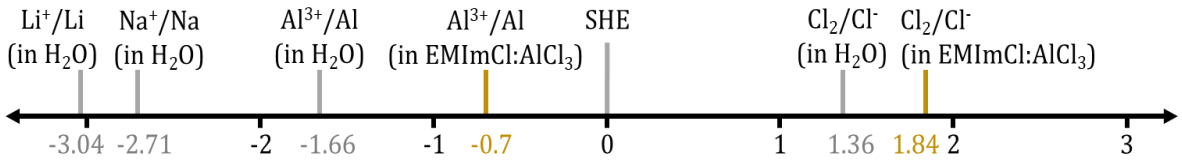

Figure 13. Evolution of the redox potential of the Al^{3+}/Al and the Cl_2/Cl^- couples in the chloroaluminate ionic liquid media, compared to their standard redox potentials. Standard redox potentials of Li^+/Li , Na^+/Na, and SHE are added as references. Adapted from [111].

Then, the compatibility between different current collector materials and the acidic ionic liquid needs to be verified. Several works described glassy carbon, platinum or molybdenum as good current collectors in this system [43,86,112]. However, the reactivity of the ionic liquid depends on its acidity (see **Chapter 3**). Therefore, in this work, the viability of these materials has been investigated, in regards to the 1:1.5 EMImCl:$AlCl_3$ electrolyte. As this experiment is not involving the titanate materials, tests were conducted in the glovebox cell configuration. The nature of the used working electrode was then varied between the three materials. Results are presented in **Figure 14.**.

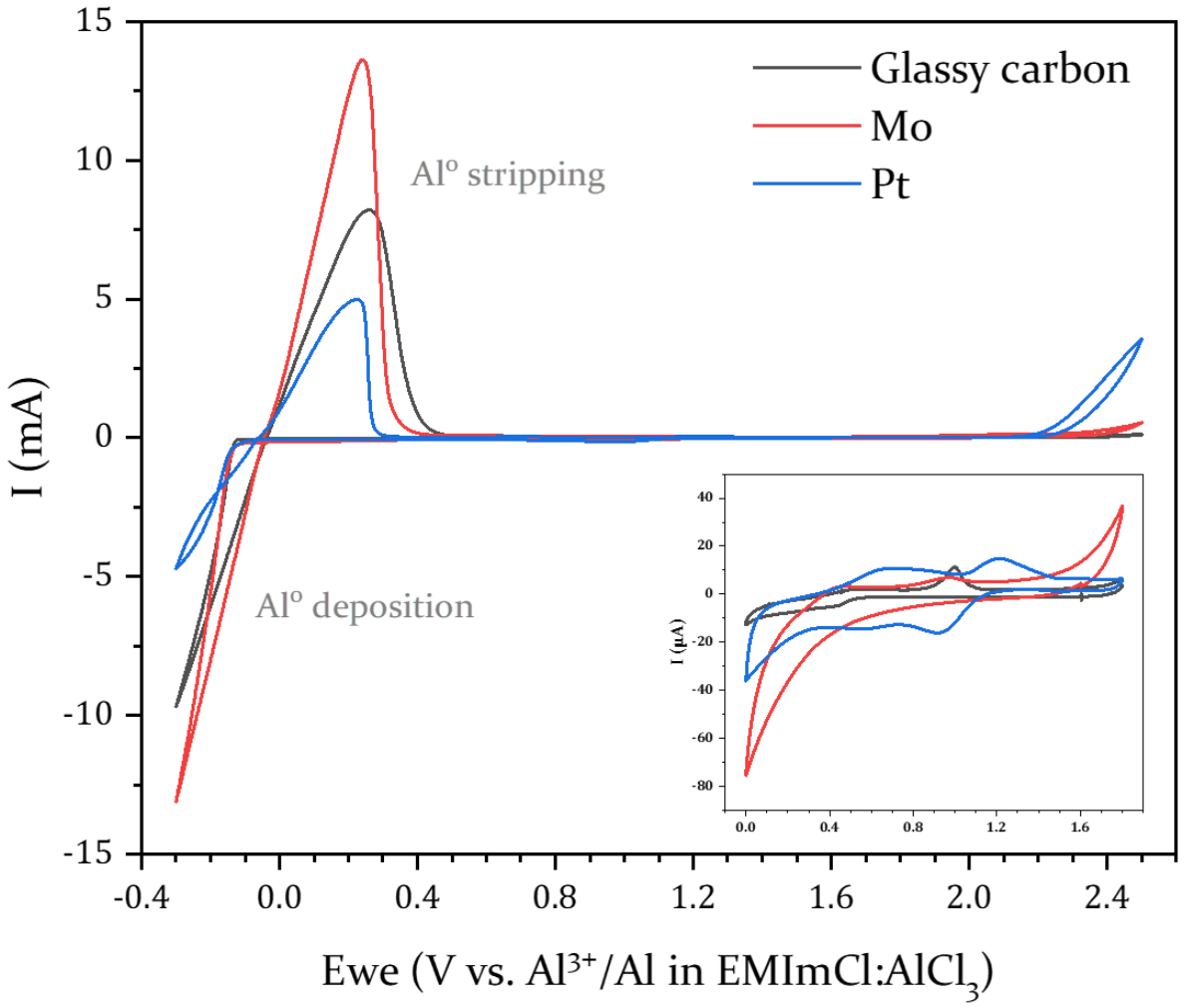

Figure 14. Stability experiments of the electrolyte considering a glassy carbon (black), a Mo (red), and a Pt (blue) working electrode. The test is a CV, performed at 50mV/s, within the -0.3 V to 2.5 V range, in the glovebox cell configuration. The inset displays a similar experiment performed in the 0.0 V to 1.8 V range.

At low voltage, the two characteristic aluminium plating/stripping intense peaks are observable for the three working electrode materials. This phenomenon is the most pronounced on the Mo electrode and is the least one for the Pt electrode. Nonetheless, the platting is recorded from -0.11 V on the three materials. Moreover, the aluminium stripping is observed to be a neat nearly vertical drop, past the corresponding peak, for the Mo and Pt systems. On the contrary, the glassy carbon electrode presents a broader Al stripping response. At higher voltage (above 2.00 V), the three electrodes show the chlorine gas evolution reaction ($Cl_{2\,(g)}\uparrow$) signal. The Pt electrode is observed to be the one favouriting this reaction the most.

From those, the stability window of the electrolyte is observed to span over around 2.10 V. Considering a few hundred millivolts of margin, the stability window of the electrolyte is ascribed from 0.00 V to 1.80 V vs. Al^{3+}/Al in EMImCl:$AlCl_3$.

The joined insert in **Figure 14.** provides more insights about the systems in this voltage window. An under-potential deposition (UPD) pattern showing pairs of peaks, is revealed using the Pt electrode. This phenomenon discards the use of platinum as the working electrode for any further measurements. The Mo electrode is recorded to exhibit two intense events, at the borders of the scan window. In contrast, the most stable signal is recorded when using the glassy carbon electrode. Indeed, only an isolated oxidative peak at 1.00 V, and a slight capacitive drop from around 0.60 V are noticeable on this flat voltammogram. For this reason, the glassy carbon electrode is preferred (or otherwise specified) over the Mo electrode for further experiments.

Concerning the titanate material electrodes, various tests were also performed to determine the best parameter adjustments. The solvent and the substrate (*i.e.* current collector) nature, used for the working electrode slurry casting, were therefore investigated through Swagelok cell experiments. In addition, the setup parameters of these cells were also varied. The acidity and volume of the electrolyte in the cell, outgassing of the EMImCl in the electrolyte, number and surface status of the glassy carbon spacers, and surface status of the counter electrode have been investigated.

The results of these investigations are presented in **Figure 15.**. There, every measurement has been performed using the 90°C lepidocrocite-type titanate synthesised material as the working electrode, and the 1:1.5 EMImCl:$AlCl_3$ ionic liquid as the electrolyte.

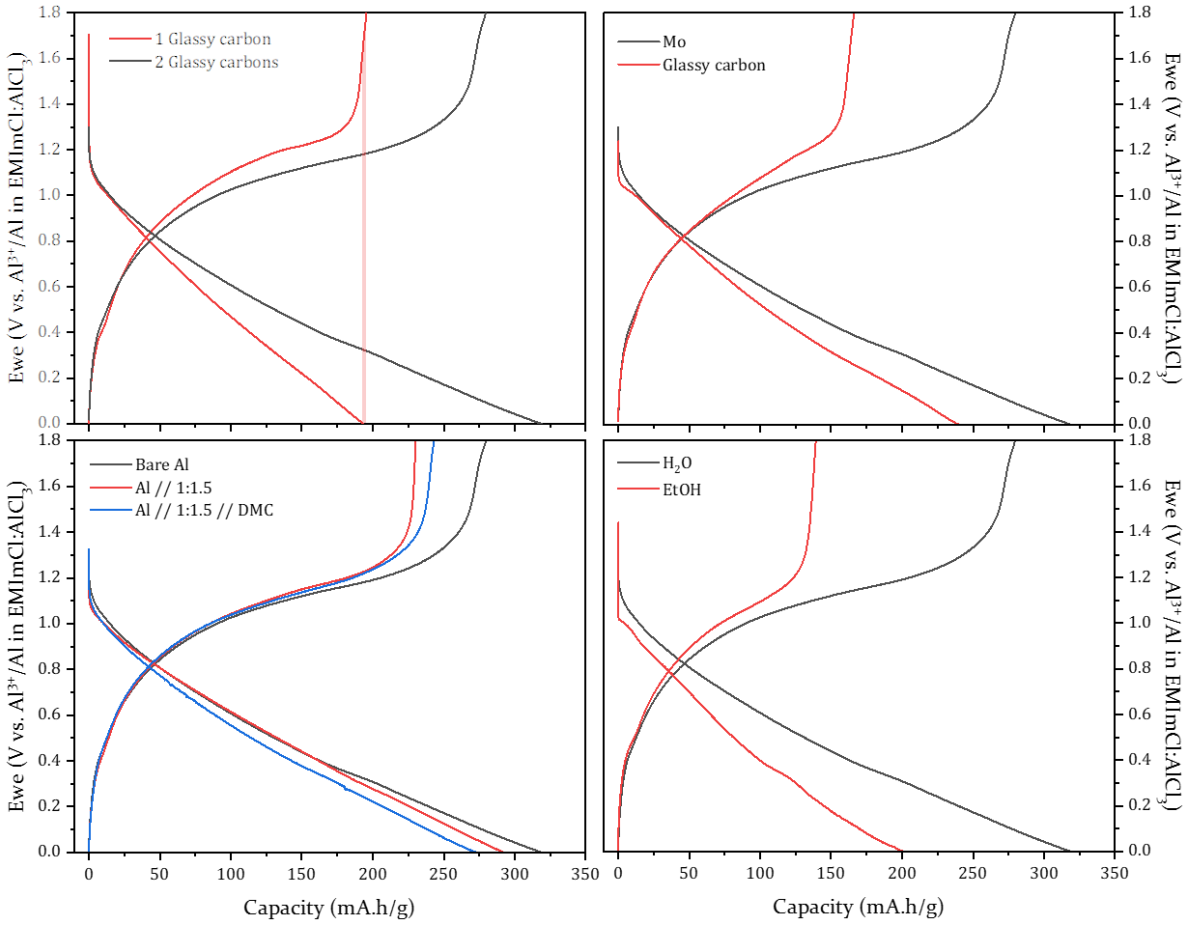

Figure 15. Swagelok cell parameters optimisation. Four displays show the results of galvanostatic discharge-charge experiments, performed at 20mA/g. The reported parameters investigated are: the number of glassy carbon spacers (top left), the substrate of the working electrode (top right), the electrode slurry solvent (bottom right), and the surface state of the Al counter electrode (bottom left).

The investigation on the number of glassy carbon spacers (**Figure 15.** top left quarter) refers to the initial cell configuration proposed by Kang [108]. In this configuration, the second spacer was a stainless-steel disc, placed right behind the aluminium counter electrode. This caused some of the ionic liquid to react in contact with this stainless-steel spacer. As a result, an extra capacity was recorded. This is why the charge curve displays a higher specific capacity than the discharge curve, as indicated by the light red area. With a two-glassy carbon spacers configuration, such corrosion is prevented, which provides higher specific capacities. The latter is then chosen to perform the next electrochemical characterisations.

The top right quarter presents the influence of the nature of the working electrode substrate (*i.e.* a current collector). Indeed, the casting of the titanate material slurry has been realised on a glassy carbon spacer and a Mo disc. The Mo current collector displays a slightly higher specific capacity, with a smoother profile, than the glassy carbon one. In addition, the recycling process (see below) is highly facilitated by the use of an intermediary current collector. When removing the working electrode material, the glassy carbon can be scratched, and therefore needs to be polished back. The Mo discs do not require such care, are they are simply laminated after wash. For these reasons, the Mo discs are used as current collectors for the titanate working electrodes.

The investigation of the solvent for the working electrode slurry (**Figure 15.** Bottom right quarter) is realised using two species: Milli-Q water, and absolut ethanol. The dispersion of particles depends on the nature of the solvent used. Therefore, the solvent choice affects the quality of the slurry casting. Here, the water provides a higher specific capacity, and is thus chosen as the solvent for the electrode slurry making.

Lastly, the bottom left quarter of **Figure 15.** shows the result of an investigation of the counter electrode surface status. Indeed, if the counter electrode is a high-purity aluminium foil, its surface is covered by a thin Al_2O_3 layer. When in contact with the acidic ionic liquid, this layer is expected to dissolve [80], ultimately altering the electrolyte. For this reason, three different surface statuses were tested for the counter electrode: the first was a bare untreated Al foil, the second was an Al foil treated 24h in the 1:1.5 EMImCl:AlCl3 ionic liquid, the last was this same treated Al foil additionally washed in DMC before use. As observed, this electrode surface treatment has only a little effect on the discharge-charge profile. Indeed, for every system, the discharge capacity remains above 270 mAh/g, and the charge one above 230 mAh/g. Moreover, the ionic liquid immersion seems to diminish the cycle reversibility (the charge over discharge capacities ratio) of the treated aluminium electrode, as a 79% reversibility is displayed. In comparison, both the untreated and the DMC-washed electrodes exhibit a cycle reversibility of around 89%. Overall, the aluminium counter electrode treatments do not show significant variation. Therefore, for experimental ease, the untreated aluminium foil is chosen as the counter electrode in the studied systems.

In addition, carbon black is used in the electrode slurry composition. This compound is used to ensure the conductivity of the electrode. However, as brought up by Kravchyk and Kovalenko [111], the use of carbonous material (such as glassy carbon and carbon black) can sometimes lead to misinterpretation of the observed electrochemical response. Indeed, these materials have been shown to intercalate $AlCl_4^-$ ions from the ionic liquid electrolyte. To estimate the contribution of these compounds over the measured signals, a negative test has been realised. A working electrode, made from carbon black and PTFE only, was therefore analysed, but only presented a negligible capacity (< 10 mAh/g).

Supplementary information

Use	Product	Manufacturer	Purity	CAS	Diameter (mm)
Titanate electrode material	Ti^{IV} isopropoxide	Sigma-Aldrich	97 %	546-68-9	-
	Isopropanol	Sigma-Aldrich	>99.5 %	67-63-0	-
	EtOH Absolut	VWR	99.96 %	64-17-5	-
Ionic liquid electrolyte	$AlCl_3$	Thermo Scientific	99.985 %	7446-70-0	-
	EMImCl	Solvionic	98 %	65039-09-0	-
Electrochemical cell	Mo sheet	Goodfellow	99.9 %	7439-98-7	Ø 8
	Al sheet	MTI	99.6 %	7429-90-5	Ø 10
	Al wire	Thermo Scientific	99.999 %	7429-90-5	Ø 0.5
	Glass fiber separators	Whatman (GF/D)	-	1823-110	Ø 12
	Glassy carbon spacers	HTW (sigradur)	-	-	Ø 10
Washing solvent	Et_2O	IPCM, SU	-	60-29-7	-
	DMC	Sigma-Aldrich	>99 %	616-38-6	-
	MeCN	Sigma-Aldrich	99.8 %	75-05-8	-
	MeOH	Alfa aesar	99 %	67-59-1	-

Figure S16. Table of the chemical products used in this work.

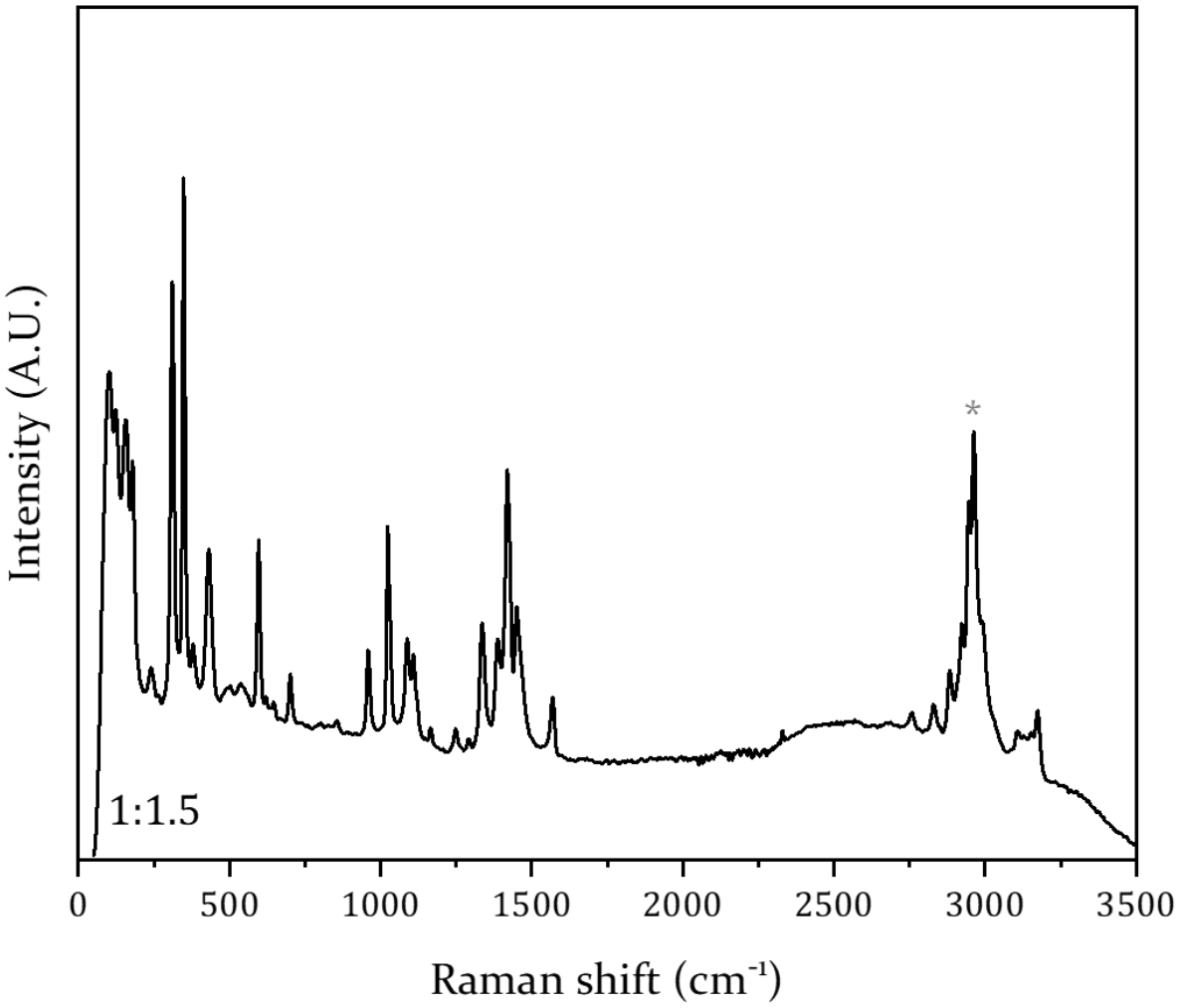

Figure S17. Untreated collected Raman spectrum of the 1:1.5 EMImCl:$AlCl_3$ ionic liquid. The irregular baseline is a consequence of the fluorescence of the studied sample. The grey * mark indicates the peak used as the reference for the later spectra normalisations.

Chapter 3. Structural features of chloroaluminate ionic liquids

The electrolyte is a central component in the electrochemical cell. Indeed, the electrolyte provides the electrodes with the reactive species, needed to undergo the various redox reactions exploited by the battery. In this view, a good electrolyte is usually defined as exhibiting a high ionic mobility (*i.e.* low viscosity and high conductivity). In addition, the electrolyte should show a wide electrochemical window, and minimise the side-reactions with the other battery components.

In battery chemistry, electrolytes have been classified into several categories: aqueous, organics, ionic liquids, or solids. The electrolytes developed for aluminium-ion batteries are mostly aqueous or ionic liquid electrolytes. Nonetheless, questions arise on the mechanisms occurring with the use of aqueous electrolytes. Indeed, Balland et al. [113,114] showed that the electrochemical signals provided by these systems might be due to a catalytic effect on the proton electrochemistry. This chapter will therefore focus on the ionic liquid electrolytes for aluminium ion batteries.

1. Non-aqueous aluminium ion electrolytes

Non-aqueous aluminium-ion electrolytes are mainly chloroaluminate ionic liquids. These have been studied since the early 1970s [39,115], and are based on the $AlCl_3$ aluminium chloride chemistry. $AlCl_3$ is a strong Lewis acid, that can oxidise various chemical species. In these ionic liquids, $AlCl_3$ is mixed with a chlorinated salt (XCl). As a result, the $AlCl_4^-$ aluminium chloride ion is formed, following:

$$XCl + AlCl_3 \rightarrow X^+ + AlCl_4^-$$

Moreover, depending on the equilibria in the systems, unreacted $AlCl_3$ can react with their $AlCl_4^-$ conjugated Lewis base, to form the $Al_2Cl_7^-$ dimeric species. This reaction can possibly be perpetuated to generate higher oligomeric species ($Al_nCl_{3n+1}^-$). These reactions are given by:

$$AlCl_3 + AlCl_4^- \rightarrow Al_2Cl_7^-$$

$$AlCl_3 + Al_2Cl_7^- \rightarrow Al_3Cl_{10}^-$$

Notably, the equilibrium between these different species affects the electrochemical properties of the ionic liquid. Indeed, the dimeric and oligomeric species are the electrochemically active species in the mix. This property originates from the slitting reactions of these species. As an example, the electrochemical splitting reaction of the dimer is provided as follows:

$$4Al_2Cl_7^- \rightarrow Al^{3+} + 7AlCl_4^-$$

In the literature, chloroaluminate ionic liquids have been classified into three categories across time [116,117]: Molten salts, Room-temperature ionic liquids (RTILs), and Neutral ligands deep eutectic solvents (NL-DES).

The first class are mixtures of aluminium chloride with alkali chloride salts (LiCl, NaCl, KCl, or CsCl) [118–121]. These systems require an external heat source in order to melt , and exchange chloride ions (between 200°C and 400°C). Nonetheless, as the alkali cations are believed to show little influence on the electrochemical properties, these systems provide ideal analytical characterisations of the anionic species behaviour.

The second class are molten salt systems, that are liquid at room temperature [122]. Such RTIL is produced by mixing $AlCl_3$ salt with a chosen organic chloride salt. These organic molecules are usually imidazole chlorides [123–126], pyridinium chlorides [48,127,128], or ammonium chlorides [129–132]. Despite being expensive, these electrolytes are easy to make and do not require external energy. These features have made RTILs the most studied systems, across the non-aqueous aluminium electrolyte systems.

The last class is the most recent class of chloroaluminate ionic liquids. NL-DES use neutral ligands (L) to complex the aluminium chloride salt. In this view, $AlCl_3$ is considered as a chloride ion supply for the system. The ionic liquid is therefore formed by disproportionation:

$$2AlCl_3 + xL \rightarrow AlCl_4^- + Al(L)_xCl_2^+$$

The ligands usually used to generate those deep eutectic solvents are amides [133–135], urea [136–139], or lactones [140]. The electrochemical systems using these NL-DESs have usually displayed lower electrochemical properties, than their RTIL counterparts. This is believed to originate from the lower ionic conductivity of the NL-DESs. Nonetheless, these ionic liquids are studied for their wide chemical tuning properties. For instance, this approach could be used to widen the electrochemical window of the Al-ion electrolytes, by totally removing the need for chloride in the mix [141].

2. The 1-ethyl-3-methylimidazolium chloride : aluminium chloride ionic liquid

Among the RTIL electrolytes for aluminium-ion systems, the most widely studied is the 1-ethyl-3-methylimidazolium chloride and aluminium chloride (EMImCl:$AlCl_3$). Both chemical and electrochemical properties are provided in the literature. Throughout the rest of this work, the EMImCl:$AlCl_3$ electrolyte will be chosen as the electrolyte for the electrochemical cells. This part will therefore provide chemical and structural characterisation of this ionic liquid.

2.1 Speciation inside the ionic liquid

Various species can be formed inside the chloroaluminate ionic liquids, Indeed, the aforementioned oligomerisation reactions have already presented the variety of anionic species, that can exist in the mix. In the EMImCl:$AlCl_3$ ionic liquid, those reactions are Lewis acid-base reactions. The chloride ion from the organic salt is exchanged with the Lewis acid $AlCl_3$, following:

$$\mathrm{EMImCl} + \mathrm{AlCl_3} \rightarrow \mathrm{EMIm^+} + \mathrm{AlCl_4^-}$$

The species equilibrium in the EMImCl:$AlCl_3$ ionic liquid is therefore parametrised by the ratio between those two compounds. In an equimolar mix, the chloride ion exchange reaction is total, and only the $EMIm^+$ and $AlCl_4^-$ species exist. When $AlCl_3$ is limiting, some chlorine species are left unreacted. Therefore $EMIm^+$, $AlCl_4^-$, and Cl^- species exist in those systems. On the contrary, when $AlCl_3$ is in excess, aluminium chloride reacts with its conjugated base $AlCl_4^-$ to form oligomeric species.

All those equilibria allowed to construct the speciation diagram of the anionic species in the EMImCl:$AlCl_3$ ionic liquid, as a function of the rate of $AlCl_3$. Fannin et al.[142] proposed one, as shown in **Figure 18.**. This is a simplified diagram that only considers the formation of Cl^-, $AlCl_4^-$, and $Al_2Cl_7^-$ species. For more acidic systems, Øye et al. [143] used a thermodynamic model. There, the oligomeric $Al_3Cl_{10}^-$ and $Al_4Cl_{13}^-$ anions are shown to form, from 0.55 and 0.65 mole fractions of $AlCl_3$ respectively.

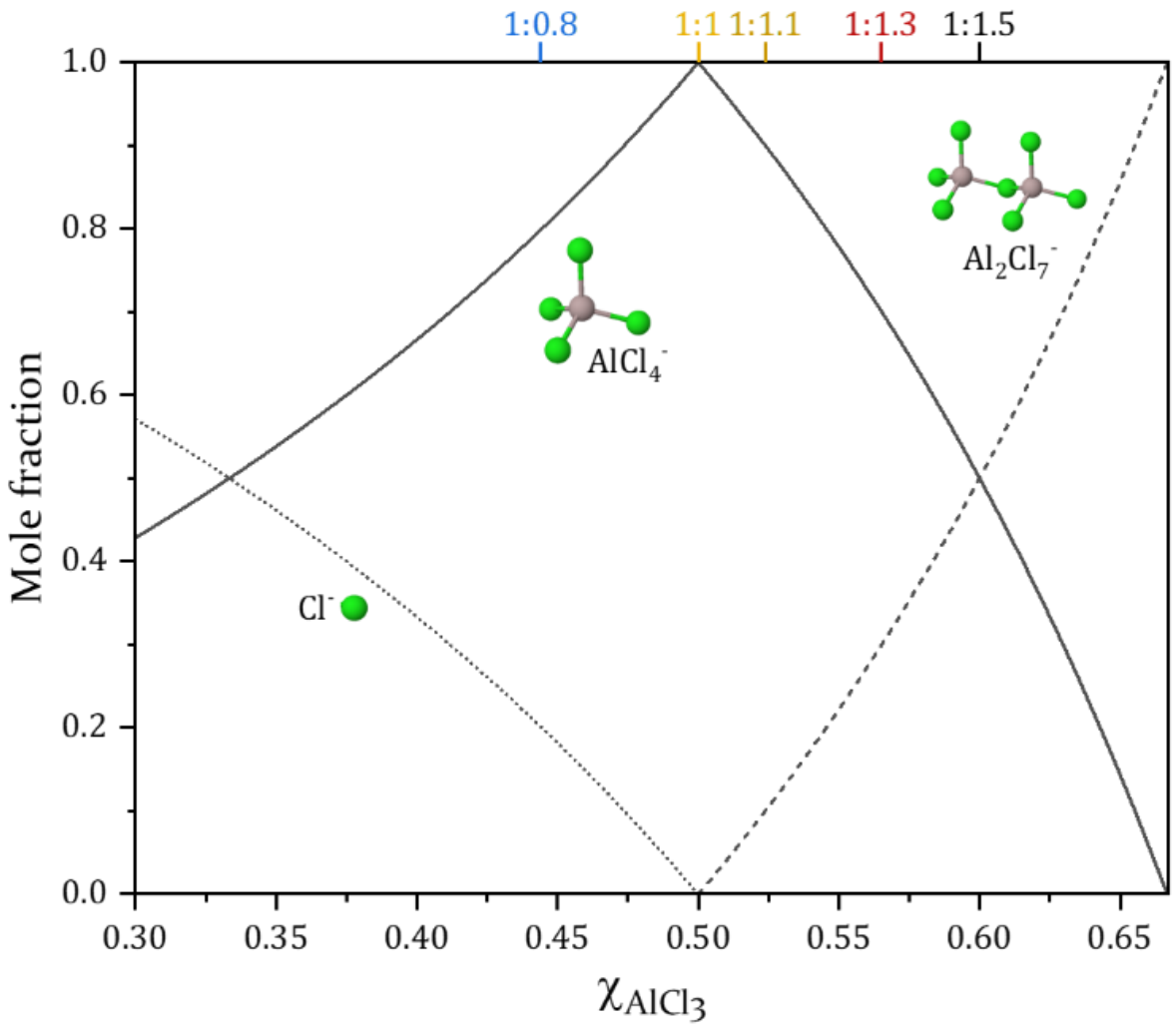

Figure 18. Simplified speciation diagram of the chloroaluminate species in the EMImCl:$AlCl_3$ mix, as a function of the $AlCl_3$ rate, from [142]. Mole fractions of Cl^-, $AlCl_4^-$, and $Al_2Cl_7^-$ are represented by dotted, solid, and dashed lines respectively. The synthesised mix realised in this work is reported on the top axis.

Notably, as the concentration of free chloride ions varies with the mix composition, chloro-acidity can be defined. The ionic liquids are therefore described as basic when rich in free Cl^- ions, or acidic when rich in dimeric or oligomeric species. In **Figure 18.**, the top axis features five coloured EMImCl:$AlCl_3$ mix compositions (1:0.8, 1:1.10, 1:1.1, 1:1.3, and 1:1.5). These compositions are those of the ionic liquids synthesised and characterised in this work. These syntheses cover basic, neutral and acidic mixes. Emphasis is put on the acidic mix, as the dimer $Al_2Cl_7^-$ ion is believed to be responsible for the electrochemical properties of the ionic liquid.

2.2 Chemical and structural characterizations

Various characterisations were performed on the different EMIm:$AlCl_3$ ionic liquids synthesised. Analyses of a wide acidity range are realised to understand the effect of the speciation on the ionic liquid properties. These characterisations aim to probe both the short-range and the longer-range scales.

Raman spectroscopy

The first characterisations were performed by Raman spectroscopy, on the 1:0.8, the 1:1.1, the 1:1.3, and the 1:1.5 Ionic liquids. Raman spectroscopy is used to probe the atomic vibrations of a sample, at the molecular scale. As shown in **Figure S28.**, the typically collected spectra feature three main regions. These are attributed to laser excitation, chloroaluminate ions, and $EMIm^+$ ions-related peak domains. Notably, no variation was observable in the $EMIm^+$ region, across the whole acidity range. Also, the signals from the laser-dependent region are unreliable data. Therefore, only the domain displaying the peaks that are relative to the chloroaluminate ions (250 cm^{-1} to 600 cm^{-1}) will be presented next.

The spectra collected from the various ionic liquids are presented in **Figure 19.**. There, three main peaks are observable at 311 cm^{-1}, 349 cm^{-1}, and 431 cm^{-1}. The central peak is observed to increase when the ionic liquid is closer to equimolar proportions, and to decrease otherwise. Hence, this signal is attributed to the monomer ion $AlCl_4^-$. On the other hand, the two other contributions are flat in the basic mix, and progressively expand along with the acidity increase. They are then ascribed to the dimer ion $Al_2Cl_7^-$. Notably, other signals appearing at 443 cm^{-1} and 596 cm^{-1} are attributed to the $EMIm^+$ cation. **Figure S29.** summarises those peak attributions.

In addition, the two broad peaks centred around 500 cm^{-1} and 540 cm^{-1} are also recorded to evolve with the ionic liquid acidity. Indeed, the basic 1:0.8 mix shows a high 500 cm^{-1} peak and a lower 540 cm^{-1} peak, whereas the acidic 1:1.5 mix presents opposite peaks magnitude.

In the literature, diverging interpretations exist about the origin of these peaks. For instance, Takahashi et al. [144] attributed a 504 cm^{-1} peak to the monomeric $AlCl_4^-$ ion. Zhu et al. [145] proposed that a 495 cm^{-1} peak is caused by the higher oligomeric species $Al_nCl_{3n+1}^-$ ($n \geq 3$). Their observations were although realised in the acidic 1-methyl-3-propylpyrrolidinium chloride and aluminium chloride mix (Py13Cl:$AlCl_3$), and were explicitly not observable in the EMImCl:$AlCl_3$ ionic liquid. Finally, Rytter et al. [121] also identified contributions at 493 cm^{-1}, and 540 cm^{-1} in the $AlCl_3$:CsCl melts. They ascribed these last to the higher oligomeric species. Also, they evoked that Fermi resonances could cause these signals.

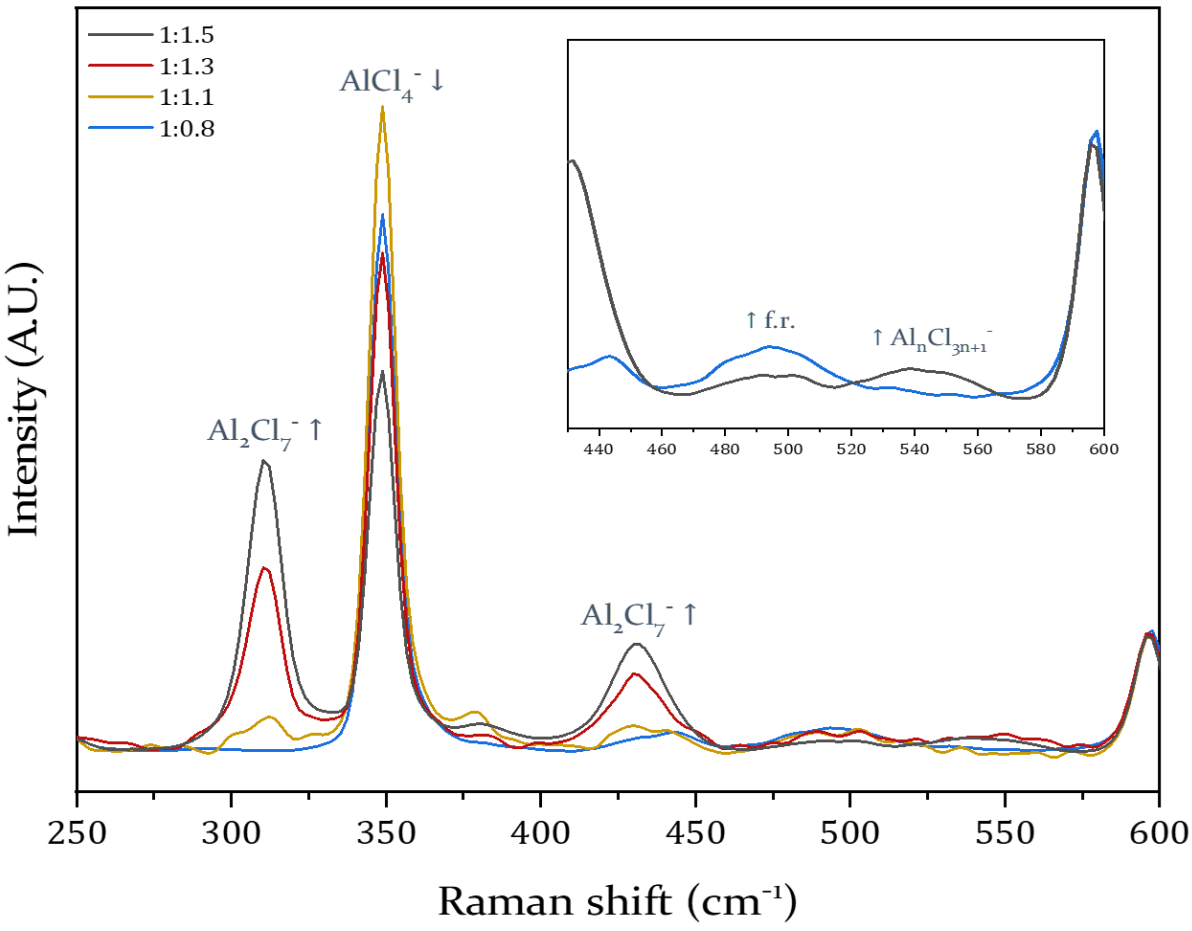

Figure 19. Raman spectra of the 1:0.8 (blue), 1:1.1 (golden), 1:1.3 (red), and 1:1.5 (black) EMImCl:$AlCl_3$ mix. The inset provides a zoom, onto the 430-600 cm^{-1} region, of both the 1:0.8 and 1:1.5 ionic liquids. The arrows next to the molecular attributions indicate the peak intensity evolution, from neutral to acidic.

Liquid-state ^{27}Al NMR

Further characterisations were performed on both the acidic 1:1.1 and 1:1.5 ionic liquids, by ^{27}Al NMR spectroscopy. These analyses aim to probe the local environments of the chloroaluminate species, as a function of the mix acidity. The results are shown in **Figure 20.**.

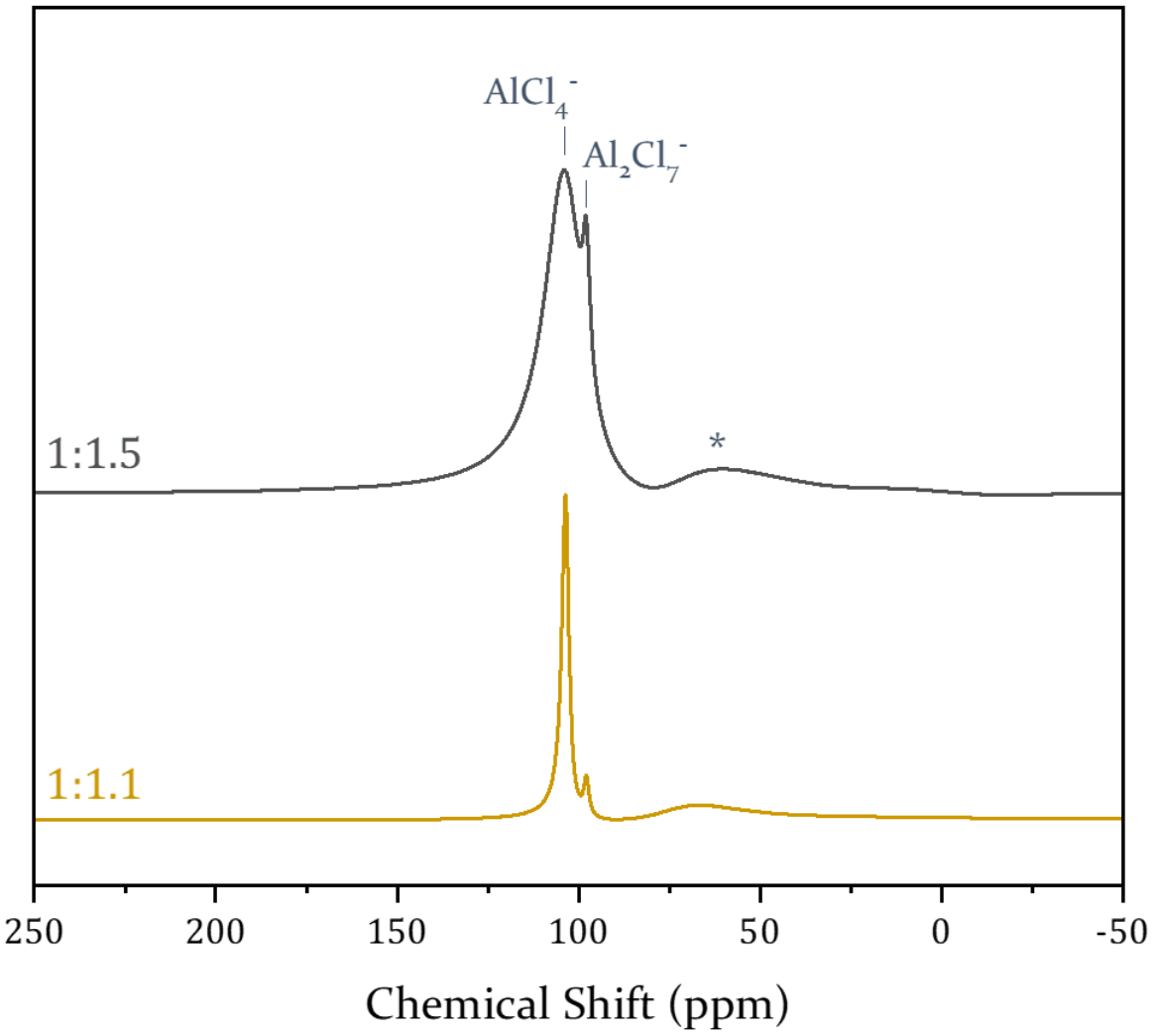

Figure 20. ^{27}Al NMR spectra of the 1:1.1 (golden) and 1:1.5 (black) EMImCl:$AlCl_3$ mix. The * mark indicates a signal coming from the NMR probe itself.

The 1:1.1 ionic liquid spectrum presents two narrowed peaks, at 98 ppm and 104 ppm. These peaks are attributed to the dimer $Al_2Cl_7^-$ and the monomer $AlCl_4^-$ ions respectively [146]. Notably, the dimer peak is small in regard to the monomer peak, indicating the sparse amount of dimeric species in the 1:1.1 mix. In the spectrum of the more acidic 1:1.5 ionic liquid, these two peaks are still observable. Nonetheless, the dimer peak has greatly been enhanced, according to the higher amount of this species in the mix. In addition, the monomer peak has also significantly been broadened. This suggests a wider distribution of bond lengths, inside the monomer ions in the acidic mix, and can be attributed to a contribution from the oligomeric species.

X-ray total scattering

Structural features of the ionic liquids are investigated by high-energy X-ray total scattering. This method allows for collecting both the Bragg and the diffuse scattering data of a sample (see **Chapter 2**). **Figure 21.** presents the collected pair distribution function (PDF) data of the 1:0.8, the 1:1.0, and the 1:1.5 EMImCl:$AlCl_3$ ionic liquids. This graph displays strong signals below 4 Å, and broad contributions until 11 Å, and no coherent signal above. Therefore, it can be divided into three different regions (noted I, II, and III).

The first one (I) exhibits two strong contributions, at 2.15 Å and 3.52 Å. These two contributions are attributed to the first and second-order neighbours respectively. The first neighbours correspond to the Al-Cl pair, whereas the second neighbours correspond to both the Cl-Cl pair (bonded to the same Al atom), and the Al-Al pair (bonded to the same Cl atom). Two close views of these peaks are joined in **Figure 21.**. Negligible shifts are observed there, showing the minimal effect of the ionic acidity on the intramolecular bond lengths. Notably, the contributions from the organic cation are also observable in this graph region. Indeed, the low-intensity peaks at 1.43 Å, 1.81 Å, 2.52 Å, and 2.83 Å can all be attributed to the C-C, C-N, and N-N signals.

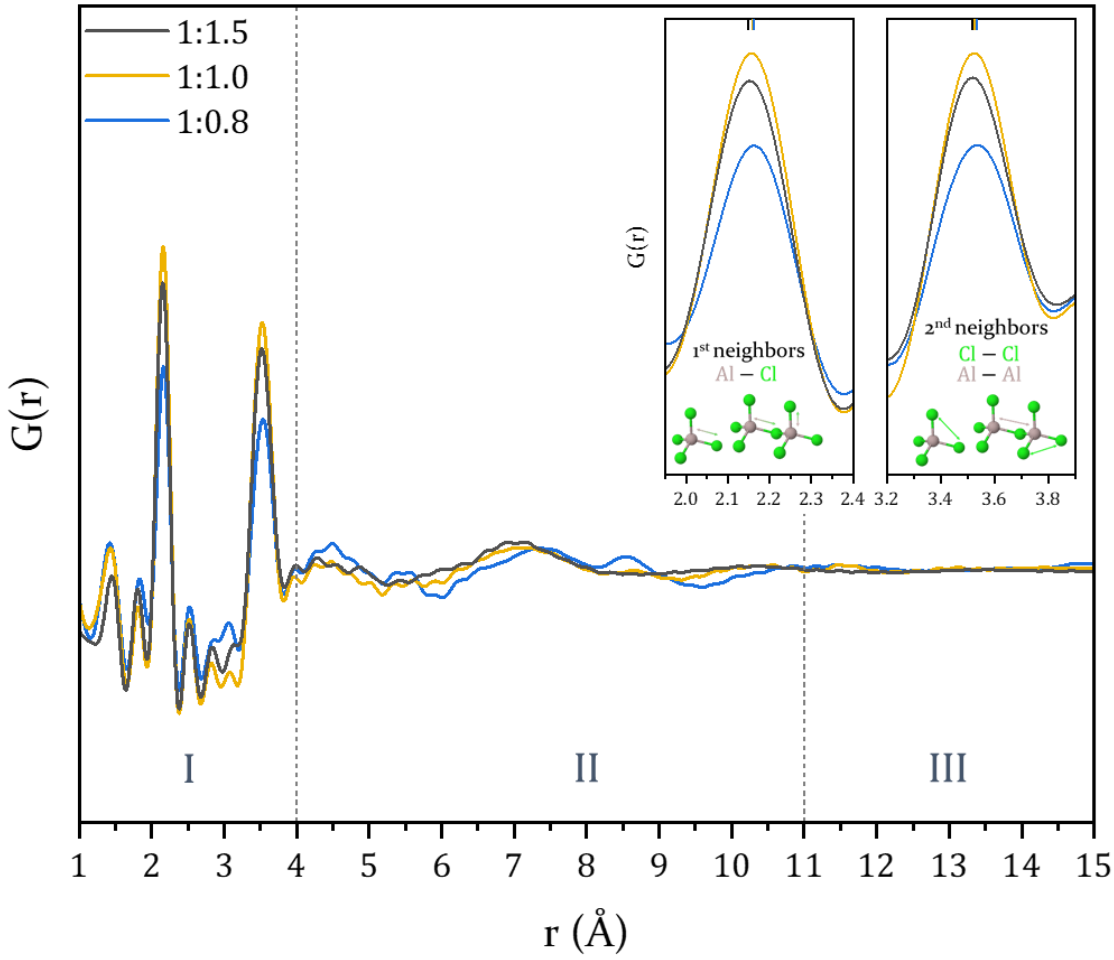

Figure 21. Pair Distribution Functions of the 1.0.8 (blue), the 1:1.0 (yellow), and the 1:1.5 (black) EMImCl:$AlCl_3$ ionic liquid. Dotted lines are used to delimit the various regions of the graph. Two inserts, with ticks indicating the precise peak positions, propose zooms onto the two main contributions. Attribution of these lasts is also provided as schemes.

The second region (II) spans from 4 to 11 Å. The recorded signal in this region describes long-range orderings in the samples. For these ionic liquids, this provides information about the intermolecular interactions. There, only broad signals are observable, thus the intermolecular interactions are diverse.

Further insights on these inter-molecular interactions are provided by the collected structure factors, shown in **Figure 22.**. Indeed, as peaks are observable below 5 $Å^{-1}$, the presence of a long-range ordering is witnessed.

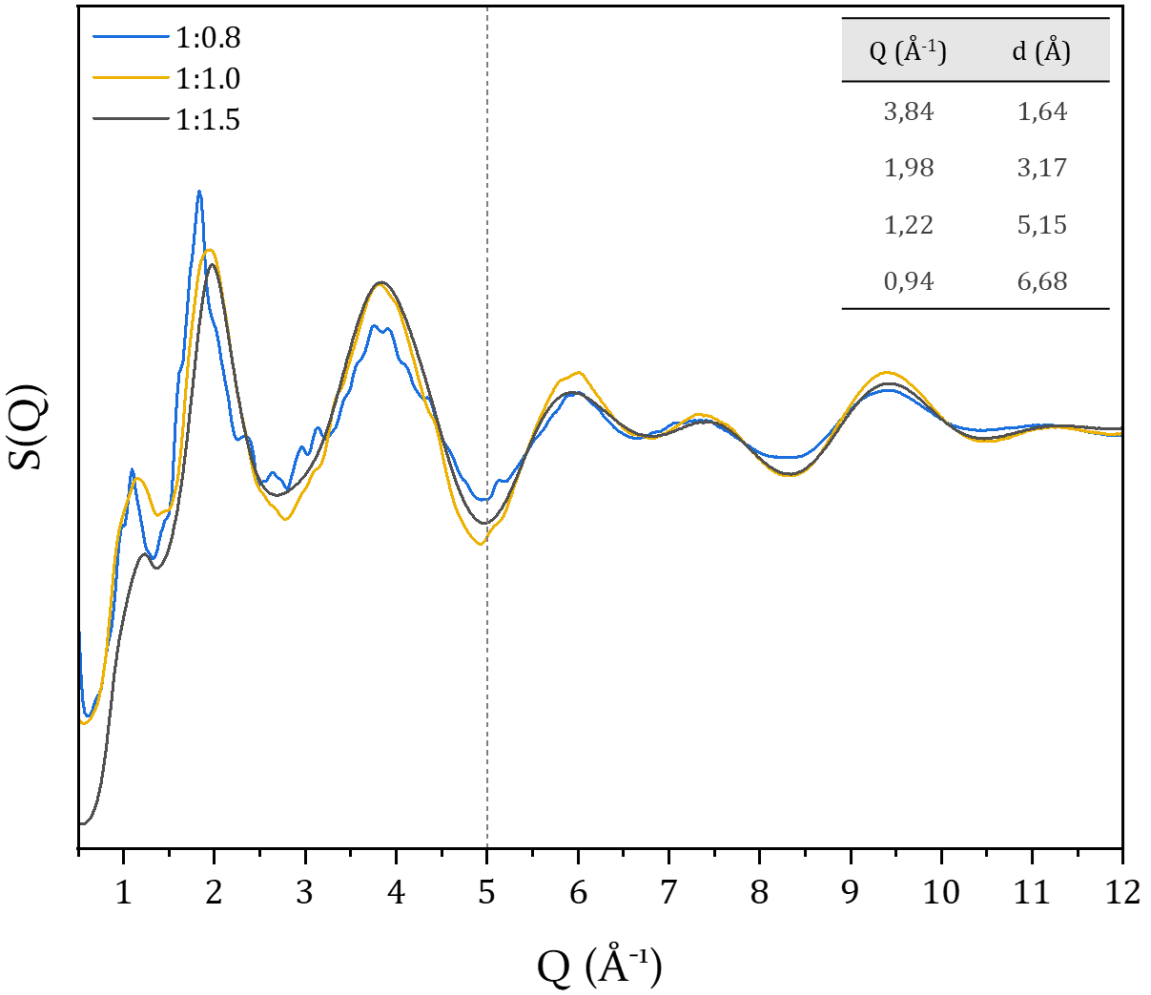

Q (Å^{-1})	d (Å)
3,84	1,64
1,98	3,17
1,22	5,15
0,94	6,68

Figure 22. Structure factor of the 1:08 (blue), 1:1.0 (yellow), and1:1.5 (black) EMImCl:$AlCl_3$ ionic liquids. Measured scattering vector and the equivalent reciprocal spacing values of the 1:1.5 mix are reported in the joined table. The dotted line delimits the coherent signal.

Gibson et al. [147] observed a similar long-range ordering, in the S(Q) data of the $AlCl_3$-KCl molten salt system. They proposed that this long-range order might originate from parallel networks of ions, separated by specific distances (d). For instance, peaks around 1 Å^{-1} are attributed to two dimer ions, interacting in close vicinity.

For the three ionic acidities probed here, the equivalent distances (given by $d=2\pi/Q$) range from 1.5 Å to 6.7 Å. Notably, the influence of the acidity of the ionic liquid on the S(Q) is observable. Indeed, the basic mix displays peaks at lower Q-values, than the acidic mix. Consequently, the distances inter-molecular distances in the acidic ionic liquids are observed to be contracted, in regards to those of the basic one.

Liquid-state ^{1}H & ^{13}C NMR

Finally, the influence of the ionic liquid acidity on the $EMIm^{+}$ cation has been investigated by NMR spectroscopy. Liquid-state ^{1}H NMR spectra of both the 1:1.1 and the 1:1.5 mix has therefore been collected. The analysis has been done by immersing a D_2O capillary inside the analysed ionic liquid. In the collected spectra, a small contribution coming from H_2O dissolved in the D_2O capillary is therefore observable (at 4.70 ppm), and has been used as an internal reference for the spectra.

Figure 23. presents close-up views from the peaks of the ^{1}H spectra (see **Figure S30.** for the whole spectra). Six peaks are observable, and are attributed to the six proton environments of the imidazolium cation. The 1:1.1 ionic liquid shows signals of higher chemical shifts, than the 1:1.5 one. In addition, some peaks display a subtle multiplicity Indeed, all the three protons bonded to the imidazolium ring (*a* and *b*-*c*), as well as the protons from the *F* carbon, display three contributions within each of their peaks. This phenomenon is observed for both the analysed ionic liquids, and is shown for the 1:1.5 mix in **Figure 24.**.

Despite not reporting it, Fannin et al. proposed an origin to this subtle multiplicity phenomenon [142]. Indeed, they considered various cation-anion interaction models to describe the $EMImCl:AlCl_3$ ionic liquid. They concluded that the organic cation must be twice coordinated by the anionic species in the mix. In the acidic ionic liquid, these species are mainly $AlCl_4^-$ and $Al_2Cl_7^-$ ions, therefore three different configurations can exist: 2-fold complexed by $AlCl_4^-$ anions, complexed by an $AlCl_4^-$ and an $Al_2Cl_7^-$ anions, or 2-fold complexed by $Al_2Cl_7^-$ anions. Each of these configurations provides a slightly different environment for the $EMIm^{+}$ cation, hence different contributions on the spectrum. As a result, and with a good enough resolution, each NMR peak appears to be composed of three signals – from the three environments. They further presented the individual chemical shifts, due to each anionic environment contribution, for the three protons bonded to the imidazolium ring [142]. Here, this data matches perfectly the one provided in **Figure 24.**.

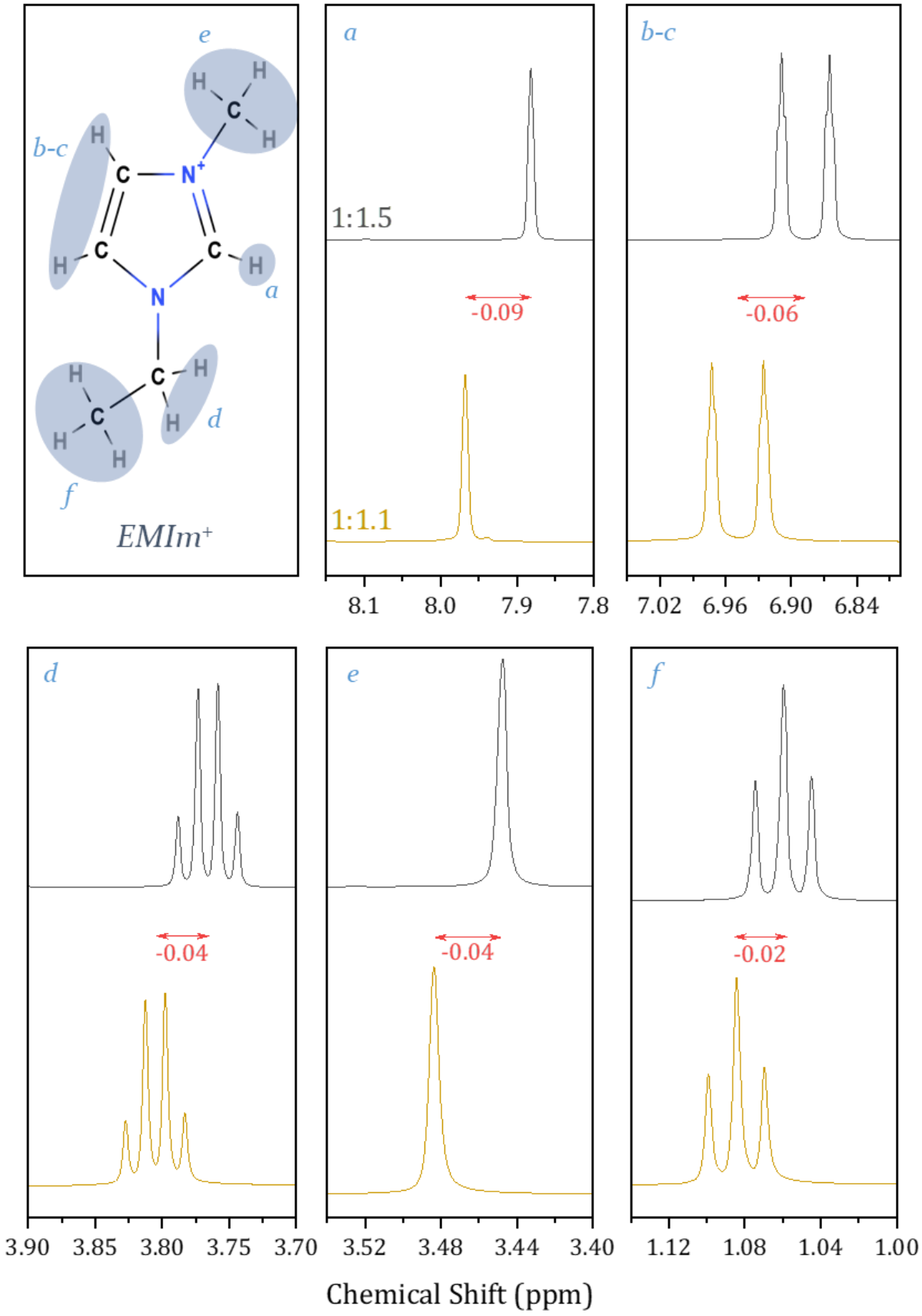

Figure 23. Close-up views of the peaks from the ^{1}H NMR spectra of the 1:1.1 (golden) and 1:1.5 (black) EMIm:$AlCl_3$ mix. Peak attribution is provided by the joined $EMIm^+$ scheme.

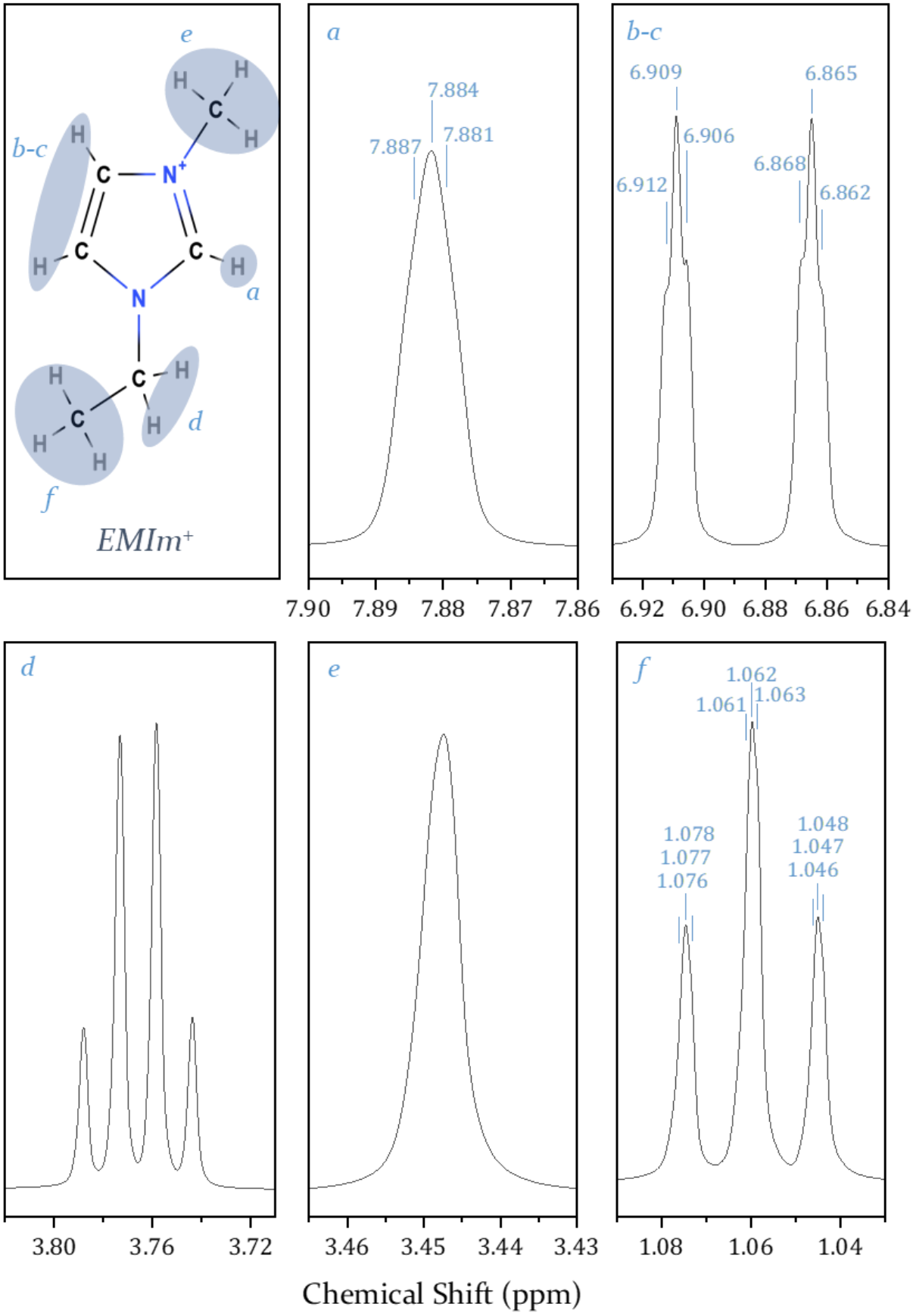

Figure 24. Close-up views of the peaks of the ^{1}H NMR spectrum of the 1:1.5 EMImCl:$AlCl_3$. Individual contributions within each peak are indicated when observable.

The organic cation complexation is therefore believed to occur via interactions between the anionic species and the protons bared by the $EMIm^+$ ions. These interactions are sometimes assimilated to hydrogen bonds. Such weak interactions have already been suggested, by calculations, in the literature [148]. Indeed, the configuration of minimal energy of the system hints towards the apparition of H-bonds between the organic cation and the chloride-rich anions. However, the reported involved protons were not the same as those observed here, via NMR (*a*, *b*-*c*, and *f*).

Notably, geometric constraints arise from this 2-fold coordination model. Indeed, this implies that two anionic species are localised on either side of the aromatic ring of the $EMIm^+$ cation. This three-bodies motif being repeated throughout the liquid, dynamic structurations can occur. These cation-anion interactions are then understood to be the cause of the long-range structurations in the ionic liquids, previously reported with the X-ray total scattering data.

Finally, ^{13}C NMR has also been realised on the same two ionic liquid samples. The collected spectra are proposed in **Figure S31.**, and zoom onto regions of interest are presented in **Figure 25.**. Without any external reference, the 49.63 ppm peak has been chosen as the internal reference for the two spectra. This peak corresponds to the N-bonded methyl carbon (*E*). It has been chosen due to the small influence of the acidity on the displacement of its bonded protons, and due to the absence of the subtle multiplicity on the corresponding proton spectrum.

Six peaks are observable on each mix spectrum, corresponding to the six carbons of the $EMIm^+$ cation. The chemical displacements of the probed carbon atoms are influenced by the mix acidity. Three behaviours are observable among the $EMIm^+$ carbons: The signal from terminal methyl carbon from the ethyl group (*F*) remains unchanged. The twice N-bonded carbon from the imidazolium ring (*A*) chemical shift is heavily reduced. Finally, the three remaining carbons (*B*, *C* and *D*) display similar shifts towards the higher ppm.

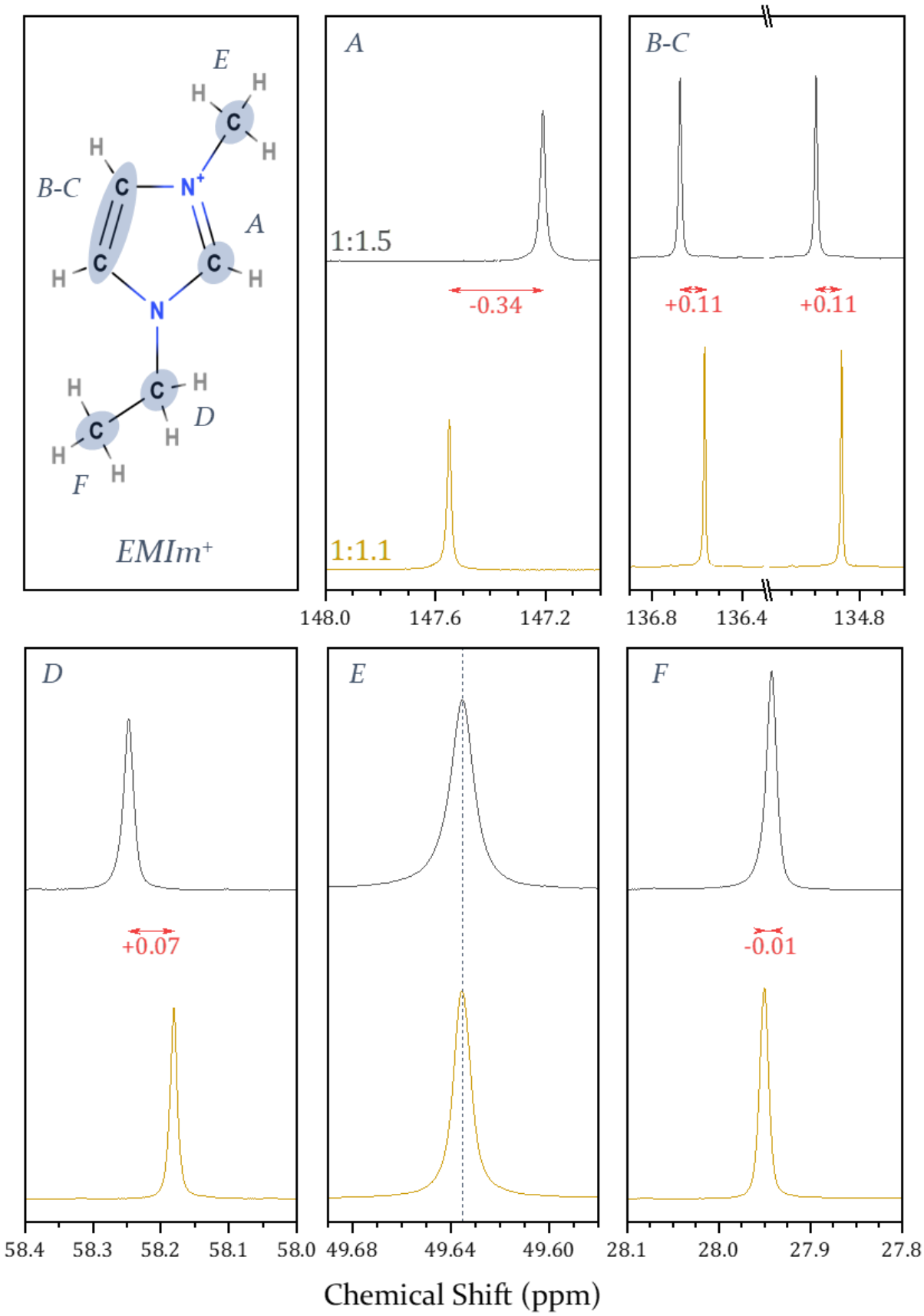

Figure 25. Close-up views on the peaks from the ^{13}C NMR spectra of the 1:1.1 (golden) and 1:1.5 (black) EMImCl:$AlCl_3$ mix. Peak attribution is provided by the joined $EMIm^+$ scheme. The red arrows indicate the chemical shift difference between the 1:1.5 and the 1:1.1 peaks.

Wilkes et al. [149] attributed these variations in ^{13}C chemical shifts, to the nature of the anions that interact with the probed imidazolium cations. To do so the same twice-coordinated cation model as Fannin et al. [142] was used. As for the ^{1}H NMR spectra, the $AlCl_4^-$ ion is believed to (indirectly) provide a higher chemical shift to the probed carbon, than the $Al_2Cl_7^-$ ion. Hence why, the ^{13}C NMR signal from the *A* carbon in the 1:1.5 ionic liquid appears at a lower chemical shift than in the 1:1.1 mix.

However, the other carbons do not exhibit such variations in chemical shifts, with the acidity variation. Indeed, despite not being engaged in cation-anion interactions, the *D* carbon is affected by the change in acidity in a similar manner to the *B* and *C* carbons. It is then considered that these changes might instead be due to variations in the C-H, C-N, and C-C bond lengths. Indeed, the change in speciation and the proton engagement in interactions might induce strains, and distortions within the organic cation. The chemical shift enhancements observed in **Figure 25.** therefore suggest a contraction of the imidazolium ring, with the increase of the ionic liquid acidity.

2.3 Computational calculations

To gain more insights into the dynamics and equilibria of the studied systems, molecular dynamic calculations have been performed by Camille Bacon and Alessandra Serva. Boxes containing $EMIm^+$, Al^{3+}, and Cl^- ions have been constructed. Four EMImCl:$AlCl_3$ mix have been considered: 1:0.9, 1:1.0, 1:1.1, and 1:1.3. For each of these mix, the radial distribution functions have been traced. The isolated contributions from the Al^{3+}-Al^{3+} pair and the Al^{3+}-Cl^- pair are available in **Figure S32.**.

There, in the Al^{3+}-Al^{3+} graph, a peak around 3.6 Å is observed to increase with the part of $AlCl_3$ in the ionic liquid. This peak is attributed to a pair of Al^{3+} ions sharing a chloride ion. This peak is very small for the 1:0.9 and the 1:1.0 mix, but increase quickly for the 1:1.1 and the 1:1.3 mix. In addition, the radial distribution functions of the Al^{3+}-Cl^- pair displays two regions. The first, below 3 Å, only exhibits a single peak corresponding to the Al-Cl bonds between first neighbours. The second region, ranging from 3 Å to 6 Å, presents several peaks corresponding to the next neighbours. The 1:0.9 and the 1:1.0 mix do not show any contributions, whereas the 1:1.1 and the 1:1.3 mix does with increasing intensity.

Figure 26. presents the calculated speciation of the anionic species in the ionic liquids. As proposed by Fannin et al.[142], the monomeric $AlCl_4^-$ ion is the major species, in all the mix studied. In addition, the free chloride ions Cl^- disappear above the 1:1.1 mix ratio. Reciprocally, only a few dimeric species exist in the mildly basic 1:0.9 mix. In addition, traces of the higher oligomeric species ($Al_3Cl_{10}^-$ and above) are already found in the mix close to the neutral composition. Indeed, their formation was expected by Øye et al. [143], from the 1:1.1 mix on.

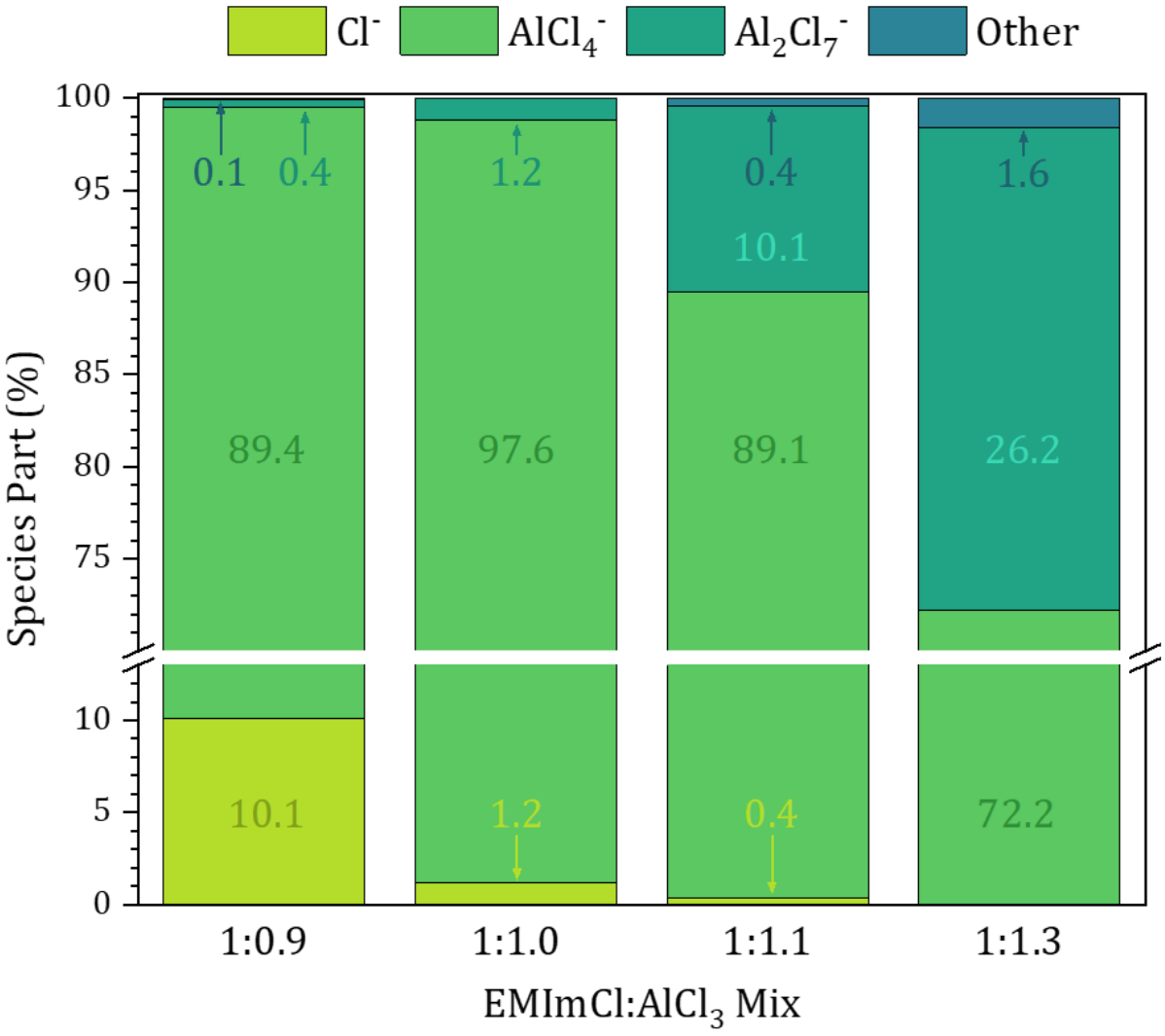

Figure 26. Calculated speciation of the anionic moieties in the 1:0.9, 1:1.0, 1:1.1, and 1:1.3 EMImCl:$AlCl_3$ ionic liquids. The anionic species referred to as 'other' are the oligomeric species higher than the dimer ($Al_3Cl_{10}^-$ and above).

Further insights are provided by examining the lifetime of the anionic species in the mix (see **Figure 27.**). Indeed, the average lifetime of the $Al_2Cl_7^-$ species remains unchanged for each ionic liquid, at about a few ns. In contrast, the one of the $AlCl_4^-$ species is higher (about a hundred ns in the 1:0.9 mix), but is diminished by two orders of magnitudes within the span of the acidity range. In addition, the high oligomeric species ($Al_3Cl_{10}^-$ and above) average lifetime is very low at 10 to 100 ps. All this describes a highly dynamic system, where $AlCl_3$ elementary bricks are exchanged between various anionic species. These dynamic exchanges are responsible for the existence of the high oligomeric species, even for mildly acidic ionic liquid systems, such as the 1:1.1 mix.

Furthermore, Gibson et al. [147] proposed reaction mechanisms for these dynamic exchanges, in $AlCl_3$-KCl molten salt systems. They considered the variation of local electric fields to gain insights into the oligomer formation (or dissociations). They conclude in a nucleophilic Sn2 reaction, and intermolecular Cl^- ion exchange mechanisms.

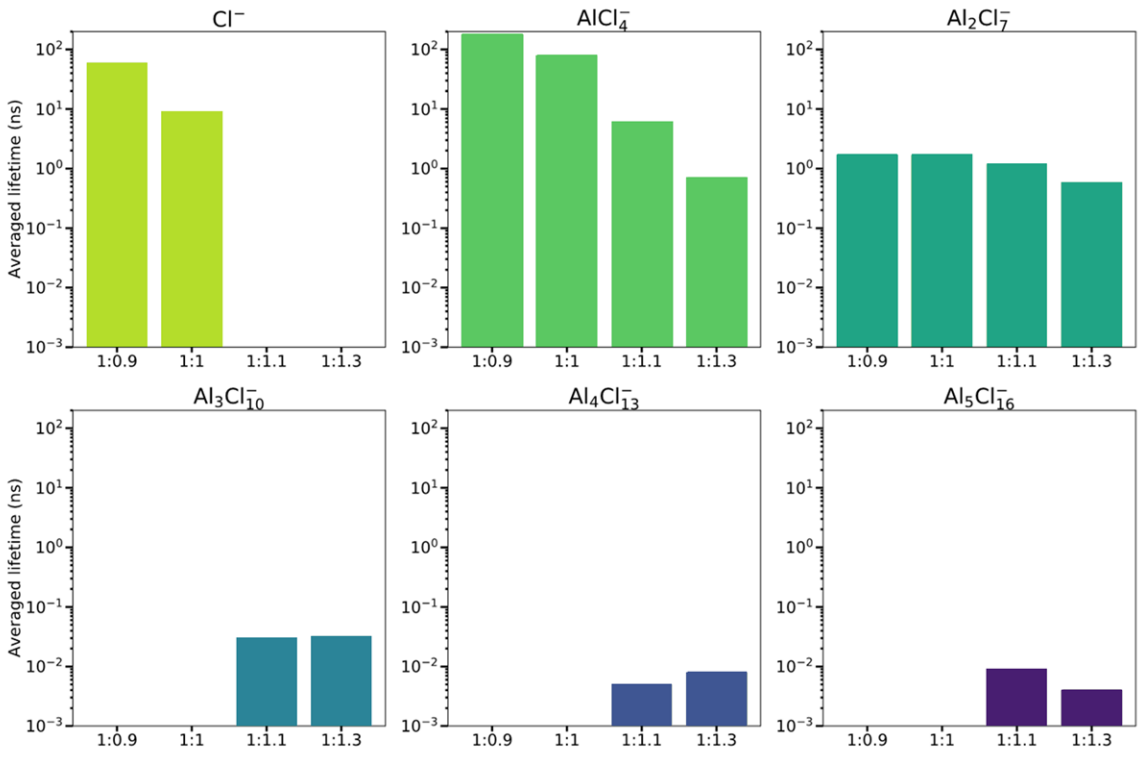

Figure 27. Calculated average lifetime of the anionic oligomers in the ionic liquids, as a function of the mix acidity.

Conclusion

In this chapter, a prospection for a suitable electrolyte to study aluminium-ion electrochemistry is proposed. Among those the EMImCl:$AlCl_3$ ionic liquid has been selected. The properties of this chloroaluminate ionic liquid electrolyte have then been presented.

The speciation inside the EMImCl:$AlCl_3$ ionic liquids has long been understood to be directly dependent on the amount of $AlCl_3$ in the mix. Various anionic species are favoured, depending on the mix equilibrium. These anionic species are short polymers of $AlCl_3$ grafted onto a chloride termination, such as: the pure chloride Cl^-, the monomer $AlCl_4^-$, the dimer $Al_2Cl_7^-$, the trimer $Al_3Cl_{10}^-$, ... As the mix is a liquid the system is dynamic, and these species are involved into mutual exchange reactions. Molecular dynamics calculations helped to show that these reactions led to the formation of short-lived anionic species of higher polymerisation degree. Notably, the electrochemical activity of the EMImCl:$AlCl_3$ ionic liquids is attributed to the electrochemical splitting of the polymerised anionic species, past the monomeric one.

The realised analyses also unveiled the internal structurations of the ionic liquid. Indeed, total scattering experiments showed evidence of medium-range order in the liquid samples. In addition, NMR spectroscopy revealed that the $EMIm^+$ cation is engaged in weak interactions with the anionic species in the mix. These interactions were verified to match the double-coordination model of the $EMIm^+$ cation, proposed by Fannin et al. [142].From all this, it has been understood that the probed structurations were caused by the local ordering, of these anion-cation-anion complexes.

Supplementary information

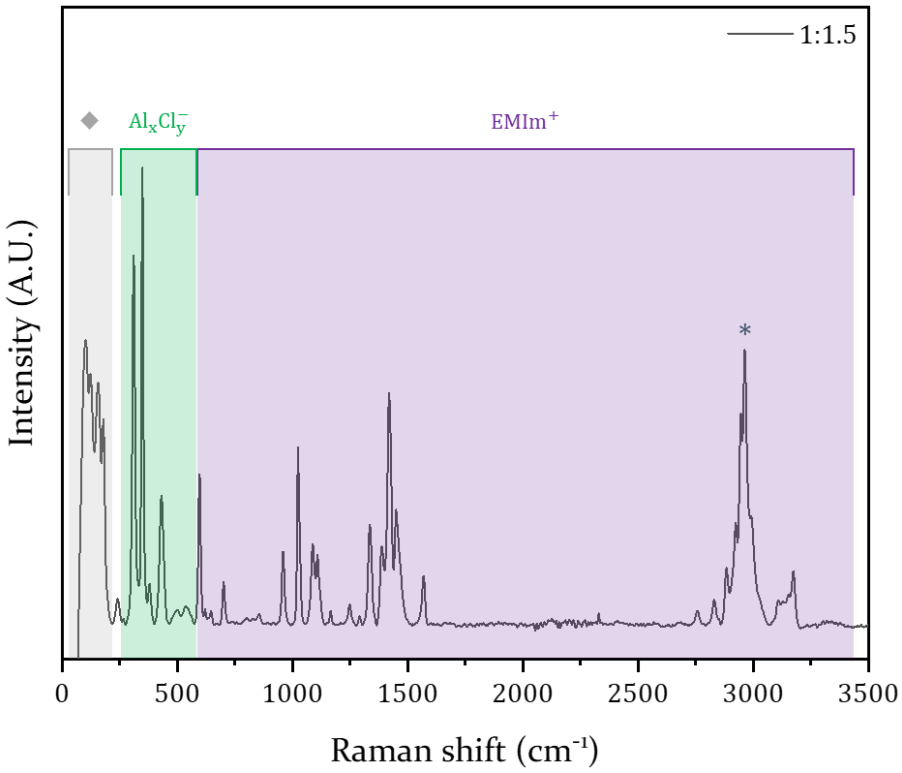

Figure S28. Raman spectrum of the 1:1.5 EMImCl:$AlCl_3$ ionic liquid. The coloured domains refer to the predominant species contributing to the recorded signals. The grey diamond mark indicates a domain in which the excitation beam contribution alters the observed signals. The * symbol indicates the peak used for normalisation.

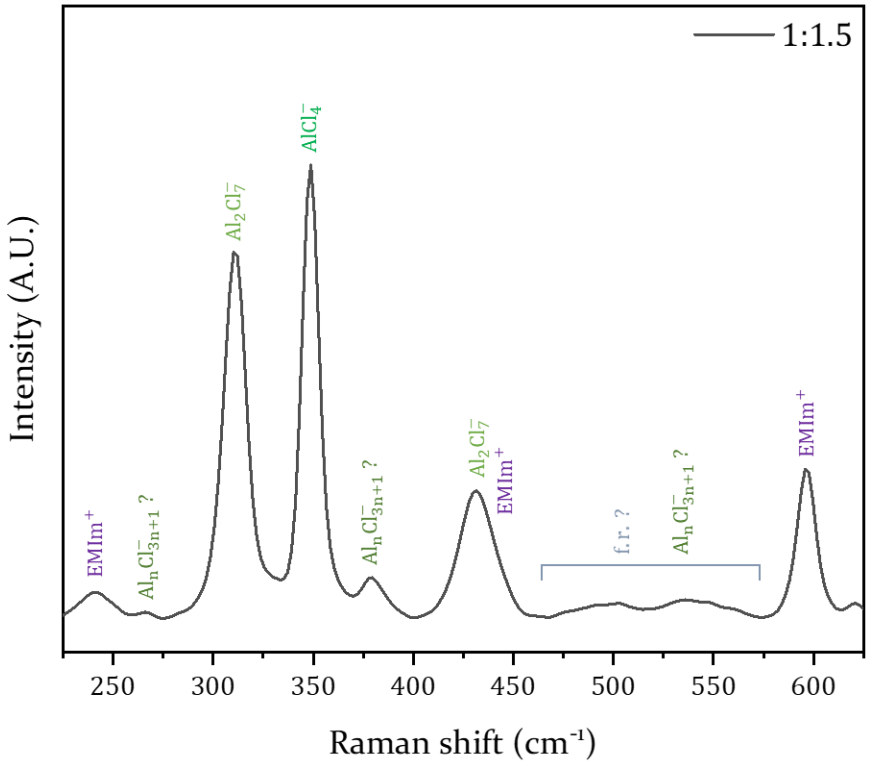

Peak position (cm^{-1})	Species attribution
241	$EMIm^+$
266	$Al_nCl_{3n+1}^-$
311	$Al_2Cl_7^-$
349	$AlCl_4^-$
379	$Al_nCl_{3n+1}^-$
431	$Al_2Cl_7^-$
443	$EMIm^+$
480-505	$Al_nCl_{3n+1}^-$ or Fermi resonance
530-550	
596	$EMIm^+$

Figure S29. Raman spectrum of the 1:1.5 EMImCl:$AlCl_3$ mix. Peak attribution is provided and is summarised in the joined table.

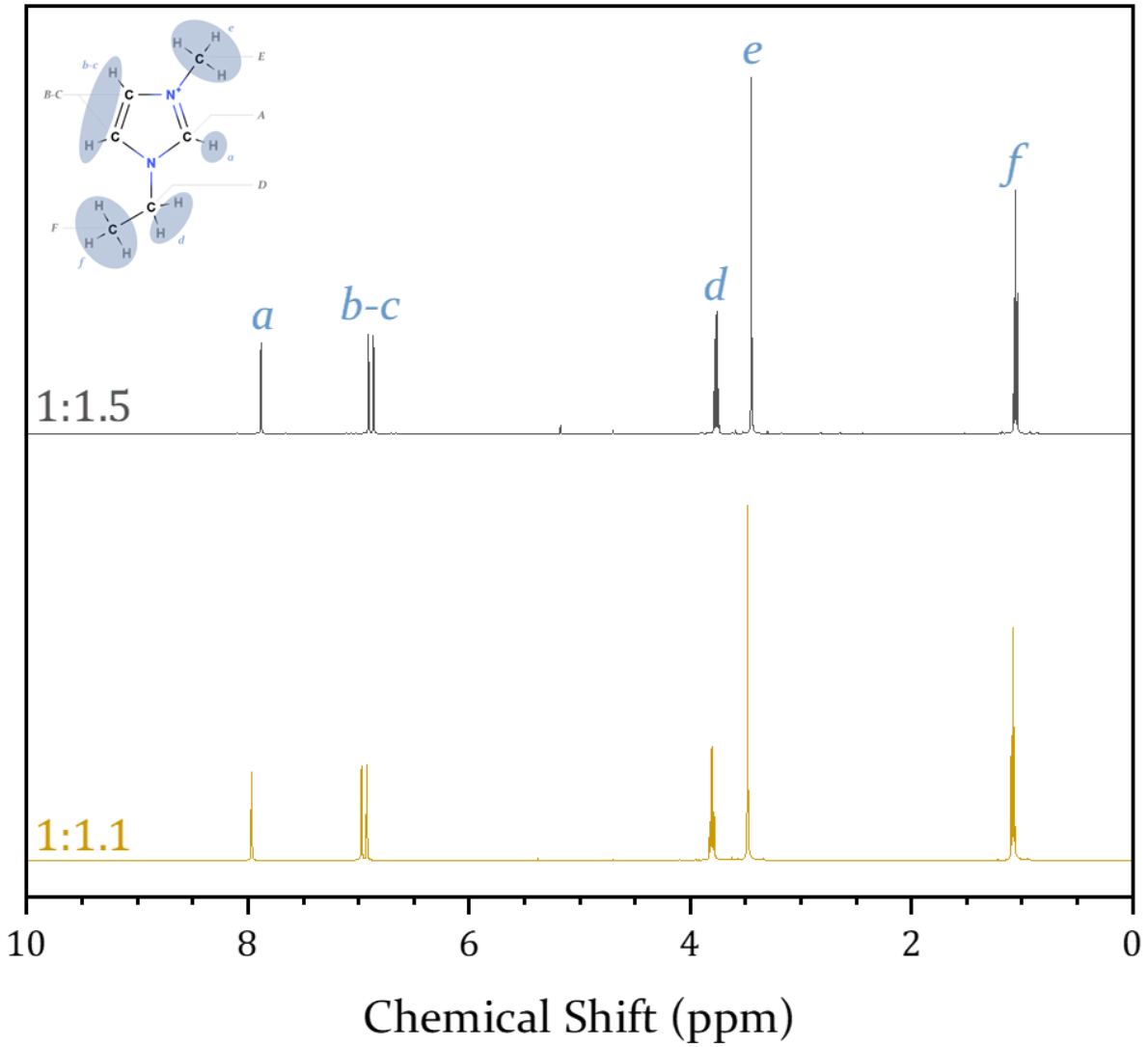

Figure S30. ^{1}H NMR spectra of both the 1:1.1 (golden), and 1:1.5 (black) EMImCl:$AlCl_3$ mix. Peak attribution is proposed as a molecular scheme of the $EMIm^+$ cation.

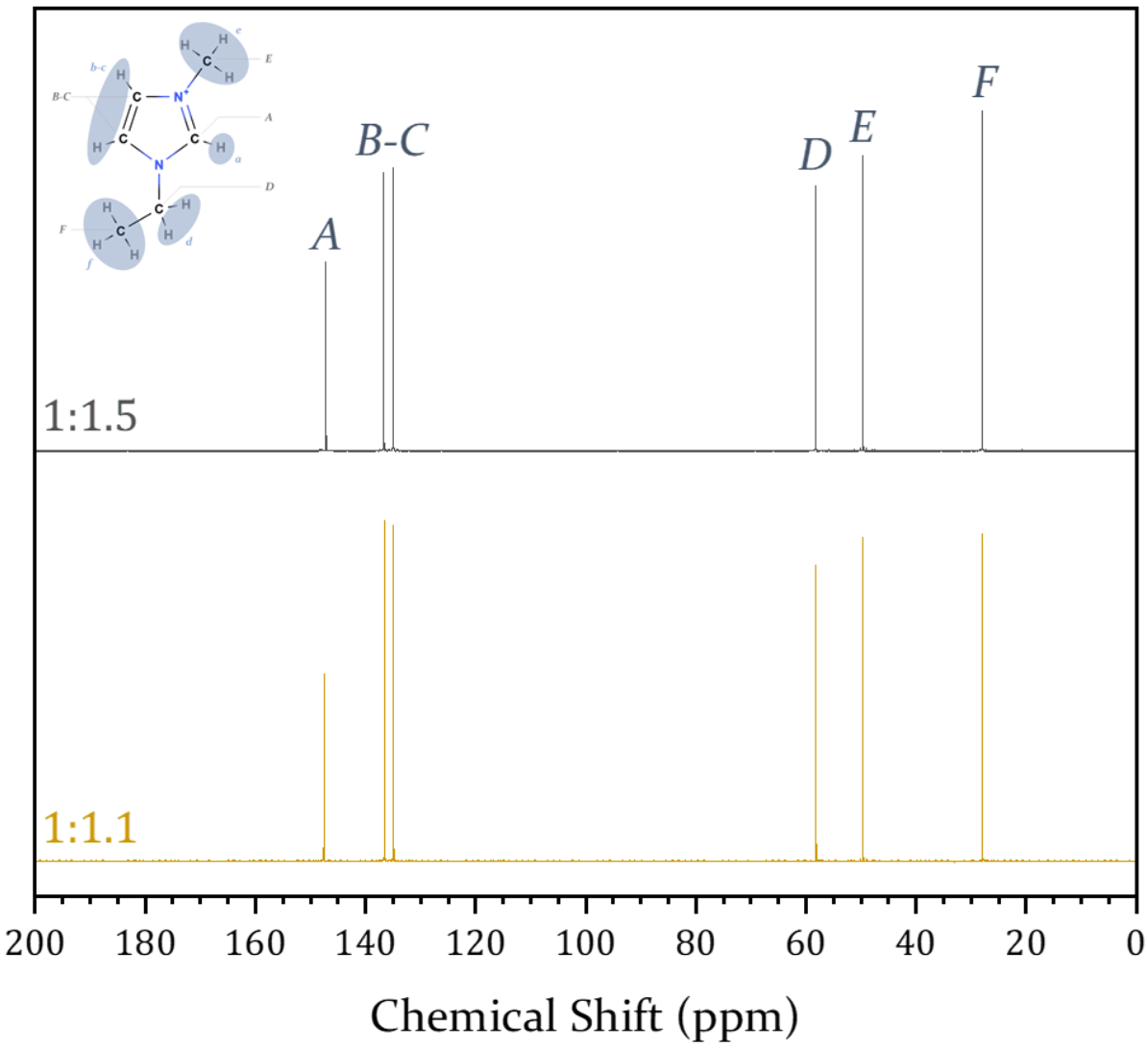

Figure S31. ^{13}C NMR spectra of both the 1:1.1 (golden), and 1:1.5 (black) EMImCl:$AlCl_3$ mix. Peak attribution is proposed as a molecular scheme of the $EMIm^+$ cation.

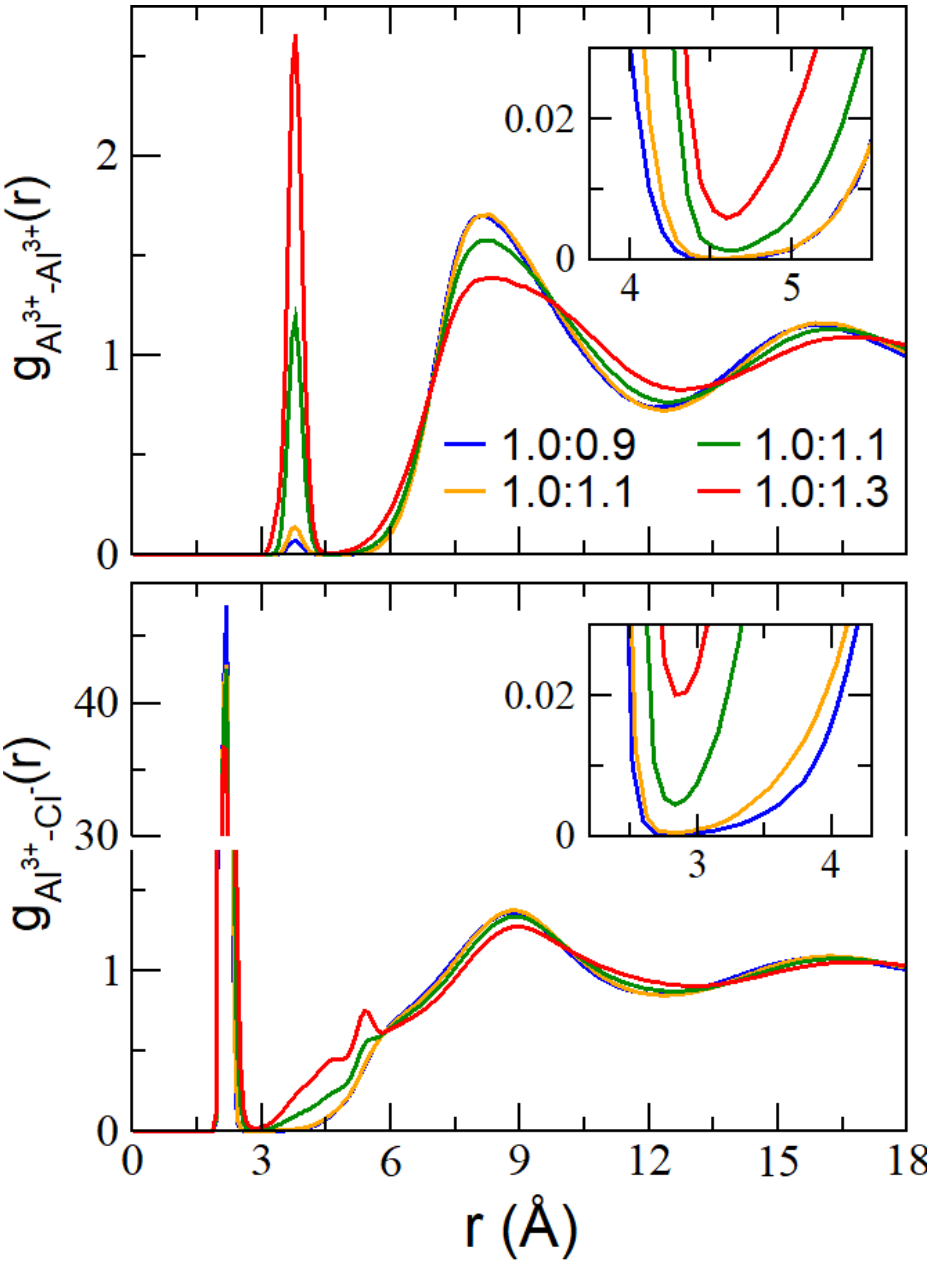

Figure S32. Calculated radial distribution functions of the Al^{3+}-Al^{3+} pair (top), and the Al^{3+}-Cl^{-} pair (bottom), in the ionic liquids as a function of the mix acidity.

Chapter 4. Structural characterisations of the titanate electrode materials

The host materials, chosen at the positive electrodes to intercalate the aluminium ion, are titanium oxide derivatives. These materials are obtained via sol-gel syntheses, as detailed in **Chapter 2**. The control of the synthesis parameters allows for a wide variety of compounds to be formed. Here, the control of the temperature led to the syntheses of three compounds: a defective lepidocrocite-type titanate material (90°C), a defective anatase material (110°C), and a pure anatase (150°C). Throughout this chapter, these materials will be referred to as L-TiO_2, dA-TiO_2, and A-TiO_2 respectively. This chapter is dedicated to characterise the structural properties of these synthesised electrode materials.

1. The local structure of the lepidocrocite-type titanate material

The first studied electrode material is the lepidocrocite-type titanate material (L-TiO2), synthesised at 90°C. This material has already been described in detail, notably by Ma et al., in several works [95,150,151]. Therefore, only the structural highlights of this material will be presented here.

The structural data of this material were first investigated by XRD. From the obtained diagram, available in **Figure 33.**, only a diffuse signal is observable. This is characteristic of an amorphous material, at a long-range scale. Order at a shorter scale is examined by high-energy X-ray total scattering measurements. The coherence length of the material is only about 7 Å. Therefore, the material only exhibits a short-range order, and is considered amorphous for longer-range scales. The PDF data was fitted against the lepidocrocite-type phase and provided satisfying results (R_W=0.32). The remaining deviation is attributed to disorders induced by local defects in the structure of the material. Notably, the fit quality is enhanced compared to the anatase phase (R_W=0.50).

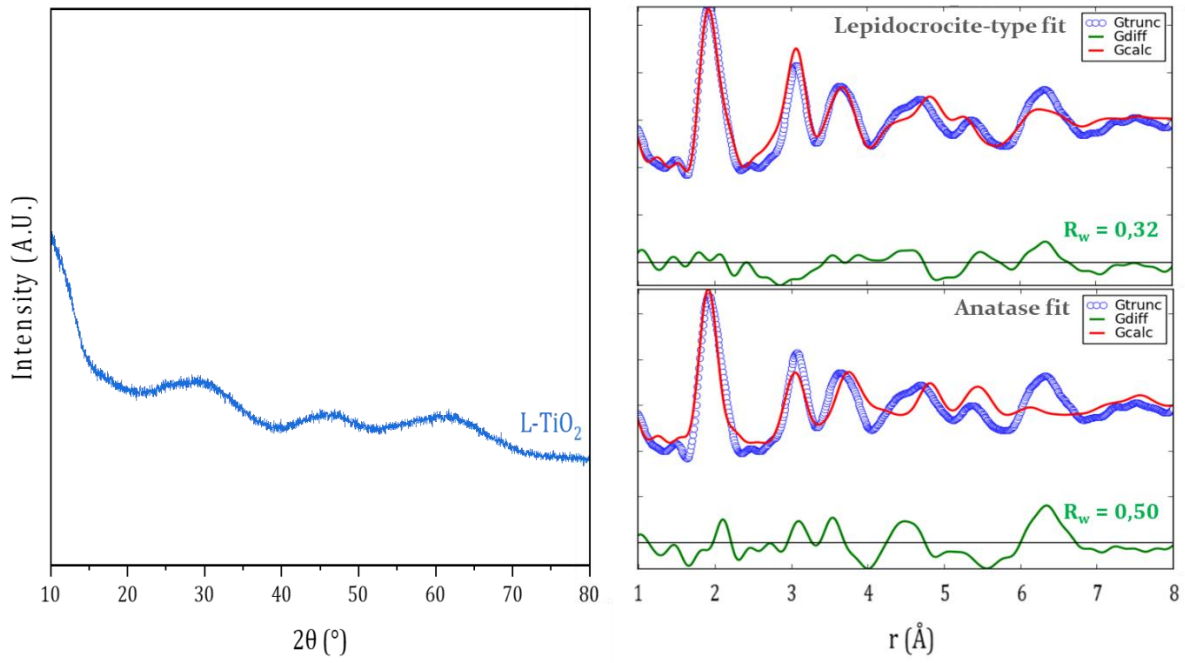

Figure 33. XRD diagram (left), and PDF data phase fitting (right) of the lepidocrocite-type titanate material.

This lepidocrocite-type titanate phase is a layered material, which structure is displayed in **Figure 34.**. Inside, TiO_6 octahedra are arranged in sheets, separated from one another by a crystal water interlayer. The titanium oxide octahedra are linked together by corners and edges. Each sheet is composed of two layers of titanium octahedra. As a result, two populations of oxygen atoms are generated. The outermost oxygens towards the water interlayer are two-fold coordinated, while the oxygens located inward the layer are bonded to four titanium atoms.

The defects, in the L-TiO_2 material, have been identified to be cationic vacancies (□). Indeed, during the synthesis, incomplete condensation and charge balance led to the formation of titanium vacancies in the structure. These vacancies are stabilized by four hydroxyl groups, around the titanium site. As an effect, these hydroxide groups are bonded to either one or three titanium atoms. This provides the general formula of the lepidocrocite-type titanate material, where x is the vacancy rate and n is the hydration number of the material:

$$Ti_{2-x}\square_x O_{4-4x}(OH)_{4x} \cdot nH_2O$$

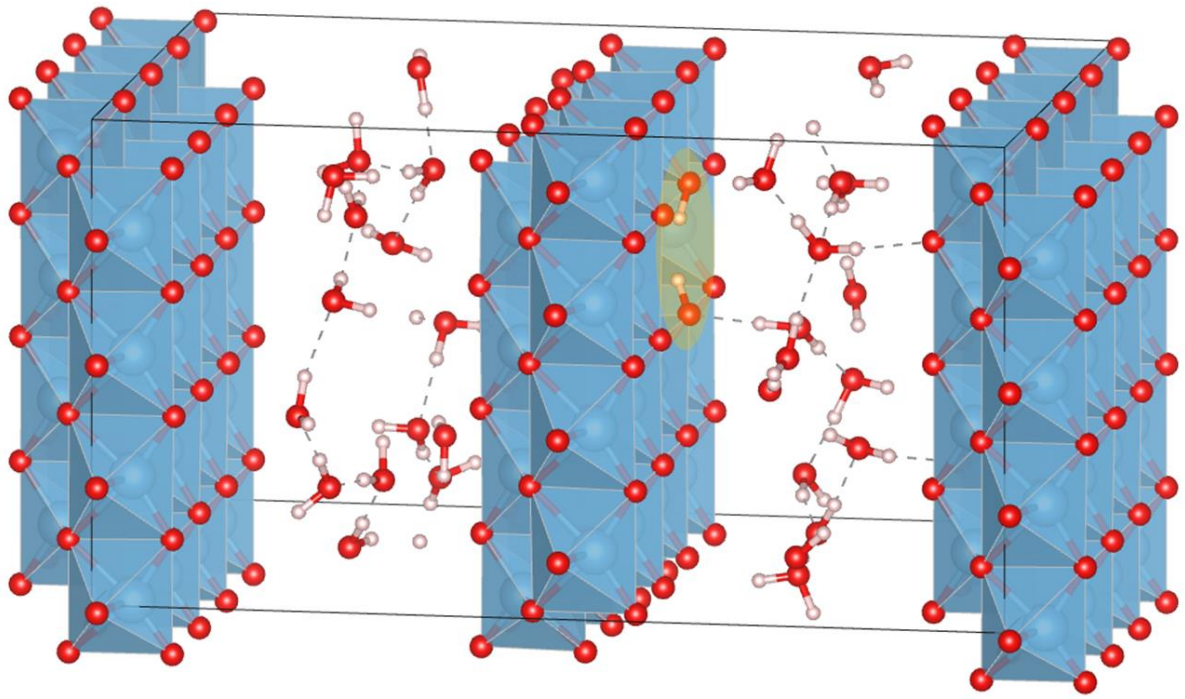

Figure 34. 3D model of the defective lepidocrocite-type titanate L-TiO_2 unit cell. A single cationic vacancy is represented in this unit cell, and highlighted by the yellow area.

The amount of cationic vacancies in the L-TiO_2 material has been estimated by thermogravimetric analysis (TGA) [95]. Indeed, during the analysis, the hydroxyl groups surrounding the titanium vacancies are removed in order to form the thermodynamically stable anatase TiO_2. In **Figure 35.**, several mass losses are observed before the formation oxide decomposition product. These have been attributed to the departure of gaseous H_2O, and have then been classified as a function of their decomposition reactions. The thermal decomposition is described as follows:

i From 20°C to 50°C, the adsorbed water is lost.

ii From 50°C to 150°C, the crystal water is lost.

iii From 150°C to 525°C, the hydroxyl groups are lost.

However, it is to be noted that the mass losses are not well defined. This indicates that the different thermally activated H_2O departures overlap. Care should then be taken with the estimated values of the thermal domains.

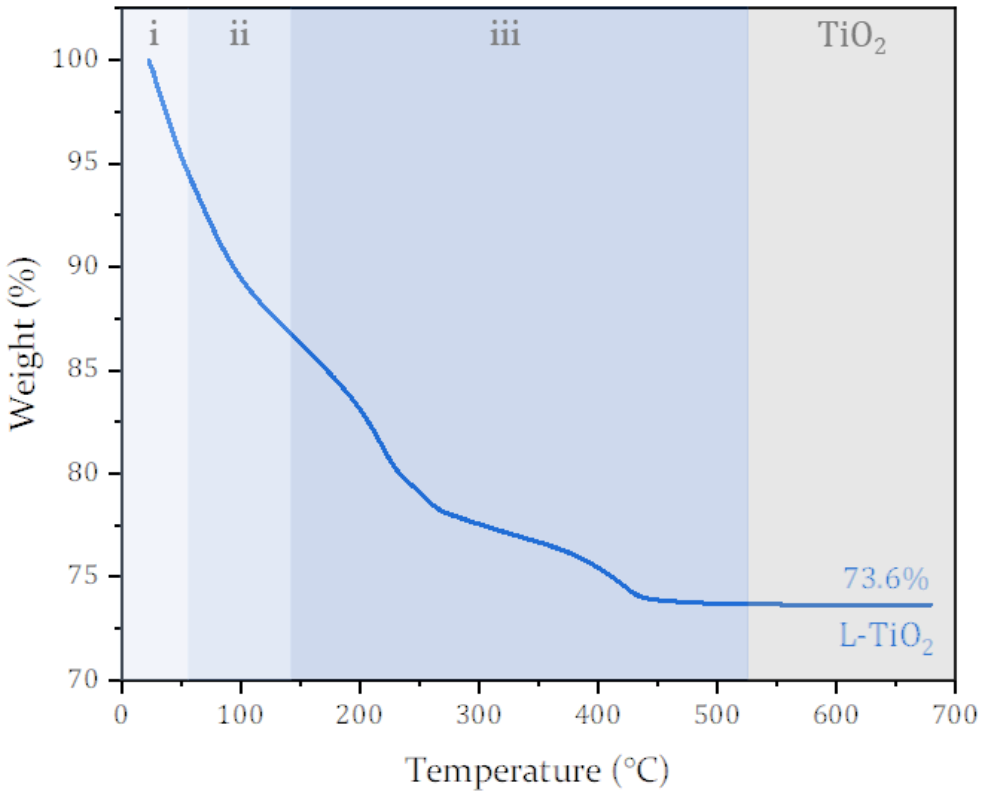

Figure 35. Thermogravimetric analysis of the L-TiO_2 lepidocrocite-type titanate material.

The removal of the hydroxyl groups occurs via condensation: two hydroxyl groups react with each other to produce a free H_2O molecule and a bridging oxygen. As a vacancy bears four hydroxyl groups, two water molecules are expected to be produced for a single vacancy removal, following :

$$Ti_{2-x}\square_x O_{4-4x}(OH)_{4x} \xrightarrow{\Delta} (2-x)TiO_2 + 2x\, H_2O$$

Considering the initial mass of the sample and the various weight losses, both the hydration number n and the vacancy rate x of the material can be determined. From the **Figure 35.** data, the L-TiO2 material is estimated to be $Ti_{1.5}\square_{0.5}O_2(OH)_2 \cdot 0.7H_2O$.

The vacancy rate is then high in this material. Nevertheless, the titanium vacancies are scattered across random titanium sites inside the material. Their localisation in the structure therefore follows a probabilistic distribution: For a low vacancy rate, defects are expected to be sparse and evenly distributed across the material. Increasing the vacancy rate then decreases the mean length between each. Eventually, vacancies might come to occupy edge-sharing or corner-sharing titanium sites.

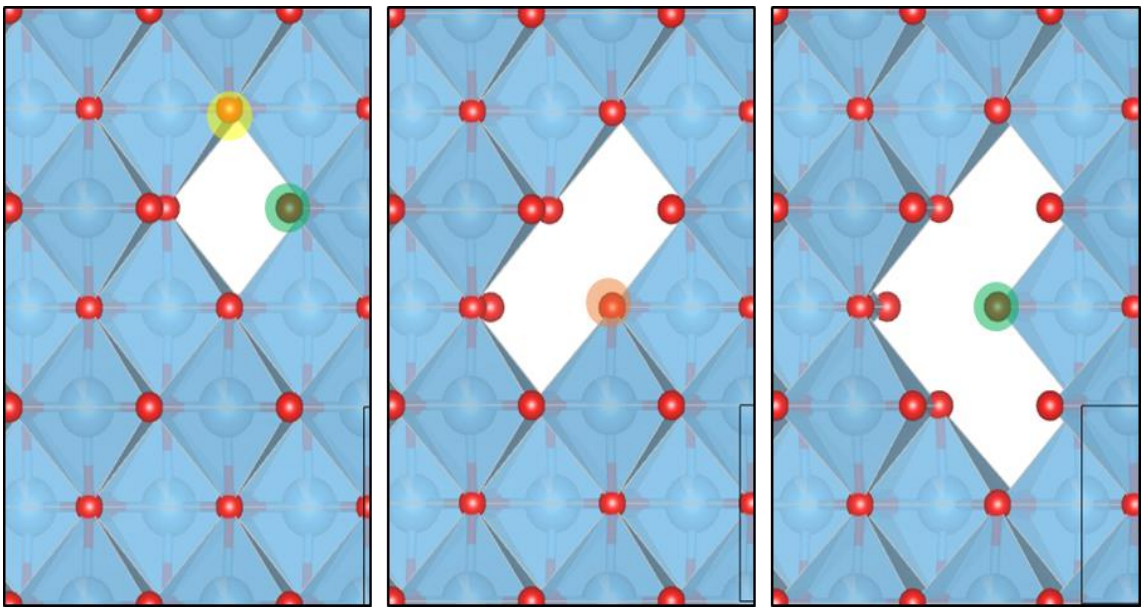

Figure 36. Snapshots of the lepidocrocite-type titanate structure considering one (left), two (centre), and three (right) neighbouring vacancies. Hydrogens are omitted for clarity. The green, orange, and yellow circles indicate examples of the single, double, and triple coordination environments of the oxygens in the structure.

New specific local environments are then generated by these adjacent vacancies. Double-coordinated and single-coordinated -OH groups can therefore exist in the material. These particular adjacent environments are illustrated in **Figure 36.**. It is to be noted that this vicinity phenomenon can adopt numerous geometries, generating a wide variety of actual environments in the material. These local environments have been probed by Monique Body and Christophe Legein, using ^{1}H MAS NMR spectroscopy [95]. **Figure 37.** reports the recorded data, and a signal. This attribution has been proposed as a function of the coordination mode of the probed hydroxide groups. Single-, double-, triple- and four-times coordinated hydroxides environments were indeed identified. Notably, the single-coordination mode is the most intense.

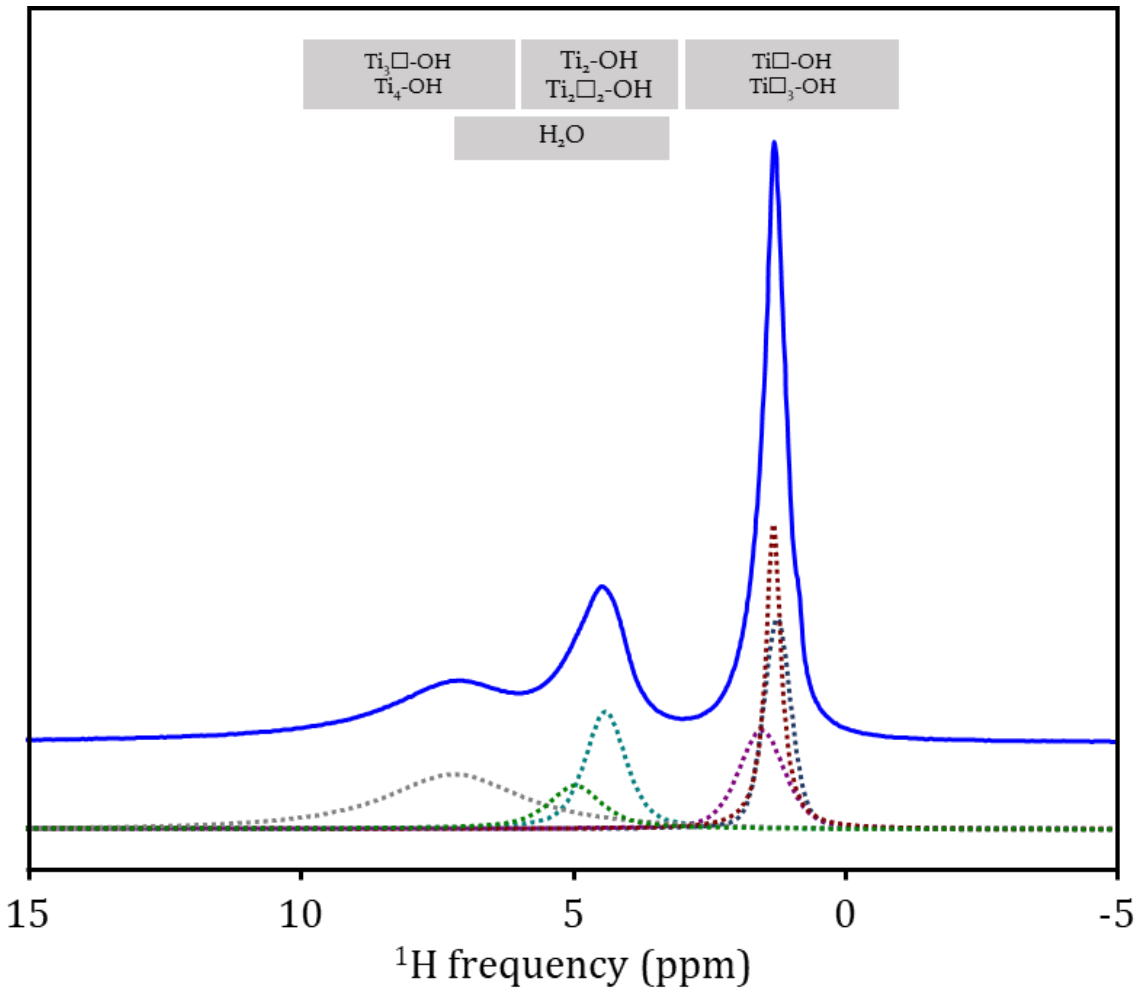

Figure 37. ^{1}H NMR spectrum of the lepidocrocite-type titanate material, with the corresponding peak deconvolution proposition. The joined environments domains are the same as previously proposed by Ma et al. in [95].

2. Structural effects of the synthesis temperature

The afore-described L-TiO_2 lepidocrocite-type titanate material was obtained via a 90°C thermal treatment. Increasing the synthesis temperature triggered different mechanisms, and therefore led to the formation of different compounds. Namely, a defective anatase dA-TiO_2 was obtained at 110°C, and a pure anatase A-TiO_2 was obtained at 150°C. This part is dedicated to present the structural features of these materials. These characterisations were performed in collaboration with Milad Toorabally [152].

The dA-TiO_2 and A-TiO_2 materials were first characterised by XRD. The diffraction diagrams, provided in **Figure 38.**, exhibit sharp Bragg peaks that are characteristic of the tetragonal anatase phase. In contrast to the L-TiO_2 material, these two synthesized materials are crystalline samples. Notably, the A-TiO_2 exhibits thinner and more resolved diffraction peaks, than the dA-TiO_2 counterpart. This suggests that the material synthesised at the higher temperature displays a higher crystallinity.

From the collaboration with Toorabally, the structural formula of each compound has been estimated. Indeed, the discrepancy between the recorded XRD diagrams and the ideal anatase diffraction diagram is only attributed to the presence of titanium vacancies in the materials. Rietveld refinements have therefore been realised on both anatase materials [152]. The results estimate the dA-TiO_2 material to $Ti_{0.83}\square_{0.17}O_{1.32}(OH)_{0.68}$ and the A-TiO_2 material to $Ti_{0.99}\square_{0.01}O_{1.96}(OH)_{0.04}$.

The morphology of the synthesised materials was investigated by Toorabally, using transmission electron microscopy (TEM) [152]. The two anatase materials have been observed to be aggregated nanoparticles. These last are anisotropic elongated particles, measured to be about 12 nm wide for 20 nm long.

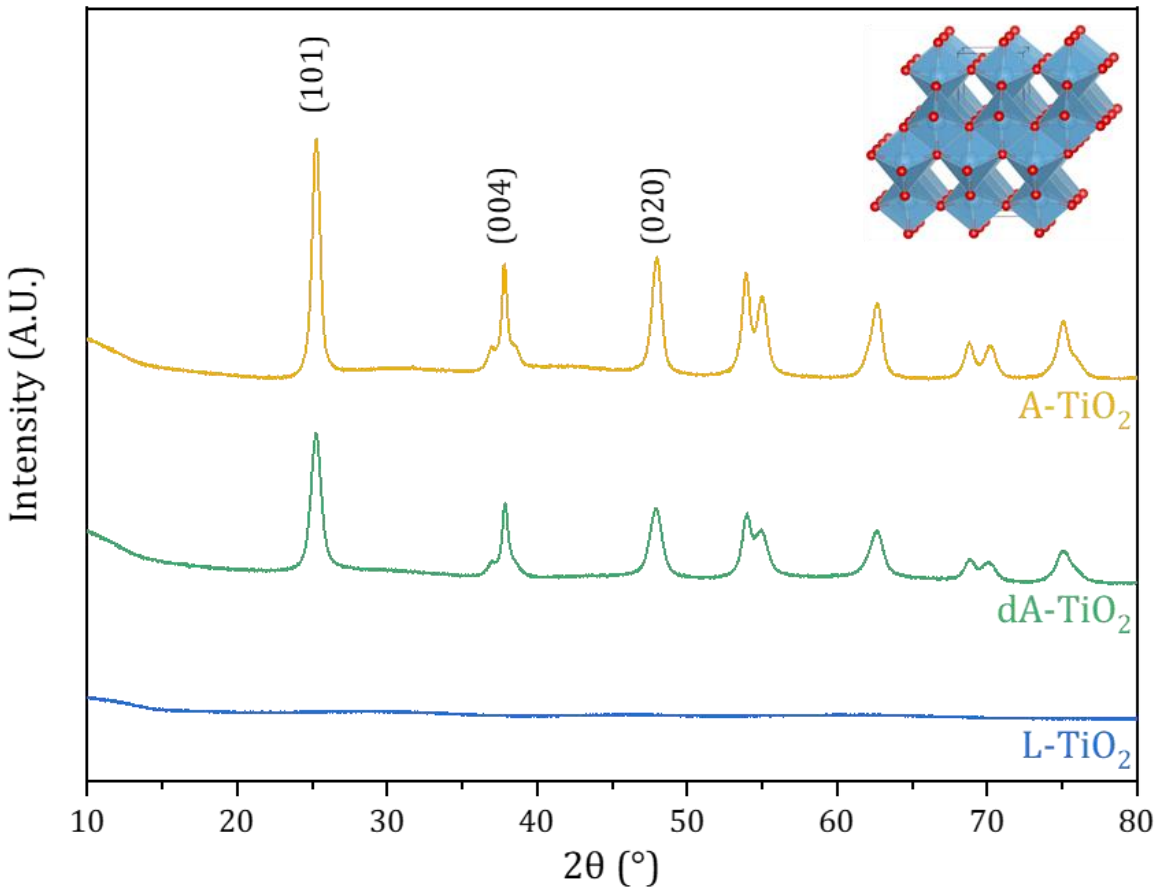

Figure 38. XRD diagrams of the L-TiO_2 (blue), the dA-TiO_2 (green), the A-TiO_2 (golden) synthesised materials. The miller plans reported refer to the anatase phase. A 3D model of the anatase phase is also joined for reference.

To gain more insights about the short-range order of these materials, high-energy X-ray total scattering measurements were performed. PDF data from these measurements are presented in **Figure 39.**. Refinements have also been performed against the anatase phase, and provided satisfying reliability factors of R_W=0.24 for the dA-TiO_2 material, and R_W=0.14 for the A-TiO_2 material. For the dA-TiO2 material, the derivation is attributed to cationic vacancies in the structure.

Notably, in **Figure 39.**, the first two peaks appear at 1.94 Å and 3.04 Å for the anatase material, and appear at 1.92 Å and 3.07 Å for the lepidocrocite-type titanate material. These peaks are attributed to the Ti-O bonds from within a TiO_6 octahedron, and the edge-sharing Ti-Ti distance respectively. The peak similarity reported here suggests the high similarities between the two phases.

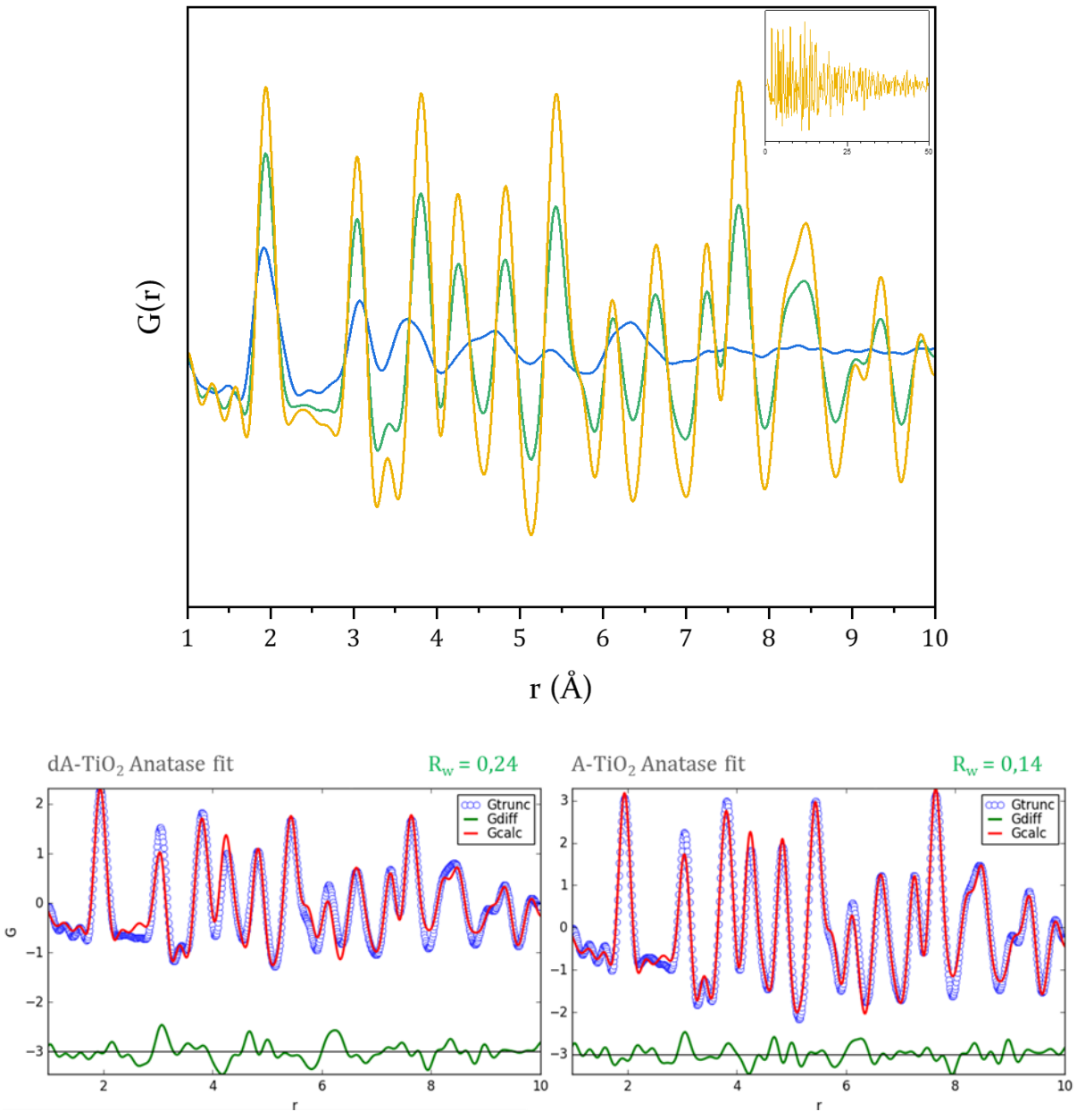

Figure 39. PDF diagrams of the L-TiO_2 (blue), the dA-TiO_2 (green), the A-TiO_2 (golden) materials, in the 1 Å to 10 Å range (top). The joined insert displays the 1 Å to 50 Å range of the A-TiO_2 material. The PDF data fits of the dA-TiO2 and the A-TiO2, against the anatase phase, are also provided (bottom).

Indeed, the anatase phase is a bulky three-dimensional phase, in which TiO_6 octahedra are only bonded by sharing edges. The anatase phase is therefore related to the lepidocrocite-type titanate phase, as a two TiO_6 octahedra-wide motif can be found inside both. Consequently, in the anatase structure, every oxygen is coordinated to three titanium atoms, and are thus equivalent. Alike the L-TiO_2 material, the cationic vacancies inside the dA-TiO_2 material are stabilized by hydroxyl groups. These last can adopt a single or a double coordination mode inside the anatase phase.

The local environments of the anatase material defects are therefore probed by ^1H NMR spectroscopy. The collected spectra, exhibited in **Figure 40.**, have been normalised by the measured mass of the analysed sample. The signal intensities vary according to the vacancy rate inside each material. Hence, the L-TiO_2 material displays the higher intensity, followed by the dA-TiO_2 and the A-TiO_2.

The anatase material spectra display three main peaks. Those are centred around 1.19 ppm, 4.19 ppm, and 6.63 ppm for the defective anatase material, and 1.07 ppm, 4.00 ppm, and 6.04 ppm for the pure anatase material. These three signals are attributed to a single, double, and triple coordination mode of the hydroxyl groups. Notably, in the anatase materials, triple-coordinated hydroxyl are not insights into vacancy environments. Indeed, the triple-coordinated hydroxyl groups are believed to be the protonated forms of the regular triple-coordinated oxygen species.

In the anatase phase, a single titanium vacancy would lead to double-coordinated hydroxyl groups. Nonetheless, this environment is the least represented. Instead, the single-coordination mode is by far the most common. Considering the low vacancy rate in the anatase materials, this repartition could originate from a segregation of the defects at the surface of the particles. Alternatively, this peak repartition could be induced by an unprobed proton population. Indeed, if the relaxation time of a proton is too quick (or long), its contribution to the spectrum is not recorded. Therefore, a ^1H population could be missing, causing this unexpected peak repartition.

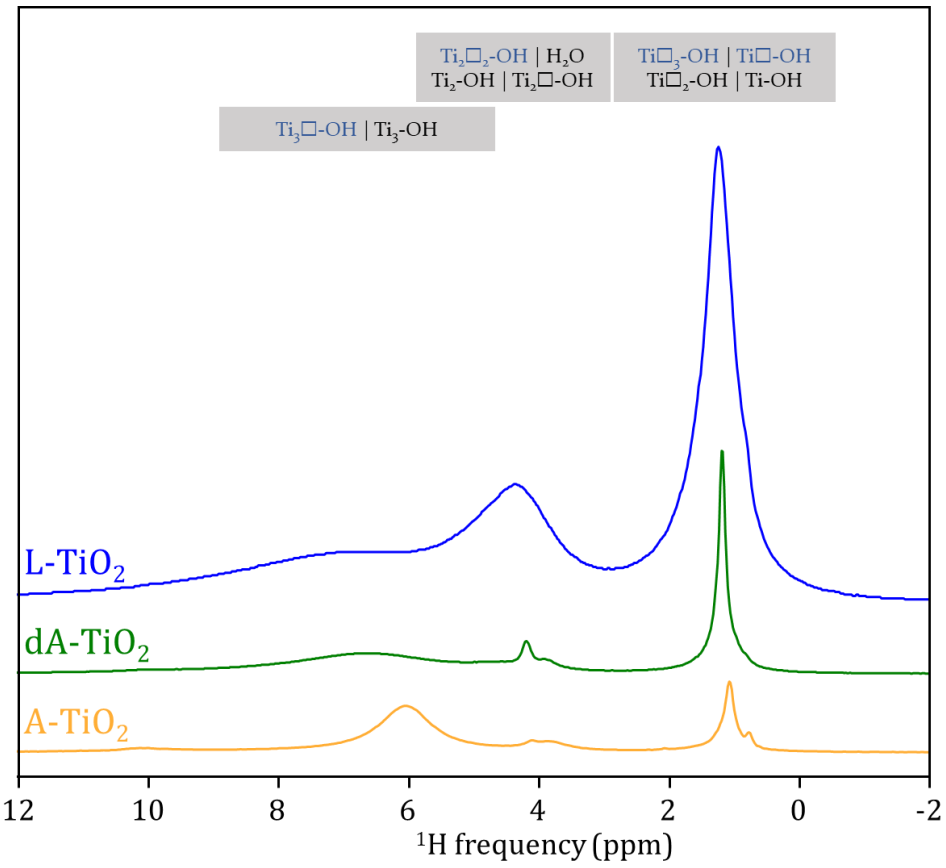

Figure 40. 1H NMR spectra of the L-TiO_2 (blue), the dA-TiO_2 (green), and A-TiO_2 (golden) synthesised materials. The chemical displacement domains provided refer to both the lepidocrocite-type titanate environments (blue) and the anatase environments (black).

Conclusion

In this chapter, the various titanate materials have been characterised. By reproducing the analyses proposed by Ma et al. [95], the synthesised L-TiO_2 material was identified to be $Ti_{1.5}\square_{0.5}O_2(OH)_2 \cdot 0.7H_2O$. This material is amorphous in regards to XRD, but refinements of its PDF data allowed to attribute its local structure to the lepidocrocite-type titanate phase. This phase is a layered titanium oxyhydroxide material, that displays crystal water interlayers. This material also exhibits a high amount of titanium vacancies, within its structure ($\square$/Ti = 1/3). These defects are responsible for the high quantity of local disorder in the material. Eventually, the high defect density generates specific local environments inside the material. This is understood to be due to the titanium vacancy sites being in the vicinity of one another. This defective layered material is intended to be the host material for aluminium ion intercalation, in **Chapter 5**.

The variation of the synthesis temperature broadened the scope of the synthesised material. Indeed, two materials were produced and characterised: the dA-TiO_2 material at 110°C, and the A-TiO_2 at 150°C. Both are crystallised materials, in the anatase phase. The former 110°C material is a defective anatase of formula $Ti_{0.83}\square_{0.17}O_{1.32}(OH)_{0.68}$. On the other hand, the latter 150°C material is a nearly pure anatase material of formula $Ti_{0.99}\square_{0.01}O_{1.96}(OH)_{0.04}$. In a temperature range of only 60°C, the synthesised materials spread from the disordered defective layered lepidocrocite-type titanate phase to the pure crystallised anatase phase. The effect of this fine structure tuning, on the electrochemical properties observed toward the aluminium ion, will be further analysed in **Chapter 6**.

Chapter 5. Chemical and electrochemical reactions between lepidocrocite-type titanate material and a chloroaluminate–based electrolyte.

The L-TiO_2 lepidocrocite-type titanate material is studied as electrode material. As described in **Chapter 4**, this $Ti_{1.5}\square_{0.5}O_2(OH)_2 \cdot 0.7H_2O$ material displays structural features making it a promising host structure for electrochemical ion intercalation. Two kinds of insertion sites are identified in this material. The inorganic lattice contains cationic vacancies that can act as host sites, while the layered architecture of the lepidocrocite-type phase provides an interlayer space, which can also serve as a host (see **Figure 41.**). Reeves et al. showed that the insertion of Li^+, Na^+, and K^+ can be achieved inside both of these sites [13]. Kang et al. then extended the scope of inserted ions to divalent Mg^{2+}, Ca^{2+}, and Zn^{2+} ions [12].

To probe the ability of this framework to intercalate the trivalent aluminium ion, calculations have been conducted. These considered the insertion of Al^{3+}, into either a titanium vacancy or the interlayer space. The result, shown in **Figure 41.**, indicates thermodynamically favourable formation energies for both sites: 171 meV when inside a cationic vacancy, and 84 meV when in the interlayer space. Nonetheless, the vacancy sites show a twice lower formation energy than the interlayer space. It is thereafter hypothesised that the aluminium insertion predominantly occurs in the titanium vacancy sites of the lepidocrocite-type titanate material.

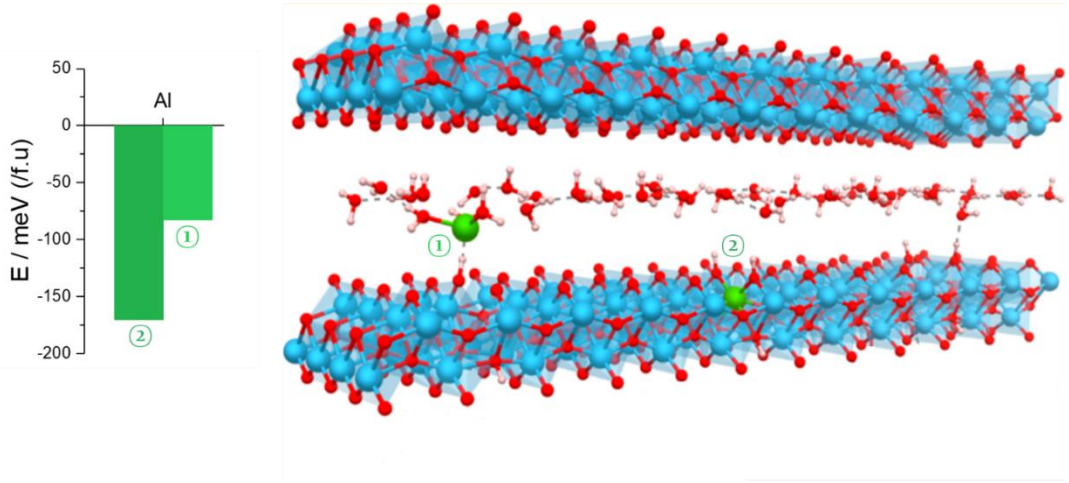

Figure 41. Scheme of the lepidocrocite-type titanate material (right), adapted from [95]. In green, ions are displayed intercalated in the interlayer (①) and vacancy (②) insertion sites. Formation energies of the Al^{3+} intercalation, inside both insertion sites of the lepidocrocite-type titanate material (left), from Reeves calculations.

In this chapter, the focus is put on the insertion of aluminium ions into the lepidocrocite-type titanate material. Electrochemical measurements are performed, using the 1:1.5 EMImCl:$AlCl_3$ ionic liquid (see **Chapter 3**), as the electrolyte. The electrochemical properties and the chemical compatibility, between the lepidocrocite-type titanate material with the acidic electrolyte, will be discussed.

1. Electrochemistry of the lepidocrocite-type titanate electrode

The electrochemical properties of the lepidocrocite-type titanate electrode were first probed by galvanostatic cycling. **Figure 42.** shows the ten first discharge-charge cycles, conducted at a held current density of 20 mA/g, in a three-electrode Swagelok cell configuration (see **Chapter 2**). A specific capacity of 318 mAh/g is achieved during the first discharge, while 277 mAh/g is obtained during the first charge. Those results are consistent with the 267 mAh/g theoretical specific capacity of the electrode material, based on the Ti^{4+}/Ti^{3+} redox couple.

The first cycle discharge exhibits smooth sloping curves, while the first charge curve is S-shaped. No phase-transition plateau are observable. This behaviour is characteristic of a solid-solution insertion into a disordered material. The following cycles show a quick capacity drop. This hints towards an alteration of the electrode material. Dissolution of the electrode material can be suspected, as it has already been reported to be observed for vanadium oxides in this electrolyte [153]. After the galvanostatic experiment, the Swagelok cells were disassembled and a bright purple compound was observed (see **Figure S60.**). The existence of this compound is indicative of side reactions.

All in all, the galvanostatic cycling experiment provided three main insights into the electrochemical behaviour of the studied system:

(i) The electrode material features a high reversible capacity, during the first cycle.

(ii) The specific capacity drops rapidly upon cycling.

(iii) An unknown purple compound is observed after the electrochemical experiment.

These three observations will be used as guidelines throughout this chapter. Each of the following parts will investigate these aforementioned observations, to build an overall understanding of the electrochemical properties of the electrode material.

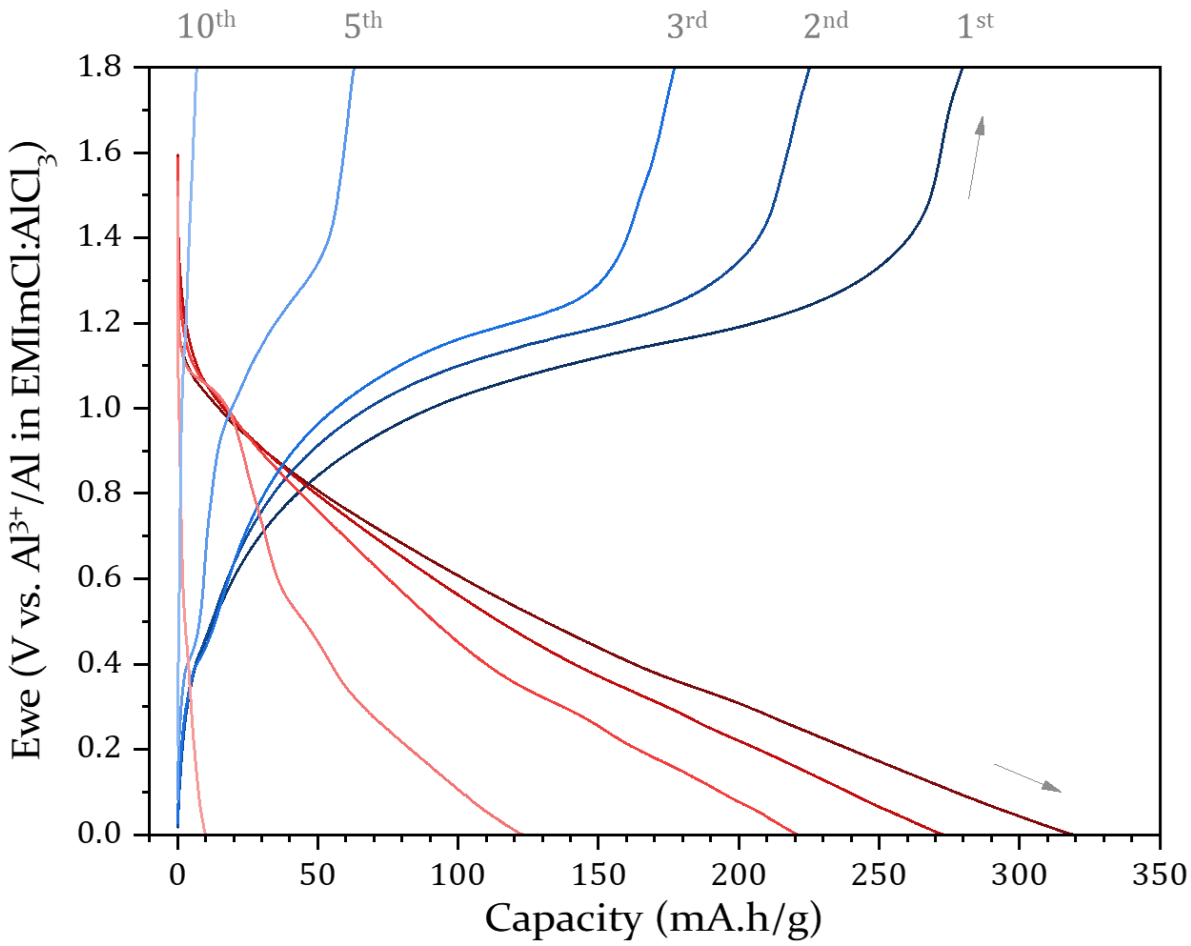

Figure 42. Ten first cycles of a 20 mA/g galvanostatic discharge-charge cycling of the lepidocrocite-type titanate electrode, using the 1:1.5 $EMImAlCl_3$ ionic liquid electrolyte. Discharge phases are displayed in shades of red, and charge phases in shades of blue.

2. Ion intercalation mechanisms

This part focuses on the first galvanostatic discharge-charge cycle. Therein, the shape of the electrochemical response suggests a solid-solution behaviour. This part is dedicated to study the electrochemical intercalation of aluminium ions, in the lepidocrocite-type titanate material electrode.

To do so, different cells were assembled to perform a single galvanostatic discharge-charge cycle. During this cycle, the electrochemical treatments were interrupted upon reaching specific states of discharge or charge (*ie.* capacity values). The cells were then immediately transferred inside a glovebox, disassembled, and washed in DMC following the protocol available in **Chapter 2**. In the end, a set of used electrodes was obtained, allowing for sampling of various states of discharge or charge, across the galvanostatic cycle.

The interactions between the lepidocrocite-type titanate electrode and the EMImCl:$AlCl_3$ electrolyte are yet unknown. To prevent possible side reactions from altering the measured elemental rates, this experiment was made so that every cell has the same exposition time to the electrolyte. This was done by imposing an open circuit voltage (OCV) period, prior to the actual galvanostatic discharge-charge. The OCV period matched the experimental time: the shorter the time of the galvanostatic experiment, the longer the OCV time; and vice-versa. For this reason, every cell was disassembled, after a known amount of time: 22h for the discharge phase experiments, and 25h for the charge ones.

2.1 Open circuit equilibrium

The evolution of the Open Circuit Voltage (OCV) of the lepidocrocite-type titanate electrode has been recorded. **Figure 43.** shows the result of a 240-hour OCV measurement experiment. There, the initial OCV value is around 1.75 V vs Al^{3+}/Al in EMImCl:$AlCl_3$. Then, the monitored potential quickly drops, until it stabilises around 1.30 V. Finally, the potential rises back and does not show any stabilisation within the 240h of experiment. As no current flows through these systems, those variations are attributed to chemical reactions between the electrode material and the ionic liquid electrolyte. This experiment therefore suggests that the electrode material might undergo chemical reactions during the galvanostatic experiment. This is a concern as it means that the various electrochemical cells might not be in the same state while they are analysed. This then raises uncertainties in all the studied systems.

Notably, this OCV experiment did not produce the previously reported unidentified purple compound. Thus, the formation of this compound is understood to only be caused by the electrochemical treatment.

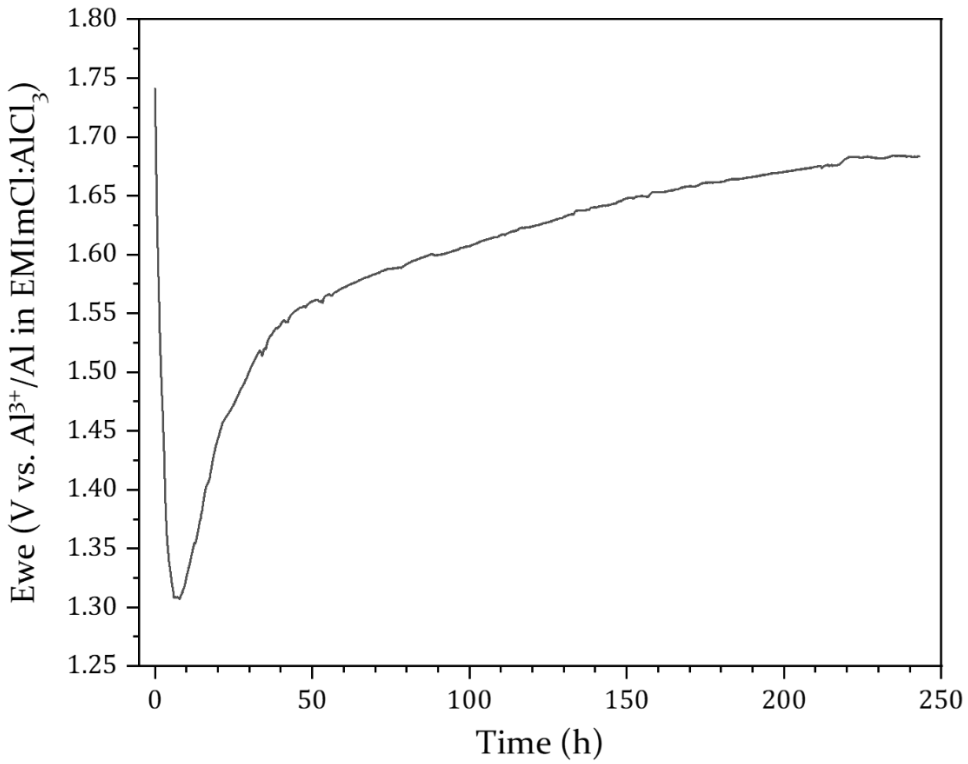

Figure 43. OCV measurements of a 240h lepidocrocite-type titanate material electrode, in the 1:1.5 EMImCl:$AlCl_3$ ionic liquid.

2.2 Characterisation of the intercalated species

As described in **Part 1.**, a high reversible specific capacity was obtained during the first cycle. This capacity is close to the theoretical capacity, which suggests a reversible reduction and oxidation of all the titanium atoms. This titanium redox is expected to be matched with ion insertion inside – or removal from – the electrode material. The main ionic species, hypothesised to be inserted from the electrolyte, is the trivalent aluminium Al^{3+} ion. However, several reports pointed to the occurrence of other charge carrier species, such as $AlCl^{2+}$ and $AlCl_2^{+}$ [53–56].

To gain more insights about the nature of the intercalated species, an elemental analysis has been conducted, by energy-dispersive X-ray spectroscopy (EDX). This analysis is performed on electrode samples, prepared at various states of charge. The aim is to monitor the insertion of the aluminium and chlorine inside the electrode material, along the first galvanostatic cycle. Measured elemental rates are available in **Figure S61.**. An uncycled electrode was used as a reference. Despite never having come in contact with the electrolyte, this electrode sample already showed a small amount of chlorine in its composition. This chlorine is believed to originate from the binder solution, used during the electrode preparation (see **Chapter 2**). As only the electrochemically inserted ions are of interest here, the chlorine rate from each EDX measurement was subtracted, by the former chlorine rate in the pristine electrode. **Figure 44.** shows the evolution of the Al/Ti and Cl/Ti molar ratios, as a function of the state of the electrochemical treatment, during the first cycle.

The first point shown in **Figure 44.** (green square) is from a 22-hour OCV electrode, for which no current was applied in the probed system. For this electrode, a 0.11 Al/Ti and a 0.06 Cl/Ti rate is measured. As suggested in the previous part, the lepidocrocite-type titanate electrode might experience chemical reactions during the OCV time. These measured elemental rates are therefore evidence of this chemical reaction.

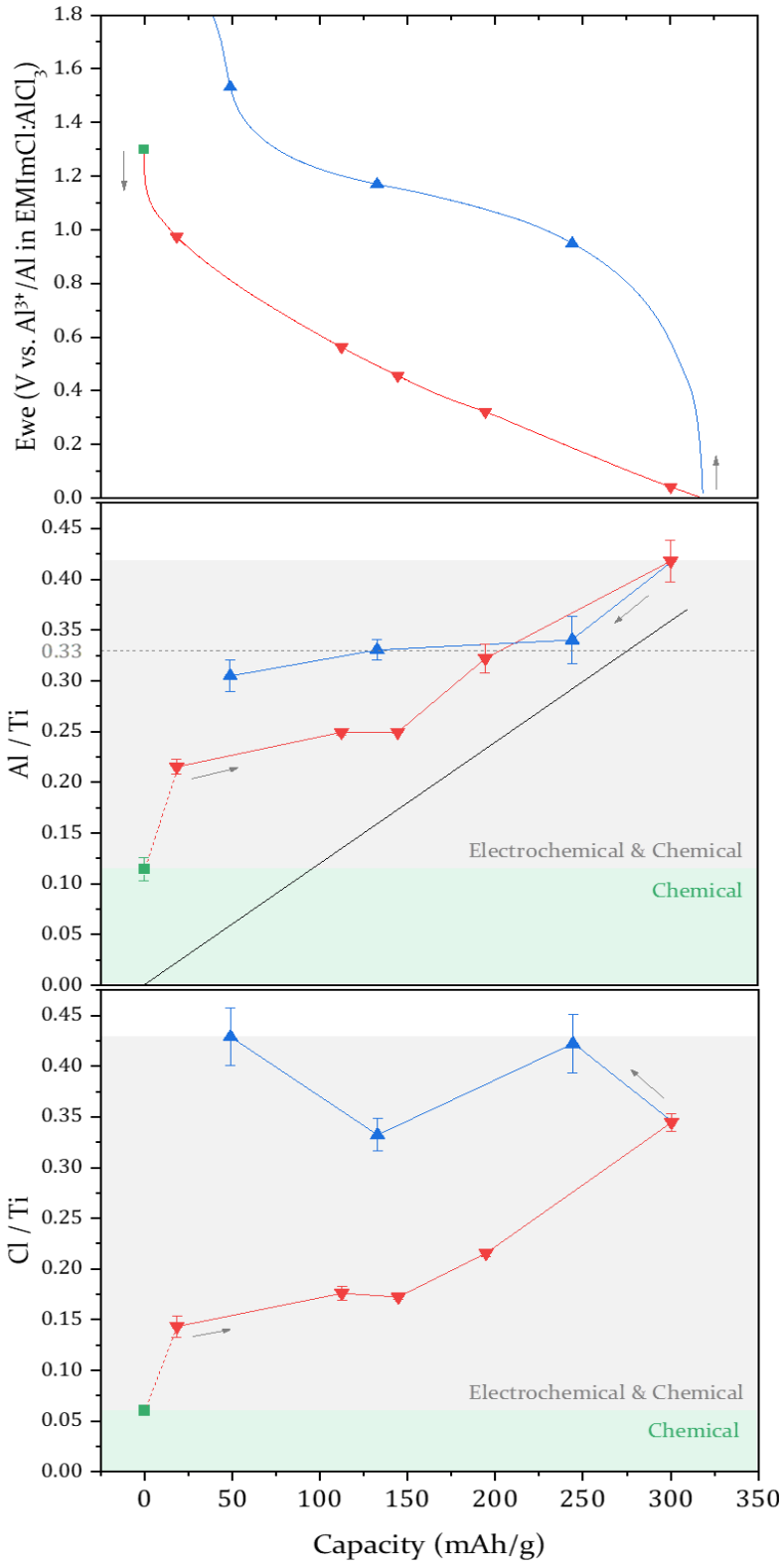

Figure 44. First cycle of the galvanostatic cycling experiment (top). EDX elemental ratios measurement of Al (middle) and Cl (bottom) against Ti, along the first galvanostatic cycle. The discharge phase is displayed in red, and the charge phase is displayed in blue. The green square indicates the OCV point measurement. The grey arrows indicate the cycle progression order. A grey dashed line is added to the Al/Ti graph as a visual aid for the 0.33 ratio value, and a black solid line for the ideal Al^{3+} ion insertion. Coloured domains are used to indicate the nature of the occurring intercalation mechanism.

During the discharge, the measured aluminium rate increases. As the contact time is the same for every cell, this indicates that this growing intercalated aluminium ratio is indeed due to the sole electrochemical treatment of the electrode material. The effect of the applied current on the aluminium insertion is particularly noticeable at the beginning of the discharge, as the Al/Ti ratio doubled for only an 18 mAh/g capacity.

During the galvanostatic charge, the titanium is oxidised back to tetravalent titanium, and reversibility of the specific capacity is achieved. Nonetheless, the so-performed measurement shows that the intercalated aluminium species are not removed. Indeed, upon reversion of the current, the Al/Ti ratio is quickly lowered, and remains around 0.33 for the whole charge. It is yet still unknown how could the retrieved capacity not affect the aluminium rate inside the electrode material.

Notably, this 0.33 Al/Ti value matches the □/Ti rate in the amorphous lepidocrocite-type titanate material. This suggests that the monitored aluminium is intercalated inside the electrode material cationic vacancies. Indeed, this was predicted by the DFT calculations (see **Figure 41.**), considering the intercalation of the trivalent Al^{3+} ion. This ideal intercalation results from a three-electron exchange reaction, and is reported in **Figure 44.** by a solid line.

Moreover, in the second half of the discharge, the trend of the monitored Al/Ti ratio seems to follow this ideal Al^{3+} insertion trend, with an offset of around 0.10. This offset is consistent with the initial 0.11 Al/Ti value observed for the OCV sample. This implies that the recorded aluminium insertion can be decomposed into two independent contributions: a chemical one, and an electrochemical one.

During the discharge, the evolution of the Cl/Ti molar ratio is comparable to the Al/Ti one, and reaches a 0.34 value. During the charge, no trend can confidently describe the Cl/Ti ratio, due to the few amount of points. Nonetheless, the recorded values are centred around 0.40.

Three charge carriers have been evoked to possibly be present in the system (Al^{3+}, $AlCl^{2+}$, and $AlCl_2^{+}$). Among these three, the insertion of the first is ruled by a three-electron exchange, the second by a two-electron exchange, and the last by a single-electron exchange. The similarity of the aluminium and chlorine ratio suggests the insertion of the $AlCl^{2+}$ ion. Whereas, the evolution of the aluminium rate during the discharge rather suggests a three-electron exchange reaction, and thus an Al^{3+} and Cl^{-} co-intercalation. Overall, no repartition of the mentioned ions can possibly match both the retrieved discharge capacity, and the measured Al/Cl ratios. This reveals that the reactions, occurring during the galvanostatic cycle, cannot be described by simple ions intercalation reactions. This further highlights the high degree of complexity of the mechanisms occurring in the system. These mechanisms include chemical and electrochemical reactions, among which intercalation of species containing aluminium and chlorine ions occurs.

Further insights on the insertion of the Al and Cl species are investigated by an EDX elemental mapping. The surface distribution of titanium, oxygen, chlorine, and aluminium have therefore been observed on the sampled electrodes. This analysis showed that the presence of both aluminium and chlorine is homogeneous across all the electrode surface, at any stage of the galvanostatic cycle. No area of high or low concentration of an element could be observed there, nor segregation of a specific species over another one. As an example, the collected data of the fully discharged electrode is presented in **Figure S62.**.

2.3 Identification of the inserted aluminium environments

The inserted aluminium species are hypothesised to be inserted inside the electrode defects. These are stabilised by hydroxyl groups. Depending on the geometry of these vacancies, specific hydroxyl environments are created inside the material (see **Chapter 4**). In this part, the focus is set on the determination of the local environment of these inserted species.

First, ^{1}H NMR spectroscopy is used to probe the coordination modes of the hydroxyl groups. Vincent Sarou-Kanian has performed spectrum acquisitions on fully discharged and fully charged electrodes. The results are presented in **Figure 45.**, normalised by the mass of the sample analysed. The spectrum of the pristine lepidocrocite-type titanate electrode is also joined for reference, normalised by its most intense peak. As described in **Chapter 4**, the pristine electrode spectrum displays three peaks. Each peak was attributed as a function of the coordination of the hydroxyl group [95]: single titanium-bonded hydroxyl environments (Ti□–OH and Ti□$_3$–OH) show the most intense peak at 1.12 ppm, twice-bonded hydroxyl environment (Ti$_2$□$_2$–OH) are responsible for the 4.28 ppm peak, and triple-bonded or four times bonded hydroxyl environments (Ti$_3$□–OH and Ti$_4$–OH) generate the broad peaks at higher chemical shifts.

In **Figure 45.**, the most distinctive feature is the disappearance of the intense 1.12 ppm peak. Indeed, on the discharged electrode spectrum, only three low peaks at 0.37 ppm, 1.12 ppm, and 1.77 ppm remain visible. On the contrary, the mildly pronounced 4.28 ppm peak has been enhanced, and has become the most intense contribution. Two other contributions, at 7.65 ppm and 8.76 ppm, also increased and have become distinguishable after the discharge. The charged electrode displays the same contributions as the discharged one, with slight variations in the intensity.

The intensity variations recorded are indicative of changes in the -OH group coordination number. During the discharge, this is attributed to the insertion of aluminium inside the vacancy sites of the electrode material. Indeed, the hydroxyl groups are then coordinated to both titanium and aluminium atoms. As a result, the signal of the single coordination mode is observed to be converted into a double coordination mode, double to triple, etc ... A diagram of the evolution of the various hydroxyl environments is proposed as a guide in **Figure S63.**.

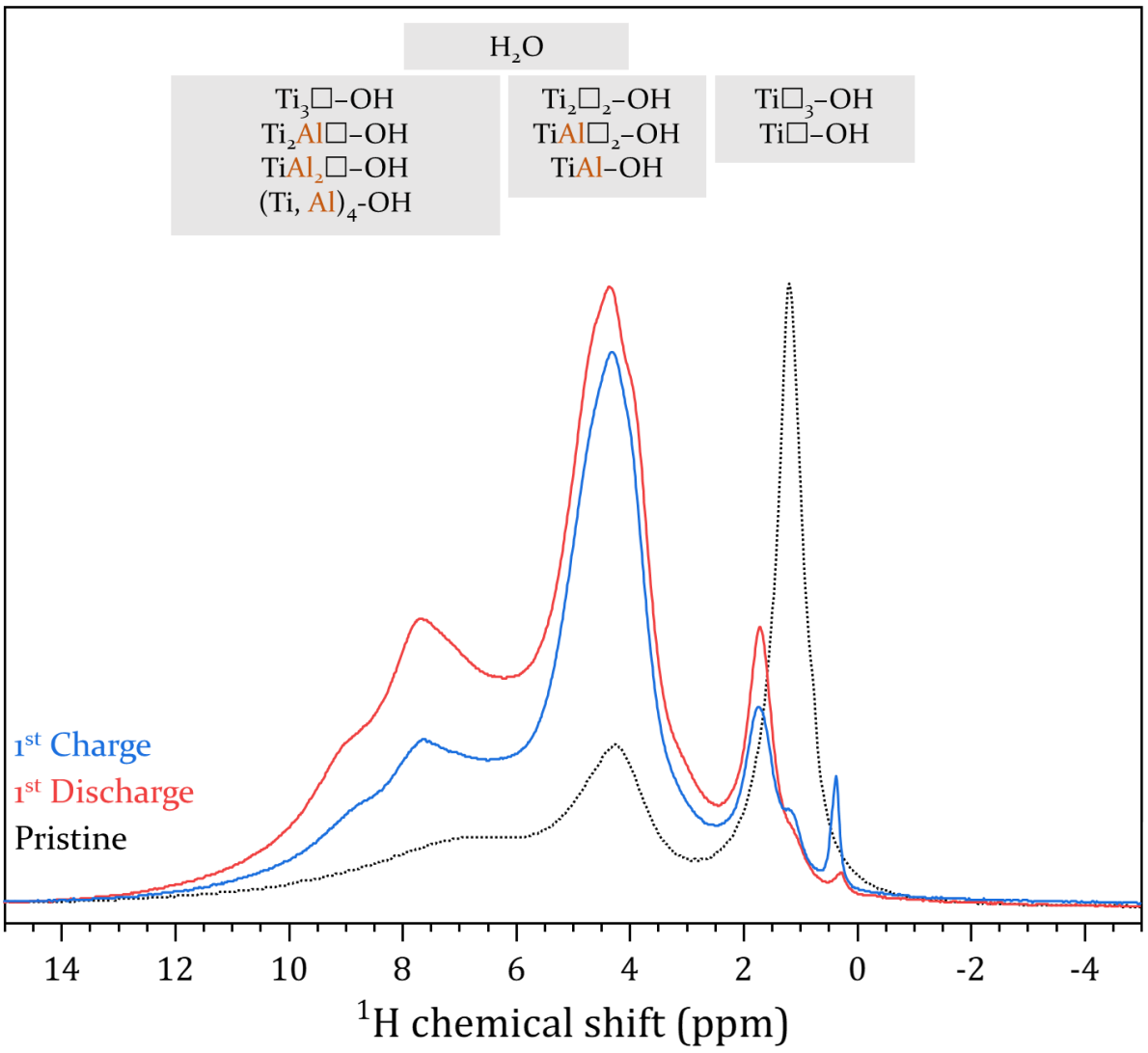

Figure 45. ^{1}H MAS NMR spectra of a pristine (dotted black), a fully discharged (red), and a fully charged (blue) lepidocrocite-type titanate electrode, during the first cycle of galvanostatic cycling. Interpretation of the probed proton environments is given as ranges.

To further characterise the aluminium insertion inside the lepidocrocite-type titanate cationic vacancies, ^{27}Al NMR spectroscopy has been realised by Vincent Sarou-Kanian. Aluminium is a magnetically active nucleus, that is abundant and exhibits good sensitivity. However, ^{27}Al is also a quadrupolar nucleus (I=5/2). Therefore, interactions are induced with both the external magnetic field, and the electric field gradient (EFG) from the sample. As an effect, the overall spectral resolution is lowered, and the peaks appear broadened. In this work, this difficulty has been overcome, by using a very high magnetic field (20 T) and magic angle spinning.

Figure 46. shows the collected ^{27}Al NMR spectra of the sampled electrodes, normalised by their masses. Notably, at around 100 ppm, no trace of chloroaluminate ions, from the remaining ionic liquid, is observable in either electrode [146]. The discharged electrode spectrum presents three broad signals, from -20 to 95 ppm. Similarly to the ^{1}H spectra, the coordination of the probed aluminium ($^{[n]}$Al) can be extracted from the observed chemical shifts: the higher chemical shifts are ascribed to lower coordination modes [154].

The peaks observed in **Figure 46.** are attributed to the 6-, 5-, and 4-fold coordination modes of the aluminium. After the discharge, the occurrence of each coordination mode is: 41.4% for $^{[6]}$Al, 34.4% for $^{[5]}$Al, and 24.1% for $^{[4]}$Al. After the galvanostatic charge, the electrode still displays the three same broad signals. The repartition between the coordination modes is although moved to 37.1% for $^{[6]}$Al, 31.5% for $^{[5]}$Al, and 31.4% for $^{[4]}$Al. As the inserted aluminium is not released during the galvanostatic charge, this shift in peak area suggests a partial break of some chemical bonds between the inserted aluminium and the surrounding hydroxyl groups.

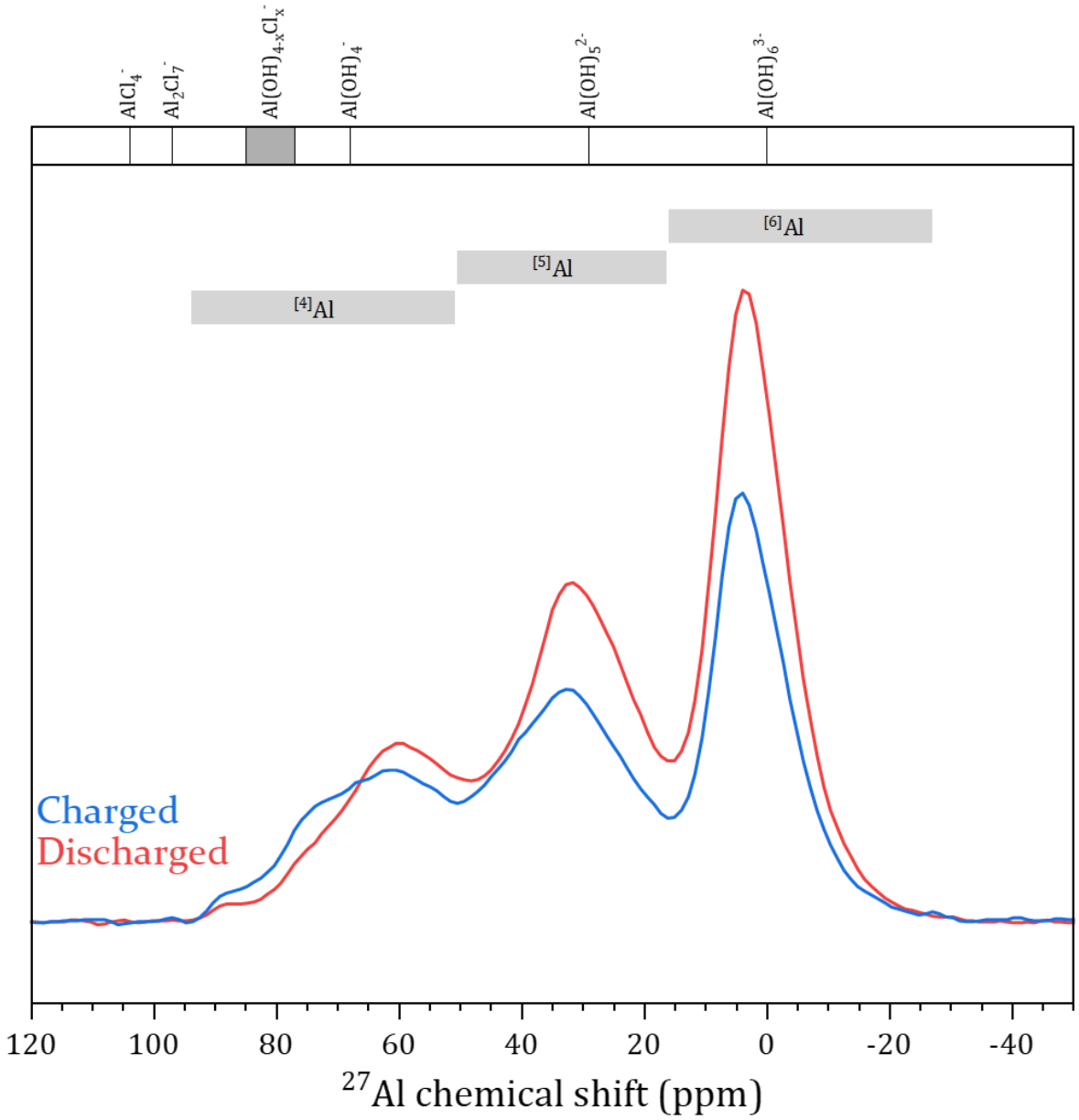

Figure 46. ^{27}Al MAS NMR spectra of fully discharged (red) and charged (blue) lepidocrocite-type titanate material electrodes, during the first cycle of galvanostatic cycling. Interpretation of the probed aluminium environments is provided as ranges of coordination modes. Standard values of chemical shift from various liquid-state aluminium complexes are reported on the x-axis, and adapted from [155].

Moreover, several contributions are distinguishable among each broad peak, in **Figure 46.**. Further spectral deconvolutions are provided in **Figure S64.** and **Figure S65.**, and their properties are summarised in **Figure 47.**. Satisfying results are obtained with a single contribution for the $^{[6]}$Al mode peak, two contributions for $^{[5]}$Al, and three contributions for the $^{[4]}$Al. These multiple peak contributions are believed to be due to the diversity of the chemical environments in the vacancies.

Notably, at the end of the discharge, the lower chemical shift contribution of each coordination mode (noted $^{[n]}$Al - α) is the prevailing contribution. After the charge, the higher chemical shift contributions (noted β and γ) have been enhanced. As a result, the α and β contributions have become levelled. These higher chemical shift peak enhancements might originate from a conversion of the former $^{[6]}$Al mode, into $^{[5]}$Al and $^{[4]}$Al modes. Finally, the furthermost signal, $^{[4]}$Al - γ at 87.57 ppm, can be attributed to the $[Al(OH)_xCl_{4-x}]$ hydroxychlorinated local environments of the aluminium ions [155].

Discharged - Peak	Position (ppm)	Area (%)
$^{[6]}$Al	7.73	41.4
$^{[5]}$Al - α	37.03	28.6
$^{[5]}$Al - β	46.65	5.8
$^{[4]}$Al - α	66.35	16.3
$^{[4]}$Al - β	78.63	7.6
$^{[4]}$Al - γ	88.15	0.2

Charged - Peak	Position (ppm)	Area (%)
$^{[6]}$Al	8.22	37.1
$^{[5]}$Al - α	35.68	17.1
$^{[5]}$Al - β	45.14	14.4
$^{[4]}$Al - α	65.86	14.1
$^{[4]}$Al - β	80.01	16.7
$^{[4]}$Al - γ	87.57	0.6

Figure 47. Tables of the area and position of the different deconvolution peaks of the discharged (top) and charged (bottom) electrodes.

Finally, to better understand the intercalation mechanism of the aluminium ions, DFT calculations were realised in collaboration with Kyle Reeves [108]. The Al^{3+} ion insertion was studied, considering the $Ti_{63}\square_1O_{124}(OH)_4{\cdot}32H_2O$ supercell. This supercell is a simplified model of the lepidocrocite-type titanate material where only a single isolated titanium vacancy is considered. The single Ti^{4+} vacancy represents a loss of four positive charges for the structure. As previously described (see **Chapter 4**), those are compensated by four hydroxyl groups, located among the six undercoordinated oxygens around the vacancy. Therefore, there are fifteen possible anionic configurations around a single vacancy. For each configuration, the relaxed geometry and corresponding formation energy were computed. The results of these calculations are plotted in **Figure 48.**.

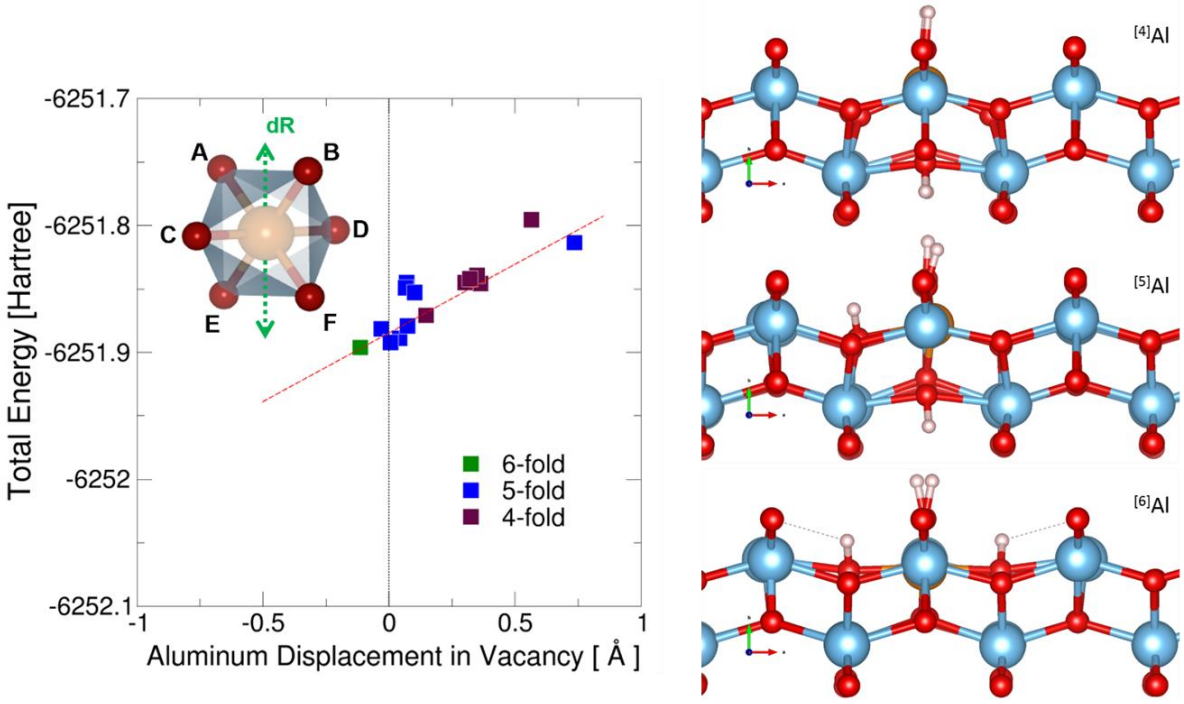

Figure 48. Total energy of each of the fifteen possible anionic environments around a vacancy as a function of the aluminium displacement inside the vacancy (left); and snapshots of the three most stable configurations where Al^{3+} ions are 6-, 5- and 4-fold coordinated (right). Both of these figures were realized by Kyle Reeves.

The DFT calculations considered the depth of the aluminium ion insertion, inside the vacancy. This depth is in regards to the virtual position of the missing titanium atom: a positive value represents an Al^{3+} ion position that is closer to the interlayer, while a negative value represents a position that is closer to the centre of the titanate layer. From this displacement, the coordination number of the inserted aluminium ion is obtained, considering a 2.0 Å cut-off radius for the Al-O bond.

Figure 48. shows that the ion intercalation depends on the anionic environment, around the vacancy. Indeed, three coordination modes can be adopted by the aluminium: 4-, 5-, and 6-fold coordinated. These modes are indeed the same as those observed by ^{27}Al NMR spectroscopy. Moreover, the fifteen anionic configurations correlate to the diversity of environments, responsible for the NMR peak distribution in broad peaks. Notably, the most stable configuration is associated with a 6-fold coordination of the Al^{3+} ion.

In addition, the coordination number of the inserted aluminium ion is observed to increase with the mean aluminium-anion distance. The calculations provide aluminium-anion distances of 1.82 Å for $^{[4]}Al$, 1.88 Å for $^{[5]}Al$, and 1.92 Å for $^{[6]}Al$. It is noted that the coordination of the Al^{3+} ion increases, when the -OH groups are located in close vicinity. Lastly, this intercalation induced local distortions in the structure. The magnitude of these distortions depends on the coordination mode adopted by the aluminium ion.

3. Evidence of the lepidocrocite-type titanate dissolution into the acidic chloroaluminate ionic liquid

The galvanostatic cycling of the lepidocrocite-type titanate electrode (see **Figure 42.**) unveiled three main observations. Among these, are the loss of the electrochemical properties along the cycles, and the generation of an unknown purple compound. These observations were hypothesised to be due to degradation in time, of the electrode material. Indeed, the electrolyte is a highly acidic medium. For instance, vanadium oxide has already been reported to dissolve, in the same chloroaluminate ionic liquid [153].

This part is therefore dedicated to characterise this generated purple compound, and to investigate such degradation in the lepidocrocite-type titanate electrode material system.

3.1 Residue from the titanium electrode in the electrolyte

After the galvanostatic treatment, traces of the electrode material degradation are searched for, in the used electrolyte. To do so, the galvanostatic cycling of the lepidocrocite-type titanate electrode has been reproduced in the glovebox cell configuration (see **Chapitre 2**). This allows for removing the titanate electrode while keeping the two other electrodes and the electrolyte unchanged. Next a glassy carbon was placed as the working electrode, to perform cyclic voltammetry on the used system. As a control experiment, a similar cycling of the pristine 1:1.5 electrolyte has also been performed.

The obtained voltammograms are presented in **Figure 49.**. The voltammogram revealed three redox peaks (noted *A*, *B*, and *C*), that were not observable in the control experiment. Hence, new redox-active species were found in the electrolyte, after the galvanostatic work on the lepidocrocite-type titanate electrode. These species are attributed to dissolved titanium complexes, that undergo redox reactions on the electrode surface. It is to be noted that the measured intensity of these peaks is very low. This would further suggest that these titanium complexes exist as very diluted species in the electrolyte.

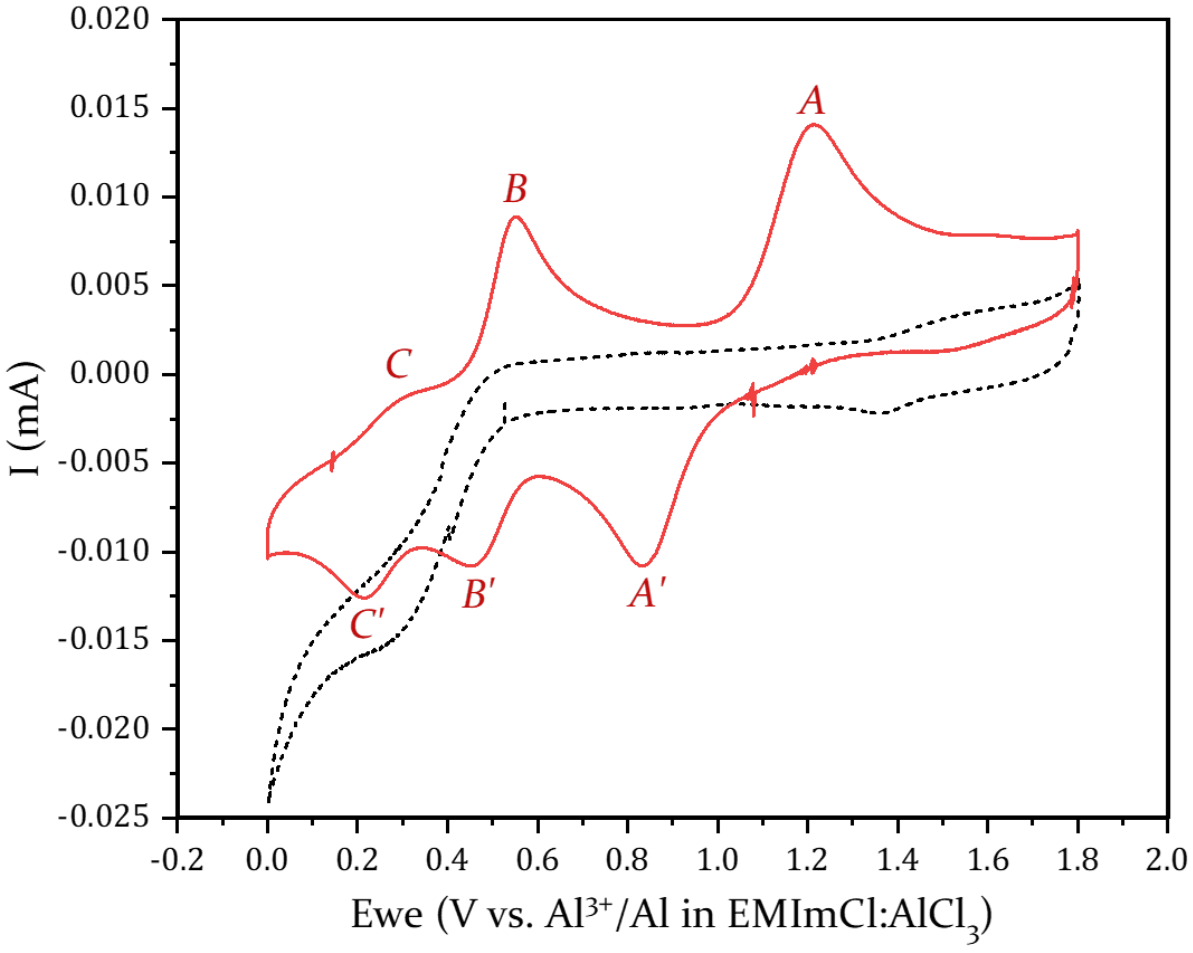

Figure 49. Voltammogram of the used electrolyte (red), after having performed galvanostatic cycling on a lepidocrocite-type titanate electrode. The voltammogram was obtained at 50 mV/s, using a glassy carbon working electrode. A control pristine 1:1.5 electrolyte (black dashes) voltammogram is added for comparative ends.

3.2 Lepidocrocite-type titanate dissolution monitoring

To further characterise the electrode material degradation, an electrochemical titanium detection experiment is built. This experiment takes place in the glovebox cell configuration, and uses glassy carbon as the working electrode. During the experiment, a lepidocrocite-type titanate material electrode is immersed in a large excess of electrolyte ionic liquid. The detection is performed by repeating fast-scanning cyclic voltametries, each hour over nine days. As the cyclic voltametries only scan the reaction occurring at the working electrode, the titanium species need to be dissolved and to diffuse through the cell, in order to be detected. The obtained results are presented in **Figure 50.**, and a scheme of the experimental setup is joined for clarity.

The first voltammogram recorded already presented three low-intensity redox peaks. Then during the following cycles, the intensity of the titanium species peaks progressively rose. The maximum intensity is obtained after 25h of experiment. For longer times of experiment, peak intensity has been observed to fall back. Eventually, after 9 days, the voltammogram displays an even lower intensity than the first one. **Figure 50.** therefore only displays the first, the 25 hours, and the 9 days voltammograms.

The observed peaks are similar to those in **Figure 49.**. Therefore, these peaks are attributed to the same titanium complexes. During the experiment, the increase (decrease) of these peak intensities is then attributed to an increase (decrease) of the concentration of the dissolved titanium complexes. Notably, the first voltammogram already displaying those redox peaks indicates that, within the time of the experimental setup (a few seconds), the titanium species already had time to dissolve and migrate through the cell. As no current flowed through the titanate electrode, this experiment shows that the dissolution of the electrode material into the electrolyte is spontaneous. This is then believed to be the cause of the OCV variations observed back in **Figure 43.**. Nonetheless, the monitored dissolution might be enhanced in **Figure 50.**, due to the large excess of ionic liquid.

Upon reaching the 25th hour of experiment, the colour of the system has changed: the golden yellow ionic liquid is now tinted with a vivid red colour. Later, as the voltammogram intensity diminished, a purple sediment appeared at the bottom of the cell. This sediment might be identical to the previously reported purple compound, found after disassembling the Swagelok cells (see **Figure S60.**).

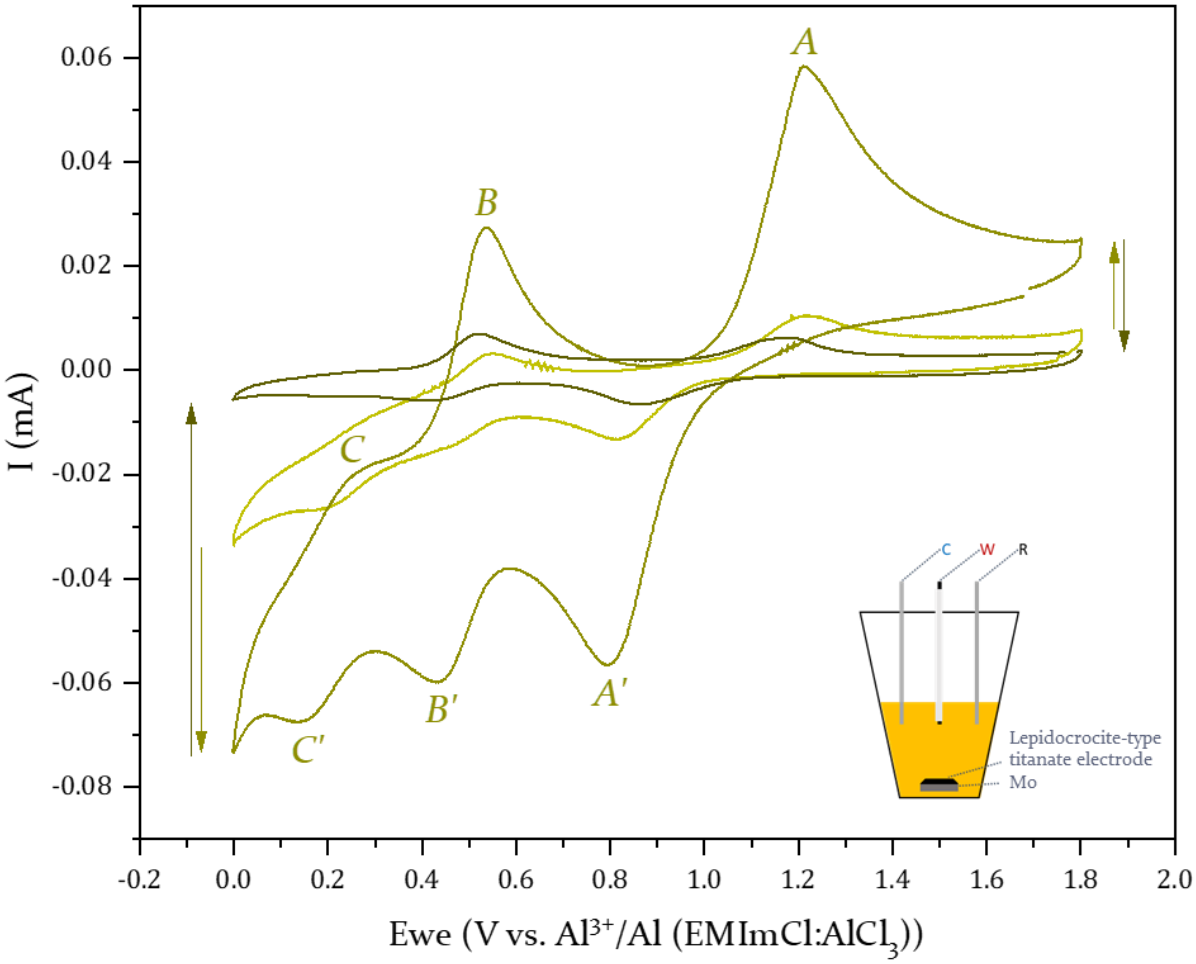

Figure 50. Cyclic voltammetries of the titanium dissolution detection experiment, from the lepidocrocite-type titanate material. Voltammograms recorded for 10 minutes (light), 25 hours (medium), and 9 days (dark) of experiment are displayed. The arrows indicate the evolution in time of the monitored profiles. A scheme of the experimental setup is also joined.

Both the red colouration and the purple sediment apparition are believed to come from the same phenomenon: As time passes, the electrode material progressively dissolves into the electrolyte. As a result, the concentration of dissolved titanium complexes increases. These complexes diffuse and undergo redox reactions at the electrodes, contributing to the measured current. Eventually, new unsoluble species are formed. Clusters then nucleate, providing the red colouration to the electrolyte. With the cycles going on, these clusters grow to form particles and sediment at the bottom of the cell. Thus, titanium centres can no longer be adsorbed on the electrode surface to perform redox reactions. This ultimately diminishes the current intensity of the monitored voltammograms.

The red-tinted electrolyte and the purple precipitate have been analysed by Raman spectroscopy. However, only the pristine ionic liquid signal was observable on these spectra. Yet, this insoluble species can be attributed to titanium trichloride. Indeed, $TiCl_3$ is a purple solid, that has been documented to be poorly soluble in the chloroaluminate ionic liquids. Several studies discussed the possibility of its formation in various chloroaluminate ionic liquids [156–159].

In this view, a control experiment has been performed by putting $TiCl_3$ in the EMImCl:$AlCl_3$ ionic liquid. After several weeks, no sign of dissolution was observable. Similarly, the Raman spectrum of this system did not present any other peak than those of the pristine electrolyte.

3.3 A state-of-charge dependent dissolution

During the galvanostatic experiment, the lepidocrocite-type material electrode is reduced and oxidized. At the same time, both aluminium and chlorine ions are intercalated in the electrode material. Therefore, across the galvanostatic cycles, the actual composition of the electrode material widely differs from the former lepidocrocite-type titanate material. Consequently, the solubility of the processed electrode might also be different from the pristine titanate one. The dissolution properties of the electrochemically treated electrodes were then investigated. The titanium dissolution monitoring experiment was reproduced on galvanostatically discharged and charged electrodes. The recorded data is presented in **Figure 51.**. As a reference, the pristine material data from **Figure 50.** is joined. For clarity, only the maximum intensity voltammograms are displayed there.

The voltammograms from the first cycles of the three samples were similar. The three voltammograms show the same three redox peaks, as described in **Figure 50.**. However, the electrodes evolve differently during the experiment. After a day, the profile of the voltammogram from the discharged electrode has flattened. On the other hand, the intensity of the charged electrode voltammogram was expanded.

Nonetheless, the pristine electrode presents higher intensities than the charged electrode does. This intensity discrepancy might originate from the former galvanostatic treatment of the electrode. Indeed, during the discharge-charge in the swagelok cell, the dissolution of the electrode material might already have occurred. When the the so-charged electrode was removed to be analysed in the glovebox cell, the electrolyte was not kept. Some of the dissolved material might therefore have remained in the electrolyte, which does not contribute to the voltammogram of the charged electrode.

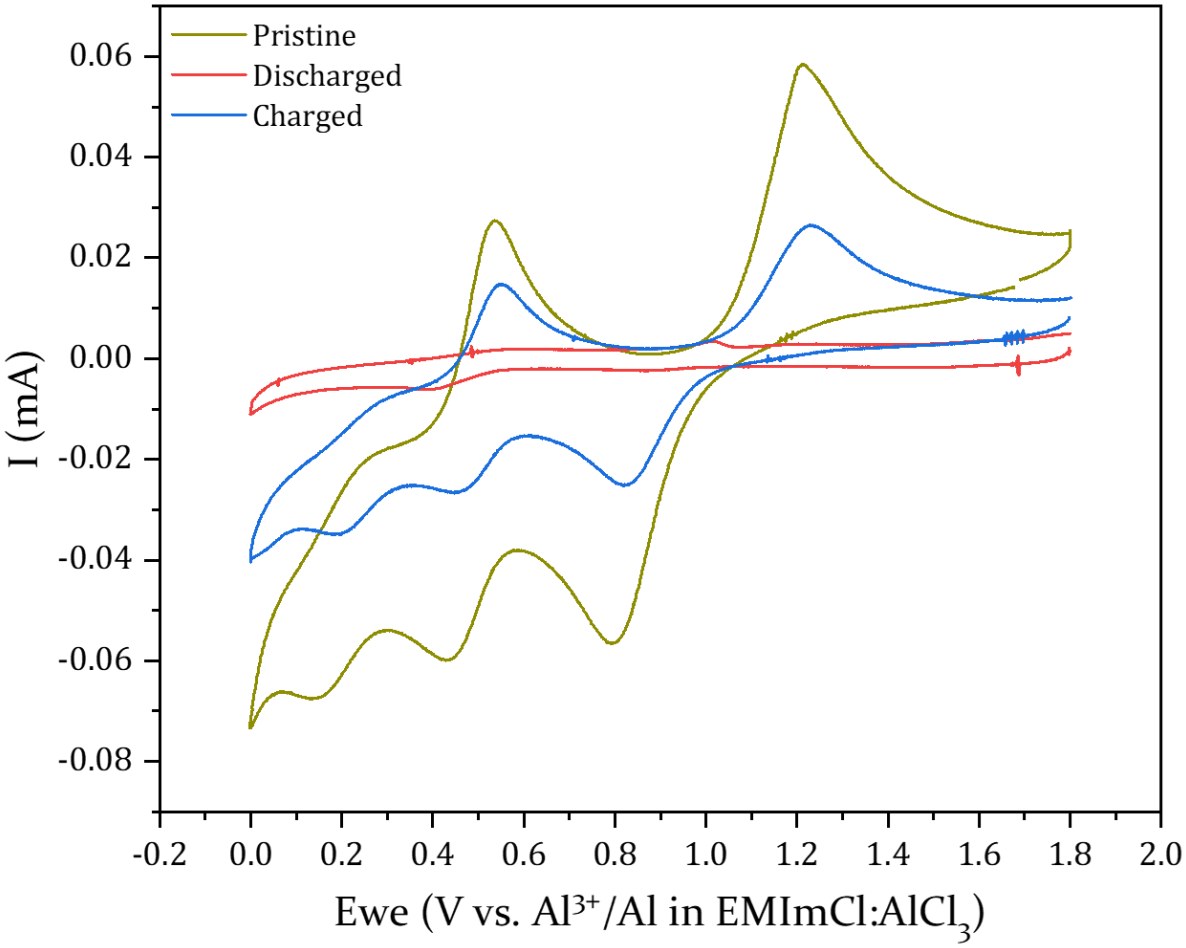

Figure 51. Dissolution monitoring cyclic voltammetries of a pristine electrode (dark golden), a discharged electrode (red), and a charged electrode (blue). Only the cycles of maximum intensity are displayed.

This experiment reveals that the reported dissolution of the electrode material can be hindered. Indeed, the observed signal from the discharged electrode does not show evidence of such dissolution. This electrode sample is the only sample probed for which the titanium has been reduced. The two other electrodes mainly present tetravalent titanium. Therefore, the correlation between the oxidation state of the titanium and the material resistance to dissolution can be pointed out.

3.4 Dissolved titanium species characterisation

To further characterise the dissolved titanium species a small amount of lepidocrocite-type titanate material has been poured into the 1:1.5 EMImCl:$AlCl_3$ ionic liquid. After a week, the total dissolution of the white powder has been witnessed. As a result, a clear ionic liquid sample, containing 10g/L of dissolved lepidocrocite material (or 0.1 mol/L of dissolved titanium ions), was obtained.

This sample solution was first characterised by Raman spectroscopy. The collected spectrum is identical to the pristine ionic liquid counterpart, except within the 200 to 600 cm^{-1} region. **Figure 52.** displays the obtained data, for this region of interest. There, the two 311 cm^{-1} and 431 cm^{-1} peaks, attributed to the $Al_2Cl_7^-$ dimer , are heavily diminished. At the same time, new contributions are observed to arise at 267 cm^{-1} and 384 cm^{-1}. In addition, the intensity of the two small broad peaks at 500 cm^{-1} and 550 cm^{-1} has been inverted. Finally, the signals from both the $EMIm^+$ cation and the $AlCl_4^-$ anion remained unchanged.

The apparition of the two new contributions is therefore associated with the dissolution of the lepidocrocite-type titanate material. In the literature, several works provide Raman spectroscopy studies, of titanium chloride species inside the chloroaluminate ionic liquid. For instance, Miyaoka et al. proposed to study $TiCl_2$, $TiCl_3$ and $TiCl_4$ [160]. From those three species, $TiCl_4$ presents the closest Raman band frequencies at 385 cm^{-1} and 490 cm^{-1} [161]. In addition, ionic chlorotitanate species have also been reported: $[TiCl_5]^-$ shows a 349 cm^{-1} band, $[TiCl_6]^{2-}$ a 320 cm^{-1} band, $[Ti_2Cl_9]^-$ a 420 cm^{-1} band, and $[Ti_2Cl_{10}]^{2-}$ a 389 cm^{-1} band [162–164]. From all these, it appears that the species responsible for the 384 cm^{-1} signal in **Figure 52.** are $TiCl_4$ derivatives.

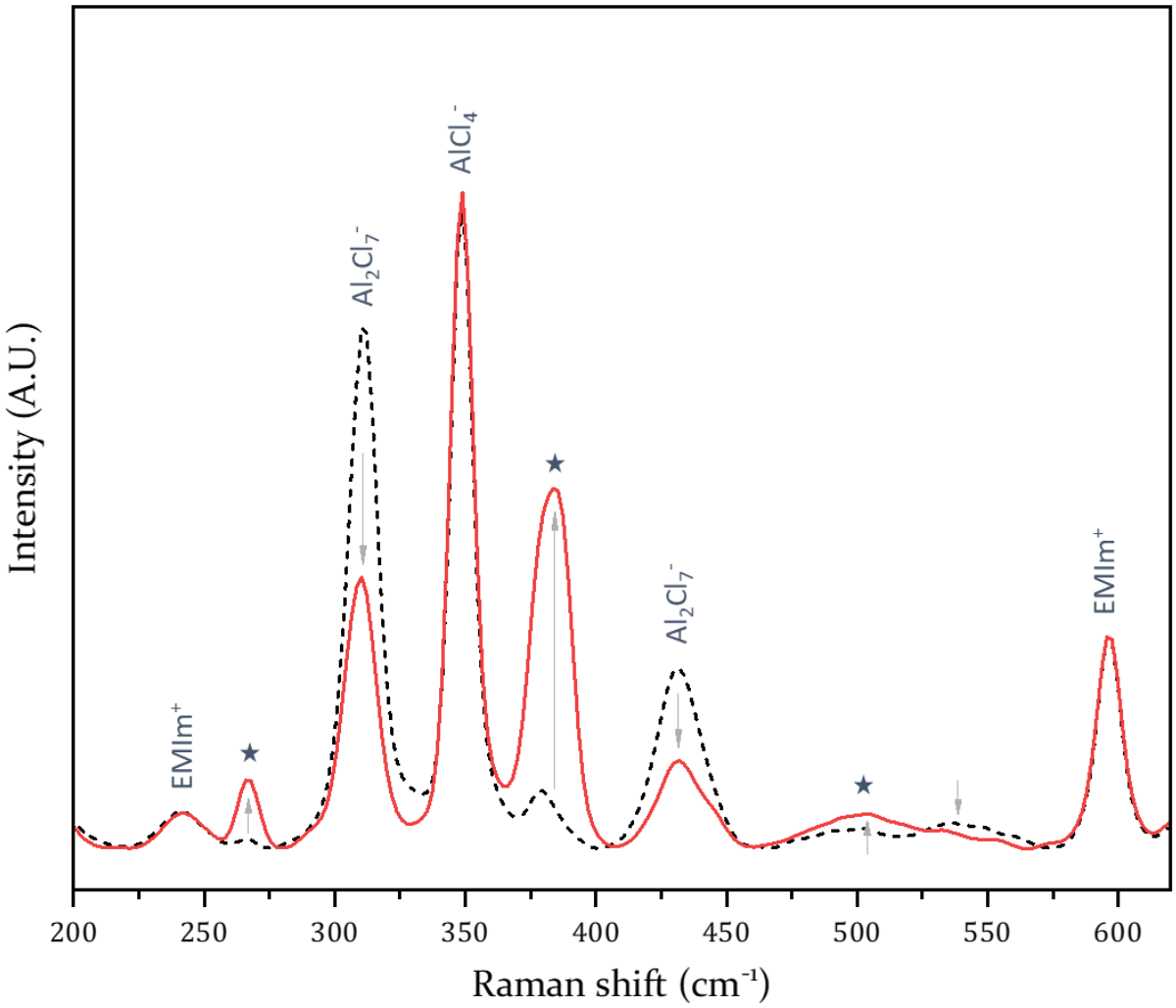

Figure 52. Raman spectra of the ionic liquid, with 10 g/L of dissolved lepidocrocite-type titanate material (red line), and the pristine ionic liquid (black dashes). The star symbols refer to the signals due to the titanate dissolution.

In order to form those $TiCl_4$-derivative species, chloride must be supplied to the dissolved Ti ions. this chlorine can be extracted through the consumption of the chloroaluminate species. Indeed, the $Al_2Cl_7^-$dimer ion peak, at 311 cm^{-1} and 431 cm^{-1}, are observed to be diminished. However, this hypothesis is unlikely. Indeed, the split up of the dimer ion generates monomer ions, which would expand the 349 cm^{-1} peak. Instead, the complexation of titanium ions by chloroaluminate ligands is considered. Indeed, several studies reported the formation of titanium complexes with either $[AlCl_4^-]$ [156,165] or $[Al_2Cl_7^-]$ [157,166] ligands, in the chloroaluminate ionic liquid media. Nonetheless, these ligands were only reported to complex divalent titanium centres, leading to the formation of the $[Ti(AlCl_4)_3]^-$ and the $[Ti(Al_2Cl_7)_4]^{2-}$ species.

In the case of the dissolution of the lepidocrocite-type titanate material, **Figure 52.** suggests that the tetravalent titanium preferably bonds with four $[Al_2Cl_7^-]$ ligands. As a result, the first neighbours of the Ti centres are four chlorine atoms, alike $TiCl_4$. In addition, this complexation would convert a terminal chlorine, from the dimeric species, into a bridging one. As an effect, specific vibrational modes, from the former $Al_2Cl_7^-$ ion, would be prevented. Consequently, the observed result is the fade of the corresponding Raman signals. Notably, the 267 cm^{-1} peak enhancement can also be ascribed to the formation of these chloroaluminate titanium complexes. Indeed, this signal is attributed to high oligomeric chloroaluminate species (see **Chapter 3**).

Finally, the lepidocrocite-type titanate material dissolution also provided the ionic liquid with oxygen atoms, hydroxyl groups, and water molecules (alongside titanium). Therefore a wider variety of chemical reactions can occur, leading to -Cl, -O, -OH, $-OH_2$, $-AlCl_4$ or $-Al_2Cl_7$ being ligands for both the titanium and aluminium complexes. Mixed ligand complexes might also be formed. For this reason, it is yet unsure which complexes are actually formed, following the lepidocrocite-type titanate material dissolution in the acidic ionic liquid.

3.5 Electrodeposition of the dissolved titanium species

Removal of the identified dissolved titanium species is now considered. In this view, the electrodeposition of the dissolved titanium species, from the ionic liquid containing 10 g/L of dissolved lepidocrocite-type titanate material, has been achieved. This has been done by performing chronoamperometries, at various set control potentials, using Mo as the working electrode. The 0.05 V chronoamperogram is provided in **Figure S66.**. This electrodeposition resulted in the deposition of a brown and black sludge on the naked Mo electrode. A similar chronoamperometry has also been realised, using the pristine 1:1.5 EMImCl:$AlCl_3$ ionic liquid as a reference. As no such deposition is observed in this control experiment, this deposition is ascribed to the dissolved titanium species. Notably, no deposition was observed for any control potential higher than 0.05 V.

The deposition product was witnessed to dissolve in the DMC used for washing. Nonetheless, after drying, a resulting compound was obtained. Elemental analysis has been conducted by EDX, on both the unwashed and the washed samples. The obtained mean atomic titanium rates, provided in **Figure S66.**, are around 10% and 27% respectively. In comparison, in the former 0.1 mol/L dissolved lepidocrocite-type titanate material ionic liquid, the atomic titanium rate is only 0.36%. For both the unwashed and the washed deposits, the measured titanium rates are largely above this former rate, validating the deposition from the titanium complexes.

Stafford, Tsuda and Hussey studied electrodeposits from dissolved divalent titanium complexes in the EMImCl:$AlCl_3$ ionic liquids [156,159,167,168]. They observed the co-deposition of metallic Ti and Al alloys. They also reported that no pure titanium deposition could be achieved. From di-, tri, or tetravalent titanium chlorides, similar results were also obtained in BMImCl:$AlCl_3$ [157,169], and BuPyCl:$AlCl_3$ [170] ionic liquids. In addition, the purple $TiCl_3$ was also found deposited in these works. Although, it is sometimes referred to as brownish, due to the wide variety of $TiCl_3$ polymorphs that can be formed in these systems. Therefore, it is sensible to consider the obtained sluggish black deposit as a titanium-aluminium alloy, while the brown part is ascribed to insoluble $TiCl_3$.

After the chronoamperometry, the remaining electrolyte was analysed by Raman spectroscopy. The obtained Raman spectrum, shown in **Figure 53.**, exhibits peak enhancements of the $Al_2Cl_7^-$ dimer ions contribution, while those of the chloroaluminate titanium complexes are extinguished. Notably, the peaks from both the $AlCl_4^-$ monomer ion and the $EMIm^+$ cation remained unchanged. Overall, after the electrodeposition, the recorded Raman profile has mostly reverted to the former pristine ionic liquid. Substantially, this indicates that the electrodeposition of the black and brownish products did not change the species equilibrium in the mix (*i.e.* the acidity of the ionic liquid), despite the income of water and oxygen atoms.

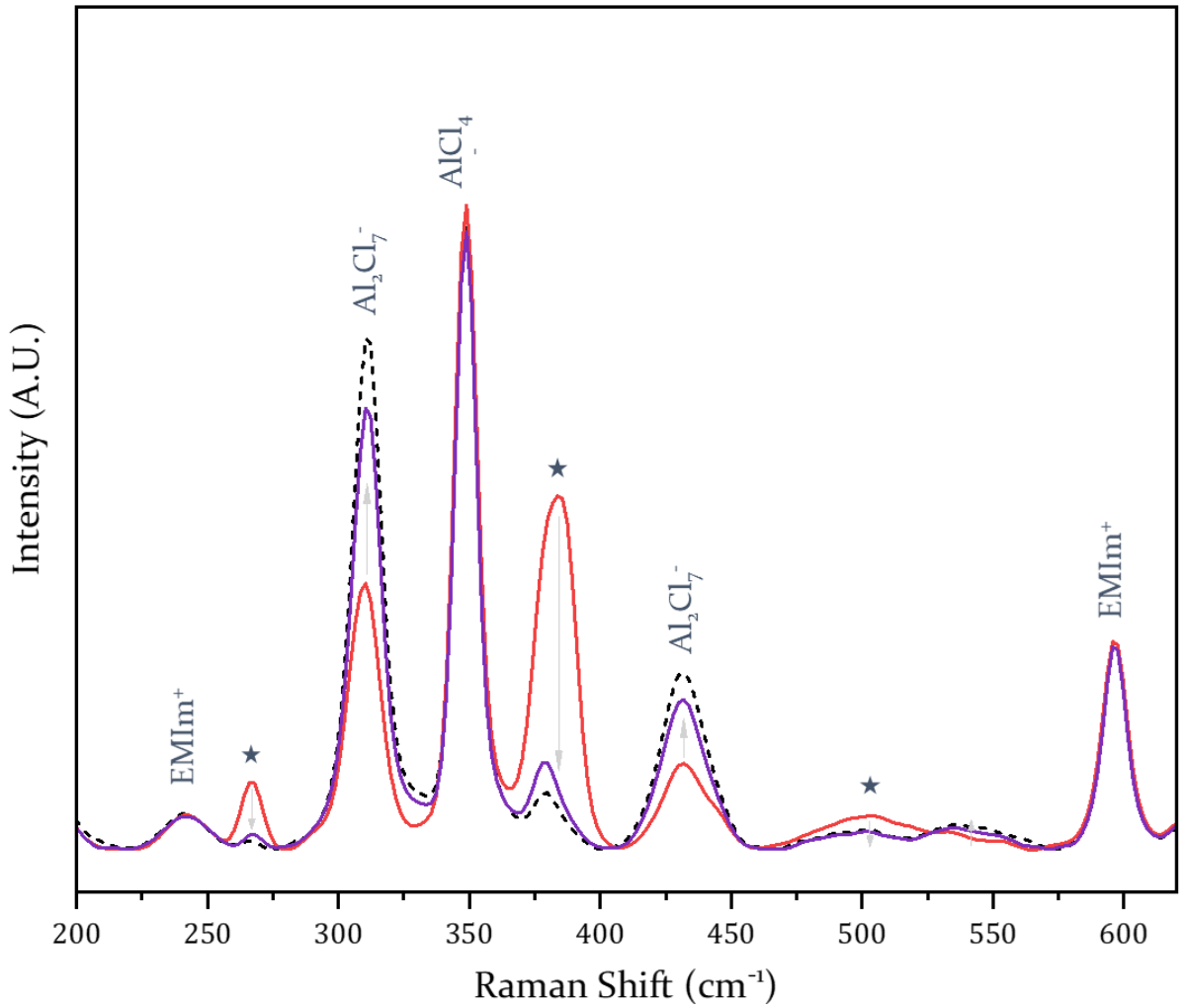

Figure 53. Raman spectra of the ionic liquid, with 0.1 mol/L of dissolved lepidocrocite-type titanate material, before (red line) and after (purple line) the electrodeposition treatment. The Raman spectrum of the pristine ionic liquid (black dashes) is joined as a reference. The star symbols refer to the signals due to the titanate dissolution.

To further characterise the effect of the electrodeposition, on the species equilibria in the mix, NMR spectra have been collected. **Figure 54.** displays the ^{27}Al spectra of the ionic liquids before and after the electrodeposition, as well as the pristine one. There, after the titanate material dissolution, the sharp signal of the $Al_2Cl_7^-$ dimer ion is observed to increase and become the most intense signal. On the contrary, after the electrodeposition, this peak is diminished back. The increase of the dimeric species peaks can seem contrary to the data collected in **Figure 53.**, but is believed to be due to the chloroaluminate titanium ions. Then the electrodeposition is monitored to cause a similar phenomenon as before: a reversion toward the pristine ionic liquid state.

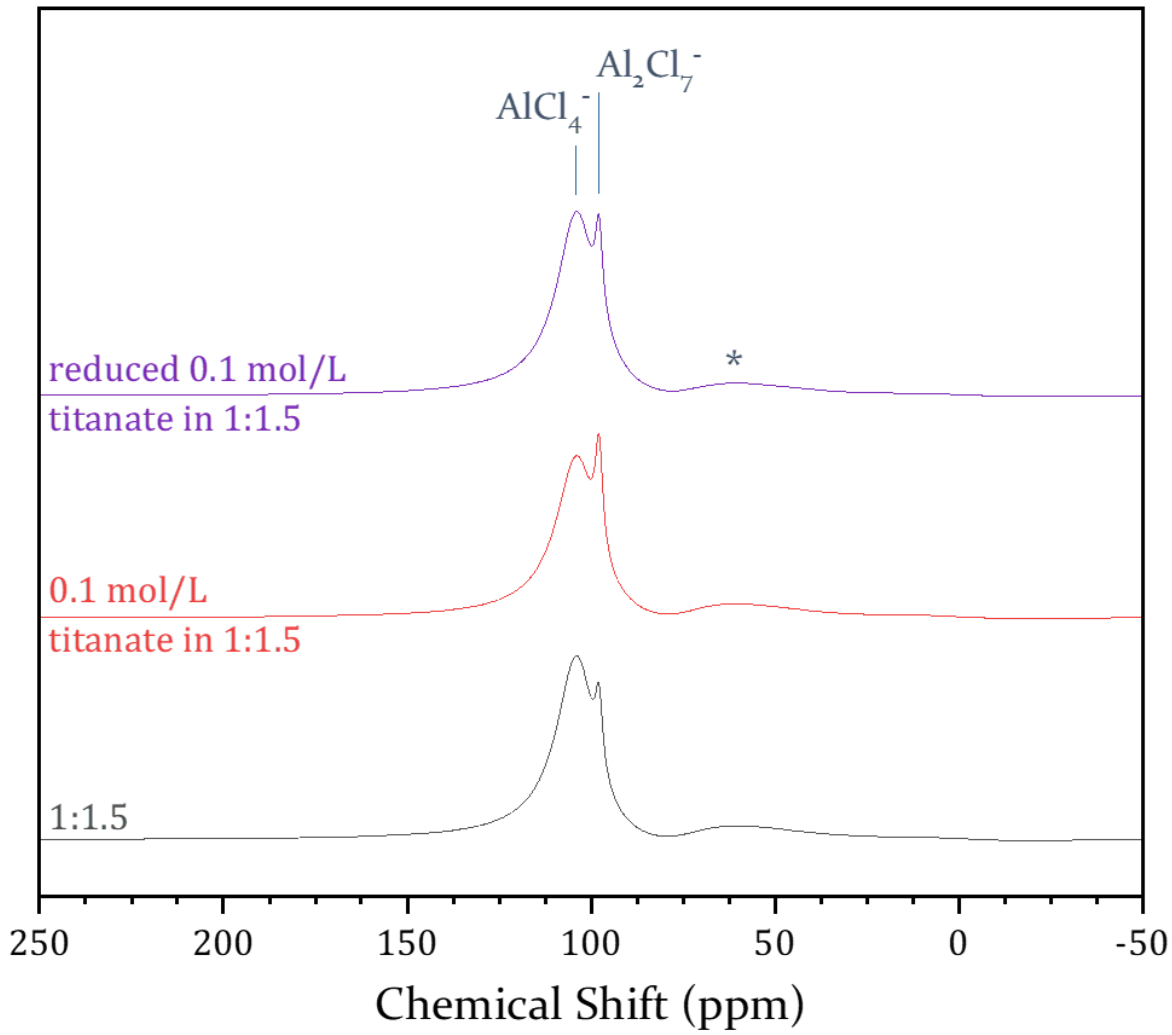

Figure 54. ^{27}Al NMR spectra of the pristine ionic liquid (black), the ionic liquid after the dissolution of 0.1 mol/L titanate (red), and the ionic liquid after the electrodeposition(purple). Each spectrum has been normalised by its most intense peak. The * mark indicates the apparatus contribution.

Finally, ^{1}H and ^{13}C spectra have been collected to study the effect of these treatments on the $EMIm^{+}$ cation. Close-up views of the peaks, from the various ionic liquids are available in **Figure 56.** and **Figure 55.**. The full spectra are available in **Figure S68.** and **Figure S67.**. As an aside, the spectrum of the sample after the electrodeposition is less resolved than those of the two other samples. This is due to shim issues, caused by the D_2O capillary (see **Chapter 2**).

In **Figure 56.**, a shift of 0.09 ppm towards the higher chemical shift values is observable after the dissolution. An opposite homogeneous shift of 0.11 ppm is observed after the electrodeposition. Notably, the subtle peak multiplicity, described in **Chapter 3**, is still observable on each spectrum. In **Figure 55.**, the dissolution of the titanate material only shows slight shifts towards the lower chemical shift values. A notable exception is the *A* carbon, exhibiting a shift of 0.07 ppm in the opposite direction. After the electrodeposition, the different signals were shifted back up, to higher values than their pristine counterparts. The exception being the *A* carbon, for which the peak remained close to its value after the titanate dissolution.

Overall, these shifts are only slight variations. Nevertheless, they revealed that the $EMIm^{+}$ cation is also affected by the dissolution of the lepidocrocite-type titanate material. The presence of the titanium complexes inside the ionic liquid is understood to elongate the bonds between the protons and their carbons. Interestingly, after the removal of those complexes, distortions are witnessed inside the imidazolium ring of the $EMIm^{+}$. Indeed, the C-H bonds are shortened, and the C-C and C-N bonds also varied. This distortion is believed to be in response to the speciation changes of the system. In this sense, the NMR study has nuanced the previous observations, made via Raman spectroscopy.

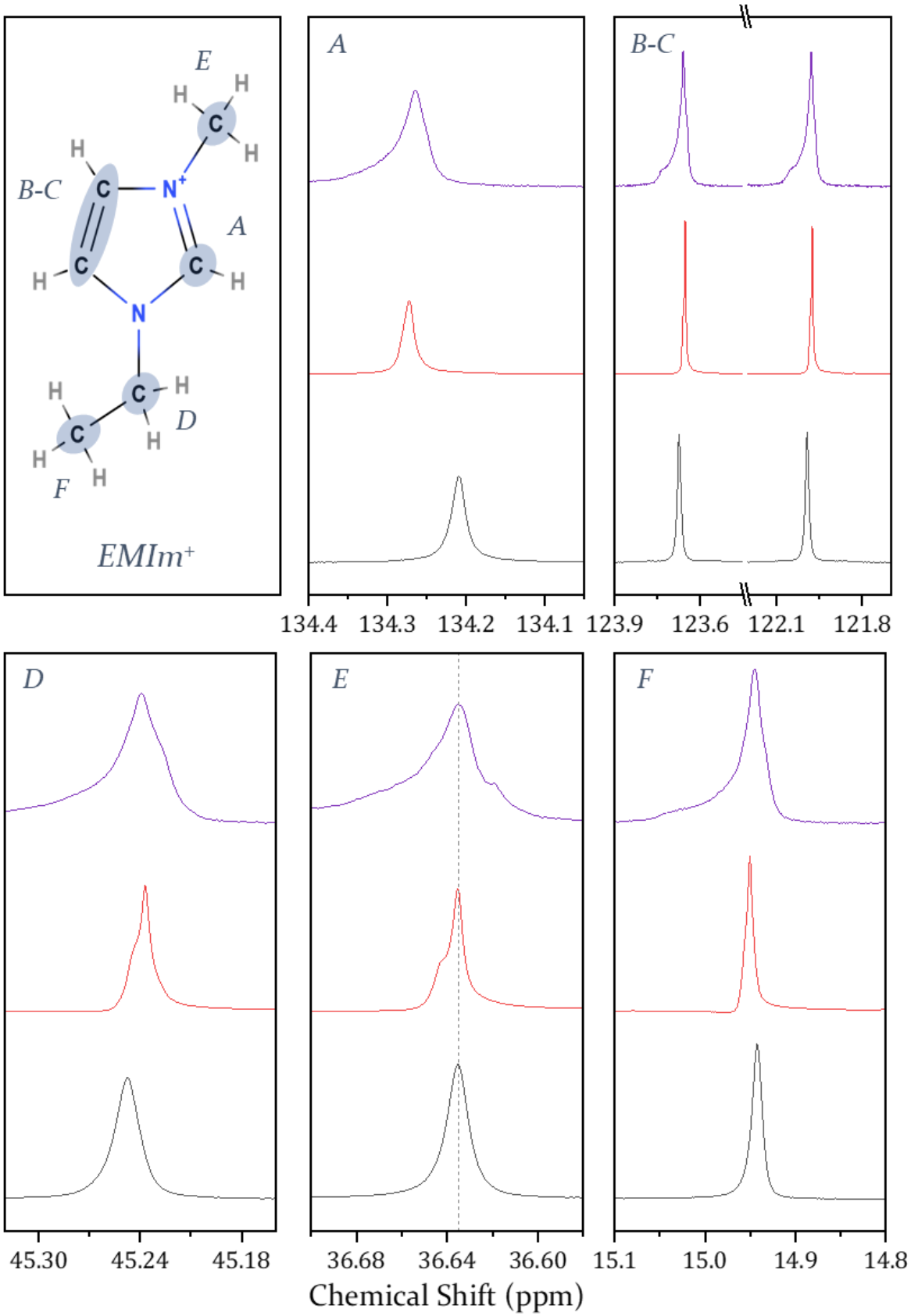

Figure 55. ^{13}C NMR spectra of the pristine ionic liquid (black), the ionic liquid after the dissolution of 0.1 mol/L titanate (red), and the ionic liquid after the electrodeposition(purple). The dashed line at 36.635 ppm indicates the chosen internal reference.

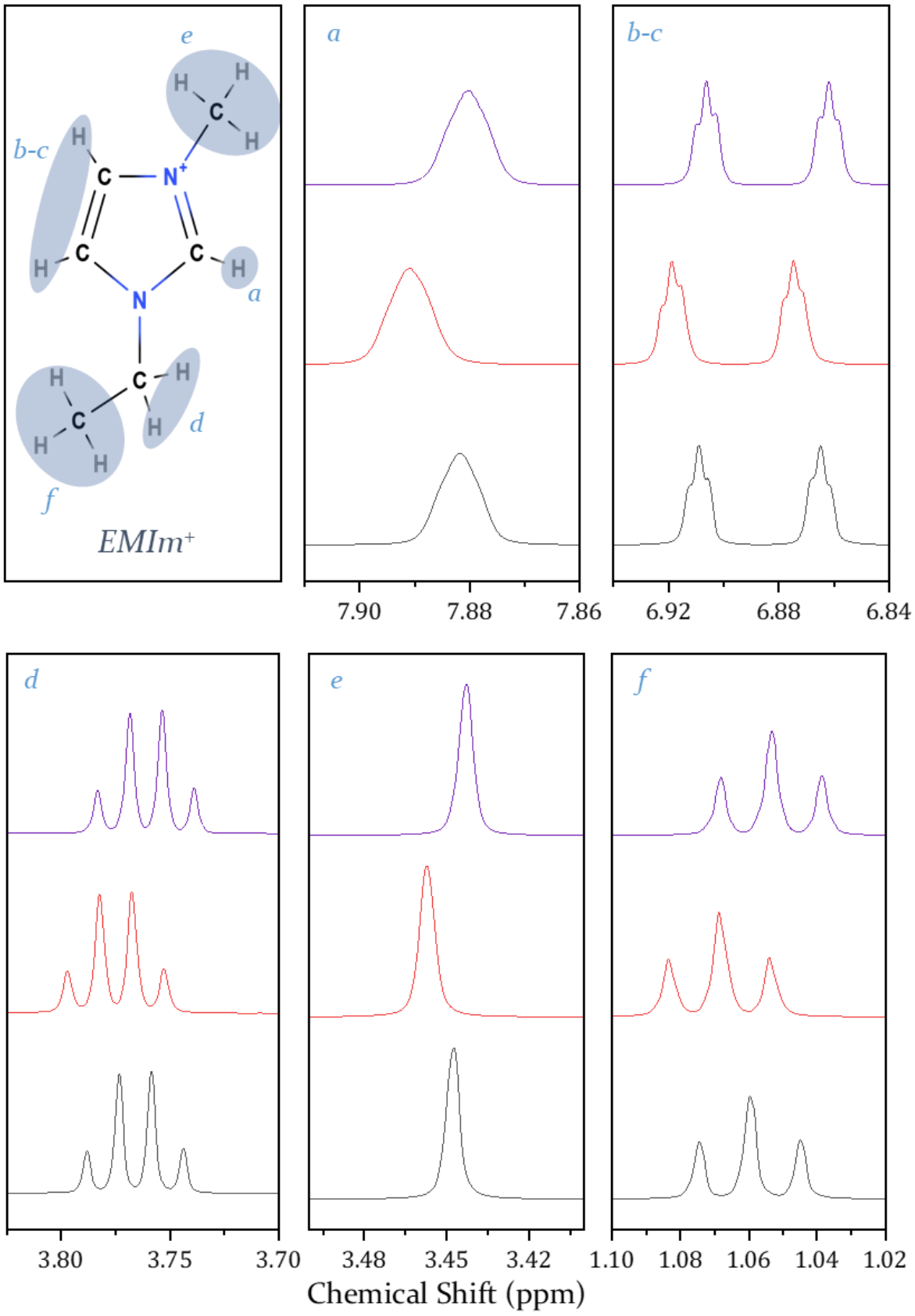

Figure 56. ^{1}H NMR spectra of the pristine ionic liquid (black), the ionic liquid after the dissolution of 0.1 mol/L titanate (red), and the ionic liquid after the electrodeposition(purple).

Notably, the formation of carbene groups has been investigated in these systems. Those N-heterocyclic carbenes (NHCs) have been reported, in various imidazolium-based ionic liquids [171,172]. These extremely reactive species have been mainly studied in organic chemistry, for their catalytic properties. Eventually, organometallic species have been observed to be formed by the complexation of various metal atoms by those NHCs [173–175]. Among those, $AlCl_3$ [176–178] and $TiCl_4$ [179] complexes have been reported to possibly be formed in different media.

However, their formation implies the deprotonation of one of the imidazolium ring carbon atoms. In **Figure 56.**, no relevant variations of the ^1H peak integrations could be observed for any of the sampled ionic liquids. Therefore, no carbene formation is reported in the EMImCl:$AlCl_3$ and lepidocrocite-type titanate material systems.

4. Characterisation of the electrochemical downfall

The galvanostatic cycling of the lepidocrocite-type titanate material electrode, provided high discharge and charge capacities for the first cycle (see **Figure 42.**). However, the recorded capacity quickly drops within the next cycles. The capacity is halves in only four cycles, and is divided by more than 30 on the tenth cycle. To gain more understanding about this phenomenon, this part will focus on studying the capacity decay.

Previously, both chlorine and aluminium have been shown to irreversibly insert into the electrode material. In addition, **Part 3.** showed that the titanate material dissolved in the ionic liquid electrolyte. Those observations will then be considered to understand the electrochemical properties of the proposed system. Emphasis will thereafter be put on the shapes of the data collected through various electrochemical techniques.

4.1 Evolution of the galvanostatic discharge-charge profile

During the galvanostatic discharge-charge cycling experiment, the capacity gradually dropped. While this decrease was monitored, the shape of the discharge-charge curves was progressively altered. Indeed, every event, on the curves, became more pronounced with each new cycle. As an example, **Figure 57.** isolates some of the recorded galvanostatic cycles, in the Swagelok cell configuration.

The first cycle exhibits smooth sloping curves. This is characteristic of a solid-solution insertion into a disordered material. However, this behaviour is not kept upon cycling. Looking at the fifth cycle, the discharge curve now exhibits two pseudo-plateau around 1.05 V and 0.50 V. Below 0.30 V the solid-solution behaviour is kept. The charge profile has also been altered. Indeed, from a S-shaped curve, three main contributions are now distinguishable at 0.40V, 1.05 V and 1.25 V.

The sloppy curve of the first discharge is ascribed to aluminium intercalation. The lepidocrocite-type titanate presents a wide variety of insertion environments. Each of these environments accordingly accepts the aluminium ion, to insert at a set potential. During the discharge, aluminium starts to insert in the most energetically favourable vacancy sites. Then, the measured potential gradually decreases, as the aluminium progressively explores new insertion sites. In the end, the variety of vacancy environments generates a distribution of insertion potentials. During the first discharge, **Part 2.2.** showed that only a few aluminium was removed from the electrode material. Thus, it is still unknown from which mechanism originates the S-shaped curve observed.

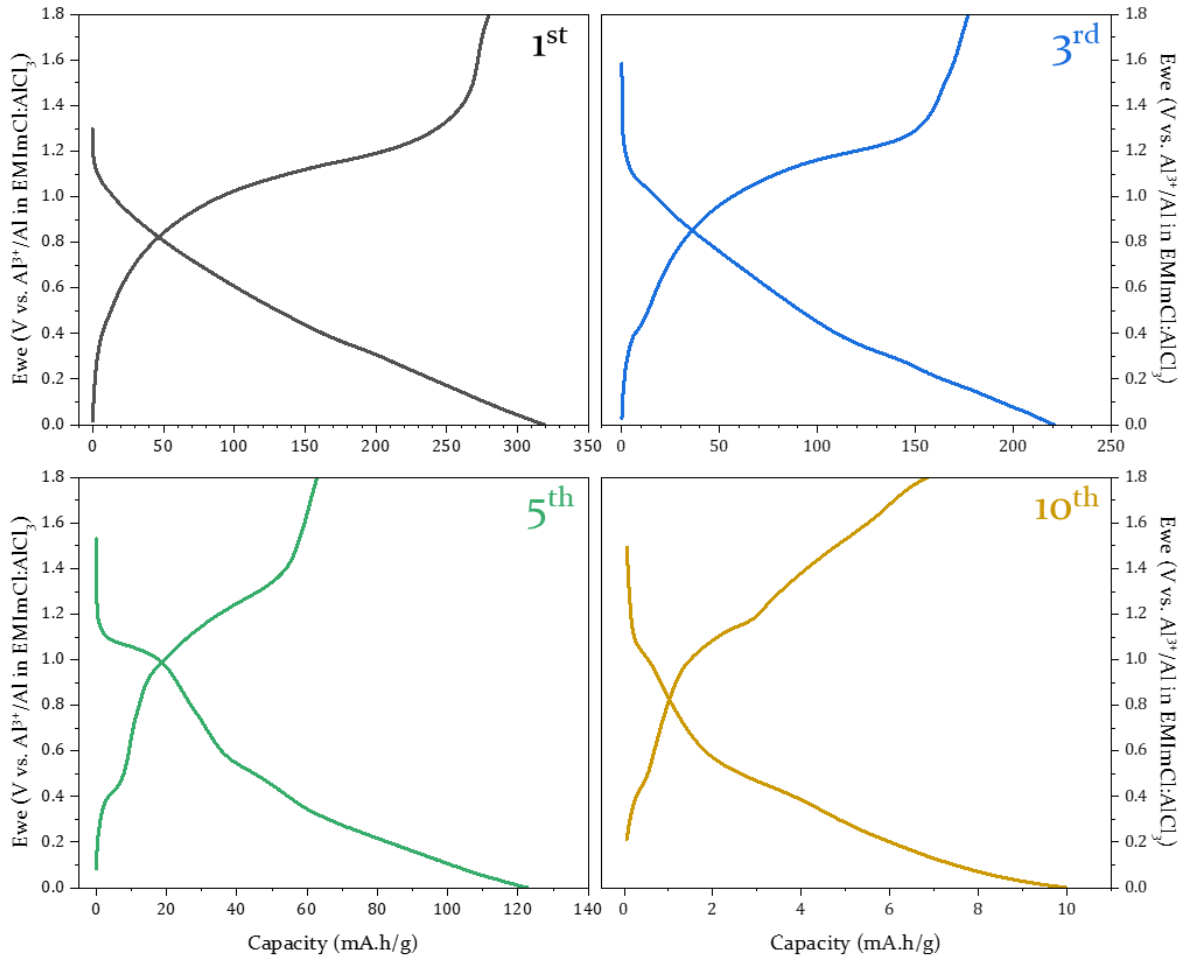

Figure 57. First (black), third (blue), fifth (green), and tenth (golden) cycles of the 20mA/g galvanostatic discharge-charge cycling of the lepidocrocite-type titanate electrode.

By the following electrochemical cycles, the lepidocrocite-type titanate response profile quickly changes. The sloppy curves are progressively lost in the capacity fade. In the meantime, new more defined events appear along the galvanograms. These events are believed to come from different electrochemical mechanisms. These might not be due to aluminium ion intercalation. Yet, more precise characterisations of these electrochemical events are needed to better understand the reactions involved here. This overall reveals drastic variations in the electrochemical mechanisms involved at the working electrode.

4.2 Investigations on the potentiodynamic profile

Further investigations about the electrochemical response profile evolution have been conducted by cyclic voltammetry. **Figure 58.** presents the collected data from a thirty-cycle cyclic voltammetry, performed at a 0.50 mV/s scan rate, in the Swagelok cell configuration. The first three cycles exhibit similar voltammogram profiles. During the reduction, these cycles show a broad diffuse current response below 1.30V. This profile is the expression of the distribution of insertion site environments, as previously described. The oxidations present a small broad peak at 0.44V and a large peak at 1.28V.

However, similarly to the galvanostatic experiment, the behaviour of the voltammograms evolves while cycling: the broad reduction response is gradually lost. Upon the fifth cycle already, no diffuse response was observable anymore. Defined redox peaks also emerge with the cycles going on. Past the tenth cycle, voltammogram profiles do not change any more, only the overall intensity keeps decreasing. Nevertheless, the peak positions correspond to the emerging events from the galvanostatic cycling. Hence, recorded reactions are identical in both the galvanostatic and the potentiodynamic experiments.

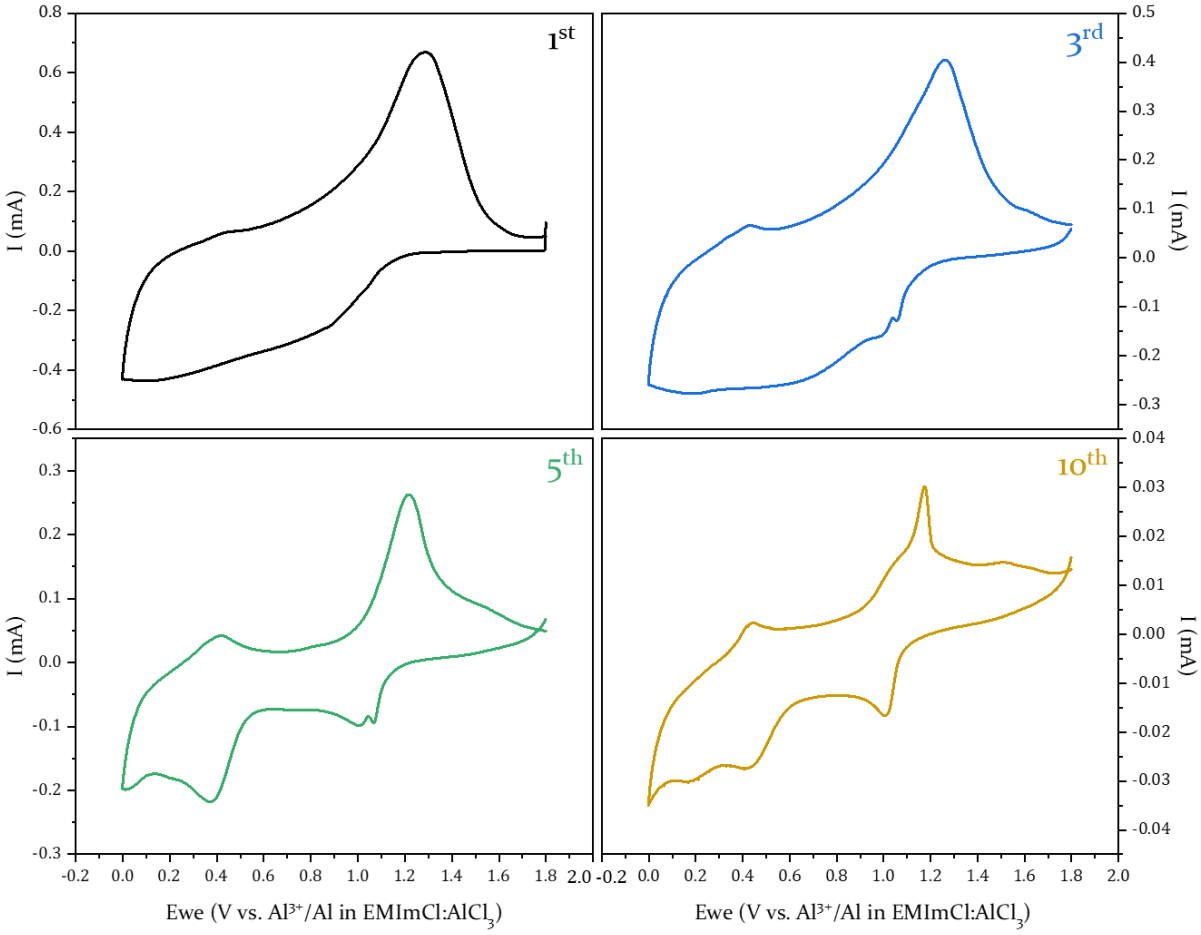

Figure 58. Isolated first (black), third (blue), fifth (green), and tenth (golden) cycles of cyclic voltammetry, performed at 0.50 mV/s, on the lepidocrocite-type titanate material electrode.

Moreover, these voltammograms share striking similarities with the voltammograms issued from the titanium detection experiment (see **Part 3.2.)**. Indeed, a comparison between those two voltammograms is proposed in **Figure 59.**. Despite having been recorded in different electrochemical cell configurations, the same profile with three redox peaks is observable, in both experiments. A potential shift is although observed between some equivalent peaks. This can be attributed to the difference in scan rate between the two experiments.

In **Part 3.2.**, the observed peaks were attributed to the dissolved titanium species. Then, the close similarity between the two voltammograms displayed in **Figure 59.** suggests that these titanium complexes are responsible for the electrochemical responses, obtained on the later cycles of the potentiodynamic analysis. Hence, these species are also the ones providing the recorded capacity during the late galvanostatic experiment. Therefore, in **Figure 59**., the redox peak at 1.00-1.17 V can confidently be ascribed to the Ti^{3+}/Ti^{4+} redox couple. Following the spread of the standard redox potentials of the elements in the system, the two other peaks can be attributed to the Ti^{0}/Ti^{2+} and Ti^{2+}/Ti^{3+} couples. This attribution has indeed already been supported in analogous systems [158,170,180–182].

Substantially, this indicates that, throughout the electrochemical experiments, the recorded signals originate from different contributions: the diffuse profile originated from intercalation in the host structure, whereas the more defined peaks came from surface redox reactions. Interestingly, the capacity drop reported during the galvanostatic experiment is understood not to be directly due to the electrode material dissolution. Indeed, as the dissolved species undergoes redox reactions, the system can still display capacity. The observed capacity decay then is attributed to the formation of the insoluble $TiCl_3$ species.

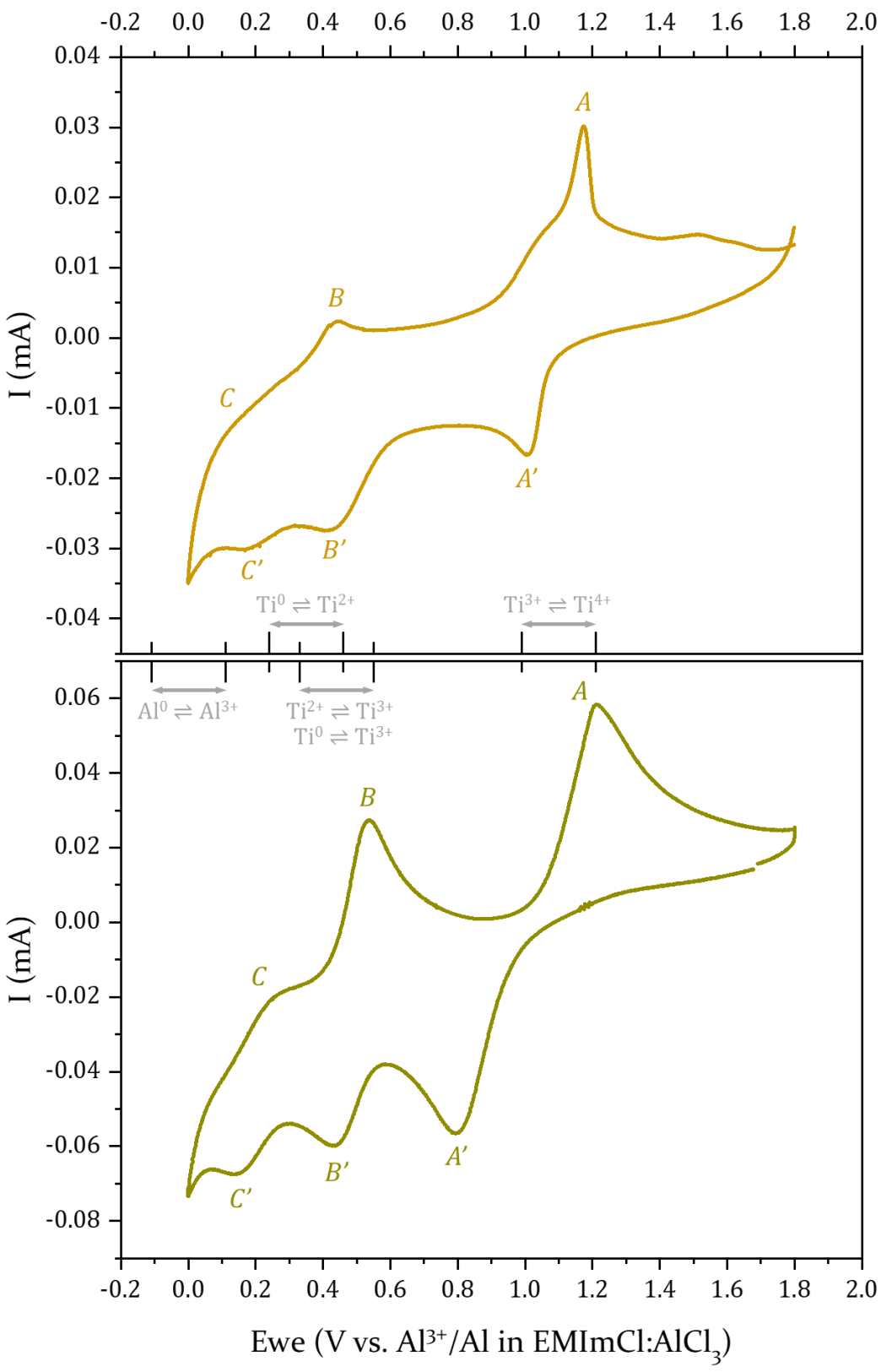

Figure 59. Comparison between two recorded voltammograms. The upper displays the 10th cycle of a 0.50 mV/s cyclic voltammetry of the lepidocrocite-type titanate material electrode, in the Swagelok cell configuration. The lower displays the 25th-hour voltammogram of the 50 mV/s dissolution monitoring of the titanate material, in the glovebox cell configuration.

Conclusion

In this chapter, the chemical and electrochemical properties of the amorphous lepidocrocite-type titanate electrode material have been analysed, in the acidic 1:1.5 EMImCl:$AlCl_3$ ionic liquid electrolyte. Indeed, the titanate material presents structural defects, which were calculated to be favourable insertion environments for the trivalent aluminium ion.

The galvanostatic cycling of this electrode material provided high 318 mAh/g and 280 mAh/g specific capacities, for the first discharge and charge respectively. This discharge-charge profile corresponds to an ion intercalation behaviour, following a solid-solution mechanism. The inserted aluminium environments were probed by NMR spectroscopy and modelized by DFT calculations. The obtained results show environments, that differ from the ones in the chloroaluminate electrolyte. Moreover, these environments correspond to a 4- to 6-fold coordination of the aluminium ion Al^{3+} in an oxyhydroxide medium. This led to the conclusion that the aluminium ion has indeed been inserted in the titanium vacancies of the amorphous titanate material. In addition, during this first cycle, the elemental rates of both the aluminium and the chloride species inserted inside the titanate electrode were monitored. This revealed that, despite the charge capacity observed, the cycle is not reversible, as the inserted ions are not released back during the charge phase.

Then, upon the next cycles, the recorded capacity quickly dropped. On the tenth cycle, barely not capacity was observable any more. In addition, the profiles of the discharge-charge curves evolve into surface redox reactions with the cycling.

Insights on this capacity decay were provided by experiments focusing on the chemical stability of the electrode material in the acidic electrolyte. Indeed, a spontaneous dissolution of the amorphous titanate was observed, within a week into a large excess of the electrolyte. As a result, $TiCl_4$ analogous titanium complexes were generated inside the ionic liquid. Within the voltage window of the electrochemical experiments, those complexes are redox active and present transitions ascribed to the Ti^{4+}/Ti^{3+}, Ti^{3+}/Ti^{2+}, and Ti^{2+}/Ti^{0} couples.

Post-mortem analyses have proven the presence of these complexes inside the electrolyte, after the electrochemical experiments on the titanate electrode. The previously reported surface redox reactions were therefore attributed to the contribution of these complexes. Finally, the capacity drop was explained to be due to the formation of $TiCl_3$ in the cell. The precipitation of this insoluble species deprives the electrode of electrochemically active material, and thus from displaying any capacity.

Notably, the dissolution of the electrode material has been observed to depend on the electrochemical state of the electrode material. Indeed, no dissolution signal could be recorded when analysing a discharged electrode sample in a large excess of acidic electrolyte.

Supplementary information

Figure S60. Picture of the used separator, showing the purple compound, after a galvanostatic discharge experiment.

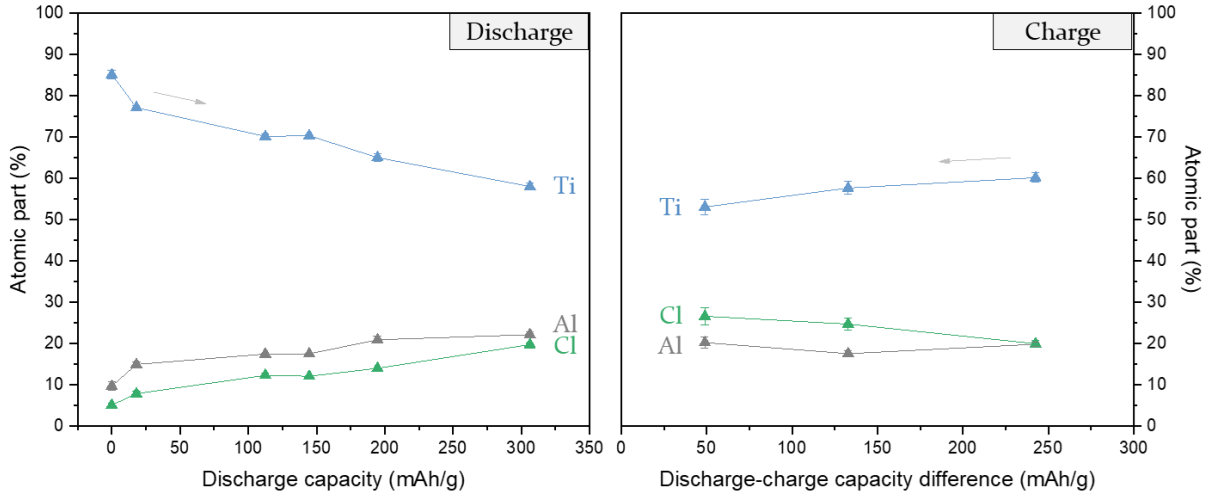

Figure S61. EDX elemental rates measurement of Ti, Al, and Cl along the first discharge (left) and charge (right) of the galvanostatic cycling experiment. The grey arrows indicate the reading order.

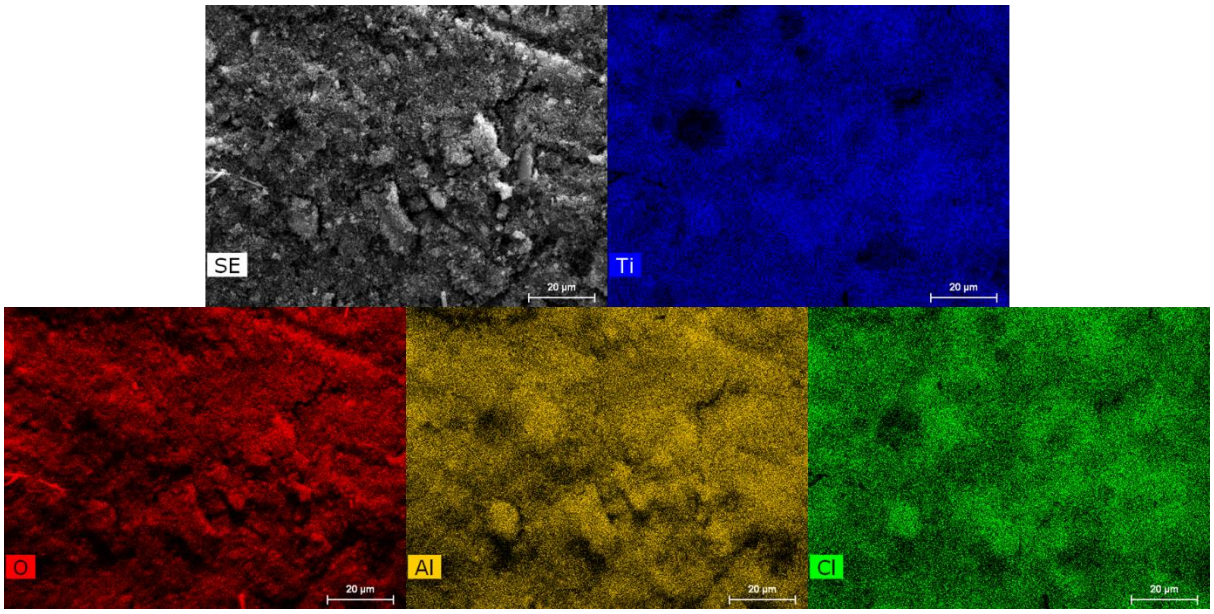

Figure S62. EDX elemental mapping of a discharged lepidocrocite-type titanate electrode. Each element is displayed by a specific colour (Ti in blue, O in red, Al, in golden, and Cl in green). The MEB picture of the probed area (SE) is joined as a reference.

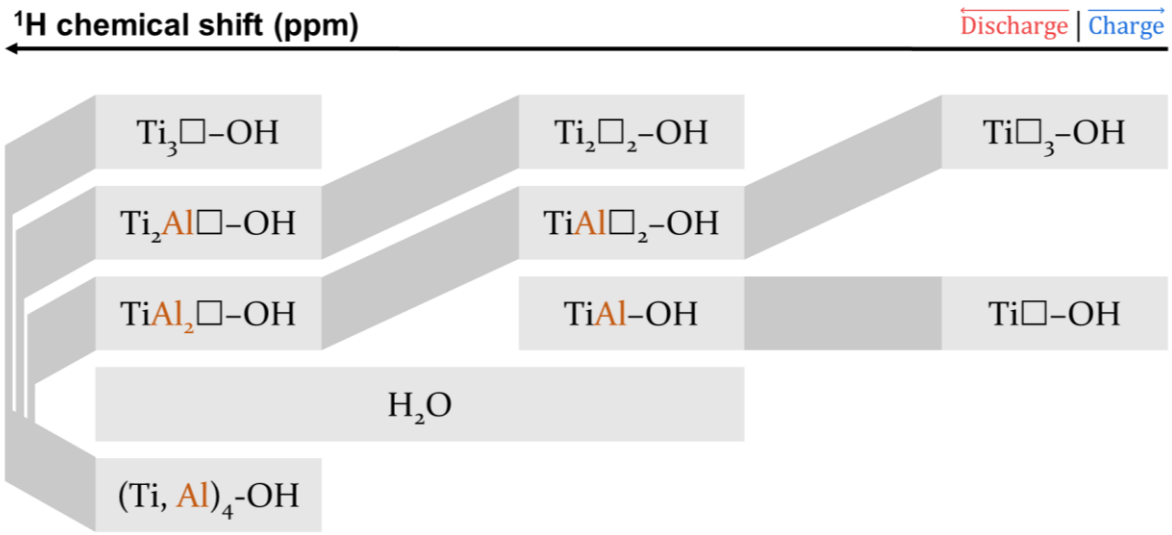

Figure S63. Diagram of the evolution of the ^{1}H chemical shift ranges throughout the galvanostatic cycle. The diagram is displayed as a function of the environment in which the aluminium is inserted.

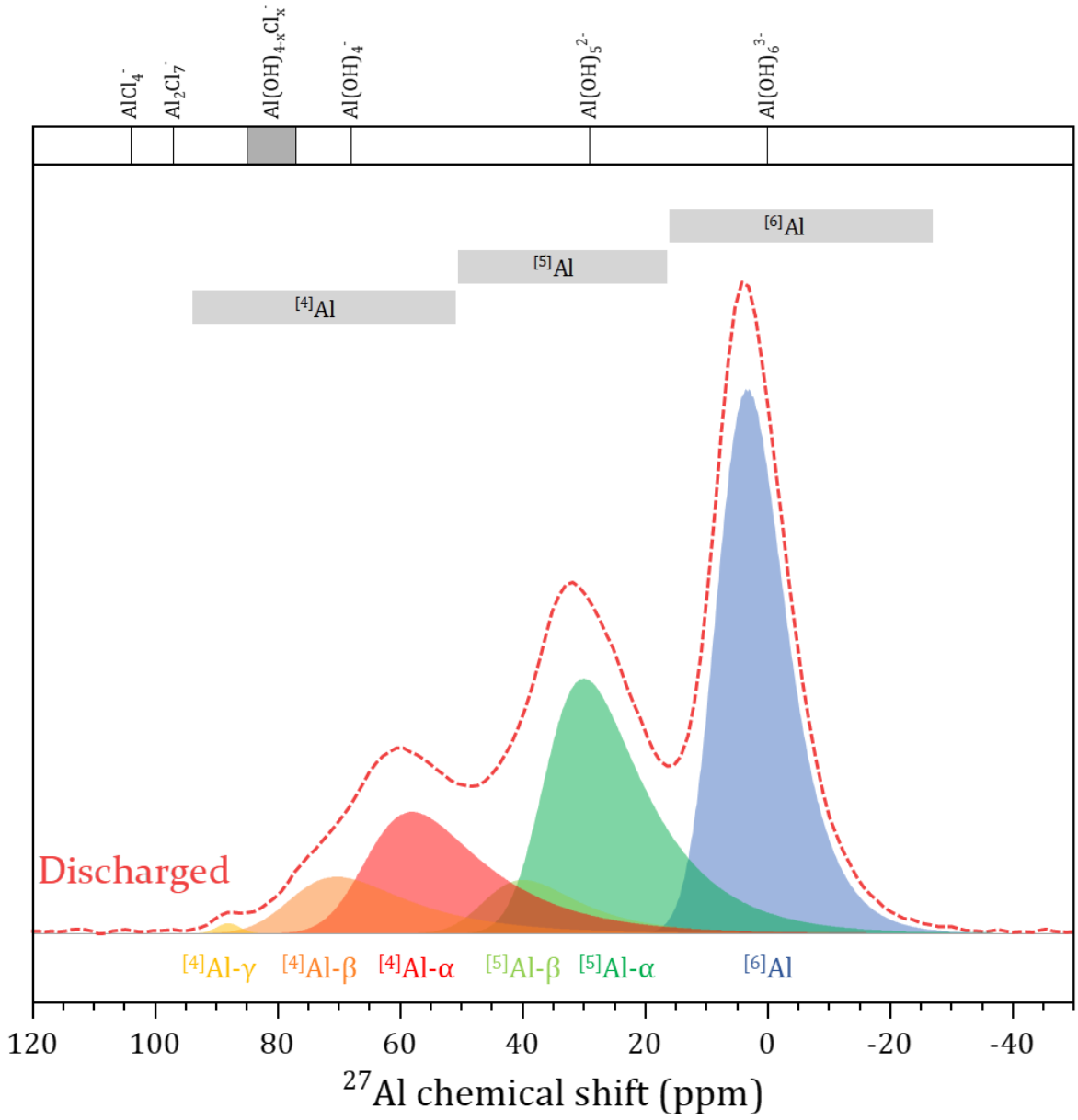

Figure S64. Spectral deconvolution of the ^{27}Al NMR spectrum of a discharged electrode of the lepidocrocite-type titanate material.

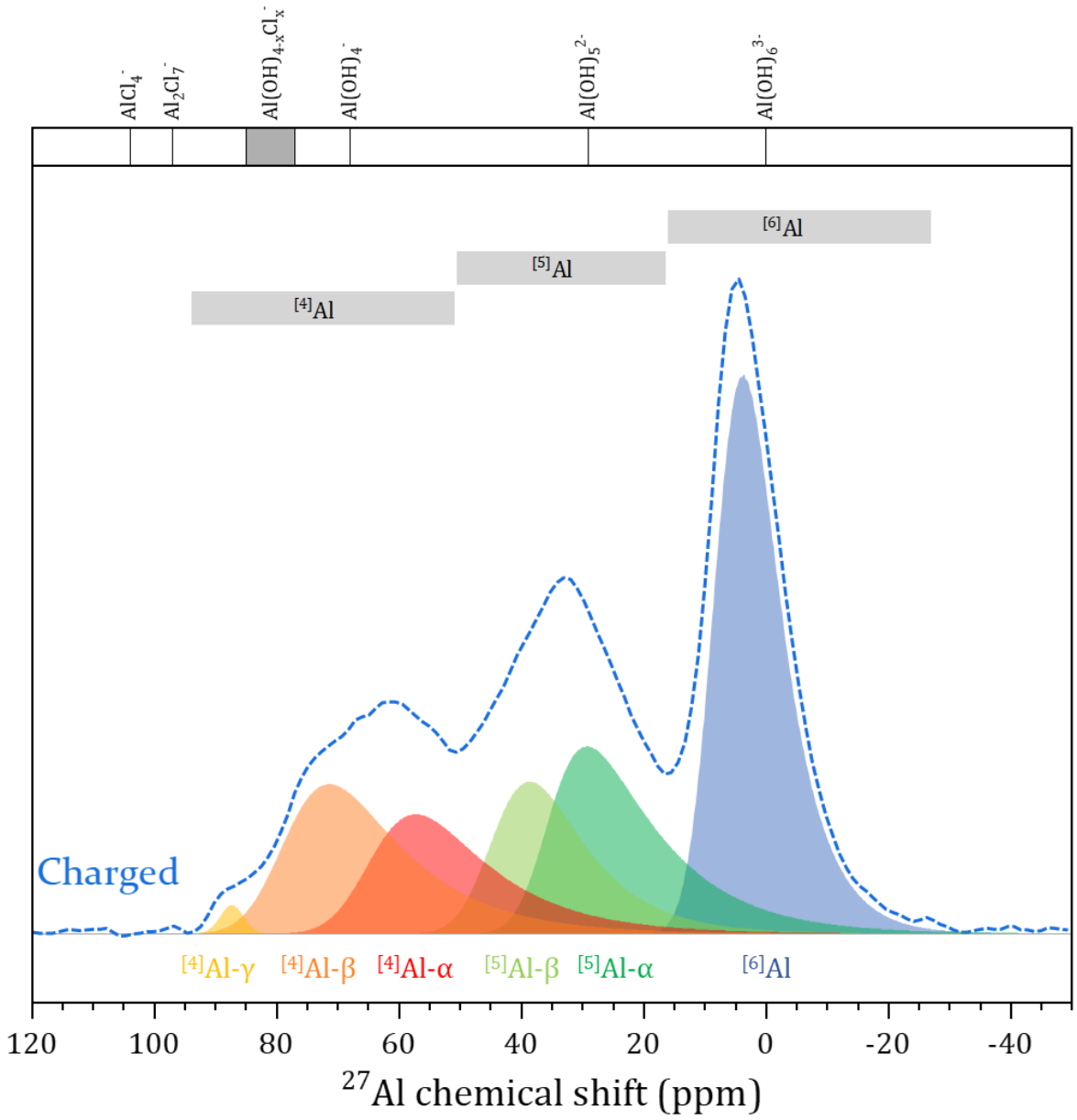

Figure S65. Spectral deconvolution of the ^{27}Al NMR spectrum of a charged electrode of the lepidocrocite-type titanate material.

Sample	Ti (%ato)	Al (%ato)	Cl (%ato)
1:1,5 ionic liquid with dissolved lepidocrocite-type titanate (0,1mol/L)	0.36	21.35	78.29
EDX measured electrodeposition sample (unwashed)	9.55	20.10	70.35
EDX measured electrodeposition sample (washed with DMC)	27.21	35.45	37.34

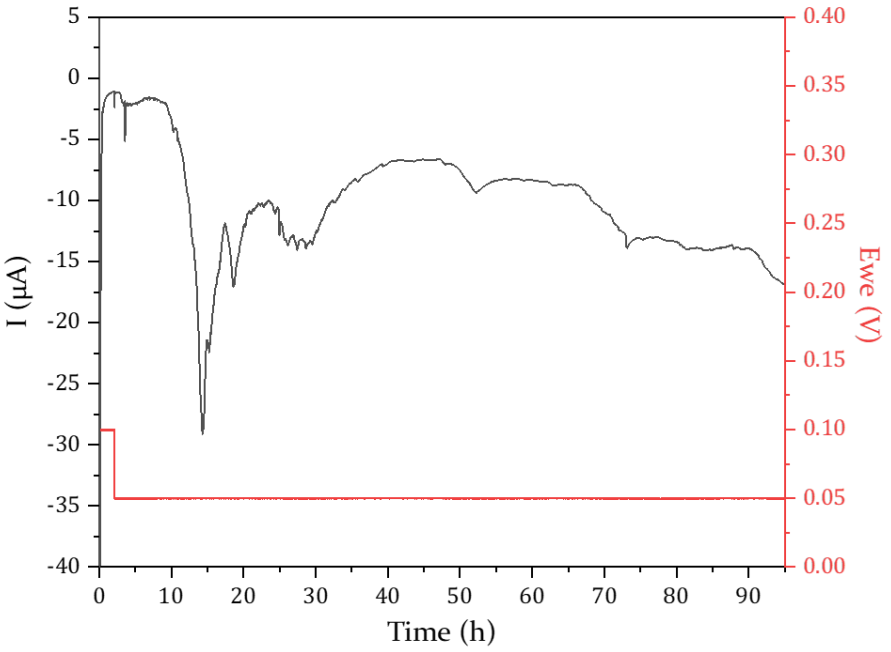

Figure S66. Chronoamperogram of the electrodeposition of the dissolved titanium species (bottom) ; and table of the EDX measured values of the atomic part from Ti, Al, and Cl in the ionic liquid, the washed, and the unwashed electrodeposit (top).

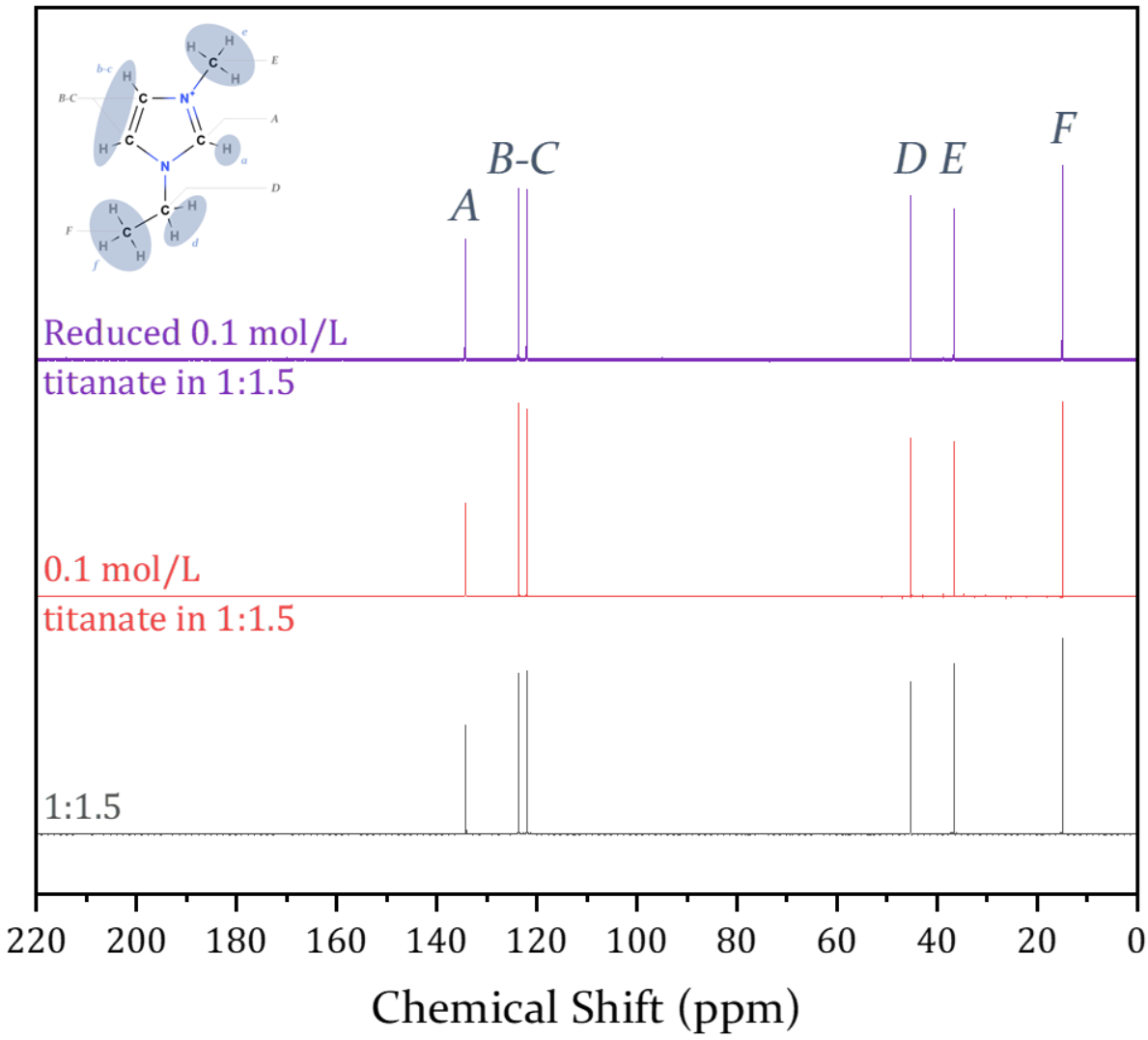

Figure S67. Full ^{13}C NMR spectra of the pristine ionic liquid (black), the ionic liquid after the dissolution of 0.1 mol/L titanate (red), and the ionic liquid after the electrodeposition(purple).

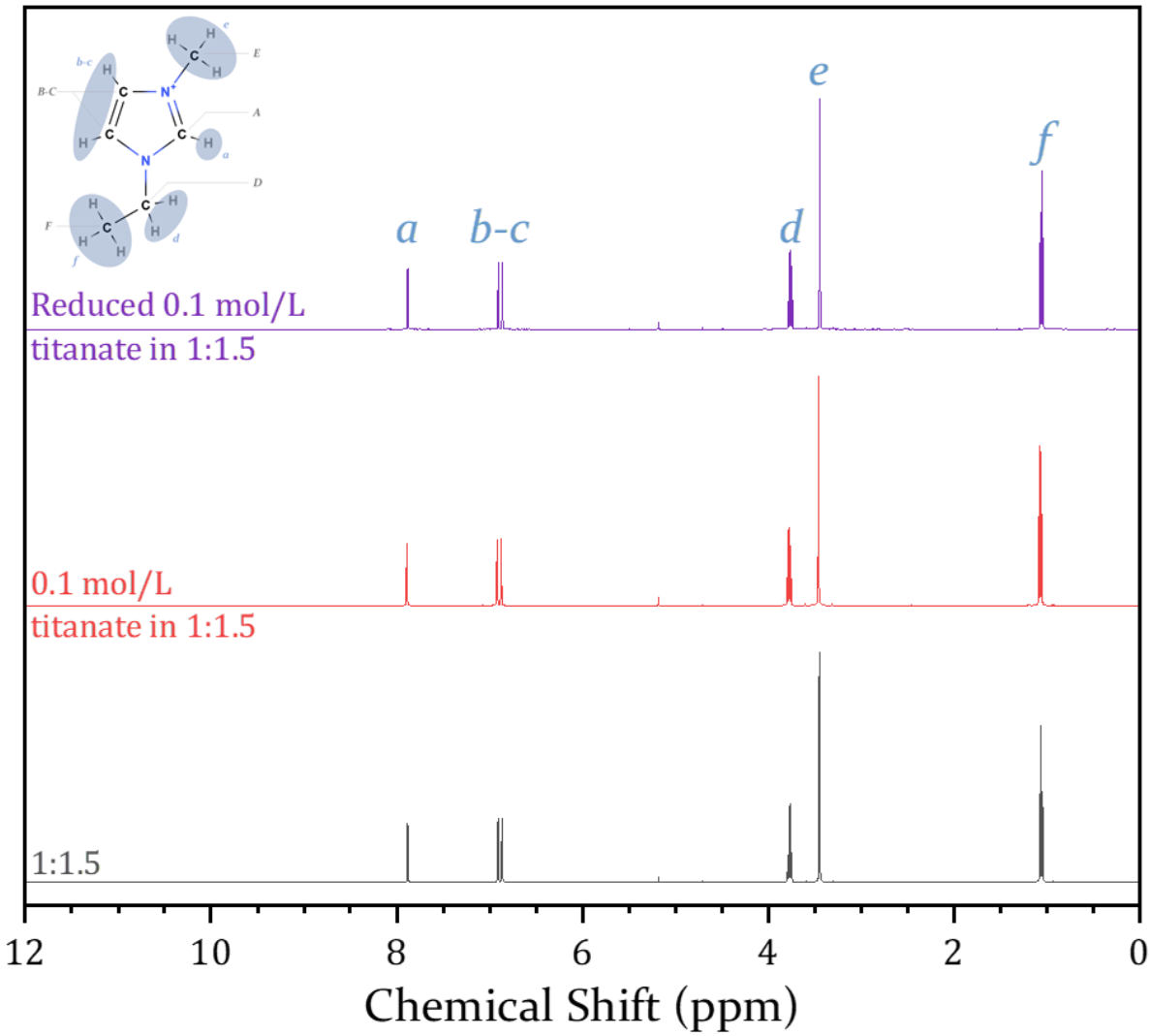

Figure S68. Full ^{1}H NMR spectra of the pristine ionic liquid (black), the ionic liquid after the dissolution of 0.1 mol/L titanate (red), and the ionic liquid after the electrodeposition(purple).

Chapter 6. Comparative study of the electrochemical properties of titanate compounds

The electrochemical properties of the L-TiO_2 lepidocrocite-type titanate material have been investigated, in the 1:1.5 EMImCl:$AlCl_3$ ionic liquid. However, the dissolution of the lepidocrocite-type titanate material hinders further considerations. In this view, the electrochemical behaviour of closely related compounds is investigated. This part is therefore dedicated to study the synthesised anatase materials dA-TiO_2 and A-TiO_2, described in **Chapter 4**.

1. Anatases solubility in the acidic ionic liquid

As the L-TiO_2 titanate material is not stable in the acidic ionic liquid, the two anatase materials undergo a similar dissolution experiment (see **Chapter 5**). Therefore, the synthesised titanate materials were introduced into the 1:1.5 EMImCl:$AlCl_3$ ionic liquid, at a 10g/L concentration, and were regularly stirred. After a week, no noticeable change was reported in the systems. After a month, the white powders were still observable at the bottom of the vials. Then, Raman spectra of the liquid phase of the mix were collected and are shown in **Figure 69.**.

This experiment shows that anatases do not dissolve inside the chloroaluminate ionic liquid. Indeed in **Figure 69.**, the samples containing the dA-TiO_2 and the A-TiO_2 materials exhibit spectra that mostly superpose with the pristine 1:1.5 ionic liquid. Nonetheless, the defective anatase sample displays two small signals at 380 cm^{-1} and 385 cm^{-1}. These peaks are the main Raman signature of the dissolved titanium complexes. This is evidence of a slight solubility of the dA-TiO2 material. Notably, the monomer ion peak remained unchanged across the four spectra. An estimation of the amount of dissolved species in the ionic liquid is left attempted here.

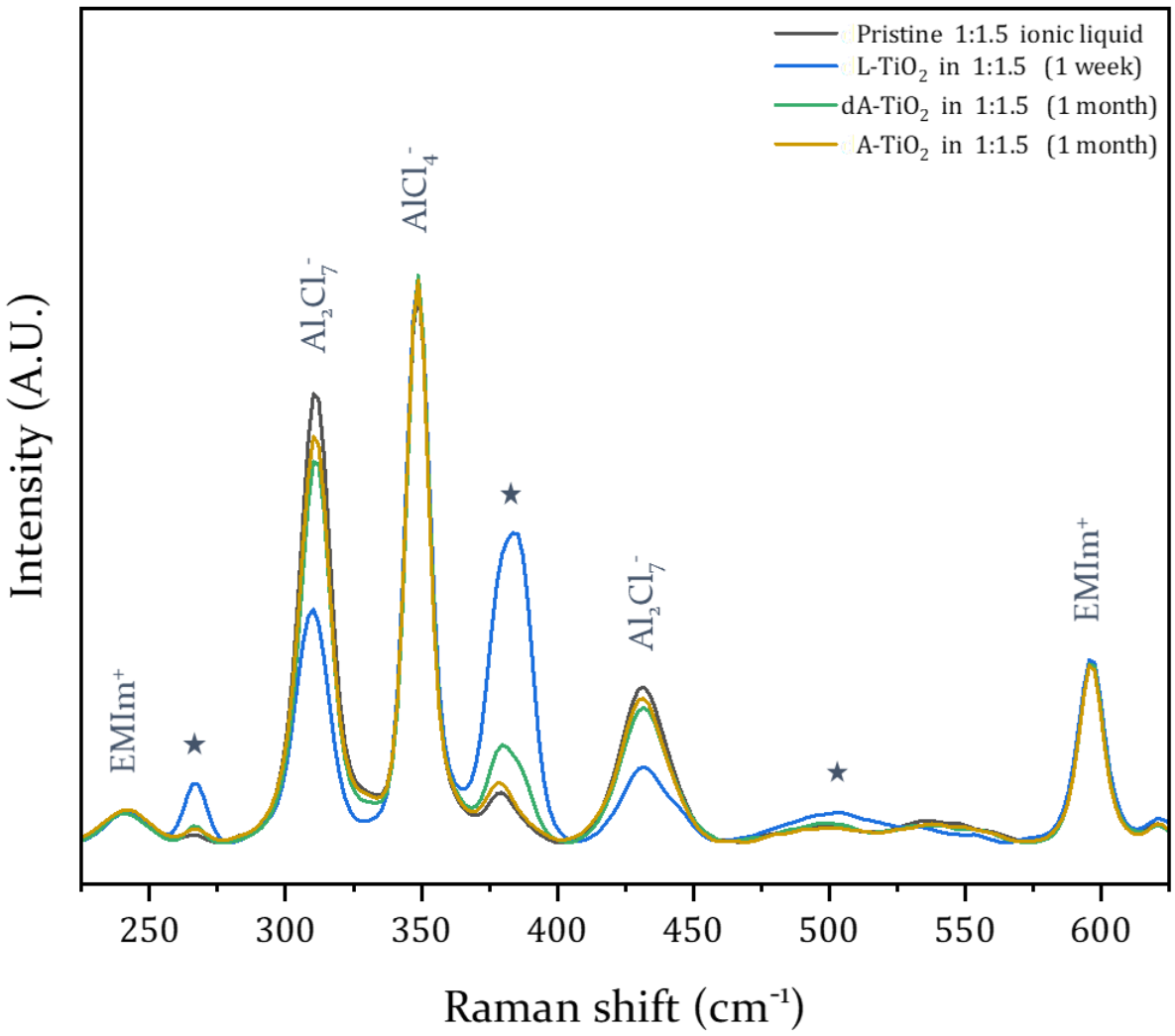

Figure 69. Raman spectra of the dissolution experiments of the L-TiO_2 lepidocrocite-type titanate (blue), the dA-TiO_2 defective anatase (green), and the A-TiO_2 pure anatase (golden) materials, in the 1:1.5 EMImCl:$AlCl_3$ ionic liquid. The spectrum of the pristine 1:1.5 ionic liquid is added as a reference. The star marks indicate signals due to the titanium material dissolution.

As described in **Chapter 4**, the main structural difference between the dA-TiO_2 and the A-TiO_2 materials resides in the presence of cationic vacancies. Indeed, the dA-TiO_2 material ($Ti_{0.83}\square_{0.17}O_{1.32}(OH)_{0.68}$) presents numerous titanium vacancies in the structure, in contrast to the pure A-TiO_2 anatase. Consequently, the slight solubility of the dA-TiO_2 materials is understood to mainly be due to the presence of these titanium vacancy sites.

2. Electrochemical properties of the anatase materials

The electrochemical response of the anatase materials was first investigated by galvanostatic cycling, in the Swagelok cell configuration. **Figure 70.** presents the first discharge-charge cycle of the three synthesised titanate materials.

The shape of the obtained discharge-charge curves resembles the one of the lepidocrocite-type titanate. The three electrode materials exhibit sloppy curved discharges, and S-shaped charges. Nonetheless, the two anatase materials displayed lower capacities than the defective lepidocrocite-type titanate material. The exact specific capacity values are provided in the table joined in **Figure 70.**. Notably, the first-cycle reversibility of the two anatase materials is similar, at about 74%. This value is low, compared to the 88% reversibility of the L-TiO_2.

Wang et al. studied anatase electrodes in a chloroaluminate electrolyte [87]. They showed the direct dependency, between the obtained capacity and the electrode material particle size, in the case of anatase electrodes. Here, the particle size of the three materials have been measured to be of the same order [152]. This size effect is therefore minimized.

Instead, the obtained capacity discrepancy is attributed to structural properties. Inside the A-TiO_2 material, only the anatase interstitial sites can contribute to the host ion for intercalation. In comparison, inside the dA-TiO_2 material, additional insertion sites are provided by the cationic vacancies. The enhanced specific capacity retrieved by the defective anatase, in regards to the pure anatase, is therefore attributed to these additional sites. On the other hand, the L-TiO_2 is amorphous, exhibits water interlayers, and counts more vacancies than the defective anatase material. Hence, the specific capacity reached by the L-TiO_2 material is even higher than the dA-TiO_2 material.

The effect of the electrochemical treatment on the titanate structure has been probed by NMR spectroscopy. **Figure 71.** displays the evolution of collected ^1H spectra of L-TiO_2 and dA-TiO_2 material electrodes, before and after the galvanostatic discharge.

	90°C Lepidocrocite-type titanate	110°C Defective anatase	150°C Pure anatase
Formula	$Ti_{1,5}\square_{0,5}O_2(OH)_2{\cdot}0{,}55H_2O$	$Ti_{0,83}\square_{0,17}O_{1,32}(OH)_{0,68}$	TiO_2
Theoretical capacity Q_{th} (mAh/g)	272	307	334
Discharge capacity Q_{dis} (mAh/g)	318	203	81
Charge capacity Q_{cha} (mAh/g)	277	152	59
Reversibility (%)	87,1	74,9	72,8

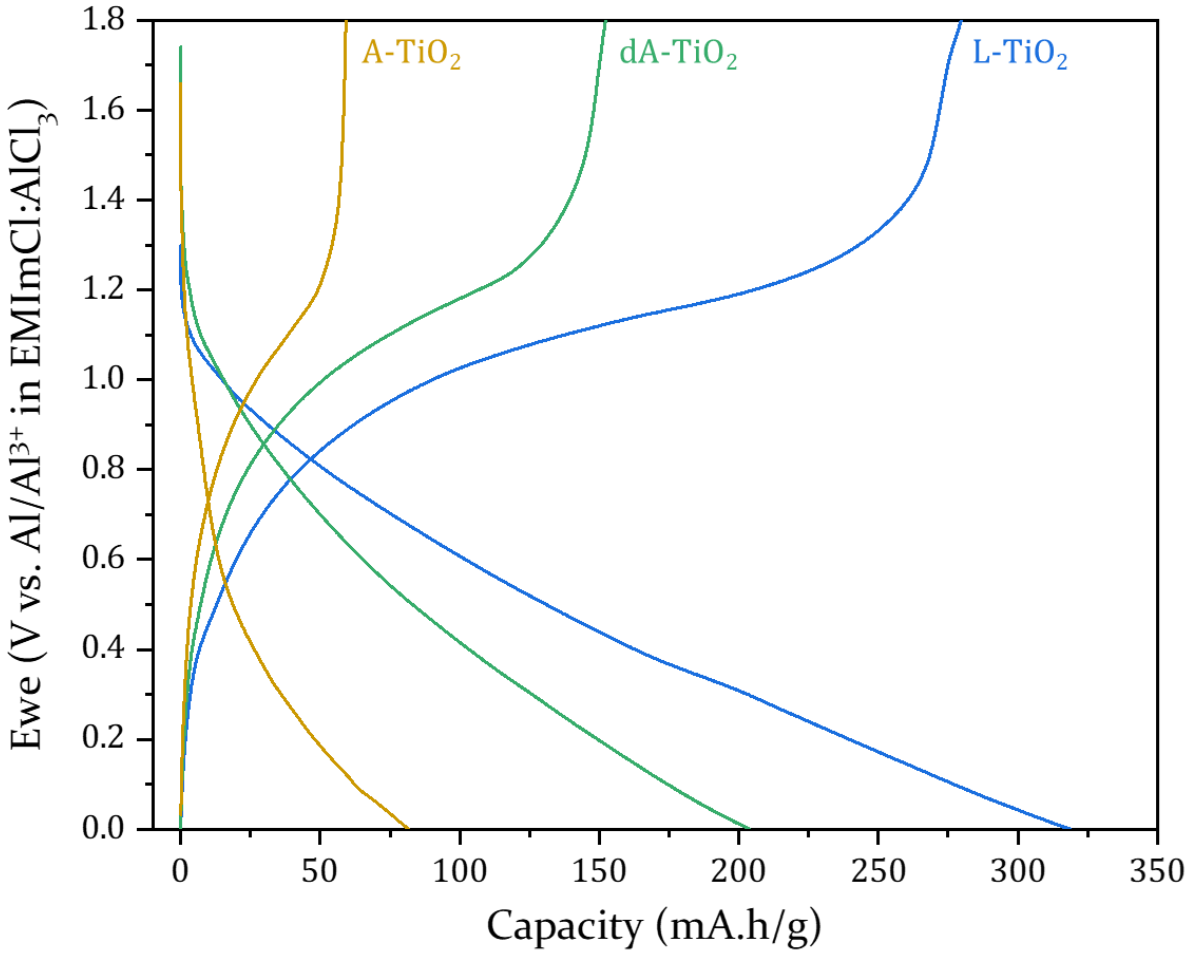

Figure 70. The first cycle of the 20mA/g galvanostatic discharge-charge cycling, using the L-TiO_2 lepidocrocite-type titanate material (blue), the dA-TiO_2 defective anatase material (green), and the A-TiO_2 pure anatase material (golden) as the working electrode. The table joined atop summarises the main data extracted from the galvanograms.

As described in **Chapter 4**, the ^{1}H spectrum of the defective anatase material resembles the one of the lepidocrocite-type titanate material. Peaks are observable in three main regions, corresponding to 1-, 2-, and 3-fold coordination modes of the hydroxyl groups around the titanium vacancies. The most intense peak is the one of the single coordination mode at 1.19 ppm.

After the galvanostatic discharge, the most intense contribution is observed to transition from a single to a twice-coordinated mode. Indeed, the 1.19 ppm peak is heavily diminished, and new peaks have been enhanced at 0.36 ppm, 1.71 ppm, 4.27 ppm, 7.69 ppm, 8.87 ppm, 10.39 ppm, and 11.42 ppm. Notably, these peaks can be distinguished due to the long-range order exhibited in the defective anatase material, in contrast to the spectrum of the amorphous L-TiO_2 material that only shows broad peaks. Overall, the defective anatase material spectrum resembles the one of the lepidocrocite-type titanate.

In addition, **Figure 71.** also shows the result of the ^{27}Al NMR spectroscopy that has been performed on a discharged dA-TiO_2 electrode sample. Notably, the dA-TiO_2 spectrum displays a pollution signal around 100 ppm. This is attributed to traces of the unwashed chloroaluminate electrolyte on the electrode sample.

Similar to the ^{1}H spectrum, the ^{27}Al spectrum of the dA-TiO_2 electrode sample closely resembles the one of the L-TiO_2 material. Therefore, three main signals are observable, and are ascribed to various coordination modes adopted by the inserted aluminium ions. Aluminium presents 4-, 5-, and 6-fold coordination modes in the probed material, the latter being the predominant mode. Notably, the signal-over-noise ratio of the spectrum is lower than the one of the L-TiO_2. This indicates that fewer amount of aluminium species are inserted inside the dA-TiO_2 material, matching the discrepancy in specific capacity observed in **Figure 70.**. Furthermore, inside both the dA-TiO_2 and the L-TiO_2 materials, the only sites for the aluminium species to experience the same local environments are inside the titanium vacancies. This further validates the favoured role of these defects in the electrochemical aluminium intercalation.

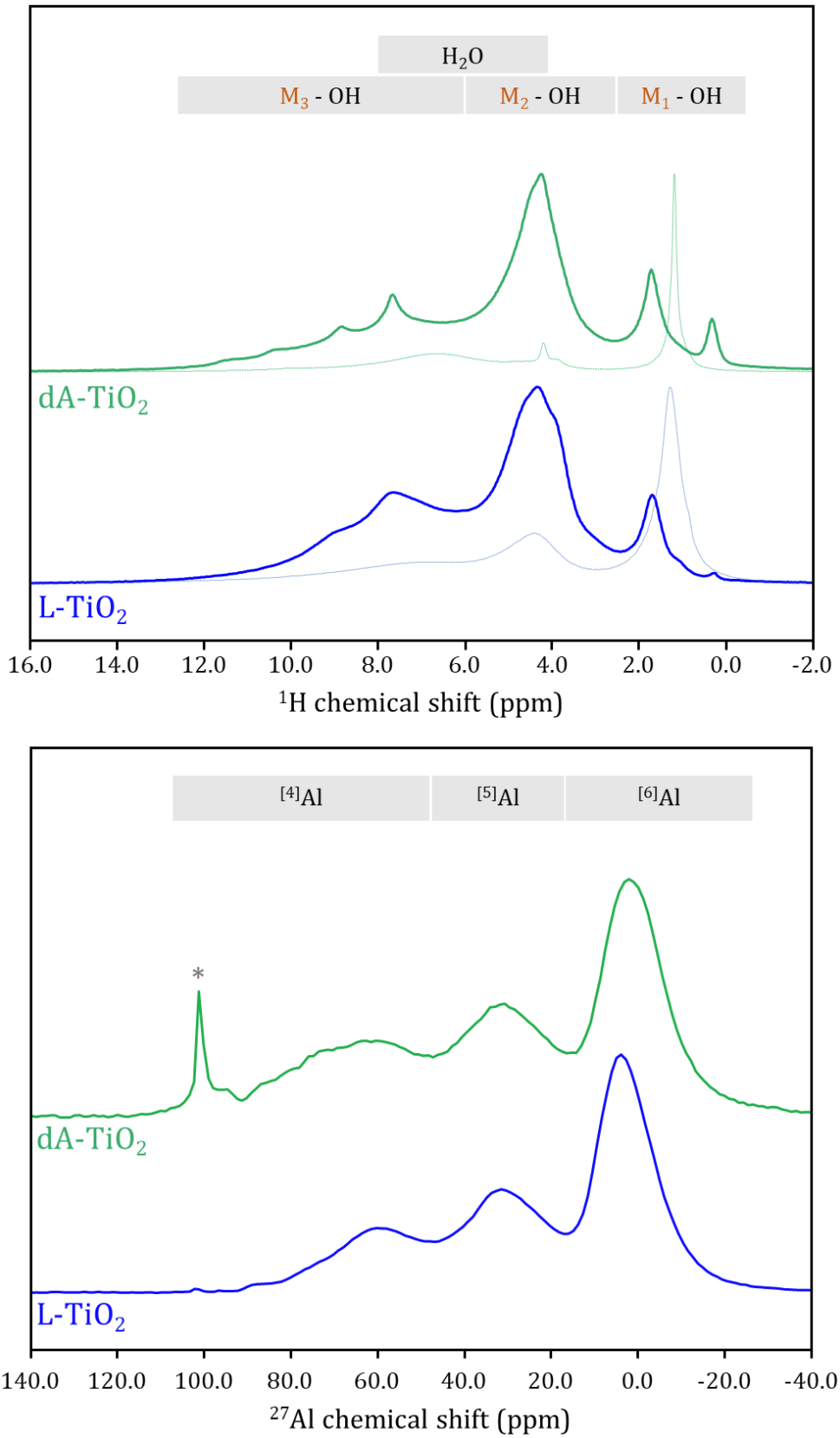

Figure 71. ^{1}H (top) and ^{27} Al (bottom) NMR spectra of fully discharged electrode materials. The dA-TiO_2 defective anatase (green) and the L-TiO_2 lepidocrocite-type titanate (blue) materials are displayed. Dotted lines refer to the respective pristine materials. Coordination modes of the probed groups are provided as a range of chemical shifts.

3. Evolution of the electrochemical profile

The electrochemical stability of the anatase materials is analysed by multiple galvanostatic discharge-charge cycling. **Figure 72.** presents the first, fifth, and tenth cycles of dA-TiO_2 and A-TiO_2 electrodes, in regard to the L-TiO_2 material. A comparative display of each cycle of these three materials is also provided in **Figure S74.**.

Among the three electrode materials, the pure anatase A-TiO_2 displayed the lowest first discharge capacity at 81 mAh/g. With cycling, the capacity is observed to slowly decrease. On the tenth cycle, the obtained discharge capacity is 46 mAh/g, which corresponds to a capacity retention of 57%. Notably, no change in the discharge-charge profile is observable. Those capacities are within the range of the analogous anatase-based systems reported [14,87].

During its first cycle, the defective anatase dA-TiO_2 material displayed sloppy discharge-charge curves, reaching a 203 mAh/g discharge capacity. Then, the profile is observed to quickly change. Indeed, most of the capacity is lost, as the capacity retention is about 14% on the tenth cycle. Notably, two events appeared on the discharge profile, at 1.05 V and 0.30 V, since the fifth cycle.

From these observations, the cycling response of the dA-TiO_2 material resembles the one of the L-TiO_2 materials (see **Chapter 5**). Indeed, the lepidocrocite-type titanate material accused a similar capacity fade, with a capacity retention of only 3% on the tenth cycle. For L-TiO_2, the apparition of events along the electrochemical profile was ascribed to surface redox reactions of the dissolved titanium species. However, this is unlikely for the defective anatase material, as only a sparse amount was observed to be dissolved after a month in the ionic liquid, in **Figure 69.**. For this reason, the origin of these events apparition is still unknown.

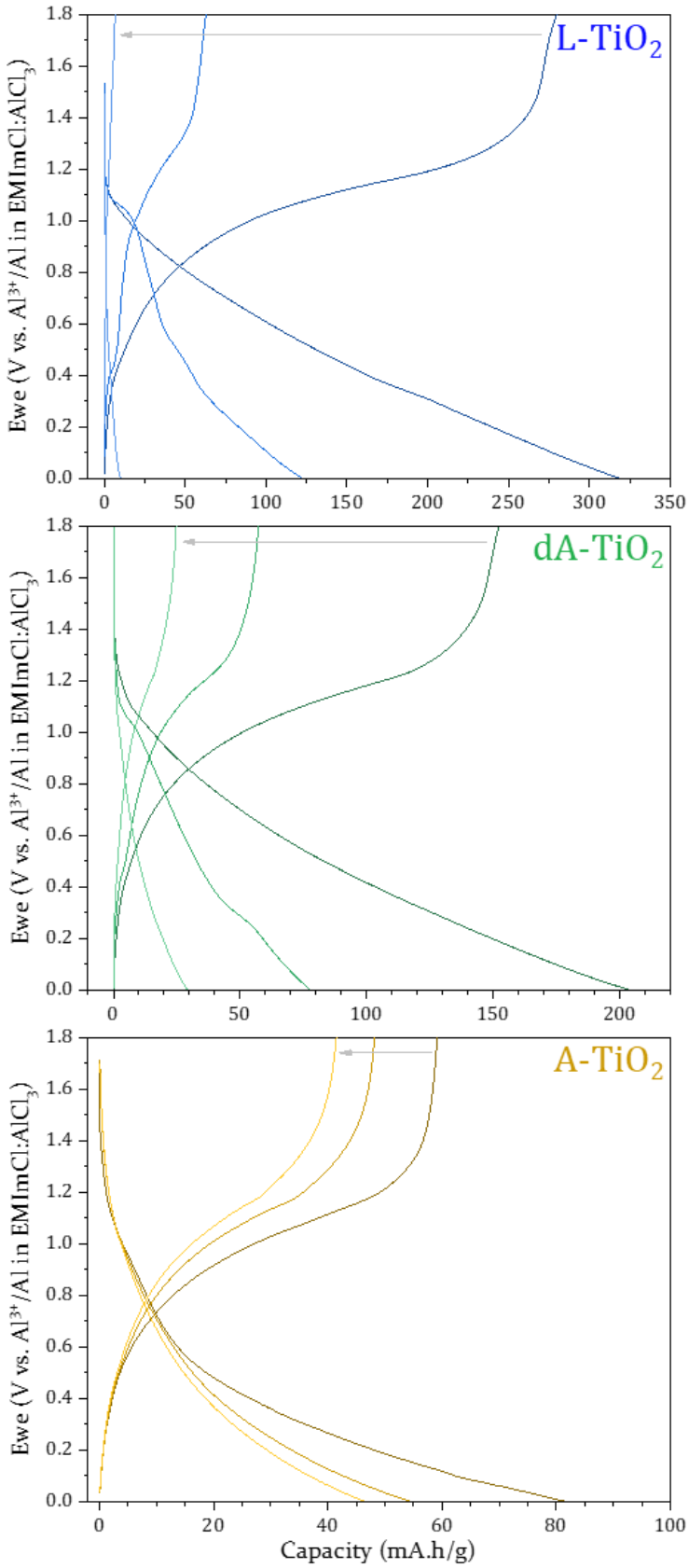

Figure 72. Ten cycles of 20 mA/g galvanostatic discharge-charge cycling, were performed on the L-TiO_2 lepidocrocite-type titanate (blue), the dA-TiO_2 defective anatase (green), and the A-TiO_2 pure anatase (golden) materials. Only the first (dark), fifth (medium), and tenth (light) cycles are displayed. The grey arrows indicate the experimental progression direction.

The evolution of the electrochemical response of the dA-TiO_2 material is further investigated by cyclic voltammetry. A CV has therefore been performed on each electrode material sample, and results are given in **Figure S75.**. In addition, **Figure 73.** displays a superposition of the first, third, fifth, and tenth cycles of the so-performed CV. The L-TiO_2 and the A-TiO_2 materials are considered as references here.

The profile of the pure anatase electrode remained quite stable during the cycling. A small reductive peak is observed at 1.00 V, and a diffuse response spans from 0.70 V to 0.00 V. The oxidation is similarly diffuse, with a small distinguishable peak at 0.46 V, and two intense peaks at 1.14 V and 1.21 V.

On the first cycle, the voltammogram of the dA-TiO_2 material closely resembles the one of the L-TiO_2 materials. And similar to the previous observations made, both their signals are diminished during the cycling, and in the same manner. Indeed, for both the diffuse profile is lost in favour of more defined redox peaks. Notably, the dA-TiO_2 voltammogram diverges from the one of the L-TiO_2, from the fifth cycle on: a 1.14 V oxidative peak becomes observable, next to the former 1.21 V peak. This couple of peaks is the signature of the A-TiO_2 anatase material. On the tenth cycle, the voltammogram of the defective anatase material is identical to the one of the pure anatase, yet with a lower intensity.

Therefore, throughout the cycling, the electrochemical response of the dA-TiO_2 material is observed to transition from the intercalation response of a defective material, to the typical anatase response. The voltammogram of the tenth cycle is considered to be the total contribution of the interstitial sites of the anatase phase. In contrast, the signal lost during the cycling was understood to be the contribution of the defective sites. The capacity fade observed, when cycling the dA-TiO2 material, is thus attributed to an inactivation of the vacancy sites mechanism. This mechanism can occur through various means (such as the irreversible intercalation of aluminium ions inside the titanium vacancies, etc ...), and would need supplementary analyses in order to be characterised.

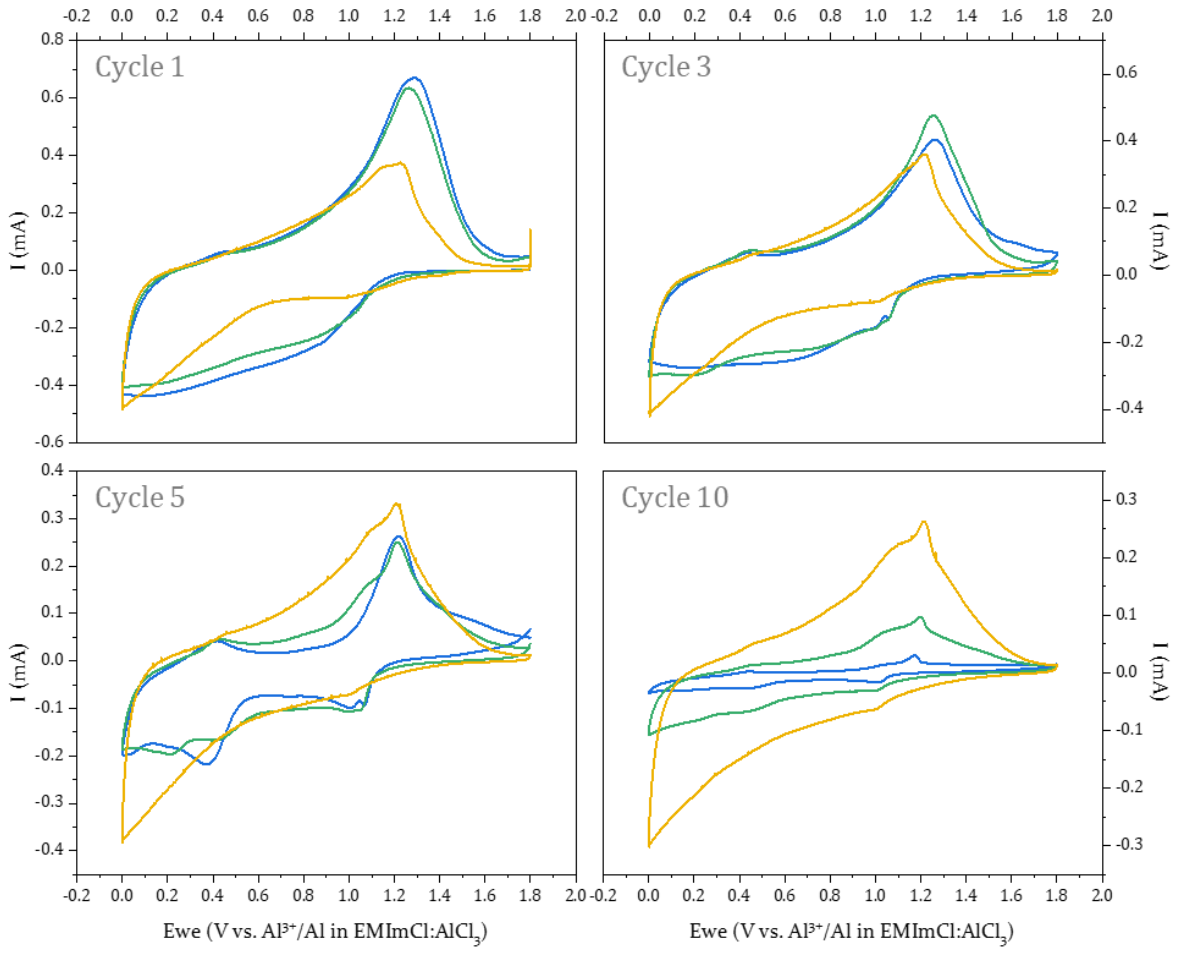

Figure 73. Voltammograms of the first, third, fifth, and tenth cycles of a 0.5 mV/s cyclic voltammetry, performed on the L-TiO_2 lepidocrocite-type titanate (blue), the dA-TiO_2 defective anatase (green), and the A-TiO_2 pure anatase (golden) materials.

Conclusion

In this chapter, the chemical and electrochemical properties of the synthetized anatase materials were analysed, in regards to the L-TiO_2 lepidocrocite-type titanate material. The stability of the anatase phase was asserted in the 1:1.5 EMImCl:$AlCl_3$ ionic liquid, as no dissolution was witnessed. The electrochemical intercalation of the aluminium ions have also been verified to occur in the anatase materials. The close resemblance between the aluminium insertion environments, inside the dA-TiO_2 and the L-TiO_2 material, led to the validation of the titanium vacancies as the intercalation site of these aluminium ions. Therefore contributions, from both the interstitial sites of the anatase phase and the vacancy sites from the defective materials, are understood to participate in the electrochemical responses monitored. Nevertheless, the capacity obtained from the dA-TiO_2 material suffers from the same dramatic capacity drop, as the L-TiO_2 counterpart. This is notably not observed for the A-TiO_2 pure anatase material. A reaction, disabling the titanium vacancies, is then hypothesised to occur during the electrochemical cycling. However, more characterisation is still needed in order to understand the different mechanisms occurring at the electrode in these systems.

Supplementary information

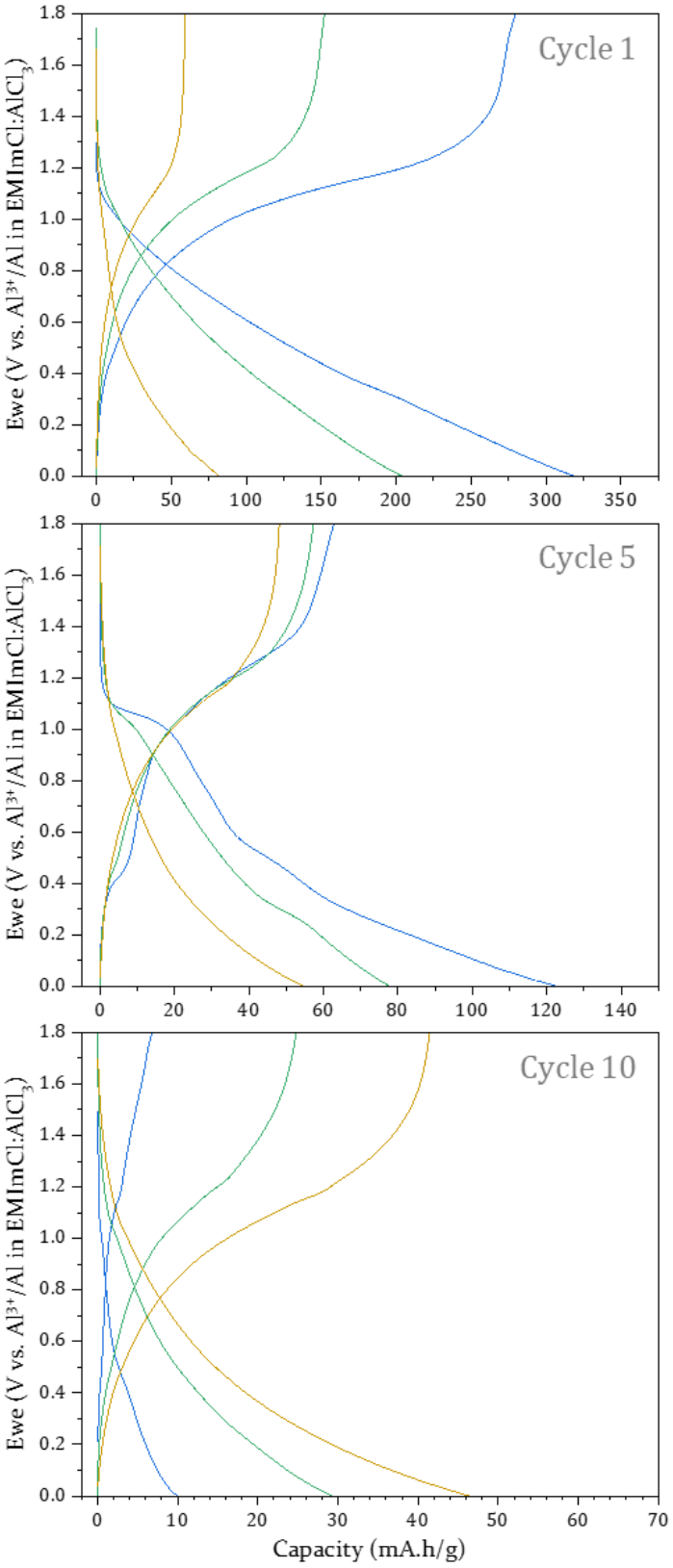

Figure S74. First (top), fifth (middle), and tenth (bottom) cycles of a 20 mA/g galvanostatic cycling of the L-TiO_2 lepidocrocite-type titanate (blue), the dA-TiO_2 defective anatase (green), and the A-TiO_2 pure anatase (golden) electrodes.

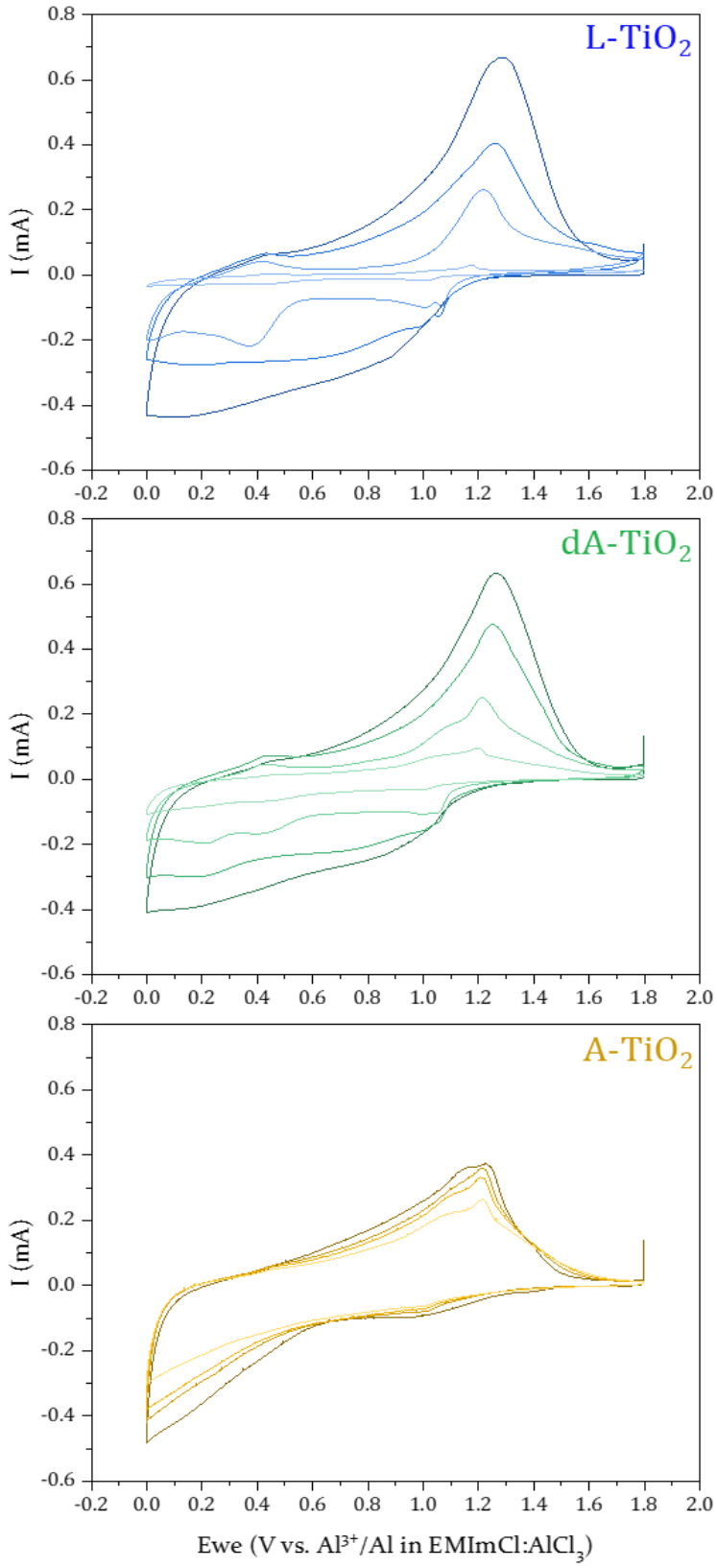

Figure S75. Cyclic voltammetries of a 90°C lepidocrocite-type titanate electrode (blue), a 110°C defective anatase electrode (green), and a 150°C pure anatase (golden) electrode, performed at 0.5 mV/s. The first, third, fifth, and tenth cycles are displayed from darker to lighter.

General conclusion

Among the beyond-lithium battery systems, the aluminium-ion battery appears particularly promising. Indeed, the high theoretical specific capacity of the aluminium ion Al^{3+} (8.05 Ah/cm^3), coupled with the fact that aluminium is the most abundant metal on earth, make Al-ion systems appropriate to take over the Li-ion systems. However, the high polarising power of the Al^{3+} ion makes the development of this battery system challenging. The main issue encountered comes from the need to design positive electrode material that reversibly intercalates the Al^{3+} ion. In addition, the electrolytes for aluminium ion delivery are highly acidic, being mainly based on the $AlCl_3$ chemistry.

This work has then shown the use of defective and amorphous materials, for the intercalation of the challenging multivalent aluminium ion, from an acidic chloroaluminate ionic liquid. **Figure 76.** visually summarises the realised investigations.

The main electrolyte for an Al-ion battery, used in the literature, the acidic EMImCl:$AlCl_3$ ionic liquid, has been studied in this work. The speciation has been described, as a function of the aluminium chloride in the ionic mix. The anionic species of $Al_nCl_{3n+1}^-$ are usually reported, with n ranging from 0 to 2. Nonetheless, molecular dynamics calculations showed that higher oligomeric species are dynamically formed, albeit for short lifespans. These oligomeric anionic species are particularly of interest as they are the electrochemically active species in the electrolyte. In addition, structural features have been observed in the EMImCl:$AlCl_3$ ionic liquids, by high energy X-ray total scattering measurements. Internal structurations were finally revealed by NMR spectroscopy, to be due to interactions between the anionic and cationic species. It is yet unknown how these structurations influence the aluminium diffusion through the liquid, nor how they evolve at the electrode interface.

Various titanate electrode materials have been synthesized. The simple sol-gel synthesis route, developed by Ma et al. [95], allowed to change the structural features of the produced titanate materials. Charge compensation and incomplete condensation led to the stabilisation of cationic vacancies within the titanate structure. Further control of the synthesis temperature alters the resulting crystallinity. Indeed, the material synthesised at the lower temperature (L-TiO_2) is an amorphous defective titanate material. Refinement performed on high energy X-ray total scattering measurements revealed the amorphous structure to be derivative of a layered water-stabilized lepidocrocite-type phase $Ti_{1.5}\square_{0.5}O_2(OH)_2{\cdot}0.7H_2O$. In contrast, a synthesis at a higher temperature stabilised a crystalline defective anatase material (dA-TiO_2) $Ti_{0.83}\square_{0.17}O_{1.32}(OH)_{0.68}$. Eventually, the synthesis at the highest temperature provides the system enough energy to fully condensate into pure anatase (A-TiO_2).

The firsts electrochemical measurements were performed on a cell, using the amorphous lepidocrocite-type material as the positive electrode, and the acidic 1:1.5 EMImCl:$AlCl_3$ ionic liquid as the electrolyte. High 318 mAh/g and 277 mAh/g specific capacities were obtained during the first discharge-charge cycle. During this cycle, ionic species of aluminium were monitored to insert into the electrode material. However, reversibility was not achieved, as the aluminium remained inside the electrode after the cell charge. On the following discharge-charge cycles, the recorded capacity quickly dropped. Barely no capacity is observed after the tenth cycle. The capacity fade is joined with changes in the electrochemical response profile. Indeed, the diffuse solid-solution behaviour observed during the first cycles, is progressively converted into surface redox signals. This cell mechanism alteration is due to the solubility of the electrode material in the acidic electrolyte. Indeed, auxiliary tests showed a spontaneous total dissolution of the material in the 1:1.5 ionic liquid. The dissolution products are titanium chloride-based complexes, that happen to also be electrochemically active. Eventually, the surface redox reactions are stopped, as the insoluble $TiCl_3$ species are formed, preventing the reactive titanium supply from the electrode.

The following electrochemical experiments were realised, using the anatase materials of the positive electrode. Only a few dissolution signals were observed in the case of the defective anatase material, while the pure anatase was tested to resist the dissolution in the acidic electrolyte. When tested, these materials showed lesser capacities than the amorphous titanate one, at 203 mAh/g and 81 mAh/g for the defective and the pure anatase material first discharges respectively. Upon the next cycles, the capacity of the pure anatase material decreases slowly, whereas the defective anatase exhibits a capacity drop similar to the one of the amorphous titanate material. In addition, the examination of the discharge-charge profile of the defective anatase material showed a similar behaviour to the lepidocrocite-type derivative material, during the first cycles. Nonetheless, as the electrode material was not dissolved, the latter cycles profile resembles the ones of the pure anatase electrode. It is although still unknown if the capacity drop of the defective anatase material results from the structural stress of the aluminium insertion, or from the deactivation of its insertion sites.

Nevertheless, the comparison between these three materials allowed to determine the insertion sites of the aluminium species. Indeed, the defective anatase shares the cationic vacancy site with the amorphous titanate, and the interstitial sites with the pure anatase material. The ^{27}Al NMR spectrum of the defective anatase material, being similar to the amorphous titanate material one, verified the insertion of the aluminium species inside the cationic vacancy sites.

Overall, side reactions and solubility of the electrode material prevented any further considerations. In order to harness the high specific capacities of the materials, research should therefore focus on the development of less constraining electrolytes for the aluminium ion battery. Otherwise, a deeper understanding of the dissolution processes and other interactions between the electrode and the electrolyte is mandatory to develop viable aluminium batteries.

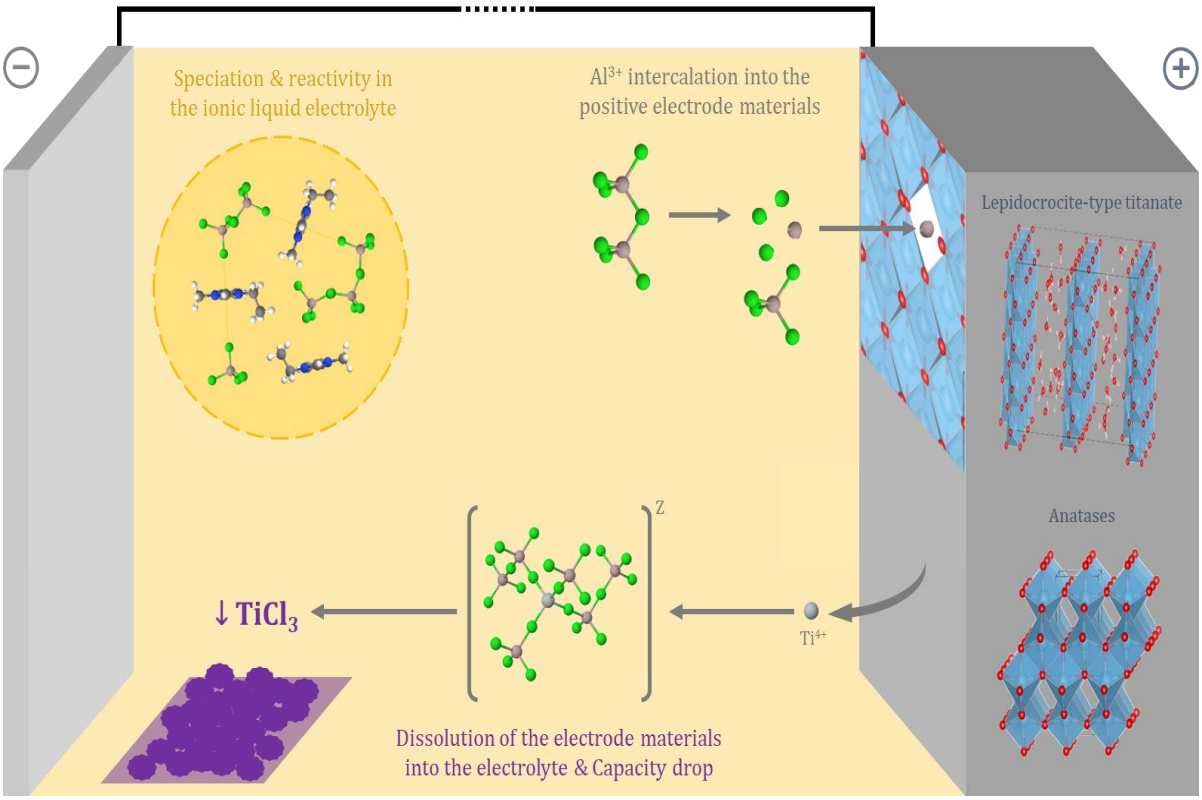

Figure 76. Visual scheme of the various structural, chemical, and electrochemical investigations performed on the proposed electrochemical system, using the titanate materials at the positive electrode and the 1:1.5 EMImCl:$AlCl_3$ ionic liquid as the electrolyte.

List of Figures

References

(1) Saunders, H. D. The Khazzoom-Brookes Postulate and Neoclassical Growth. *The Energy Journal* **1992**, *13* (4), 131–148. https://doi.org/10.5547/ISSN0195-6574-EJ-Vol13-No4-7.

(2) Davenport, J.; Wayth, N. Statistical Review of World Energy.Pdf, 2023.

(3) Intergovernmental Panel on Climate Change (IPCC). *Climate Change 2021 – The Physical Science Basis: Working Group I Contribution to the Sixth Assessment Report of the Intergovernmental Panel on Climate Change*; Cambridge University Press: Cambridge, 2023. https://doi.org/10.1017/9781009157896.

(4) United Nations. Paris Agreement, 2015.

(5) European Commission. Joint Research Centre. *RMIS, Raw Materials in the Battery Value Chain: Final Content for the Raw Materials Information System : Strategic Value Chains : Batteries Section*; Publications Office: LU, 2020.

(6) Karduri, R. K. R. Cobalt in Battery Production: Implications for the Mining Community. *SSRN Journal* **2023**. https://doi.org/10.2139/ssrn.4636499.

(7) Maskuroh, N.; Widyanty, W.; Nurhidajat, R.; Wardhana, I. W.; Fahlevi, M. Green Human Resource Management and Green Supply Chain Management on Sustainable Performance of Nickel Mining Companies in Indonesia. *10.5267/j.uscm* **2023**, *11* (1), 203–212. https://doi.org/10.5267/j.uscm.2022.10.006.

(8) Banza Lubaba Nkulu, C.; Casas, L.; Haufroid, V.; De Putter, T.; Saenen, N. D.; Kayembe-Kitenge, T.; Musa Obadia, P.; Kyanika Wa Mukoma, D.; Lunda Ilunga, J.-M.; Nawrot, T. S.; Luboya Numbi, O.; Smolders, E.; Nemery, B. Sustainability of Artisanal Mining of Cobalt in DR Congo. *Nat Sustain* **2018**, *1* (9), 495–504. https://doi.org/10.1038/s41893-018-0139-4.

(9) Mudd, G. M. Sustainable/Responsible Mining and Ethical Issues Related to the Sustainable Development Goals. *SP* **2021**, *508* (1), 187–199. https://doi.org/10.1144/SP508-2020-113.

(10) Leung, O. M.; Schoetz, T.; Prodromakis, T.; Ponce De Leon, C. Review—Progress in Electrolytes for Rechargeable Aluminium Batteries. *J. Electrochem. Soc.* **2021**, *168* (5), 056509. https://doi.org/10.1149/1945-7111/abfb36.

(11) Lin, Z.; Mao, M.; Yang, C.; Tong, Y.; Li, Q.; Yue, J.; Yang, G.; Zhang, Q.; Hong, L.; Yu, X.; Gu, L.; Hu, Y.-S.; Li, H.; Huang, X.; Suo, L.; Chen, L. Amorphous Anion-Rich Titanium Polysulfides for Aluminum-Ion Batteries. *Sci. Adv.* **2021**, *7* (35), eabg6314. https://doi.org/10.1126/sciadv.abg6314.

(12) Kang, S.; Reeves, K. G.; Koketsu, T.; Ma, J.; Borkiewicz, O. J.; Strasser, P.; Ponrouch, A.; Dambournet, D. Multivalent Mg^{2+}, Zn^{2+}, and Ca^{2+} Ion Intercalation Chemistry in a Disordered Layered Structure. *ACS Appl. Energy Mater.* **2020**, *3* (9), 9143–9150. https://doi.org/10.1021/acsaem.0c01530.

(13) Reeves, K. G.; Ma, J.; Fukunishi, M.; Salanne, M.; Komaba, S.; Dambournet, D. Insights into Li^+, Na^+, and K^+ Intercalation in Lepidocrocite-Type Layered TiO_2 Structures. *ACS Appl. Energy Mater.* **2018**, *1* (5), 2078–2086. https://doi.org/10.1021/acsaem.8b00170.

(14) Koketsu, T.; Ma, J.; Morgan, B. J.; Body, M.; Legein, C.; Dachraoui, W.; Giannini, M.; Demortière, A.; Salanne, M.; Dardoize, F.; Groult, H.; Borkiewicz, O. J.;

Chapman, K. W.; Strasser, P.; Dambournet, D. Reversible Magnesium and Aluminium Ions Insertion in Cation-Deficient Anatase TiO2. *Nature Mater* **2017**, *16* (11), 1142–1148. https://doi.org/10.1038/nmat4976.
(15) Borah, R.; Hughson, F. R.; Johnston, J.; Nann, T. On Battery Materials and Methods. *Materials Today Advances* **2020**, *6*, 100046. https://doi.org/10.1016/j.mtadv.2019.100046.
(16) Manthiram, A. An Outlook on Lithium Ion Battery Technology. *ACS Cent. Sci.* **2017**, *3* (10), 1063–1069. https://doi.org/10.1021/acscentsci.7b00288.
(17) Gajan, A.; Lucas, I. Le stockage de l'énergie électrochimique en technologie Lithium-ion, 2021. https://cnrs.hal.science/hal-04021376.
(18) Xiao, J.; Li, Q.; Bi, Y.; Cai, M.; Dunn, B.; Glossmann, T.; Liu, J.; Osaka, T.; Sugiura, R.; Wu, B.; Yang, J.; Zhang, J.-G.; Whittingham, M. S. Understanding and Applying Coulombic Efficiency in Lithium Metal Batteries. *Nat Energy* **2020**, *5* (8), 561–568. https://doi.org/10.1038/s41560-020-0648-z.
(19) Rahman, Md. A.; Wang, X.; Wen, C. A Review of High Energy Density Lithium–Air Battery Technology. *J Appl Electrochem* **2014**, *44* (1), 5–22. https://doi.org/10.1007/s10800-013-0620-8.
(20) Elazari, R.; Salitra, G.; Garsuch, A.; Panchenko, A.; Aurbach, D. Sulfur-Impregnated Activated Carbon Fiber Cloth as a Binder-Free Cathode for Rechargeable Li-S Batteries. *Advanced Materials* **2011**, *23* (47), 5641–5644. https://doi.org/10.1002/adma.201103274.
(21) McDowell, M. T.; Lee, S. W.; Nix, W. D.; Cui, Y. 25th Anniversary Article: Understanding the Lithiation of Silicon and Other Alloying Anodes for Lithium-Ion Batteries. *Advanced Materials* **2013**, *25* (36), 4966–4985. https://doi.org/10.1002/adma.201301795.
(22) Leenheer, A. J.; Jungjohann, K. L.; Zavadil, K. R.; Harris, C. T. Phase Boundary Propagation in Li-Alloying Battery Electrodes Revealed by Liquid-Cell Transmission Electron Microscopy. *ACS Nano* **2016**, *10* (6), 5670–5678. https://doi.org/10.1021/acsnano.6b02200.
(23) Ye, Y.; Xie, H.; Yang, Y.; Xie, Y.; Lu, Y.; Wang, J.; Kong, X.; Jin, S.; Ji, H. Solid-Solution or Intermetallic Compounds: Phase Dependence of the Li-Alloying Reactions for Li-Metal Batteries. *J. Am. Chem. Soc.* **2023**, *145* (45), 24775–24784. https://doi.org/10.1021/jacs.3c08711.
(24) An, S. J.; Li, J.; Daniel, C.; Mohanty, D.; Nagpure, S.; Wood, D. L. The State of Understanding of the Lithium-Ion-Battery Graphite Solid Electrolyte Interphase (SEI) and Its Relationship to Formation Cycling. *Carbon* **2016**, *105*, 52–76. https://doi.org/10.1016/j.carbon.2016.04.008.
(25) Pinson, M. B.; Bazant, M. Z. Theory of SEI Formation in Rechargeable Batteries: Capacity Fade, Accelerated Aging and Lifetime Prediction. *J. Electrochem. Soc.* **2013**, *160* (2), A243–A250. https://doi.org/10.1149/2.044302jes.
(26) Kim, T.; Ono, L. K.; Qi, Y. Understanding the Active Formation of a Cathode–Electrolyte Interphase (CEI) Layer with Energy Level Band Bending for Lithium-Ion Batteries. *J. Mater. Chem. A* **2023**, *11* (1), 221–231. https://doi.org/10.1039/D2TA07565B.
(27) Yabuuchi, N.; Kubota, K.; Dahbi, M.; Komaba, S. Research Development on Sodium-Ion Batteries. *Chem. Rev.* **2014**, *114* (23), 11636–11682. https://doi.org/10.1021/cr500192f.

(28) Min, X.; Xiao, J.; Fang, M.; Wang, W. (Alex); Zhao, Y.; Liu, Y.; Abdelkader, Amr. M.; Xi, K.; Kumar, R. V.; Huang, Z. Potassium-Ion Batteries: Outlook on Present and Future Technologies. *Energy Environ. Sci.* **2021**, *14* (4), 2186–2243. https://doi.org/10.1039/D0EE02917C.
(29) Deivanayagam, R.; Ingram, B. J.; Shahbazian-Yassar, R. Progress in Development of Electrolytes for Magnesium Batteries. *Energy Storage Materials* **2019**, *21*, 136–153. https://doi.org/10.1016/j.ensm.2019.05.028.
(30) Arroyo-de Dompablo, M. E.; Ponrouch, A.; Johansson, P.; Palacín, M. R. Achievements, Challenges, and Prospects of Calcium Batteries. *Chem. Rev.* **2020**, *120* (14), 6331–6357. https://doi.org/10.1021/acs.chemrev.9b00339.
(31) Zhang, X.; Hu, J.; Fu, N.; Zhou, W.; Liu, B.; Deng, Q.; Wu, X. Comprehensive Review on ZINC-ION Battery Anode: Challenges and Strategies. *InfoMat* **2022**, *4* (7), e12306. https://doi.org/10.1002/inf2.12306.
(32) Liu, T.; Lv, G.; Liu, M.; Zhao, C.; Liao, L.; Liu, H.; Shi, J.; Zhang, J.; Guo, J. Cation-Intercalation and Conversion-Type Cathode Materials for Rechargeable Aluminum Batteries. *Mater. Chem. Front.* **2022**, *6* (3), 280–296. https://doi.org/10.1039/D1QM01267C.
(33) Li, C.; Hou, C.-C.; Chen, L.; Kaskel, S.; Xu, Q. Rechargeable Al-Ion Batteries. *EnergyChem* **2021**, *3* (2), 100049. https://doi.org/10.1016/j.enchem.2020.100049.
(34) Elia, G. A.; Kravchyk, K. V.; Kovalenko, M. V.; Chacón, J.; Holland, A.; Wills, R. G. A. An Overview and Prospective on Al and Al-Ion Battery Technologies. *Journal of Power Sources* **2021**, *481*, 228870. https://doi.org/10.1016/j.jpowsour.2020.228870.
(35) Das, S. K.; Mahapatra, S.; Lahan, H. Aluminium-Ion Batteries: Developments and Challenges. *J. Mater. Chem. A* **2017**, *5* (14), 6347–6367. https://doi.org/10.1039/C7TA00228A.
(36) Yang, H.; Li, H.; Li, J.; Sun, Z.; He, K.; Cheng, H.; Li, F. The Rechargeable Aluminum Battery: Opportunities and Challenges. *Angew Chem Int Ed* **2019**, *58* (35), 11978–11996. https://doi.org/10.1002/anie.201814031.
(37) Johnston, J. Aluminium-Ion Batteries A Solution to the Emerging Trillion Dollar Energy Storage Market. *The University of Newcastle* **2023**, 203.
(38) Holleck, G. L.; Giner, J. The Aluminum Electrode in $AlCl_3$-Alkali-Halide Melts. *J. Electrochem. Soc.* **1972**, *119* (9), 1161.
(39) Mamantov, G.; Torsi, G. Potentiometric Study of the Dissociation of the Tetrachloroaluminate Ion in Molten Sodium Chloroaluminates at 175-400.Deg. *Inorg. Chem.* **1971**, *10* (9), 1900–1902. https://doi.org/10.1021/ic50103a012.
(40) Lin, M.-C.; Gong, M.; Lu, B.; Wu, Y.; Wang, D.-Y.; Guan, M.; Angell, M.; Chen, C.; Yang, J.; Hwang, B.-J.; Dai, H. An Ultrafast Rechargeable Aluminium-Ion Battery. *Nature* **2015**, *520* (7547), 324–328. https://doi.org/10.1038/nature14340.
(41) Wang, D.-Y.; Wei, C.-Y.; Lin, M.-C.; Pan, C.-J.; Chou, H.-L.; Chen, H.-A.; Gong, M.; Wu, Y.; Yuan, C.; Angell, M.; Hsieh, Y.-J.; Chen, Y.-H.; Wen, C.-Y.; Chen, C.-W.; Hwang, B.-J.; Chen, C.-C.; Dai, H. Advanced Rechargeable Aluminium Ion Battery with a High-Quality Natural Graphite Cathode. *Nat Commun* **2017**, *8* (1), 14283. https://doi.org/10.1038/ncomms14283.

(42) Wang, S.; Yu, Z.; Tu, J.; Wang, J.; Tian, D.; Liu, Y.; Jiao, S. A Novel Aluminum-Ion Battery: Al/$AlCl_3$-[EMIm]Cl/Ni_3S_2@Graphene. *Advanced Energy Materials* **2016**, *6* (13), 1600137. https://doi.org/10.1002/aenm.201600137.
(43) Wang, S.; Kravchyk, K. V.; Filippin, A. N.; Müller, U.; Tiwari, A. N.; Buecheler, S.; Bodnarchuk, M. I.; Kovalenko, M. V. Aluminum Chloride-Graphite Batteries with Flexible Current Collectors Prepared from Earth-Abundant Elements. *Advanced Science* **2018**, *5* (4), 1700712. https://doi.org/10.1002/advs.201700712.
(44) Jiao, H.; Wang, J.; Tu, J.; Lei, H.; Jiao, S. Aluminum-Ion Asymmetric Supercapacitor Incorporating Carbon Nanotubes and an Ionic Liquid Electrolyte: Al/$AlCl_3$-[EMIm]Cl/CNTs. *Energy Tech* **2016**, *4* (9), 1112–1118. https://doi.org/10.1002/ente.201600125.
(45) Kravchyk, K. V.; Wang, S.; Piveteau, L.; Kovalenko, M. V. Efficient Aluminum Chloride–Natural Graphite Battery. *Chem. Mater.* **2017**, *29* (10), 4484–4492. https://doi.org/10.1021/acs.chemmater.7b01060.
(46) Chen, C.-Y.; Tsuda, T.; Kuwabata, S.; Hussey, C. L. Rechargeable Aluminum Batteries Utilizing a Chloroaluminate Inorganic Ionic Liquid Electrolyte. *Chem. Commun.* **2018**, *54* (33), 4164–4167. https://doi.org/10.1039/C8CC00113H.
(47) Yolshina, L. A.; Shevelin, P. Yu.; Druzhinin, K. V.; Elterman, V. A.; Yolshina, V. A.; Muradymov, R. V. Fast-Charged Aluminum-Ion Battery with Aluminum-Graphene Nanocomposite Anode. *Ionics* **2021**, *27* (1), 249–258. https://doi.org/10.1007/s11581-020-03799-9.
(48) Xu, C.; Zhao, S.; Du, Y.; Wang, Z.; Zhang, J. AlCl3/Pyridinium Chloride Electrolyte-Based Rechargeable Aluminum Ion Battery. *Materials Letters* **2020**, *275*, 128040. https://doi.org/10.1016/j.matlet.2020.128040.
(49) Agiorgousis, M. L.; Sun, Y.-Y.; Zhang, S. The Role of Ionic Liquid Electrolyte in an Aluminum–Graphite Electrochemical Cell. *ACS Energy Lett.* **2017**, *2* (3), 689–693. https://doi.org/10.1021/acsenergylett.7b00110.
(50) Bhauriyal, P.; Mahata, A.; Pathak, B. The Staging Mechanism of $AlCl_4$ Intercalation in a Graphite Electrode for an Aluminium-Ion Battery. *Phys. Chem. Chem. Phys.* **2017**, *19* (11), 7980–7989. https://doi.org/10.1039/C7CP00453B.
(51) Wu, M. S.; Xu, B.; Chen, L. Q.; Ouyang, C. Y. Geometry and Fast Diffusion of AlCl4 Cluster Intercalated in Graphite. *Electrochimica Acta* **2016**, *195*, 158–165. https://doi.org/10.1016/j.electacta.2016.02.144.
(52) Liang, Y.; Yao, Y. Halfway Through. *Nat Energy* **2018**, *4* (1), 10–11. https://doi.org/10.1038/s41560-018-0300-3.
(53) Bitenc, J.; Lindahl, N.; Vizintin, A.; Abdelhamid, M. E.; Dominko, R.; Johansson, P. Concept and Electrochemical Mechanism of an Al Metal Anode – Organic Cathode Battery. *Energy Storage Materials* **2020**, *24*, 379–383. https://doi.org/10.1016/j.ensm.2019.07.033.
(54) Wang, S.; Huang, S.; Yao, M.; Zhang, Y.; Niu, Z. Engineering Active Sites of Polyaniline for $AlCl_2^+$ Storage in an Aluminum-Ion Battery. *Angew Chem Int Ed* **2020**, *59* (29), 11800–11807. https://doi.org/10.1002/anie.202002132.
(55) Yoo, D.-J.; Heeney, M.; Glöcklhofer, F.; Choi, J. W. Tetradiketone Macrocycle for Divalent Aluminium Ion Batteries. *Nat Commun* **2021**, *12* (1), 2386. https://doi.org/10.1038/s41467-021-22633-y.
(56) Canever, N.; Nann, T. Unraveling the Multivalent Aluminium-Ion Redox Mechanism in 3,4,9,10-Perylenetetracarboxylic Dianhydride (PTCDA). *Phys.*

Chem. Chem. Phys. **2022**, *24* (10), 5886–5893. https://doi.org/10.1039/D1CP05716B.
(57) Donahue, F. M.; Mancini, S. E.; Simonsen, L. Secondary Aluminium-Iron (III) Chloride Batteries with a Low Temperature Molten Salt Electrolyte. *J Appl Electrochem* **1992**, *22* (3), 230–234. https://doi.org/10.1007/BF01030182.
(58) Suto, K.; Nakata, A.; Murayama, H.; Hirai, T.; Yamaki, J.; Ogumi, Z. Electrochemical Properties of Al/Vanadium Chloride Batteries with $AlCl_3$-1-Ethyl-3-Methylimidazolium Chloride Electrolyte. *J. Electrochem. Soc.* **2016**, *163* (5), A742–A747. https://doi.org/10.1149/2.0991605jes.
(59) Wu, F.; Yang, H.; Bai, Y.; Wu, C. Paving the Path toward Reliable Cathode Materials for Aluminum-Ion Batteries. *Advanced Materials* **2019**, *31* (16), 1806510. https://doi.org/10.1002/adma.201806510.
(60) Jadhav, A. L.; Xu, J. H.; Messinger, R. J. Quantitative Molecular-Level Understanding of Electrochemical Aluminum-Ion Intercalation into a Crystalline Battery Electrode. *ACS Energy Lett.* **2020**, *5* (9), 2842–2848. https://doi.org/10.1021/acsenergylett.0c01138.
(61) Geng, L.; Lv, G.; Xing, X.; Guo, J. Reversible Electrochemical Intercalation of Aluminum in Mo_6S_8. *Chem. Mater.* **2015**, *27* (14), 4926–4929. https://doi.org/10.1021/acs.chemmater.5b01918.
(62) Geng, L.; Scheifers, J. P.; Zhang, J.; Bozhilov, K. N.; Fokwa, B. P. T.; Guo, J. Crystal Structure Transformation in Chevrel Phase Mo_6S_8 Induced by Aluminum Intercalation. *Chem. Mater.* **2018**, *30* (23), 8420–8425. https://doi.org/10.1021/acs.chemmater.8b03312.
(63) Li, Z.; Gao, C.; Zhang, J.; Meng, A.; Zhang, H.; Yang, L. Mountain-like Nanostructured 3D Ni3S2 on Ni Foam for Rechargeable Aluminum Battery and Its Theoretical Analysis on Charge/Discharge Mechanism. *Journal of Alloys and Compounds* **2019**, *798*, 500–506. https://doi.org/10.1016/j.jallcom.2019.05.270.
(64) Hu, Y.; Ye, D.; Luo, B.; Hu, H.; Zhu, X.; Wang, S.; Li, L.; Peng, S.; Wang, L. A Binder-Free and Free-Standing Cobalt Sulfide@Carbon Nanotube Cathode Material for Aluminum-Ion Batteries. *Advanced Materials* **2018**, *30* (2), 1703824. https://doi.org/10.1002/adma.201703824.
(65) Latha, M.; Vatsala Rani, J. WS_2/Graphene Composite as Cathode for Rechargeable Aluminum-Dual Ion Battery. *J. Electrochem. Soc.* **2020**, *167* (7), 070501. https://doi.org/10.1149/2.0012007JES.
(66) Li, Z.; Niu, B.; Liu, J.; Li, J.; Kang, F. Rechargeable Aluminum-Ion Battery Based on MoS_2 Microsphere Cathode. *ACS Appl. Mater. Interfaces* **2018**, *10* (11), 9451–9459. https://doi.org/10.1021/acsami.8b00100.
(67) Yang, W.; Lu, H.; Cao, Y.; Xu, B.; Deng, Y.; Cai, W. Flexible Free-Standing MoS_2 /Carbon Nanofibers Composite Cathode for Rechargeable Aluminum-Ion Batteries. *ACS Sustainable Chem. Eng.* **2019**, *7* (5), 4861–4867. https://doi.org/10.1021/acssuschemeng.8b05292.
(68) Geng, L.; Scheifers, J. P.; Fu, C.; Zhang, J.; Fokwa, B. P. T.; Guo, J. Titanium Sulfides as Intercalation-Type Cathode Materials for Rechargeable Aluminum Batteries. *ACS Appl. Mater. Interfaces* **2017**, *9* (25), 21251–21257. https://doi.org/10.1021/acsami.7b04161.
(69) Ju, S.; Chen, X.; Yang, Z.; Xia, G.; Yu, X. Atomic Scale Understanding of Aluminum Intercalation into Layered TiS2 and Its Electrochemical Properties.

Journal of Energy Chemistry **2020**, *43*, 116–120. https://doi.org/10.1016/j.jechem.2019.09.003.
(70) Wu, L.; Sun, R.; Xiong, F.; Pei, C.; Han, K.; Peng, C.; Fan, Y.; Yang, W.; An, Q.; Mai, L. A Rechargeable Aluminum-Ion Battery Based on a VS_2 Nanosheet Cathode. *Phys. Chem. Chem. Phys.* **2018**, *20* (35), 22563–22568. https://doi.org/10.1039/C8CP04772C.
(71) Barbosa, J.; Prestipino, C.; Hernandez, O. J.; Paofai, S.; Dejoie, C.; Guilloux-Viry, M.; Boulanger, C. In Situ Synchrotron Powder Diffraction Study of Cd Intercalation into Chevrel Phases: Crystal Structure and Kinetic Effect. *Inorg. Chem.* **2019**, *58* (3), 2158–2168. https://doi.org/10.1021/acs.inorgchem.8b03259.
(72) Lei, H.; Wang, M.; Tu, J.; Jiao, S. Single-Crystal and Hierarchical VSe_2 as an Aluminum-Ion Battery Cathode. *Sustainable Energy Fuels* **2019**, *3* (10), 2717–2724. https://doi.org/10.1039/C9SE00288J.
(73) Yang, W.; Lu, H.; Cao, Y.; Jing, P.; Hu, X.; Yu, H. A Flexible Free-Standing Cathode Based on Graphene-like MoSe2 Nanosheets Anchored on N-Doped Carbon Nanofibers for Rechargeable Aluminum-Ion Batteries. *Ionics* **2020**, *26* (7), 3405–3413. https://doi.org/10.1007/s11581-020-03476-x.
(74) Yu, Z.; Jiao, S.; Tu, J.; Luo, Y.; Song, W.-L.; Jiao, H.; Wang, M.; Chen, H.; Fang, D. Rechargeable Nickel Telluride/Aluminum Batteries with High Capacity and Enhanced Cycling Performance. *ACS Nano* **2020**, *14* (3), 3469–3476. https://doi.org/10.1021/acsnano.9b09550.
(75) Cohn, G.; Ma, L.; Archer, L. A. A Novel Non-Aqueous Aluminum Sulfur Battery. *Journal of Power Sources* **2015**, *283*, 416–422. https://doi.org/10.1016/j.jpowsour.2015.02.131.
(76) Gao, T.; Li, X.; Wang, X.; Hu, J.; Han, F.; Fan, X.; Suo, L.; Pearse, A. J.; Lee, S. B.; Rubloff, G. W.; Gaskell, K. J.; Noked, M.; Wang, C. A Rechargeable Al/S Battery with an Ionic-Liquid Electrolyte. *Angew Chem Int Ed* **2016**, *55* (34), 9898–9901. https://doi.org/10.1002/anie.201603531.
(77) Zhang, K.; Lee, T. H.; Cha, J. H.; Varma, R. S.; Choi, J.-W.; Jang, H. W.; Shokouhimehr, M. Two-Dimensional Boron Nitride as a Sulfur Fixer for High Performance Rechargeable Aluminum-Sulfur Batteries. *Sci Rep* **2019**, *9* (1), 13573. https://doi.org/10.1038/s41598-019-50080-9.
(78) Huang, X.; Liu, Y.; Liu, C.; Zhang, J.; Noonan, O.; Yu, C. Rechargeable Aluminum–Selenium Batteries with High Capacity. *Chem. Sci.* **2018**, *9* (23), 5178–5182. https://doi.org/10.1039/C8SC01054D.
(79) Jiao, H.; Tian, D.; Li, S.; Fu, C.; Jiao, S. A Rechargeable Al–Te Battery. *ACS Appl. Energy Mater.* **2018**, *1* (9), 4924–4930. https://doi.org/10.1021/acsaem.8b00905.
(80) Choi, S.; Go, H.; Lee, G.; Tak, Y. Electrochemical Properties of an Aluminum Anode in an Ionic Liquid Electrolyte for Rechargeable Aluminum-Ion Batteries. *Phys. Chem. Chem. Phys.* **2017**, *19* (13), 8653–8656. https://doi.org/10.1039/C6CP08776K.
(81) Giraldo, D. A.; Almodóvar, P.; Álvarez-Serrano, I.; Chacón, J.; López, M. L. Electrochemical Performance of Tunnelled and Layered MnO_2 Electrodes in Aluminium-Ion Batteries: A Matter of Dimensionality. *J. Electrochem. Soc.* **2022**, *169* (10), 100538. https://doi.org/10.1149/1945-7111/ac9a7a.

(82) Wang, W.; Jiang, B.; Xiong, W.; Sun, H.; Lin, Z.; Hu, L.; Tu, J.; Hou, J.; Zhu, H.; Jiao, S. A New Cathode Material for Super-Valent Battery Based on Aluminium Ion Intercalation and Deintercalation. *Sci Rep* **2013**, *3* (1), 3383. https://doi.org/10.1038/srep03383.
(83) Wang, H.; Bai, Y.; Chen, S.; Luo, X.; Wu, C.; Wu, F.; Lu, J.; Amine, K. Binder-Free V_2O_5 Cathode for Greener Rechargeable Aluminum Battery. *ACS Appl. Mater. Interfaces* **2015**, *7* (1), 80–84. https://doi.org/10.1021/am508001h.
(84) Chiku, M.; Takeda, H.; Matsumura, S.; Higuchi, E.; Inoue, H. Amorphous Vanadium Oxide/Carbon Composite Positive Electrode for Rechargeable Aluminum Battery. *ACS Appl. Mater. Interfaces* **2015**, *7* (44), 24385–24389. https://doi.org/10.1021/acsami.5b06420.
(85) Gu, S.; Wang, H.; Wu, C.; Bai, Y.; Li, H.; Wu, F. Confirming Reversible Al^{3+} Storage Mechanism through Intercalation of Al^{3+} into V_2O_5 Nanowires in a Rechargeable Aluminum Battery. *Energy Storage Materials* **2017**, *6*, 9–17. https://doi.org/10.1016/j.ensm.2016.09.001.
(86) Das, S. K.; Palaniselvam, T.; Adelhelm, P. Electrochemical Study on the Rechargeability of TiO2 as Electrode Material for Al-Ion Batteries with Chloroaluminate Ionic Liquid Electrolyte. *Solid State Ionics* **2019**, *340*, 115017. https://doi.org/10.1016/j.ssi.2019.115017.
(87) Wang, S.; Kravchyk, K. V.; Pigeot-Rémy, S.; Tang, W.; Krumeich, F.; Wörle, M.; Bodnarchuk, M. I.; Cassaignon, S.; Durupthy, O.; Zhao, S.; Sanchez, C.; Kovalenko, M. V. Anatase TiO_2 Nanorods as Cathode Materials for Aluminum-Ion Batteries. *ACS Appl. Nano Mater.* **2019**, *2* (10), 6428–6435. https://doi.org/10.1021/acsanm.9b01391.
(88) Zhu, N.; Wu, F.; Wang, Z.; Ling, L.; Yang, H.; Gao, Y.; Guo, S.; Suo, L.; Li, H.; Xu, H.; Bai, Y.; Wu, C. Reversible Al3+ Storage Mechanism in Anatase TiO2 Cathode Material for Ionic Liquid Electrolyte-Based Aluminum-Ion Batteries. *Journal of Energy Chemistry* **2020**, *51*, 72–80. https://doi.org/10.1016/j.jechem.2020.03.032.
(89) Tang, W.; Xuan, J.; Wang, H.; Zhao, S.; Liu, H. Aluminum Intercalation and Transport in TiO2(B) from First Principles. *Journal of Energy Storage* **2019**, *24*, 100800. https://doi.org/10.1016/j.est.2019.100800.
(90) Wen, X.; Liu, Y.; Jadhav, A.; Zhang, J.; Borchardt, D.; Shi, J.; Wong, B. M.; Sanyal, B.; Messinger, R. J.; Guo, J. Materials Compatibility in Rechargeable Aluminum Batteries: Chemical and Electrochemical Properties between Vanadium Pentoxide and Chloroaluminate Ionic Liquids. *Chem. Mater.* **2019**, *31* (18), 7238–7247. https://doi.org/10.1021/acs.chemmater.9b01556.
(91) Famprikis, T.; Bouyanfif, H.; Canepa, P.; Zbiri, M.; Dawson, J. A.; Suard, E.; Fauth, F.; Playford, H. Y.; Dambournet, D.; Borkiewicz, O. J.; Courty, M.; Clemens, O.; Chotard, J.-N.; Islam, M. S.; Masquelier, C. Insights into the Rich Polymorphism of the Na^+ Ion Conductor Na_3PS_4 from the Perspective of Variable-Temperature Diffraction and Spectroscopy. *Chem. Mater.* **2021**, *33* (14), 5652–5667. https://doi.org/10.1021/acs.chemmater.1c01113.
(92) Ren, Y.; Zuo, X. Synchrotron X-Ray and Neutron Diffraction, Total Scattering, and Small-Angle Scattering Techniques for Rechargeable Battery Research. *Small Methods* **2018**, *2* (8), 1800064. https://doi.org/10.1002/smtd.201800064.

(93) Christiansen, T. L.; Cooper, S. R.; Jensen, K. M. Ø. There's No Place like Real-Space: Elucidating Size-Dependent Atomic Structure of Nanomaterials Using Pair Distribution Function Analysis. *Nanoscale Adv.* **2020**, *2* (6), 2234–2254. https://doi.org/10.1039/D0NA00120A.
(94) Dove, M. T.; Li, G. Review: Pair Distribution Functions from Neutron Total Scattering for the Study of Local Structure in Disordered Materials. *Nuclear Analysis* **2022**, *1* (4), 100037. https://doi.org/10.1016/j.nucana.2022.100037.
(95) Ma, J.; Reeves, K. G.; Porras Gutierrez, A.-G.; Body, M.; Legein, C.; Kakinuma, K.; Borkiewicz, O. J.; Chapman, K. W.; Groult, H.; Salanne, M.; Dambournet, D. Layered Lepidocrocite Type Structure Isolated by Revisiting the Sol–Gel Chemistry of Anatase TiO_2 : A New Anode Material for Batteries. *Chem. Mater.* **2017**, *29* (19), 8313–8324. https://doi.org/10.1021/acs.chemmater.7b02674.
(96) Hutter, J.; Iannuzzi, M.; Schiffmann, F.; VandeVondele, J. CP2K: Atomistic Simulations of Condensed Matter Systems. *WIREs Comput Mol Sci* **2014**, *4* (1), 15–25. https://doi.org/10.1002/wcms.1159.
(97) VandeVondele, J.; Krack, M.; Mohamed, F.; Parrinello, M.; Chassaing, T.; Hutter, J. Quickstep: Fast and Accurate Density Functional Calculations Using a Mixed Gaussian and Plane Waves Approach. *Computer Physics Communications* **2005**, *167* (2), 103–128. https://doi.org/10.1016/j.cpc.2004.12.014.
(98) VandeVondele, J.; Hutter, J. Gaussian Basis Sets for Accurate Calculations on Molecular Systems in Gas and Condensed Phases. *The Journal of Chemical Physics* **2007**, *127* (11), 114105. https://doi.org/10.1063/1.2770708.
(99) Goedecker, S.; Teter, M.; Hutter, J. Separable Dual Space Gaussian Pseudo-Potentials. *Phys. Rev. B* **1996**, *54* (3), 1703–1710. https://doi.org/10.1103/PhysRevB.54.1703.
(100) Coretti, A.; Bacon, C.; Berthin, R.; Serva, A.; Scalfi, L.; Chubak, I.; Goloviznina, K.; Haefele, M.; Marin-Laflèche, A.; Rotenberg, B.; Bonella, S.; Salanne, M. MetalWalls: Simulating Electrochemical Interfaces between Polarizable Electrolytes and Metallic Electrodes. *The Journal of Chemical Physics* **2022**, *157* (18), 184801. https://doi.org/10.1063/5.0101777.
(101) Canongia Lopes, J. N.; Deschamps, J.; Pádua, A. A. H. Modeling Ionic Liquids Using a Systematic All-Atom Force Field. *J. Phys. Chem. B* **2004**, *108* (6), 2038–2047. https://doi.org/10.1021/jp0362133.
(102) Salanne, M.; Siqueira, L. J. A.; Seitsonen, A. P.; Madden, P. A.; Kirchner, B. From Molten Salts to Room Temperature Ionic Liquids: Simulation Studies on Chloroaluminate Systems. *Faraday Discuss.* **2012**, *154*, 171–188. https://doi.org/10.1039/C1FD00053E.
(103) Brehm, M.; Kirchner, B. A Free Analyzer and Visualizer for Monte Carlo and Molecular Dynamics Trajectories. *J. Chem. Inf. Model.* **2011**, *51* (8), 2007–2023. https://doi.org/10.1021/ci200217w.
(104) Elgrishi, N.; Rountree, K. J.; McCarthy, B. D.; Rountree, E. S.; Eisenhart, T. T.; Dempsey, J. L. A Practical Beginner's Guide to Cyclic Voltammetry. *J. Chem. Educ.* **2018**, *95* (2), 197–206. https://doi.org/10.1021/acs.jchemed.7b00361.
(105) Sandford, C.; Edwards, M. A.; Klunder, K. J.; Hickey, D. P.; Li, M.; Barman, K.; Sigman, M. S.; White, H. S.; Minteer, S. D. A Synthetic Chemist's Guide to Electroanalytical Tools for Studying Reaction Mechanisms. *Chem. Sci.* **2019**, *10* (26), 6404–6422. https://doi.org/10.1039/C9SC01545K.

(106) Talaie, E.; Bonnick, P.; Sun, X.; Pang, Q.; Liang, X.; Nazar, L. F. Methods and Protocols for Electrochemical Energy Storage Materials Research. *Chem. Mater.* **2017**, *29* (1), 90–105. https://doi.org/10.1021/acs.chemmater.6b02726.
(107) Poetz, S.; Handel, P.; Fauler, G.; Fuchsbichler, B.; Schmuck, M.; Koller, S. Evaluation of Decomposition Products of EMImCl·1.5AlCl3 during Aluminium Electrodeposition with Different Analytical Methods. *RSC Adv.* **2014**, *4* (13), 6685. https://doi.org/10.1039/c3ra46249h.
(108) Kang, S. Design of New Electrode Materials by Soft Chemistry for Multivalent Ion Batteries. *Sorbonne Université* **2020**.
(109) Sun, H.; Wang, W.; Yu, Z.; Yuan, Y.; Wang, S.; Jiao, S. A New Aluminium-Ion Battery with High Voltage, High Safety and Low Cost. *Chem. Commun.* **2015**, *51* (59), 11892–11895. https://doi.org/10.1039/C5CC00542F.
(110) Jiao, S.; Lei, H.; Tu, J.; Zhu, J.; Wang, J.; Mao, X. An Industrialized Prototype of the Rechargeable Al/$AlCl_3$-[EMIm]Cl/Graphite Battery and Recycling of the Graphitic Cathode into Graphene. *Carbon* **2016**, *109*, 276–281. https://doi.org/10.1016/j.carbon.2016.08.027.
(111) Kravchyk, K. V.; Kovalenko, M. V. The Pitfalls in Nonaqueous Electrochemistry of Al-Ion and Al Dual-Ion Batteries. *Advanced Energy Materials* **2020**, *10* (45), 2002151. https://doi.org/10.1002/aenm.202002151.
(112) Shi, J.; Zhang, J.; Guo, J. Avoiding Pitfalls in Rechargeable Aluminum Batteries Research. *ACS Energy Lett.* **2019**, *4* (9), 2124–2129. https://doi.org/10.1021/acsenergylett.9b01285.
(113) Kim, Y.-S.; Harris, K. D.; Limoges, B.; Balland, V. On the Unsuspected Role of Multivalent Metal Ions on the Charge Storage of a Metal Oxide Electrode in Mild Aqueous Electrolytes. *Chem. Sci.* **2019**, *10* (38), 8752–8763. https://doi.org/10.1039/C9SC02397F.
(114) Balland, V.; Mateos, M.; Harris, K. D.; Limoges, B. The Role of Al3+-Based Aqueous Electrolytes in the Charge Storage Mechanism of MnOx Cathodes.
(115) Trémillon, B.; Letisse, G. Proprietes en solution dans le tetrachloroaluminate de sodium fondu I. systemes “acide-base.” *Journal of Electroanalytical Chemistry and Interfacial Electrochemistry* **1968**, *17* (3–4), 371–386. https://doi.org/10.1016/S0022-0728(68)80217-7.
(116) Kujime, T.; Ando, F.; Gunji, T.; Matsumoto, F. Review of the Electrochemical Deposition of an Aluminum Layer Using Aprotic Solvents, Old and New Solvents, Additives, and New Technologies. *Curr. Top. Electrochem 21* (1–20).
(117) Kravchyk, K. V.; Kovalenko, M. V. Aluminum Electrolytes for Al Dual-Ion Batteries. *Commun Chem* **2020**, *3* (1), 120. https://doi.org/10.1038/s42004-020-00365-2.
(118) Torsi, G.; Mamantov, G. Acid-Base Properties of the Systems Aluminum Chloride-Metal Chloride (Metal = Lithium, Sodium, Potassium, Cesium). *Inorg. Chem.* **1972**, *11* (6), 1439–1439. https://doi.org/10.1021/ic50112a059.
(119) Ødegard, R.; Bjørgum, A.; Sterten, Å.; Thonstad, J.; Tunold, R. Kinetics of Aluminium Deposition from Aluminium Chloride—Alkali Chloride Melts. *Electrochimica Acta* **1982**, *27* (11), 1595–1598. https://doi.org/10.1016/0013-4686(82)80085-6.
(120) Trémillon, B.; Bermond, A.; Molina, R. Electrochemistry in Molten $NaAlCl_4$ (at 210°C): Identification of Dissolved Oxide-Containing Species, Solubility of

Alumina in Terms of pCl^- and Properties Related to H_2O in This Melt. *Journal of Electroanalytical Chemistry and Interfacial Electrochemistry* **1976**, *74* (1), 53–67. https://doi.org/10.1016/S0022-0728(76)80213-6.
(121) Rytter, E.; Øye, H. A.; Cyvin, S. J.; Cyvin, B. N. Raman Spectra of $AlCl_3$-AlkCl and Trends in Species Formation. *Journal of Inorganic and Nuclear Chemistry* **1973**, *35* (4), 1185–1198. https://doi.org/10.1016/0022-1902(73)80191-5.
(122) Wang, Q.; Zhang, Q.; Lu, X.; Zhang, S. Electrodeposition of Al from Chloroaluminate Ionic Liquids with Different Cations. *Ionics* **2017**, *23* (9), 2449–2455. https://doi.org/10.1007/s11581-017-2074-1.
(123) Fannin, A. A.; Floreani, D. A.; King, L. A.; Landers, J. S.; Piersma, B. J.; Stech, D. J.; Vaughn, R. L.; Wilkes, J. S.; Williams, J. L. Properties of 1,3-Dialkylimidazolium Chloride-Aluminum Chloride Ionic Liquids. 2. Phase Transitions, Densities, Electrical Conductivities, and Viscosities. *J. Phys. Chem.* **1984**, *88* (12), 2614–2621. https://doi.org/10.1021/j150656a038.
(124) Karthika, B.; Mohan, S.; Bera, A.; Rajasekaran, N. Structure, Microstructure and Electrodeposition Behaviours of Aluminium from $AlCl_3$-EMIC and $AlCl_3$-BMIC Ionic Liquid Electrolytes – a Comparative Study. *Surface Engineering* **2020**, *36* (9), 1012–1021. https://doi.org/10.1080/02670844.2020.1777024.
(125) Sun, X.-G.; Fang, Y.; Jiang, X.; Yoshii, K.; Tsuda, T.; Dai, S. Polymer Gel Electrolytes for Application in Aluminum Deposition and Rechargeable Aluminum Ion Batteries. *Chem. Commun.* **2016**, *52* (2), 292–295. https://doi.org/10.1039/C5CC06643C.
(126) Wang, S.; Xu, C.; Hua, Y.; Ren, X.; Lu, J.; Li, J.; Chen, X.; Xiang, Q.; Li, Y. Anodic Dissolution of Aluminum in AlCl3-[BzMIM]Cl Ionic Liquid. *Journal of Electroanalytical Chemistry* **2021**, *900*, 115715. https://doi.org/10.1016/j.jelechem.2021.115715.
(127) Lai, P. K.; Skyllas-Kazacos, M. Aluminium Deposition and Dissolution in Aluminium Chloride—n-Butylpyridinium Chloride Melts. *Electrochimica Acta* **1987**, *32* (10), 1443–1449. https://doi.org/10.1016/0013-4686(87)85083-1.
(128) Li, C.; Patra, J.; Li, J.; Rath, P. C.; Lin, M.; Chang, J. A Novel Moisture-Insensitive and Low-Corrosivity Ionic Liquid Electrolyte for Rechargeable Aluminum Batteries. *Adv Funct Materials* **2020**, *30* (12), 1909565. https://doi.org/10.1002/adfm.201909565.
(129) Mukundan, C.; Eckert, M.; Drillet, J. Impact of Aluminium Electrode Potential during Charging on Aluminium-Ion Battery Performance with TEA-$AlCl_3$ Electrolyte. *Batteries & Supercaps* **2023**, *6* (6), e202300042. https://doi.org/10.1002/batt.202300042.
(130) Liu, X.; Li, S.; Wang, D.; Ma, Y.; Liu, X.; Ning, M. Theoretical Study on the Structure and Cation–Anion Interaction of Triethylammonium Chloroaluminate Ionic Liquid. *Computational and Theoretical Chemistry* **2015**, *1073*, 67–74. https://doi.org/10.1016/j.comptc.2015.09.012.
(131) Su, C.-J.; Hsieh, Y.-T.; Chen, C.-C.; Sun, I.-W. Electrodeposition of Aluminum Wires from the Lewis Acidic AlCl3/Trimethylamine Hydrochloride Ionic Liquid without Using a Template. *Electrochemistry Communications* **2013**, *34*, 170–173. https://doi.org/10.1016/j.elecom.2013.05.040.
(132) Jiang, T.; Chollier Brym, M. J.; Dubé, G.; Lasia, A.; Brisard, G. M. Electrodeposition of Aluminium from Ionic Liquids: Part II - Studies on the

Electrodeposition of Aluminum from Aluminum Chloride (AICl3) - Trimethylphenylammonium Chloride (TMPAC) Ionic Liquids. *Surface and Coatings Technology* **2006**, *201* (1–2), 10–18. https://doi.org/10.1016/j.surfcoat.2005.12.024.
(133) Paterno, D.; Rock, E.; Forbes, A.; Iqbal, R.; Mohammad, N.; Suarez, S. Aluminum Ions Speciation and Transport in Acidic Deep Eutectic AlCl3 Amide Electrolytes. *Journal of Molecular Liquids* **2020**, *319*, 114118. https://doi.org/10.1016/j.molliq.2020.114118.
(134) Li, M.; Gao, B.; Liu, C.; Chen, W.; Wang, Z.; Shi, Z.; Hu, X. AlCl3/Amide Ionic Liquids for Electrodeposition of Aluminum. *J Solid State Electrochem* **2017**, *21* (2), 469–476. https://doi.org/10.1007/s10008-016-3384-3.
(135) Abood, H. M. A.; Abbott, A. P.; Ballantyne, A. D.; Ryder, K. S. Do All Ionic Liquids Need Organic Cations? Characterisation of $[AlCl_2{\cdot}nAmide]^+$ $AlCl_4^-$ and Comparison with Imidazolium Based Systems. *Chem. Commun.* **2011**, *47* (12), 3523. https://doi.org/10.1039/c0cc04989a.
(136) Angell, M.; Zhu, G.; Lin, M.; Rong, Y.; Dai, H. Ionic Liquid Analogs of $AlCl_3$ with Urea Derivatives as Electrolytes for Aluminum Batteries. *Adv Funct Materials* **2020**, *30* (4), 1901928. https://doi.org/10.1002/adfm.201901928.
(137) Abood, H. M. A.; Fadhil, M. H. Investigation of Lewis Acid-Base Reaction of Acidic Species Present in Aluminum Chloride-Urea Ionic Liquid $[AlCl_2.nUrea]^+$. *Al-Nahrain Journal of Science* **2014**, *17* (1), 71–75.
(138) Abbott, A. P.; Harris, R. C.; Hsieh, Y.-T.; Ryder, K. S.; Sun, I.-W. Aluminium Electrodeposition under Ambient Conditions. *Phys. Chem. Chem. Phys.* **2014**, *16* (28), 14675–14681. https://doi.org/10.1039/C4CP01508H.
(139) Angell, M.; Pan, C.-J.; Rong, Y.; Yuan, C.; Lin, M.-C.; Hwang, B.-J.; Dai, H. High Coulombic Efficiency Aluminum-Ion Battery Using an $AlCl_3$ -Urea Ionic Liquid Analog Electrolyte. *Proc. Natl. Acad. Sci. U.S.A.* **2017**, *114* (5), 834–839. https://doi.org/10.1073/pnas.1619795114.
(140) Wen, X.; Liu, Y.; Xu, D.; Zhao, Y.; Lake, R. K.; Guo, J. Room-Temperature Electrodeposition of Aluminum via Manipulating Coordination Structure in $AlCl_3$ Solutions. *J. Phys. Chem. Lett.* **2020**, *11* (4), 1589–1593. https://doi.org/10.1021/acs.jpclett.0c00256.
(141) Peters, W.; Duong, H. T.; Lee, S.; Drillet, J.-F. Investigation of $Al(TfO)_3$-Based Deep Eutectic Solvent Electrolytes for Aluminium-Ion Batteries. Part I: Understanding the Positively Charged Al Complex Formation. *Phys. Chem. Chem. Phys.* **2021**, *23* (38), 21923–21933. https://doi.org/10.1039/D1CP01711J.
(142) Fannin, A. A.; King, L. A.; Levisky, J. A.; Wilkes, J. S. Properties of 1,3-Dialkylimidazolium Chloride-Aluminum Chloride Ionic Liquids. 1. Ion Interactions by Nuclear Magnetic Resonance Spectroscopy. *J. Phys. Chem.* **1984**, *88* (12), 2609–2614. https://doi.org/10.1021/j150656a037.
(143) Øye, H. A.; Jagtoyen, M.; Oksefjell, T.; Wilkes, J. S. Vapour Pressure and Thermodynamics of the System 1-Methyl-3-Ethyl-Imidazolium Chloride - Aluminium Chloride. *MSF* **1991**, *73–75*, 183–190. https://doi.org/10.4028/www.scientific.net/MSF.73-75.183.
(144) Takahashi, S.; Curtiss, L. A.; Gosztola, D.; Koura, N.; Saboungi, M.-L. Molecular Orbital Calculations and Raman Measurements for 1-Ethyl-3-

Methylimidazolium Chloroaluminates. *Inorg. Chem.* **1995**, *34* (11), 2990–2993. https://doi.org/10.1021/ic00115a029.
(145) Zhu, G.; Angell, M.; Pan, C.-J.; Lin, M.-C.; Chen, H.; Huang, C.-J.; Lin, J.; Achazi, A. J.; Kaghazchi, P.; Hwang, B.-J.; Dai, H. Rechargeable Aluminum Batteries: Effects of Cations in Ionic Liquid Electrolytes. *RSC Adv.* **2019**, *9* (20), 11322–11330. https://doi.org/10.1039/C9RA00765B.
(146) Ferrara, C.; Dall'Asta, V.; Berbenni, V.; Quartarone, E.; Mustarelli, P. Physicochemical Characterization of $AlCl_3$–1-Ethyl-3-Methylimidazolium Chloride Ionic Liquid Electrolytes for Aluminum Rechargeable Batteries. *J. Phys. Chem. C* **2017**, *121* (48), 26607–26614. https://doi.org/10.1021/acs.jpcc.7b07562.
(147) Gibson, L. D.; Roy, S.; Khanal, R.; Chahal, R.; Sedova, A.; Bryantsev, V. Tracing Mechanistic Pathways and Reaction Kinetics Toward Equilibrium in Reactive Molten Salts. *Chem. Sci.* **2024**, 10.1039.D3SC06587A. https://doi.org/10.1039/D3SC06587A.
(148) Zheng, Y.; Zheng, Y.; Wang, Q.; Wang, Z.; Tian, D. Density and Viscosity of Binary Mixtures of 1-Ethyl-3-Methylimidazolium Heptachlorodialuminate and Tetrachloroaluminate Ionic Liquids. *J. Chem. Eng. Data* **2017**, *62* (11), 4006–4014. https://doi.org/10.1021/acs.jced.7b00702.
(149) Wilkes, J. S.; Frye, J. S.; Reynolds, G. F. Aluminum-27 and Carbon-13 NMR Studies of Aluminum Chloride-Dialkylimidazolium Chloride Molten Salts. *Inorg. Chem.* **1983**, *22* (26), 3870–3872. https://doi.org/10.1021/ic00168a011.
(150) Sutrisno, H.; Sunarto, S. Polymorphic Transformation of Titanium Dioxide Caused by Heat Treatment of Protonic Lepidocrocite Titanate. *Indones. J. Chem.* **2010**, *10* (2), 143–148. https://doi.org/10.22146/ijc.21451.
(151) Sasaki, T.; Watanabe, M.; Michiue, Y.; Komatsu, Y.; Izumi, F.; Takenouchi, S. Preparation and Acid-Base Properties of a Protonated Titanate with the Lepidocrocite-like Layer Structure. *Chem. Mater.* **1995**, *7* (5), 1001–1007. https://doi.org/10.1021/cm00053a029.
(152) Toorabally, M. Development of Negative TiO2-Based Electrodes by Soft Chemistry for Aqueous Proton Ions Batteries, Sorbonne Université, 2023.
(153) Wen, X.; Liu, Y.; Jadhav, A.; Zhang, J.; Borchardt, D.; Shi, J.; Wong, B. M.; Sanyal, B.; Messinger, R. J.; Guo, J. Materials Compatibility in Rechargeable Aluminum Batteries: Chemical and Electrochemical Properties between Vanadium Pentoxide and Chloroaluminate Ionic Liquids. *Chem. Mater.* **2019**, *31* (18), 7238–7247. https://doi.org/10.1021/acs.chemmater.9b01556.
(154) Sarou-Kanian, V.; Gleizes, A. N.; Florian, P.; Samélor, D.; Massiot, D.; Vahlas, C. Temperature-Dependent 4-, 5- and 6-Fold Coordination of Aluminum in MOCVD-Grown Amorphous Alumina Films: A Very High Field ^{27}Al-NMR Study. *J. Phys. Chem. C* **2013**, *117* (42), 21965–21971. https://doi.org/10.1021/jp4077504.
(155) Černý, Z.; Macháček, J.; Fusek, J.; Čásenský, B.; Kříž, O.; Tuck, D. G. 27Al NMR Studies of the Hydrolysis of Aluminium(III) Chloride in Non-Aqueous Media. *Inorganica Chimica Acta* **2000**, *300–302*, 556–564. https://doi.org/10.1016/S0020-1693(00)00017-7.
(156) Tsuda, T.; Hussey, C. L.; Stafford, G. R.; Bonevich, J. E. Electrochemistry of Titanium and the Electrodeposition of Al-Ti Alloys in the Lewis Acidic

Aluminum Chloride–1-Ethyl-3-Methylimidazolium Chloride Melt. *J. Electrochem. Soc.* **2003**, *150* (4), C234. https://doi.org/10.1149/1.1554915.
(157) Pradhan, D.; Reddy, R. G. Electrochemical Production of Ti–Al Alloys Using TiCl4–AlCl3–1-Butyl-3-Methyl Imidazolium Chloride (BmimCl) Electrolytes. *Electrochimica Acta* **2009**, *54* (6), 1874–1880. https://doi.org/10.1016/j.electacta.2008.10.022.
(158) Carlin, R. T.; Osteryoung, R. A.; Wilkes, J. S.; Rovang, J. Studies of Titanium(IV) Chloride in a Strongly Lewis Acidic Molten Salt: Electrochemistry and Titanium NMR and Electronic Spectroscopy. *Inorg. Chem.* **1990**, *29* (16), 3003–3009. https://doi.org/10.1021/ic00341a030.
(159) Tsuda, T. Electrodeposition of Titanium-Aluminum Alloys in the Lewis Acidic Aluminum Chloride-1-Ethyl-3-Methylimidazolium Chloride Molten Salt. *Proc. Vol.* **2002**, *19* (1), 650–659. https://doi.org/10.1149/200219.0650PV.
(160) Miyaoka, H.; Kuze, T.; Sano, H.; Mori, H.; Mizutani, G.; Otsuka, N.; Terano, M. Raman Spectra of Titanium Di-, Tri-, and Tetra-Chlorides. *Int. J. Mod. Phys. B* **2001**, *15* (28n30), 3865–3868. https://doi.org/10.1142/S021797920100886X.
(161) Griffiths, J. E. Molecular Association in TiCl4: Laser Raman Spectroscopy and Chlorine Isotope Effects. *The Journal of Chemical Physics* **1968**, *49* (2), 642–647. https://doi.org/10.1063/1.1670121.
(162) Gao, L.; Wang, L.; Qi, T.; Chu, J.; Qu, J. Preparation and Characterization of Titanium Tetrachloride-Based Ionic Liquids. *J. Electrochem. Soc.* **2009**, *156* (3), P49. https://doi.org/10.1149/1.3046160.
(163) Creaser, C. S.; Creighton, J. A. Pentachloro- and Pentabromo-Titanate (IV) Ions. *J. Chem. Soc., Dalton Trans.* **1975**, No. 14, 1402–1405. https://doi.org/10.1039/DT9750001402.
(164) Fung, K. W.; Mantov, G. Electrochemistry of Titanium(II) in AlCl3+NaCl Melts. *Journal of Electroanalytical Chemistry and Interfacial Electrochemistry* **1972**, *35* (1), 27–34. https://doi.org/10.1016/S0022-0728(72)80291-2.
(165) Brynestad, J.; Von Winbush, S.; Yakel, H. L.; Smith, G. P. Titanium(II) Tetrachloroaluminate, Titanium Aluminum Pentachloride, and Solutions of Titanium(II) in Liquid Aluminum Chloride. *Inorganic and Nuclear Chemistry Letters* **1970**, *6* (12), 889–893. https://doi.org/10.1016/0020-1650(70)80070-8.
(166) Oye, H. A.; Gruen, D. M. Octahedral Absorption Spectra of the Dipositive 3d Metal Ions in Molten Aluminum Chloride. *Inorg. Chem.* **1964**, *3* (6), 836–841. https://doi.org/10.1021/ic50016a011.
(167) Stafford, G. R.; Tsuda, T.; Hussey, C. L. The Structure of Electrodeposited Aluminum Alloys from Chloroaluminate Ionic Liquids: Let's Not Ignore the Temperature. *ECS Trans.* **2014**, *64* (4), 535–547. https://doi.org/10.1149/06404.0535ecst.
(168) Stafford, G. R.; Tsuda, T.; Hussey, C. L. Order/Disorder in Electrodeposited Aluminum-Titanium Alloys. *Journal of Mining and Metallurgy, Section B: Metallurgy* **2003**, *39* (1–2), 23–42.
(169) Shinde, P. S.; Peng, Y.; Reddy, R. G. Electrodeposition of Titanium Aluminide (TiAl) Alloy from AlCl3–BMIC Ionic Liquid at Low Temperature. In *TMS 2020 149th Annual Meeting & Exhibition Supplemental Proceedings*; The Minerals, Metals & Materials Society, Ed.; The Minerals, Metals & Materials Series;

Springer International Publishing: Cham, 2020; pp 1659–1667. https://doi.org/10.1007/978-3-030-36296-6_153.
(170) Ali, M. R.; Nishikata, A.; Tsuru, T. Electrodeposition of AI-Ti Alloys from Aluminum Chloride-N-(n-Butyl)Pyridinium Chloride Room Temperature Molten Salt. *Indian Journal of Chemical Technology* **2003**, *10*, 14–20.
(171) Daud, N. M. A. N.; Bakis, E.; Hallett, J. P.; Weber, C. C.; Welton, T. Evidence for the Spontaneous Formation of N-Heterocyclic Carbenes in Imidazolium Based Ionic Liquids. *Chem. Commun.* **2017**, *53* (81), 11154–11156. https://doi.org/10.1039/C7CC06112A.
(172) Kar, B. P.; Sander, W. Reversible Carbene Formation in the Ionic Liquid 1-Ethyl-3-Methylimidazolium Acetate by Vaporization and Condensation. *ChemPhysChem* **2015**, *16* (17), 3603–3606. https://doi.org/10.1002/cphc.201500729.
(173) Albrecht, M. Normal and Abnormal N-Heterocyclic Carbene Ligands. In *Advances in Organometallic Chemistry*; Elsevier, 2014; Vol. 62, pp 111–158. https://doi.org/10.1016/B978-0-12-800976-5.00002-3.
(174) Herrmann, W. A.; Weskamp, T.; Böhm, V. P. W. Metal Complexes of Stable Carbenes. In *Advances in Organometallic Chemistry*; Elsevier, 2001; Vol. 48, pp 1–69. https://doi.org/10.1016/S0065-3055(01)48001-4.
(175) Hopkinson, M. N.; Richter, C.; Schedler, M.; Glorius, F. An Overview of N-Heterocyclic Carbenes. *Nature* **2014**, *510* (7506), 485–496. https://doi.org/10.1038/nature13384.
(176) Schnee, G.; Nieto Faza, O.; Specklin, D.; Jacques, B.; Karmazin, L.; Welter, R.; Silva López, C.; Dagorne, S. Normal-to-Abnormal NHC Rearrangement of Al^{III}, Ga^{III}, and In^{III} Trialkyl Complexes: Scope, Mechanism, Reactivity Studies, and H_2 Activation. *Chemistry A European J* **2015**, *21* (49), 17959–17972. https://doi.org/10.1002/chem.201503000.
(177) Bantu, B.; Manohar Pawar, G.; Wurst, K.; Decker, U.; Schmidt, A. M.; Buchmeiser, M. R. CO_2, Magnesium, Aluminum, and Zinc Adducts of N-Heterocyclic Carbenes as (Latent) Catalysts for Polyurethane Synthesis. *Eur J Inorg Chem* **2009**, No. 13, 1970–1976. https://doi.org/10.1002/ejic.200801161.
(178) Stasch, A.; Singh, S.; Roesky, H. W.; Noltemeyer, M.; Schmidt, H. Adducts of Aluminum and Gallium Trichloride with a N-Heterocyclic Carbene and an Adduct of Aluminum Trichloride with a Thione. *Eur J Inorg Chem* **2004**, No. 20, 4052–4055. https://doi.org/10.1002/ejic.200400247.
(179) Tonner, R.; Heydenrych, G.; Frenking, G. Bonding Analysis of N-Heterocyclic Carbene Tautomers and Phosphine Ligands in Transition-Metal Complexes: A Theoretical Study. *Chemistry An Asian Journal* **2007**, *2* (12), 1555–1567. https://doi.org/10.1002/asia.200700235.
(180) Stafford, G. R. The Electrodeposition of Al_3Ti from Chloroaluminate Electrolytes. *J. Electrochem. Soc.* **1994**, *141* (4), 945–953.
(181) Stafford, G. R.; Moffat, T. P. Electrochemistry of Titanium in Molten $2AlCl_3$-NaCl. *J. Electrochem. Soc.* **1995**, *142* (10), 3288–3296.
(182) Tsuda, T.; Hussey, C. L.; Stafford, G. R.; Bonevich, J. E. Electrochemistry of Titanium and the Electrodeposition of Al-Ti Alloys in the Lewis Acidic Aluminum Chloride–1-Ethyl-3-Methylimidazolium Chloride Melt. *J. Electrochem. Soc.* **2003**, *150* (4), C234. https://doi.org/10.1149/1.1554915.